



HAL
open science

Microfluidics at the service of intensification of distillation : design, characterization and optimization of a continuous laboratory tool

Farah El Masri

► To cite this version:

Farah El Masri. Microfluidics at the service of intensification of distillation : design, characterization and optimization of a continuous laboratory tool. Material chemistry. Université de Bordeaux; Institut français du pétrole Énergies nouvelles (Rueil-Malmaison, Hauts-de-Seine), 2021. English. NNT : 2021BORD0231 . tel-04371723

HAL Id: tel-04371723

<https://theses.hal.science/tel-04371723>

Submitted on 4 Jan 2024

HAL is a multi-disciplinary open access archive for the deposit and dissemination of scientific research documents, whether they are published or not. The documents may come from teaching and research institutions in France or abroad, or from public or private research centers.

L'archive ouverte pluridisciplinaire **HAL**, est destinée au dépôt et à la diffusion de documents scientifiques de niveau recherche, publiés ou non, émanant des établissements d'enseignement et de recherche français ou étrangers, des laboratoires publics ou privés.

THESIS PRESENTED

TO OBTAIN THE GRADE OF

DOCTOR OF

UNIVERSITY OF BORDEAUX

DOCTORAL SCHOOL OF CHEMICAL SCIENCES

PROCESS ENGINEERING

Farah EL MASRI

**MICROFLUIDICS AT THE SERVICE OF INTENSIFICATION OF DISTILLATION: DESIGN,
CHARACTERIZATION AND OPTIMIZATION OF A CONTINUOUS LABORATORY TOOL**

Under the supervision of Cyril AYMONIER and Samuel MARRE

Defended on October 6, 2021

Reviewers:

Mrs. AUBIN, Joelle
Mr. HARTMAN, Ryan

Director of Research CNRS, LGC - UMR 5503
Associate Professor, New York University

Examinators:

Mr. AYMONIER, Cyril
Mr. BERGEOT, Ghislain
Mr. BONNIN, Charles
Mr. BOUTIN, Olivier
Mr. MARRE, Samuel

Director of Research CNRS, ICMCB– UMR5026
Research Engineer, IFP Energies Nouvelles
Research Engineer, IFP Energies Nouvelles
Professor, Aix-Marseille University
Director of Research CNRS, ICMCB– UMR5026

Acknowledgement

After the completion of the PhD project “Microfluidics at the service of intensification of distillation: design, characterization and optimization of a continuous laboratory tool”, I would like to express my deepest gratitude to Mr. Denis Guillaume (director of the R15 department in IFP Energies Nouvelles), Herve Cauffriez (director of the R151 department in IFP Energies Nouvelles) and Mario Maglione (director of the ICMCB) for welcoming me to their laboratories and departments.

These years were amazing and rewarding on both personal and professional levels and they flew by very fast. I can only say that I am overwhelmed with emotions and very grateful to all my colleagues.

In the beginning, I would like to start by thanking my supervisors: Charles Bonnin, Samuel Marre, Ghislain Bergeot and Cyril Aymonier, who have provided me with guidance throughout this entire research journey, starting from my thesis title selection to finding the results. Their immense knowledge, motivation and patience have pushed me forward and inspired me to excel in this research topic. My thesis, of course, was not short of obstacles and difficulties. Conducting the academic study regarding such a difficult topic could not have been an easy task without my supervisors’ support.

Apart from my supervisors, I will not forget to express gratitude to Olivier Nguyen, who not only helped me to build the experimental setup, but also helped me on a personal level by providing me with encouragement and sharing insightful suggestions.

A special thanks to Sophie Drozd and Ninon Nafi for their appreciated help in the experimental setup and tests at IFPEN.

I would also like to thank Alexis Tourbier and Lionel Gamet who were in charge of the computational fluid dynamics simulations. They have shown great interest in the work of this thesis and contributed to fruitful and insightful scientific discussions.

Moreover, I am also pleased to say thank you to Olivier Delpoux, Corinne Sagnard, Marine Collaudin and Cedric Plassais from the Department of Material characterization in R053 for their efforts regarding Raman measurements and associated discussions. They were always dynamic and motivating. Their collaboration was very much appreciated.

Acknowledgement

I would like to thank also all the colleagues from both Supercritical fluids Group in ICMCB and Experimentation process R151 in IFPEN who made my access simpler to the research facilities and laboratory and gave me the opportunity to become a part of their team.

I will always remember my fellow ICMCB labmates: Cyrielle, Valentina, Rabie, Thomas J., Emeline, Elham, Liza, Fatima, Brian, Iulia, Gustavo, Zack, Nicolas, Erwan, Abdellatif, Issam, Thomas V. and Elen, for all the fun-times we spent together, the lunch and coffee breaks, and the many ups and downs we shared together. Their immense support is hard to forget throughout my life.

I will also not miss this chance to thank my IFPEN colleagues, especially Sabah, Judy, Alexis, Loïc, Wassim, Elsy, Mahmoud and Mohammad for their support, motivation, unforgettable lunch and coffee breaks and all the precious moments we shared on both personal and professional levels. It wouldn't have been possible to conduct this research without their precious support. They all really mean a lot to me.

Last but not least, I am grateful to my parents, my brothers (Nachaat and Ziad), friends (Maya, Nadine, Lara, Tarek, Moustafa, Jacinthe, Tonina, Elise and all the ones that I could have missed) and all acquaintances who remembered me in their prayers and were always there to help me, listen to me and motivate me. They were the main reason behind this success. I consider myself nothing without them. They gave me the moral support, encouragement and motivation that pushed me to accomplish all the personal goals that I have set for myself.

At the end, I dedicate the whole work to my mother, father and both brothers because without them I would have never been the person I am today and would have never achieved and reached this success.

Résumé de la thèse

Les colonnes de distillation classiques utilisées dans les procédés de séparation sont généralement de grande taille, limitant ainsi leur utilisation aux procédés semi- ou industriels. Par conséquent, ils ne sont pas toujours adaptés aux procédés de synthèse en continu à plusieurs étapes ou à des fins de recherche, pour lesquels les quantités de fluides et les débits utilisés sont faibles. Par conséquent, il existe un besoin croissant d'unités de microdistillation robustes capables de fonctionner avec des débits de fluides inférieurs au $\text{mL}\cdot\text{h}^{-1}$, qui pourraient être connectées à la sortie d'une usine pilote à petite échelle ou de prototypes de recherche.

La réduction d'échelle de la distillation se heurte à plusieurs difficultés : en premier lieu, à l'échelle de quelques dizaines de microns, l'effet de la gravité (force motrice de la séparation gaz-liquide dans les colonnes de distillation classiques) s'efface au profit des forces de surface. Il est alors nécessaire de proposer des conceptions utilisant les forces capillaires afin d'établir l'écoulement entre les phases liquide et vapeur. La caractérisation de ces écoulements et du transfert entre les phases ainsi que la compréhension des phénomènes qui les régissent est un préalable incontournable à l'optimisation de l'efficacité de la séparation. Par ailleurs, les principaux obstacles au développement de la distillation aux petites échelles sont le contrôle des pertes de chaleur, du profil thermique, et du reflux. En effet, la miniaturisation induit l'accroissement du rapport surface sur volume qui va exacerber les problèmes de perte de chaleur aux parois. Le contrôle de la température et du soutirage sont des verrous technologiques essentiels à lever pour une distillation stable et efficace.

Dans ce contexte, le premier chapitre de la thèse récapitule les différentes études déjà réalisées sur la problématique de miniaturisation de dispositifs de distillation continue. Les études sont principalement divisées en trois catégories : (i) les microdistillations en mode fermé, (ii) les microdistillations continues de taille intermédiaire (traitant des débits entre 5 et $30 \text{ mL}\cdot\text{h}^{-1}$) et (iii) les microdistillations continues sur puce. Les mises en œuvre peuvent être assez différentes : structure ordonnée de piliers lorsqu'il s'agit d'une puce de silicium, mousse métallique entre deux plaques ou autres éléments à forte porosité dans le cas de dispositifs de plus grandes tailles; la majorité des dispositifs repose sur des phénomènes capillaires pour séparer les écoulements gaz et liquide. Quelques-unes seront détaillées ci-dessous.

La première étude sur le sujet, souvent citée, est l'adaptation d'un caloduc par Seok *et al.* en 1985 [1], de 10 mm de diamètre interne et 540 mm de long. Ce type de dispositif est conçu pour échanger des calories entre une source chaude et une source froide *via* la vaporisation et la condensation d'un fluide. Un milieu poreux est utilisé en paroi du tube pour y cantonner l'écoulement liquide grâce aux forces capillaires, et permettre l'écoulement à contre-courant des phases gaz et liquide. La principale modification à apporter pour le transformer en colonne de distillation est l'ajout de points d'injection de charge et de soutirages. La hauteur d'un étage théorique dans ce type de dispositif est de l'ordre de la dizaine de centimètres, pour des débits traités d'environ 60 mL/h. Etant donné les faibles débits traités, il n'y a pas de condenseur externe.

Sundberg *et al.* ont longtemps étudié un dispositif s'inspirant de ce « design ». La colonne est constituée d'un canal de 30 mm de large, 5 mm de haut et 290 mm de long rempli partiellement ou totalement avec une mousse métallique pour aider à la stratification de l'écoulement gaz - liquide [2–5]. Les débits sont du même ordre de grandeur, mais l'efficacité est augmentée avec une hauteur

d'étage théorique de l'ordre du centimètre. L'aspect innovant dans ces travaux est l'incorporation de systèmes de reflux et de rebouilleurs externes à la colonne [5], bien que la technologie utilisée soit des plus classiques (mesure du niveau par différence de pression couplée à des pompes délivrant de petits débits). Une application intéressante de ce même dispositif est son utilisation en sortie d'un réacteur d'estérification du 2-ethoxy-2-methylbutane ; la microdistillation est utilisée pour récupérer le réactif non converti en tête de colonne et le recycler en entrée de réacteur. Plus récemment, l'équipe a étudié un système de microdistillation obtenu par impression 3D [6].

La gravure sur puces de silicium peut permettre de créer des dispositifs avec moins de volumes internes, permettant d'accéder à des débits plus faibles. Peu d'équipes ont travaillé sur ce sujet. Celle de Klavs F. Jensen a étudié un système microfluidique « simple » où un seul étage théorique peut être atteint [7], et a souligné l'importance qu'aura ce type de dispositifs pour la réalisation de procédés miniaturisés [8]. Lam *et al.* ont travaillé sur des dispositifs de ce type avec des structures en pilier pour conditionner l'écoulement liquide (**Figure 1**) [9, 10]. Les débits entrants sont de l'ordre de 0,1 à 0,4 mL/h, avec une hauteur équivalente à un plateau théorique d'environ 10 cm. Compte tenu des très faibles débits mis en jeu, le soutirage est délicat et réalisé avec une seringue à un débit constant. Pour les mêmes raisons, le reflux est induit par un condenseur interne.

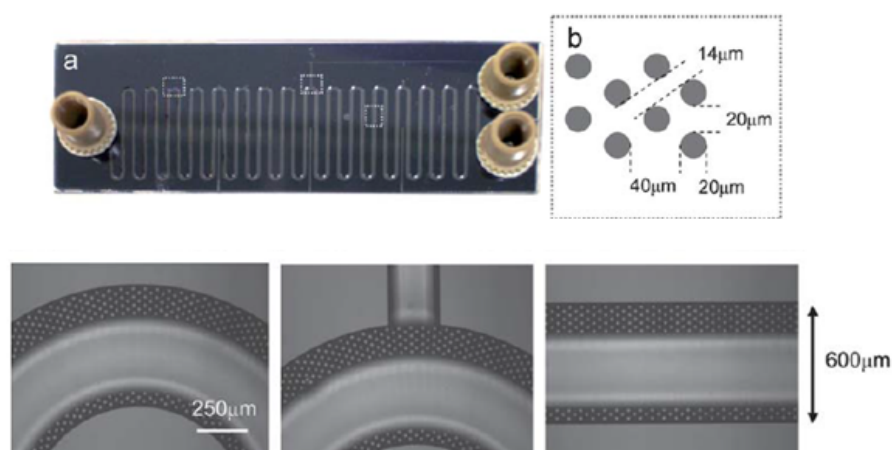


Figure 1 Microdistillation conçue par Lam *et al.* [9, 10].

Un bilan de l'état de l'art permet de montrer que les technologies de miniaturisation développées aboutissent à deux gammes de débit : de l'ordre du mL/min ou inférieur au mL/h. La gamme visée dans le cadre de la thèse est légèrement supérieure à celle utilisée dans les micropuces. Le dispositif expérimental développé pourra bénéficier de ce savoir-faire. Le verrou principal pour arriver à un dispositif complet de distillation est l'incorporation des différents périphériques pour retrouver les fonctions d'une colonne de distillation classique : maintenir un débit de soutirage constant et incorporer un système de reflux, tout en minimisant la rétention liquide du système.

Pour répondre aux limitations techniques et fondamentales et obtenir un aperçu approfondi des processus de microdistillation, ce travail de thèse avait les objectifs suivants :

- i) concevoir un canal de distillation à plusieurs étages sur puce,
- ii) développer un outil de microdistillation utilisant les forces capillaires sur puce à contre-courant continu,

iii) caractériser son comportement hydrodynamique et évaluer ses performances de distillation.

Parmi toutes les études mentionnées dans l'état de l'art, aucune ne s'est penchée sur l'étude hydrodynamique des écoulements mis en jeu dans ces dispositifs microfluidiques. De la même manière, le cas des contre-courants gaz-liquide sur micropuce n'a, à notre connaissance, pas été étudié. Le fait de s'appuyer sur les forces capillaires pour segmenter les écoulements gaz et liquide offre une grande liberté sur la géométrie de la colonne pour maximiser son efficacité, mais les données de la littérature sont à l'heure actuelle, insuffisantes. Le fait que la phase liquide soit continue peut impliquer un rétro-mélange qui pourrait pénaliser le nombre d'étages théoriques de la colonne si elle n'est pas correctement dimensionnée. Connaître la dispersion de l'écoulement ainsi que les rétentions gaz et liquide est donc une étape essentielle pour optimiser l'efficacité de séparation. De la même manière, les coefficients de transfert de matière à l'interface gaz liquide sont des données essentielles qui doivent être étudiées.

Le second chapitre expose les principes de conception concernant les écoulements gaz-liquide à contre-courant dans des microcanaux. Le défi consiste à maintenir une interface stable pour un écoulement gaz-liquide à contre-courant. Il s'agit donc de maintenir, à chaque endroit à l'intérieur du canal, une différence de pression gaz-liquide comprise entre une valeur minimale et une valeur maximale de pression capillaire. Ainsi, une gamme de conditions opératoires, plus précisément un débit d'alimentation maximal au-dessus duquel l'interface gaz-liquide serait rompue, peut être définie. Les différentes stratégies de détermination des conditions opératoires et d'estimation des performances des dispositifs publiées dans la littérature ont été brièvement passées en revue. Dans ce travail, la perte de charge pour l'écoulement gazeux a été estimée sur la base de l'équation de Hagen-Poiseuille. Concernant la perte de charge du liquide dans la région des micro-piliers, plusieurs chercheurs ont tenté d'établir une corrélation pour la prédiction du facteur de frottement. Certaines de ces corrélations ont été examinées dans ce chapitre ainsi que leur plage de fonctionnement. Par conséquent, la perte de charge pour l'écoulement liquide a été estimée sur la base de plusieurs de ces corrélations. Les propriétés du fluide ont été obtenues à partir d'une étude simulée à l'aide du logiciel Pro II et les différents résultats de simulation ont été illustrés. Inspiré de la géométrie des canaux de Lam *et al.* [9, 10], un « design » innovant composé de deux canaux gaz-liquide superposés a été suggéré (**Figure 2**).

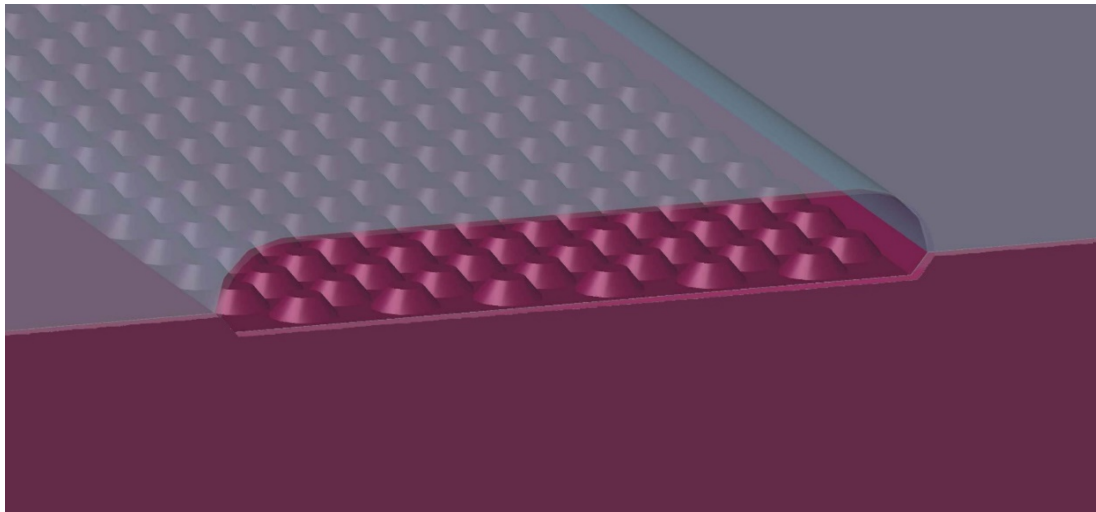


Figure 2 Nouveau concept de canaux gaz-liquide superposés proposé dans le cadre de la présente étude.

Le microcanal présenté ci-dessus est destiné à être utilisé en distillation, qui est un procédé de séparation thermique ; ainsi, la puce doit se caractériser par un bon transfert thermique et une large compatibilité chimique. Par conséquent, la technologie Si/Pyrex a été choisie pour fabriquer les systèmes. Par conséquent, le procédé de microfabrication Si/Pyrex est brièvement décrit (**Figure 3** et **Figure 4**).

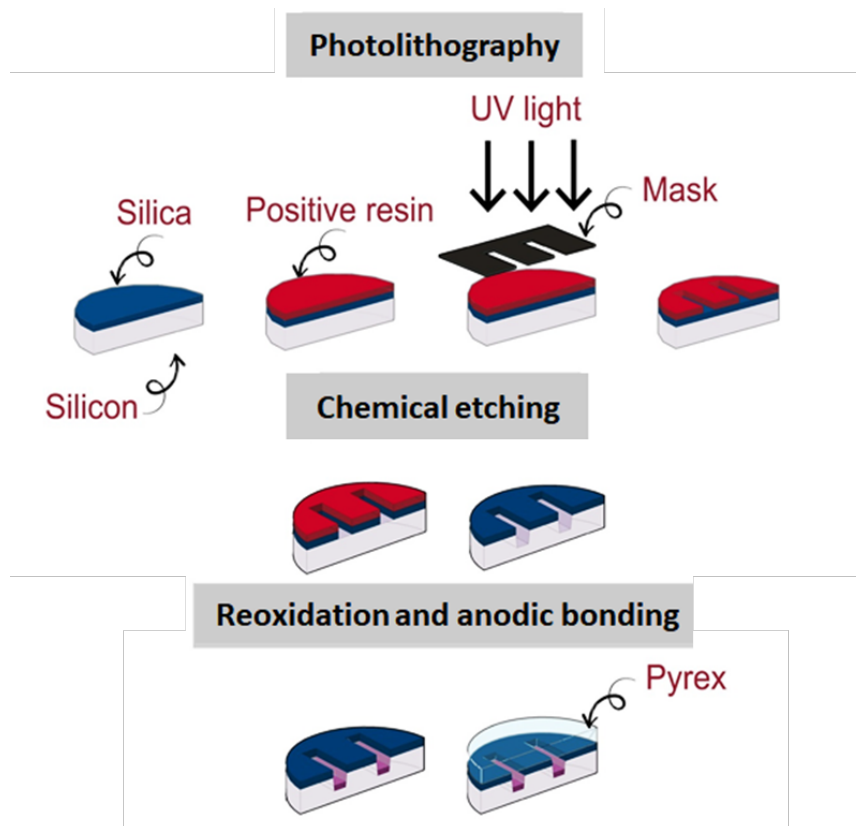


Figure 3 Différentes étapes d'un procédé de microfabrication de puces Si/Pyrex.

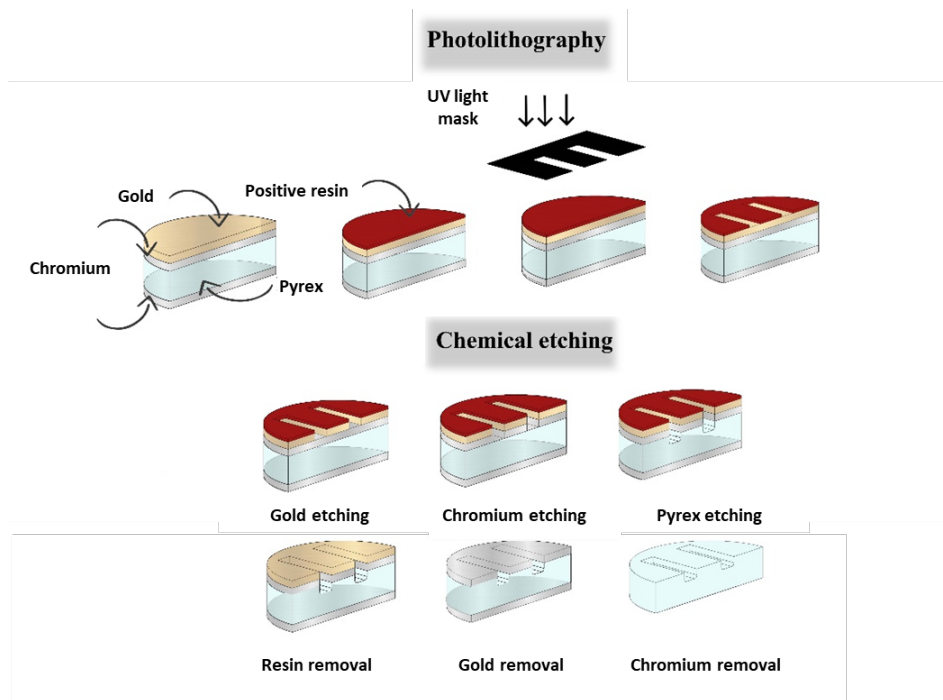


Figure 4 Procédé de gravure du Pyrex.

L'appareil est connecté au dispositif expérimental à l'aide de pièces de compression compatibles (**Figure 5**) avec une large gamme de produits chimiques, résistantes à des températures élevées et réutilisables.

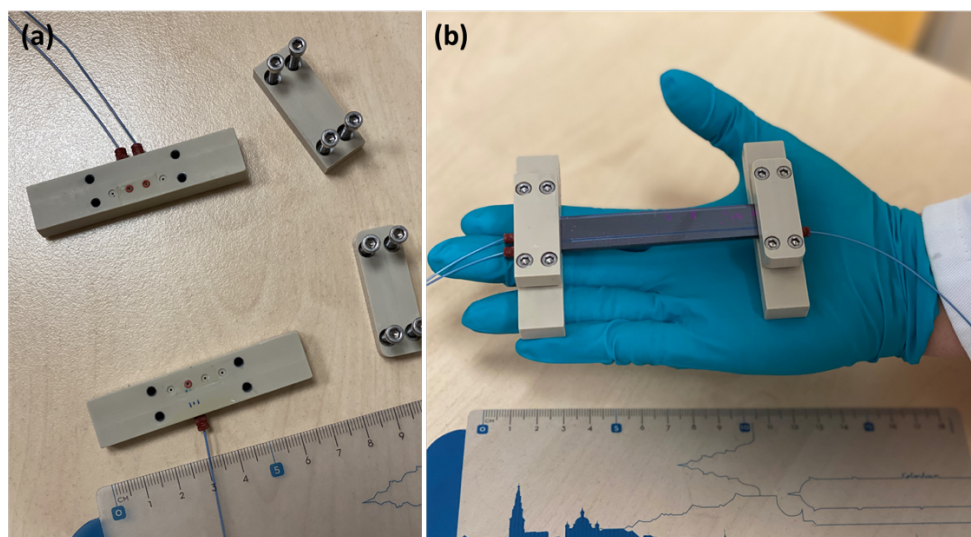


Figure 5 (a) photographie détaillée des différentes parties des pièces de compression et (b) de la puce connectée.

Le troisième chapitre traite des travaux expérimentaux sur l'étude de l'hydrodynamique de l'écoulement liquide au sein des puces développées. Afin d'étudier la dispersion liquide dans la région des micro-piliers, un dispositif expérimental a été développé pour mesurer la distribution du temps de séjour (DTS). L'injection d'un traceur selon une fonction échelon a été choisie en raison du faible

volume de la puce ($\sim 1.2 \mu\text{L}$). La microscopie Raman a été choisie pour étudier la distribution des temps de séjour (DTS). Les mesures à l'entrée et à la sortie de la puce ont été enregistrées indépendamment. Cependant, des problèmes de reproductibilité ont été rencontrés et une étude plus approfondie a été réalisée. Des caractérisations locales ont été effectuées à différentes profondeurs à l'intérieur du microcanal, révélant une forte variation du modèle de temps de séjour en fonction de la position et du débit. Par conséquent, il a été conclu que l'approche DTS locale adoptée ici n'est pas adaptée aux besoins de l'étude, et que l'approche DTS globale est plus représentative. Néanmoins, cette dernière n'a pas été tentée en raison du faible volume de la puce ($\sim 1.2 \mu\text{L}$) comparé au volume mort du système entier avec les pièces de compression ($\sim 48 \mu\text{L}$). Finalement, un travail de CFD (« Computational Fluid Dynamics ») a permis de donner un aperçu du comportement hydrodynamique de la micropuce. Un comportement d'écoulement piston de la phase liquide est identifié, ce qui est particulièrement intéressant pour les performances de microdistillation. Des interrogations ont cependant été notées concernant les valeurs de la perte de charge à travers le banc de micro-piliers, car la valeur prédite à l'aide de la CFD est supérieure de deux ordres de grandeur à celle estimée à l'aide des corrélations présentés dans le chapitre 2.

Les performances de distillation de l'outil de microdistillation nouvellement développé ont été évaluées dans le chapitre 4. Un dispositif dédié à l'évaluation expérimentale des performances de la microdistillation a été construit et validé (**Figure 6** et **Figure 7**). Malgré les problèmes de stabilisation et de vieillissement de la puce, une étude paramétrique a été menée avec succès sur la conception proposée. Les effets du débit d'alimentation, du débit de résidus, de la composition de l'alimentation et de la température de chauffage sur l'efficacité de séparation de l'outil développé ont été étudiés.

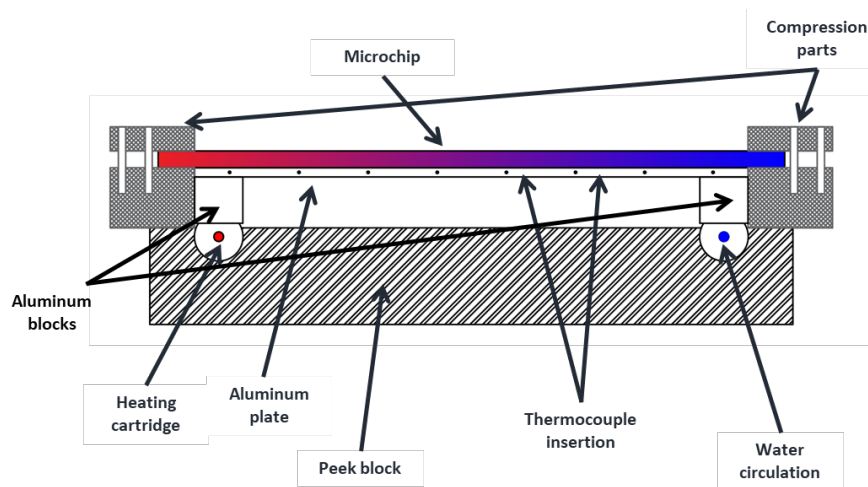


Figure 6 Vue de face du dispositif expérimental de microdistillation.

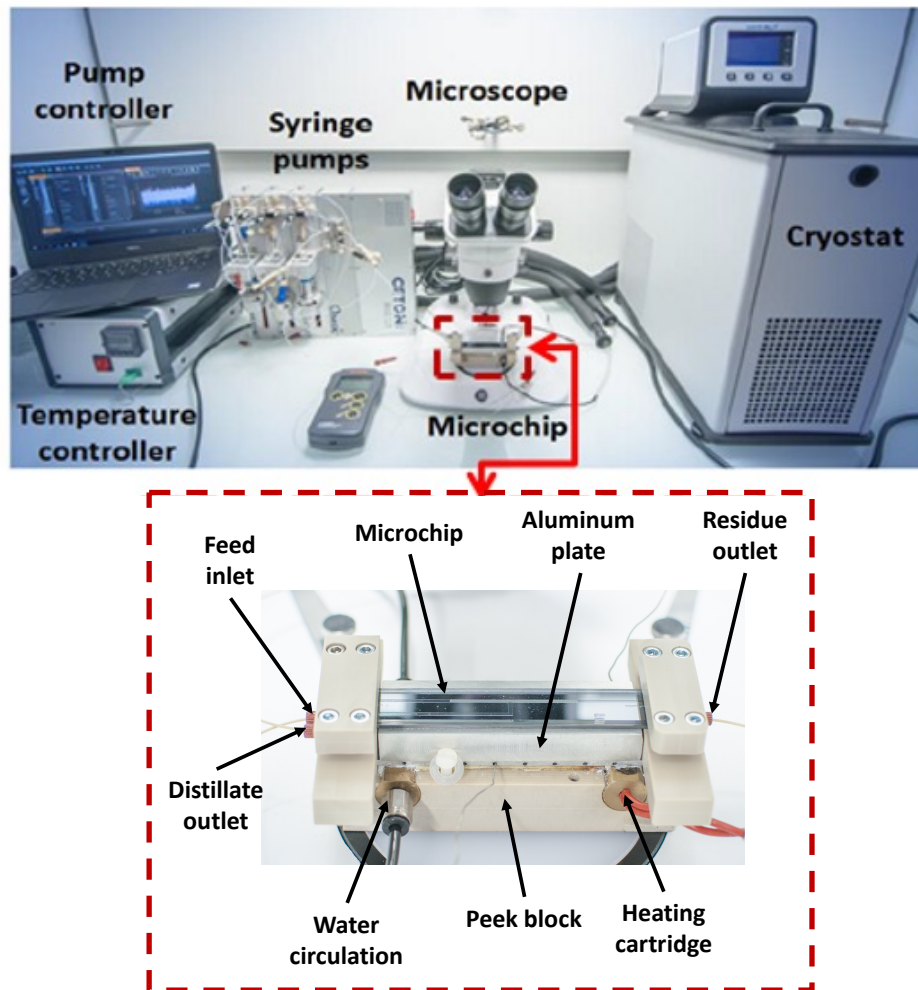


Figure 7 Photo réelle du montage expérimental de microdistillation développé.

Un résultat intéressant concerne la diminution de l'efficacité de séparation avec le débit d'alimentation pour un rapport de débit de soutirage de résidu sur débit d'alimentation fixe (**Figure 8**). Ce résultat est principalement lié à la réduction du temps de séjour avec l'augmentation du débit d'alimentation. Ainsi, un transfert de matière insuffisant entre les phases gazeuse et liquide est souligné.

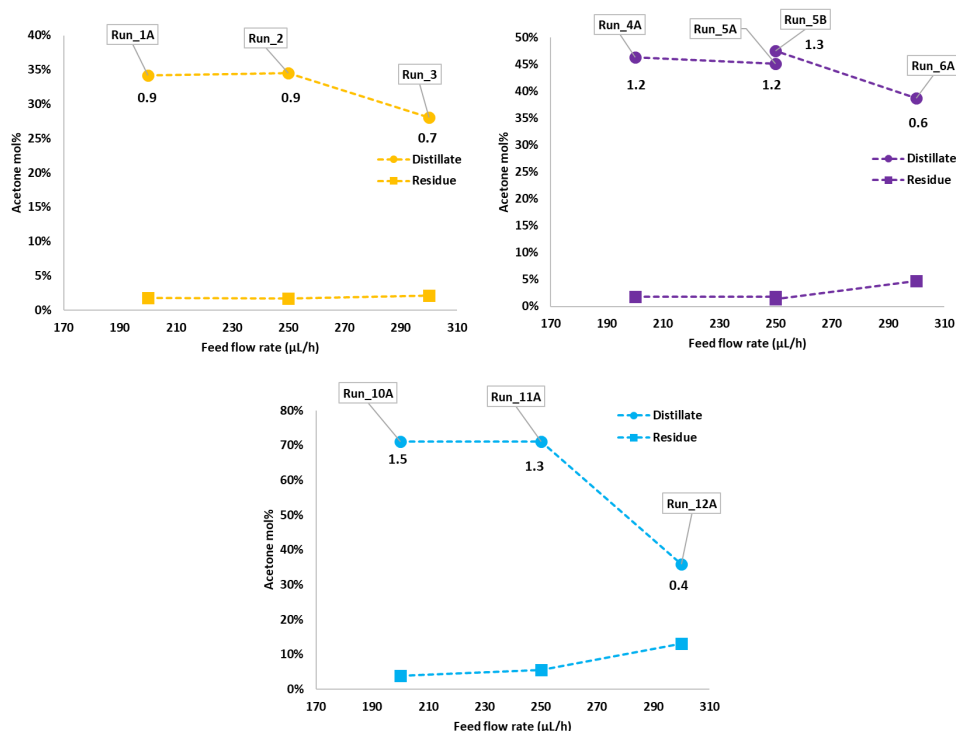


Figure 8 Effet du débit d'alimentation sur la fraction molaire d'acétone dans le distillat et résidu pour un rapport débit résidu sur charge de 0,3 (jaune), 0,4 (violet) et 0,6 (bleu). Les étiquettes de chaque point correspondent au nombre d'étages théoriques calculé.

Un autre résultat notable concerne la possibilité d'ajuster le débit de résidus pour un même débit d'alimentation (**Figure 9**). Ceci est permis grâce à la continuité de la phase liquide au sein de la microdistillation et offre de nouvelles voies pour ajuster les performances globales. Ce paramètre ne peut pas être contrôlé avec une distillation conventionnelle car les températures du rebouilleur et du condenseur fixent la composition des produits et les débits. Pour la microdistillation, il semble que l'équilibre thermodynamique ne soit pas encore atteint à l'intérieur du canal. Il a été constaté que la pureté du distillat augmente et que celle du résidu diminue lorsque le rapport de débit résidu sur charge augmente. Étant donné que les produits sont retirés en phase liquide, l'augmentation du rapport induira un liquide plus lourd retiré de la sortie du résidu et moins de composants à haut point d'ébullition. Par conséquent, un distillat plus pur est récupéré à un rapport débit résiduel/débit d'alimentation élevé pour un débit d'alimentation fixe.

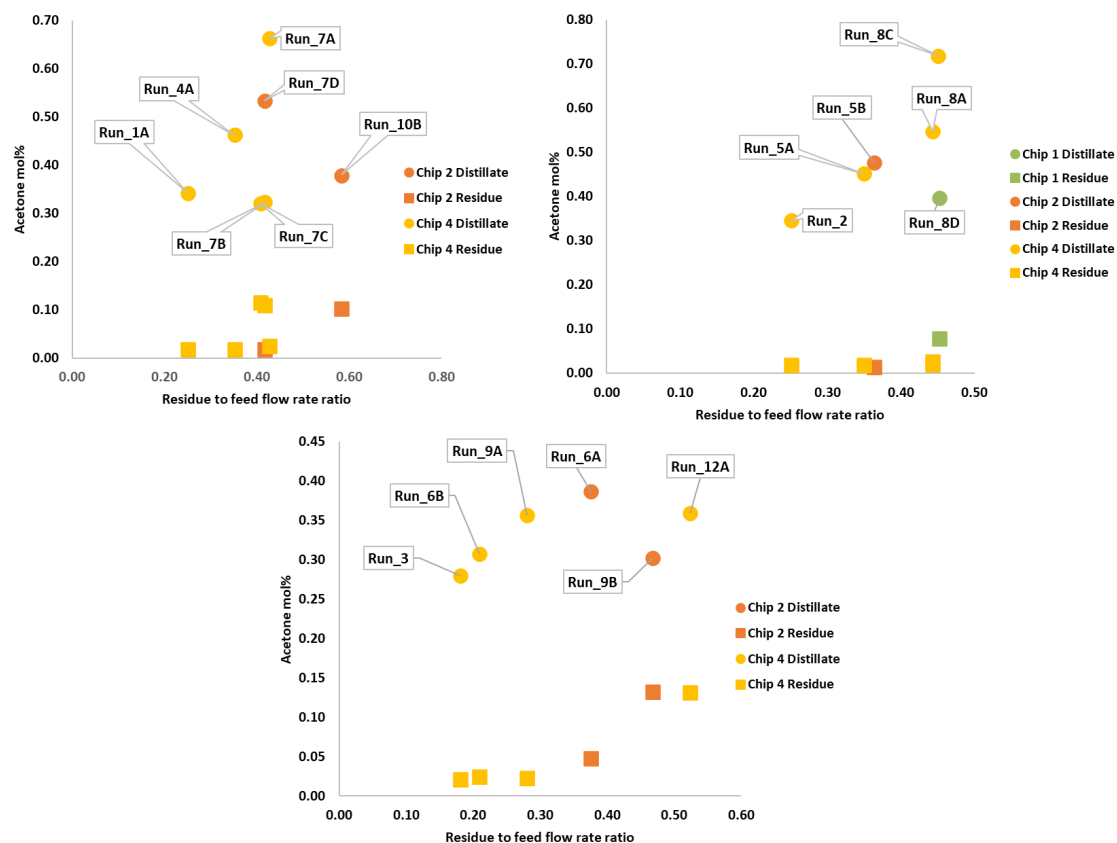


Figure 9 Impact du débit de soutirage des résidus sur la fraction molaire d'acétone dans le distillat et le résidu pour un débit d'alimentation de 200 µL/h (en haut à gauche), 250 µL/h (en haut à droite) et 300 µL/h (en bas).

L'impact de la température de chauffage et de la composition sur l'efficacité de séparation n'a pas conduit à des conclusions claires car d'autres paramètres ont été modifiés avec la température du rebouilleur ou la composition, en particulier le rapport débit de soutirage du résidu sur débit d'alimentation. Cependant, il semble qu'une augmentation de la température du rebouilleur augmente la génération de vapeur et augmente le reflux interne au sein du canal. Par conséquent, une meilleure séparation est obtenue et un distillat plus riche en composant à bas point d'ébullition est récupéré. De plus, lorsque la quantité de composant à bas point d'ébullition est augmentée dans l'alimentation, la quantité de vapeur générée à proximité du rebouilleur est augmentée, induisant un reflux plus élevé et une meilleure séparation.

Enfin, un suivi *in situ* des expériences de distillation a été réalisé grâce à la spectroscopie Raman. Une courbe d'étalonnage a été établie en traçant le logarithme du rapport de l'intensité des bandes d'acétone et d'eau en fonction de la composition du mélange en eau. Par conséquent, le profil de composition de deux essais de distillation a été enregistré en fonction de la position à l'intérieur du canal. Un bon accord a été trouvé entre les produits analysés par GC et la composition mesurée par spectroscopie Raman aux sorties du canal, même si des instabilités de la distillation ont été constatées. En effet, les résultats GC sont moyennés sur 4 heures alors que ceux mesurés par spectroscopie Raman sont instantanés. La spectroscopie Raman a montré que pour les conditions testées, la distillation se produit sur deux tiers du microcanal.

Des problèmes de vieillissement ont été rencontrés. Cela s'est traduit par une dégradation des performances dans le temps (avec le nombre de tests subis), ce qui a rendu l'étude paramétrique assez complexe. Ce phénomène n'est pas encore compris et peut être lié à une modification de l'interaction de surface à l'intérieur de la micropuce.

Perspectives

Concernant la conception du canal de microdistillation, il est nécessaire de mesurer avec précision la perte de charge à l'intérieur du canal de microdistillation et de proposer de nouvelles conceptions pour lesquelles la perte de charge est minimisée autant que possible pour éviter les engorgements. De plus, la zone interfaciale et le transfert de matière doivent être maximisés tout en minimisant autant que possible l'épaisseur du film liquide (réduction du temps de diffusion du liquide) pour améliorer l'efficacité de séparation de la microdistillation.

La mesure des coefficients de transfert de matière et la présence de rétro-mélange de liquide ou de gaz sont d'une grande importance et n'ont pas encore été abordées dans la littérature. Ce sont des paramètres critiques directement liés aux performances de l'appareil.

Dans le cas d'un mélange à plusieurs composants à distiller, plusieurs micropuces de distillation pourraient être utilisées en série pour réaliser la séparation du mélange en ses composés purs. Cependant, cela reste coûteux en raison du nombre d'appareils nécessaires et pourrait être évité en envisageant un prélèvement latéral des effluents. Par conséquent, des mélanges complexes pourraient être séparés en plusieurs effluents différents pour se rapprocher du fonctionnement d'une colonne de distillation conventionnelle et obtenir un processus de séparation multicomposants efficace à l'échelle microscopique.

Enfin, l'appareil devra être testé en conditions réelles afin de faire la preuve de concept sur des charges complexes et évaluer l'efficacité de l'outil développé à distiller des charges réelles.

Références

- [1] D. R. Seok and S.-T. Hwang, "Zero-gravity distillation utilizing the heat pipe principle(micro-distillation)," *AIChE J.*, vol. 31, no. 12, pp. 2059–2065, 1985.
- [2] A. T. Sundberg, P. Uusi-Kyyny, and V. Alopaeus, "Microscale distillation," *Russ J Gen Chem*, vol. 82, no. 12, pp. 2079–2087, 2012.
- [3] A. Sundberg, P. Uusi-Kyyny, and V. Alopaeus, "Novel micro-distillation column for process development," *Chemical Engineering Research and Design*, vol. 87, no. 5, pp. 705–710, 2009.
- [4] A. T. Sundberg, P. Uusi-Kyyny, and V. Alopaeus, "The use of microplants in process development— Case study of etherification of 2-ethoxy-2-methylbutane," *Chemical Engineering and Processing: Process Intensification*, vol. 74, pp. 75–82, 2013.
- [5] A. T. Sundberg, P. Uusi-Kyyny, K. Jakobsson, and V. Alopaeus, "Control of reflux and reboil flow rates for milli and micro distillation," *Chemical Engineering Research and Design*, vol. 91, no. 5, pp. 753–760, 2013.
- [6] S. Mardani, L. S. Ojala, P. Uusi-Kyyny, and V. Alopaeus, "Development of a unique modular distillation column using 3D printing," *Chemical Engineering and Processing: Process Intensification*, vol. 109, pp. 136–148, 2016.
- [7] R. L. Hartman, H. R. Sahoo, B. C. Yen, and K. F. Jensen, "Distillation in microchemical systems using capillary forces and segmented flow," (eng), *Lab on a chip*, vol. 9, no. 13, pp. 1843–1849, 2009.
- [8] R. L. Hartman, J. R. Naber, S. L. Buchwald, and K. F. Jensen, "Multistep microchemical synthesis enabled by microfluidic distillation," (eng), *Angewandte Chemie (International ed. in English)*, vol. 49, no. 5, pp. 899–903, 2010.
- [9] K. F. Lam, E. Cao, E. Sorensen, and A. Gavriilidis, "Development of multistage distillation in a microfluidic chip," (eng), *Lab on a chip*, vol. 11, no. 7, pp. 1311–1317, 2011.
- [10] K. F. Lam, E. Sorensen, and A. Gavriilidis, "Towards an understanding of the effects of operating conditions on separation by microfluidic distillation," *Chemical Engineering Science*, vol. 66, no. 10, pp. 2098–2106, 2011.

Nomenclature

Latin Letters

a	Channel cross sectional area	(m^2)
a'	Surface area of packing per unit of packed volume	(m^2/m^3)
a_μ	Spacing between the micropillars	(m)
A	Cross-sectional area of the column	(m^2)
A_w	Cross-sectional area of the wick phase	(m^2)
A_{min}	Minimum cross-sectional area of the channel	(m^2)
$A_{\mu pillar}$	Cross sectional-area of a micropillar	(m^2)
B'	Bottom molar flow rate	(mol/h)
Bo	Bond number	
C	Liquid concentration	(mol/L)
C_1, C_2, C_3	Constants	
C^{eq}	Equilibrium concentration	(mol/L)
$C_{CO_2}^{in}$	Concentration of CO_2 in the entering liquid flow	(mol/L)
$C_{CO_2}^{out}$	Concentration of CO_2 in the exiting liquid flow	(mol/L)
d_μ	Micropillars diameter	(m)
d'	Distance between the inlet and outlet of the channel	
d	Depth of the channel	(m)
D_{ax}	Axial dispersion coefficient	(m^2/s)
D	Hydraulic diameter of a micropillar	(m)
D'	Distillate molar flow rate	(mol/h)
D_{wick}	Capillary diameter of the wick	(m)
D_{coeff}	Diffusion coefficient	(m^2/s)
$E(t)$	Distribution function $E(t)$	
f	Friction factor	
F'	Feed molar flow rate	(mol/h)
$F(t)$	Cumulative function of the residence time distribution function	
$F(x)$	Distribution function of heat flow rate	
g	Gravitational acceleration	(m/s^2)
G	Mass flux	$(g.cm^{-2}.min^{-1})$
G_v	Mass velocity of the vapor	(kg/s)
h_{fg}	Latent heat of vaporization	$(J/Kmol)$
h	Channel's height	(m)
H	Micropillars height	(m)
H_{column}	Height of the column	(m)
HETP	Height of a theoretical plate	(cm)
HTU	Height of a transfer unit	(cm)
K	Kozeny constant	
K'	Absorption coefficient	(cm^{-1})
$K_L a$	Volumetric mass transfer coefficient	(m/s)
K_{xa}	Overall capacity coefficient	$(mol/(h.m^3))$
K_p	Wick permeability	(m^2)
L	Length of the channel	(m)
L_c	Length of the condensation section	(m)
L_e	Length of evaporation section	(m)
L'	Constant liquid molar flow rate in the distillation column	(mol/h)
L_{m-1}	Liquid molar flow rate in the bottom section of the distillation column	(mol/h)

Nomenclature

L_n	Liquid molar flow rate in the top section of the distillation column	(mol/h)
L_r	External liquid flow rate recycled to the column	(mol/h)
M	Molecular weight	(g/mol)
M_v	Average molecular weight of the vapor stream	(g/mol)
\dot{m}	Liquid mass flow rate	(kg/s)
N_{\min}	Minimum number of theoretical stages	
N_{column}	Number of columns of micropillars	
N_{row}	Number of rows of micropillars	
NTU	Number of transfer unit	
\dot{N}	Molar liquid flow rate	(mol/h)
p	Partial pressure of the most volatile component	(Pa)
P	Total pressure	(Pa)
Pe	Peclet number	
P_1	Pressure at the convex side of the interface	(Pa)
P_2	Pressure at the concave side of the interface	(Pa)
$P_{\mu\text{pillar}}$	Wetting perimeter of a micropillar	(m)
q	Liquid fraction of the feed	
Q	Volumetric flow rate	(m ³ /s)
Q_{cond}	Heat removed by condenser	(J/mol)
Q_H	Axial heat flow rate	(J/s)
Q_{reb}	Heat supplied by reboiler	(J/mol)
R	Radius of curvature of the interface	(m)
R_r	Reflux ratio	
R_1, R_2	Principal radii of curvature	(m)
R_{\min}	Minimum reflux ratio	
Re_{μ}	Reynolds number in the micropillar region	
r_p	Pore radius	(m)
r_n	Nucleation radius	
S	Specific surface area of the micropillars	(m ² /m ³)
S_T	Transverse pitch	(m)
S_L	Longitudinal pitch	(m)
S_D	Diagonal pitch	(m)
S_v	External volumetric source	
t	Time	(s)
t_{diff}	Diffusion time	(s)
t_{res}	Residence time	(s)
t_{conv}	Convection time	(s)
T	Temperature	(°C)
u	Fluid velocity	(m/s)
u_L	Superficial velocity of the liquid phase	(m/s)
u'_i	Flux velocity in an empty channel (without the micropillars)	(m/s)
U_i	Superficial inlet velocity	(m/s)
V	Channel volume	(m ³)
V'	Constant vapor molar flow rate in the distillation column	(mol/h)
V_m	Vapor molar flow rate in the bottom section of the distillation column	(mol/h)
V_{n+1}	Vapor molar flow rate in the top section of the distillation column	(mol/h)
w	Width of the channel	(m)
w_{bottom}	Bottom width of the liquid channel	(m)

Nomenclature

We	Weber number	
w_{top}	Top width of the liquid channel	(m)
W_d	Distance between the micropillar and the wall of the channel	(m)
X	Diffusion distance	(m)
x'	Mole fraction in the liquid phase	
y'	Mole fraction in the vapor phase	
z_F	Mole fraction in the feed	

Greek letters

α	Relative volatility	
α_{avg}	Average relative volatility	
α'	Tilt angle with respect to the horizontal position of the device	
γ	The surface tension between the gas and liquid phases	(N/m)
$\Delta\rho$	Density difference between both phases	(kg/m ³)
ΔP	Pressure drop	
ΔP_c	Capillary pressure	
δ	Angle between the vertical and the tangent to the gas-liquid interface	
ϵ	Porosity	
θ	Contact angle between the gas-liquid interface and the solid surface of the pore	
μ_l	Liquid dynamic viscosity	(Pa.s)
μ_g	Gas dynamic viscosity	(Pa.s)
μ	Moments of the distribution function	
ν_l	Kinematic viscosity of the liquid	(m ² /s)
ρ_l	Liquid density	(Kg/m ³)
ρ_g	Gas density	(Kg/m ³)
Σ	Viscous stress tensor	
σ^2	Variance	
τ	Time constant	

Subscripts

A	The more volatile component of the binary mixture
B	Bottom product
Cond	Condenser
D	Distillate
F	Feed
g	Gas phase
l	Liquid phase
m,m-1	Bottom section of the distillation column
n,n+1	Top section of the distillation column
reb	Reboiler
ref	Reflux

Table of contents

INTRODUCTION	1
1. CHAPTER 1: STATE OF THE ART	3
1. DISTILLATION	3
1.1. VARIOUS CONTINUOUS DISTILLATION MODES	3
1.1.1. Flash distillation	3
1.1.2. Fractional distillation	3
1.1.3. Azeotropic distillation	5
1.1.4. Molecular or short path distillation	5
1.1.5. Extractive distillation	5
1.1.6. Reactive distillation	6
1.2. MASS BALANCES	6
1.3. MCCABE-THIELE DIAGRAM	7
1.4. FENSKE'S EQUATION TO COMPUTE N_{MIN}	9
1.5. DEGREE OF FREEDOM	9
1.6. IMPACT OF VARIOUS OPERATING PARAMETERS ON THE SEPARATION EFFICIENCY	10
1.7. DISTILLATION COLUMNS INTERNALS	11
1.8. CONCLUSION	12
2. MICRODISTILLATION	13
2.1. BATCH MICRODISTILLATION	15
2.2. CONTINUOUS MICRODISTILLATION OF INTERMEDIATE SIZE	21
2.2.1. Gravity assisted microdistillation	22
2.2.1.1. Plate microdistillation column	22
2.2.1.2. Falling film microdistillation column	23
2.2.1.3. Packed microdistillation column	25
2.2.2. Capillary driven microdistillation	26
2.2.2.1. Principle	26
2.2.2.2. Wick based capillary network	29
2.2.2.3. Metal foam based capillary network	31
2.2.2.4. Stainless steel mesh capillary network	33
2.2.3. Conclusion	34
2.3. CONTINUOUS ON-CHIP MICRODISTILLATION	36
2.3.1. Single-stage on-chip microdistillation	37
2.3.2. Multistage on-chip microdistillation	43
2.3.2.1. Counter-current capillary microdistillation	43
2.3.2.2. Counter-current membrane microdistillation	47
2.3.2.3. Counter-current centrifugal microdistillation	50
2.3.3. Conclusion	51
2.4. CONCLUSION ON MICRODISTILLATION DOWNSIZING	53
3. DIFFERENCE BETWEEN DISTILLATION AND MICRODISTILLATION	54

4. CONCLUSION	56
2. CHAPTER 2: DESIGN AND MICROFABRICATION	59
1. INTRODUCTION	59
2. GENERAL PRINCIPLES	59
3. OPERATING LIMIT	62
4. ADDITIONAL CONSIDERATIONS TO TAKE INTO ACCOUNT	63
4.1. ENTRAINMENT LIMITATION	64
4.2. BOILING LIMITATION	64
4.3. VISCOUS LIMITATION	65
4.4. SONIC LIMITATION	65
5. PERFORMANCE ESTIMATION	66
6. DESIGN AND PRESSURE DROP CALCULATION	67
6.1. WORKFLOW	67
6.2. GAS PRESSURE DROP	69
6.3. LIQUID PRESSURE DROP	69
6.4. PERFORMANCE ESTIMATION	73
6.5. PRESSURE DROP CALCULATION	74
7. MICROFABRICATION	90
7.1. INTRODUCTION	90
7.2. MATERIALS	91
7.2.1. Wafers	91
7.2.2. Chemicals	91
7.2.3. Instruments	92
7.2.4. Si/Pyrex based microdevices	93
7.2.5. Silicon wafer preparation	93
7.2.6. Pyrex etching	95
7.3. PACKAGING AND CONNECTIONS	98
8. CONCLUSION	99
3. CHAPTER 3: HYDRODYNAMIC CHARACTERIZATION	101
1. INTRODUCTION	101
2. RTD MEASUREMENT METHODOLOGY	101
3. EXPERIMENTAL SETUP	103
4. TRACER ANALYSIS BY RAMAN SPECTROSCOPY	105
5. EXPERIMENTAL PROCEDURE	107
6. RESULTS AND DISCUSSION	108
6.1. DATA TREATMENT OF A TYPICAL CASE	108
6.2. MEASUREMENT OF THE RTD AS A FUNCTION OF THE DEPTH OF THE CHANNEL	110
7. SIMULATION OF THE LIQUID FLOW WITHIN THE MICROPILLARS	113
8. MASS TRANSFER COEFFICIENT	116
9. CONCLUSION	118

4. CHAPTER 4: MICRODISTILLATION EXPERIMENTS	121
1. INTRODUCTION	121
2. EXPERIMENTAL SETUP	121
2.1. FLUIDS	121
2.2. MICROCHIP ASSEMBLY	121
2.3. DISTILLATION EXPERIMENTAL SETUP	122
2.4. THERMAL PROFILE	124
2.4.1. THERMOCOUPLE INSERTED IN THE ALUMINUM PLATE	124
2.4.2. THERMAL CAMERA	125
3. EXPERIMENTAL PROCEDURE	126
3.1. DISTILLATION EXPERIMENTS	126
3.2. MASS BALANCE	128
3.3. SAMPLE CHARACTERIZATION	128
4. RESULTS AND DISCUSSION	129
4.1. EXPERIMENTAL CONDITIONS	129
4.2. PRELIMINARY RESULTS	131
4.3. DISTILLATION RESULTS	131
4.3.1. Effect of feed and residue flow rates	132
4.3.2. Effect of the reboiler temperature	137
4.3.3. Effect of feed composition	138
4.3.4. Overall performances	139
5. <i>IN SITU</i> MONITORING OF DISTILLATION EXPERIMENTS USING RAMAN SPECTROSCOPY	140
5.1. CALIBRATION CURVES	141
5.2. COMPOSITION PROFILE	142
6. CONCLUSION	144
CONCLUSION AND PERSPECTIVES	145
APPENDICES	155
APPENDIX A	156
APPENDIX B	162
APPENDIX C	163

Introduction

Since several years, the concept of 'mini' and 'micro' chemical plants is seen as the future chemical industry thanks to the process intensification and equipment miniaturization. The main advantages associated with process downsizing are mainly intensified heat and mass transfers, fast implementation, design flexibility according to needs, device portability and many others.

In view of these advantages, the research domain has focused on the transposition of reaction tests in microreactors. Indeed, microreactors have higher specific surface area than laboratory scale reactors. When dealing with gas-liquid systems, this high surface to volume ratio offers a large interfacial area between the gas and liquid phases, thus enhancing mass transfer between both phases. In addition, this intensification of chemical processes allows the same chemical reactions to be carried out on a smaller scale with reduced residence and data acquisition times. However, there is an increasing need toward the conception of a continuous microseparation unit that can be placed at the outlet of the microreactor and be able to separate the low flow rate effluents into usable or analyzable fractions. One of the most adapted and needed microseparators is the microscale distillation. This is of prior interest in the case of gas liquid reactions for example, where a simple flash separation would result in a wide product distribution in both phases. Indeed, distillation is a key step for the chemical industry, being an efficient process for recovering pure compounds from complex mixtures based on differences in their boiling points.

Distillation downscaling comes up against several difficulties: first, at the micron scale, the effect of gravity is dominated by surface forces. It is then necessary to suggest new designs for the distillation channel internals to establish a counter-current two-phase flow and to favor the contact between both phases. Other significant challenges associated with small-scale distillation development are thermal control, reflux and products' withdrawal. Indeed, the high surface area to volume ratio will exacerbate the problems of heat losses from the channel's walls. Temperature control and withdrawal management are challenges that must be overcome for a stable and efficient operation of the microscale distillation.

Therefore, the first chapter of this manuscript is depicted for the description of the fundamental principles of distillation. Then, it is followed by a brief description of the different microdistillation concepts already reported with a special focus on their performances and how the researchers managed to solve the technological challenges.

The second chapter describes the guiding principles used to design the microchips. It consists of developing a theoretical approach to verify that a counter-current gas liquid flow is able to be stabilized within the proposed device. Once a design is able to satisfy the imposed conditions, it is fabricated to be further tested experimentally; this also has to validate the developed theoretical approach. Hence the microfabrication process used to manufacture the device is detailed.

Thereafter, the device is characterized hydrodynamically by studying the residence time distribution of the liquid and computing the liquid dispersion coefficient. The hydrodynamic parameters are evaluated for several flow rates and then related to the distillation efficiency.

Finally, the distillation performances of the device are measured. Therefore, an experimental setup dedicated for distillation experiments is developed within this work and detailed. The ability of the device to distill binary mixtures is evaluated and the impact of operating conditions on the separation performance of the device is investigated.

1. Chapter 1: State of the art

1. Distillation

Distillation, a ubiquitous thermal process for separating miscible liquid mixtures, is widely used in chemical and petroleum industries. It consists of splitting off liquid mixtures into two streams based on differences in volatility. The most volatile components, those having the lower boiling points, accumulate in the vapor phase while the less volatile components enriched the liquid phase. The vapor is then condensed and referred as distillate product, whereas the liquid phase is known as residue. [1,2]

1.1. Various continuous distillation modes

Different distillation modes exist. As aforementioned, the principle is to put in contact a liquid with a gas phase until they reach equilibrium then separating both phases. The process could be done in a discontinuous or continuous mode. Thereafter are listed the different distillation modes.

1.1.1. Flash distillation

Flash distillation consists of partially vaporizing a liquid mixture, thus having a two-phase system in which the vapor, richer in the most volatile component, is in equilibrium with the liquid. This phase equilibrium is achieved due to vapor-liquid contacting and mass transfer. Flash distillation is equivalent to a single-stage distillation process (**Figure 1-1, left**). The process is similar to a batch distillation with the main difference that the mixture to separate is continuously fed into the system and both products are recovered as they are produced. The separation efficiency could be improved by combining several flash distillations in a cascade and thus achieving a multistage flash process (**Figure 1-1, right**).

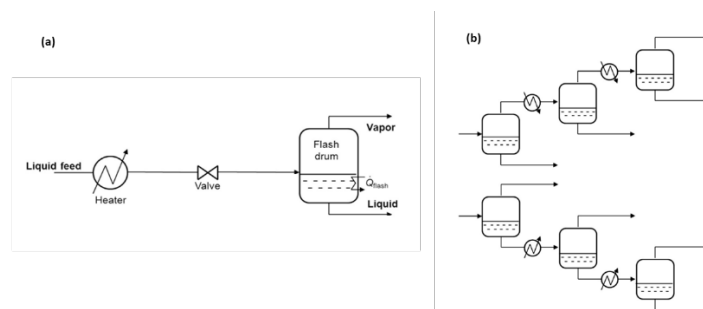


Figure 1-1 Scheme of (a) a flash distillation unit and (b) a cascade of flash units [1].

1.1.2. Fractional distillation

Fractional distillation, so-called rectification, is a process in which the liquid and vapor flow counter-currently, inducing a better separation than a multistage flash process. It is the most common form of thermal separation technique used in the chemical industry. It is undergone within a tower of separation. Indeed, the most important parameter to carry out a distillation process is to manage the contacting of the gas and liquid phases. The column is equipped with a condenser at its top and a

reboiler at its bottom. Therefore, a temperature gradient is thermally established across the column from its bottom (hottest temperature) towards its top (coolest temperature). The column is made up of a specific configuration of its internal geometry in order to increase as much as possible the contact between the phases. For all the possible configurations, the separation tower could be assimilated to a column made up of several theoretical trays. Inside the column, the liquid will be driven downwardly by means of gravity forces toward the reboiler implemented at the bottom of the column. In the reboiler, the liquid will partially vaporize and the generated steam is recycled to the bottom of the column where it bubbles through the liquid lying on the bottom plate. Thus, partial condensation of the vapor and material exchange between both phases take place. The heat released during the condensation will cause the vaporization of part of the liquid. The vapor flows upwardly inside the column by means of pressure difference. This phenomenon of partial condensation and re-vaporization takes place on each plate. Consequently, at each tray inside the column, the vapor phase will be enriched in the lightest products whereas the liquid one is mainly concentrated with the heaviest compounds. Theoretically, on each tray, thermal equilibrium is reached between the vapor and liquid phases at the temperature of the tray. Hence, the vapor and liquid entering the tray are not in equilibrium whereas those exiting are in a thermodynamic equilibrium with each other. At the top of the column, the vapor is partially or totally condensed in the condenser and collected in a reflux drum. The product collected at the top of the column is known as the distillate and the non-vaporized liquid inside the reboiler is recovered as bottom product, so-called residue. As shown in **Figure 1-2**, the feed is injected into the column at a specific position that gives the best separation. The feed injection split the column into two main sections. The upper section is known as rectification section whereas the lower one is called stripping section. To achieve better separations, part of the condensed distillate is re-pumped into the column at the top plate. This externally supplied cold liquid stream that flows downwardly in the column due to gravitational forces is called reflux (external reflux).

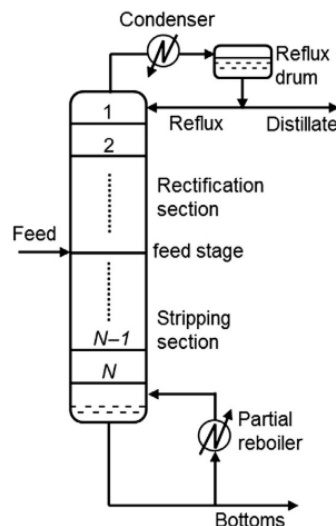


Figure 1-2 Schematic view of a fractional distillation column [1].

It is essential to mention that the number of theoretical stages to achieve a desired separation is highly related to the liquid to vapor flow rate ratio established internally within the column (internal reflux ratio). The number of theoretical stages is obtained from the real number of trays (height of the packing) by taking into consideration the tray efficiency. However, another important parameter in determining the number of theoretical stages is the external reflux ratio. It represents the ratio

between the externally recycled liquid and the distillate. Reducing the reflux ratio implies less liquid sent back to the top of the column, thus less mass exchange takes place. Therefore, more theoretical stages are needed in the column to achieve the desired separation.

1.1.3. Azeotropic distillation

To describe this type of distillation, it is crucial to explain what ‘azeotrope’ stands for. An azeotropic mixture is a multi-constituent mixture characterized by the same vapor and liquid compositions at equilibrium. The temperature that corresponds to this composition could be higher or lower than the boiling temperature of the pure compounds. If it was higher, then the mixture is called negative azeotrope (**Figure 1-3, left**). In the other case, it is known as a positive azeotrope (**Figure 1-3, right**). Accordingly, the separation of binary azeotropic mixtures by classic distillation is not easily achievable since it will reach the azeotropic composition, preventing further separation.

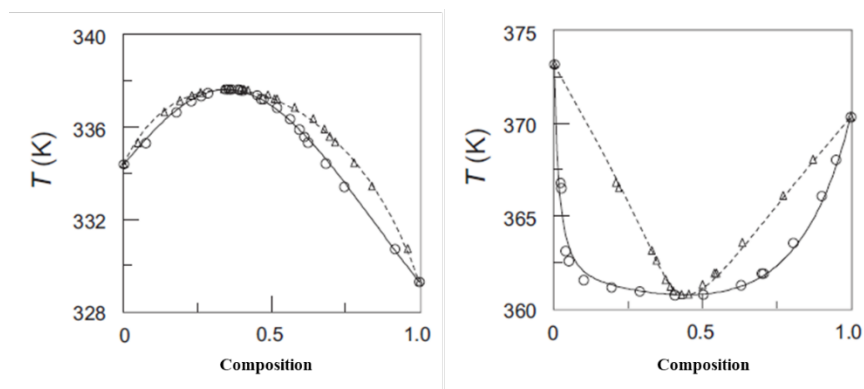


Figure 1-3 Vapor liquid equilibrium diagrams of a negative (left) and a positive (right) azeotropes [1].

A specific technique is then needed to break the azeotrope. One of these techniques is to use an external component, so-called the ‘entrainer’ able to change the interactions between the compounds, hence alters the relative volatility of the mixture. This entrainer can, for example, form with one of the compounds a heterogeneous azeotrope (two-immiscible liquids) of a lower boiling temperature. Their separation is then possible by decantation or distillation. Other possible techniques can be also used such as pressure-swing distillation. The latter is based on operating distillation at different pressures. By altering the operating pressure, the azeotropic composition could be avoided and the separation is possible since the azeotrope is pressure dependent.

1.1.4. Molecular or short path distillation

This type of separation aims to purify some thermo-sensitive products having high molecular weights. It is mainly used in food, pharmaceutical and chemical industries. Two main factors have to be taken into consideration to avoid component degradation. The first factor is the temperature of separation which is reduced by operating at low pressure in the range of 0.1 Pa. The second factor is the residence time at this temperature that has to be shortened as much as possible. It is done thanks to a thin film evaporator. This separation is almost equivalent to a single-stage distillation and for higher performances, cascade configurations could be considered as for the flash distillations units.

1.1.5. Extractive distillation

This distillation is very similar to the azeotropic one. The main difference between both processes is that in this case no azeotrope has to be formed. Extractive distillation relies on using an entrainer to alter the relative volatility of the constituents. The entrainer is usually a solvent or a salt that has a high boiling point and drives out several constituents from the mixture. Then, a regeneration column is used to recover the entrainer from the other constituents.

1.1.6. Reactive distillation

This is a distillation process used to separate continuously the products of a specific reaction in order to shift the equilibrium and reach a conversion of almost 100%. The column consists mainly of three sections rather than two: rectification, reaction and stripping sections.

Whatever the distillation type is, the size of a distillation column depends on the feed flow rate as well as the rate at which one material diffuses from one phase to another. Distillation column has a broad range in capacity; column diameter and height ranges from 0.3 to 12 m and from 1 to 75 m, respectively. Optimizing the distillation process relies on determining the optimum operating conditions such as the reflux to distillate ratio, the duties, number of trays, column pressure, *etc.*, required to achieve the desired separation at the lowest investment and operating costs.

1.2. Mass balances

For calculation simplifications, the mixture to distill is considered to be a two-component system. The overall material balance for a system fed with F' (mol/h) and separated into a distillate of D' (mol/h) and a bottom product of B' (mol/h) in its continuous steady state gives:

$$F' = D' + B' \quad (1-1)$$

Let A be the most volatile component. Applying **equation (1-1)** to component A gives:

$$F' z_{F,A} = D' x'_{D,A} + B' x'_{B,A} \quad (1-2)$$

where $z_{F,A}$, $x'_{D,A}$ and $x'_{B,A}$ designate the molar concentration of A in the feed, distillate and bottom product, respectively. The mass balances could also be computed over the column subsections such as the top and bottom part of the column.

For the column top (above the feed injection point), the overall and the component A mass balances are respectively:

$$V_{n+1} = L_n + D' \quad (1-3)$$

$$V_{n+1} y'_{n+1,A} = L_n x'_{n,A} + D' x'_{D,A} \quad (1-4)$$

where V_{n+1} and L_n stands for the vapor and liquid molar flow rates in the top section of the distillation as shown in **Figure 1-4 (left)** and ' y'_A ' and ' x'_A ' are the mole fractions of A in the vapor and liquid phases, respectively.

Whereas those for the bottom part of the column are:

$$V_m = L_{m-1} - B' \quad (1-5)$$

$$V_m y'_{m,A} = L_{m-1} x'_{m-1,A} - B' x'_{B,A} \quad (1-6)$$

V_m and L_{m-1} stand for the vapor and liquid molar flow rates in the bottom section of the column as shown in **Figure 1-4 (right)**. [1,2]

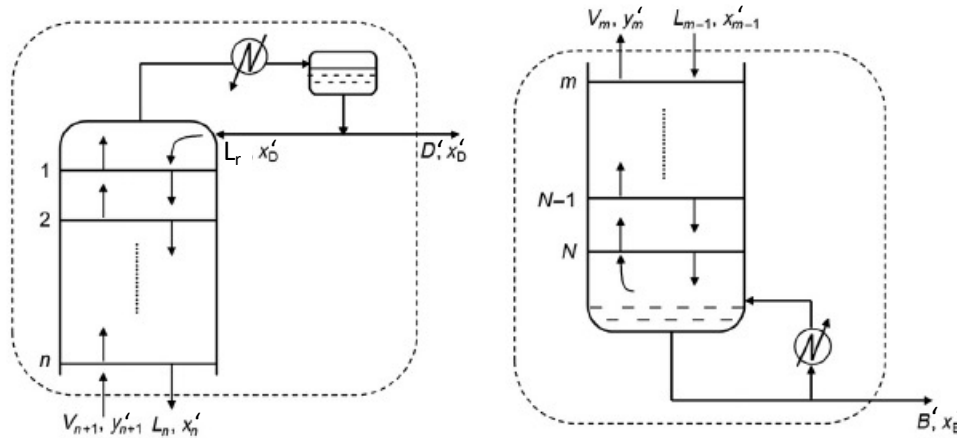


Figure 1-4 Mass Balance over the top (left) and bottom (right) sections of a distillation column [1].

1.3. McCabe-Thiele diagram

This is a simple graphical method used to design a distillation column with binary mixtures in terms of feed plate location, minimum reflux ratio as well as minimum number of theoretical trays. It could also be used to characterize a separation by estimating the number of theoretical plates needed to achieve this separation based on the experimental results and within the operated conditions.

A crucial parameter must be defined before illustrating the McCabe-Thiele method. It is the external reflux ratio ' R_r '. It corresponds to the ratio of the external liquid recycled to the column to the liquid distillate withdrawn from the top of the column as expressed below:

$$R_r = \frac{L_r}{D'} \quad (1-7)$$

To apply McCabe-Thiele graphical method, many assumptions have to be taken. First, the feedstock has to be a binary mixture as mentioned before. Second, the system has to be at constant pressure and in a steady state. Equilibrium between vapor and liquid occurs at each tray. Additionally, the heat loss or release from mixing is negligible. Finally, the molar heats of vaporization for both components are assumed to be equal and constant.

For constant molar overflow in both sections of the column (as assumed), **equations 1-4** and **1-6** become respectively:

$$y'_{n+1,A} = \frac{R_r}{R_r+1} x'_{n,A} + \frac{1}{R_r+1} x'_{D,A} \quad (1-8)$$

$$y'_{m,A} = \frac{L'}{V'} x'_{m-1,A} - \frac{B'}{V'} x'_{B,A} \quad (1-9)$$

where L' and V' are the liquid and vapor molar overflows in the column.

Equations 1-8 and **1-9** are the operating lines in the rectification (above the feed plate) and the stripping section (below the feed plate), respectively, and are plotted in a (x',y) diagram. The operating line in the rectification section passes through the points $(0, \frac{x'_{D,A}}{R_r+1})$ and $(x'_{D,A}, x'_{D,A})$. A third

equation is needed to apply McCabe-Thiele method. This equation depends on the feed conditions and is rather known as the feed line. In fact, the binary mixture can be:

- a subcooled liquid inducing the condensation of part of the vapor entering the feed plate
- a liquid at its bubble point, thus flowing with the liquid leaving the feed plate
- a two-phase system (partially vaporized)
- a vapor at its dew point that flowing upwardly with the vapor leaving the feed plate
- a superheated vapor that will cause the evaporation of part of the liquid entering the feed plate

Considering that 'q' is the liquid fraction of the feed, the feed plate material balance is the following:

$$L' = L + qF' \quad (1-10)$$

$$V = V' + (1 - q)F' \quad (1-11)$$

where L, V, L' and V' are the flow rates of the inlet and outlet liquid and vapor streams to the feed plate, respectively.[1,2]

At the feed plate $y_{n+1} = y_m$ and $x'_n = x'_{m-1}$. By substituting **equation 1-9** from **equation 1-8** and considering **equations 1-2, 1-10 and 1-11**, the feed line equation that passes through the point $(z_{F,A}, z_{F,A})$ is obtained and expressed as follows:

$$y'_A = \left(\frac{q}{q-1}\right) x'_A - \left(\frac{z_{F,A}}{q-1}\right) \quad (1-12)$$

Gathering all these previously mentioned data, it is possible to plot the operating and feed lines on the composition diagram according to McCabe-Thiele graphical method. The stripping section operating line passes through the point $(x'_{B,A}, x'_{B,A})$ as well as through the intersection between the feed line and the operating lines in the rectification section. It is then possible to compute the number of theoretical stages knowing the equilibrium curve, as illustrated in **Figure 1-5** [1,2].

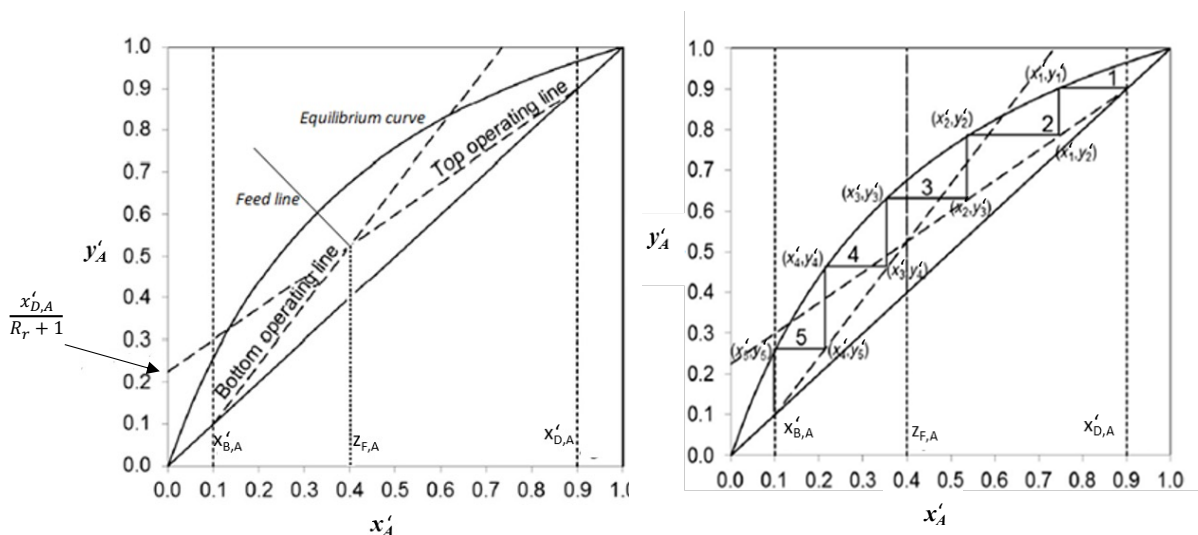


Figure 1-5 Plot of the operating lines and estimation of the number of theoretical stages using McCabe-Thiele graphical method [1].

The minimum reflux ratio ($R_{r,min}$) and the minimum number of theoretical stages (N_{min}) are essential parameters that must be defined and can be deduced from the McCabe Thiele diagram. The

former represents the ratio for which the desired separation requires an infinite number of theoretical stages; whereas the latter illustrates the minimum number of theoretical stages that must have a column with an infinite reflux so-called total reflux, to attain the desired separation. This means that the entire overhead product is recycled back into the column.

A higher reflux ratio constrains less theoretical stages, so a lower investment (fixed) cost but a higher operating cost because of the important amount of duties needed at the reboiler to face the vaporization requirement of the increased liquid flow. Contrarily, a lower reflux ratio requires higher number of theoretical stages, therefore a higher investment cost but a lower operating cost because of less needed duties. Hence, there is a need to find a compromise between the two extreme cases. The optimum reflux ratio $R_{r,opt}$ corresponds to the lowest total costs which is usually in the range of 1.1 to 1.5 times $R_{r,min}$. [1,2]

A noteworthy information is that for an azeotropic mixture, if the separation is not stopped before reaching the azeotropic composition, then the vapor-liquid equilibrium curve crosses the line of equation $x = y$. Hence, their separation by conventional distillation is no longer possible regardless of the number of theoretical stages.

1.4.Fenske's equation to compute N_{min}

An empirical **equation 1-13** developed by Fenske allows the estimation of the minimum number of theoretical stages based on the distillate and bottom composition, as well as the average relative volatility of the light component to the heavy one (α_{avg}). It should be noted that the volatility varies through the column and an average value of the relative volatility is taken over the column (**equation 1-14**). [1] Fenske's equation is a purely theoretical equation derived on the following assumptions:

- ideal Vapor-liquid equilibrium behavior,
- constant relative volatility,
- constant molal overflow,
- large reflux.

$$N_{min} = \frac{\log\left[\left(\frac{x'_{D,A}}{1-x'_{D,A}}\right)\left(\frac{1-x'_{B,A}}{x'_{B,A}}\right)\right]}{\log \alpha_{avg}} \quad (1-13)$$

$$\text{and } \alpha_{avg} = \sqrt{\alpha_B \alpha_D} \quad \text{or even } \alpha_{avg} = \sqrt[3]{\alpha_B \alpha_F \alpha_D} \quad (1-14)$$

where α_B , α_F and α_D are the relative volatility of the more volatile component to the less volatile component in the bottom, feed and distillate products, respectively. It is computed according to the following equation:

$$\alpha = \frac{(y'_A/x'_A)}{(y'_B/x'_B)} \quad (1-15)$$

where A and B indices designate the more and less volatile components of the binary mixture, respectively.

1.5.Degree of freedom

The degree of freedom (DOF) analysis is crucial for any chemical process design. It aims to define the number of variables that have to be imposed while designing a process. The analysis consists of enumerating the process variables and the different equations relating them. The DOF parameter is defined as the difference between the number of variables and equations. This parameter defines the state of the system whether it is an underspecified ($DOF > 0$), overspecified ($DOF < 0$) or well-defined ($DOF = 0$) system. It can also be further used to study the system optimization.

The case of a binary distillation without lateral withdrawal in a column of N trays operated at a fixed pressure is developed within this paragraph [3]. Feed conditions in terms of temperature, composition, pressure and flow rate are known input variables. The different equations and variables are listed below:

Equations

- two equilibrium equations (binary mixture) per tray ($2N$),
- 1 equation derived from the enthalpy balance per tray (N),
- 2 equations derived from the material balance per tray ($2N$).

Variables

- Number of trays ' N ' (1),
- partial molar flow rates of each constituent leaving each tray in both phases liquid and vapor ($2 \cdot N \cdot 2$),
- temperature of each tray (N),
- heat supplied by the reboiler (Q_{reb}) (1),
- heat removed by the condenser (Q_{cond}) (1).

Consequently, for the total number of trays, the number of equations is $5N$ and the total number of variables is $5N+3$ giving a DOF of 3. This result means that 3 variables must be imposed while designing a column. Some variables could not be imposed simultaneously such as both products' flow rate since their sum must be equal to the feed flow rate. A combination of 3 imposed variables can be:

- Distillate and residue purities and the reflux ratio,
- Number of trays, reflux ratio and distillate or residue flow rate,
- Reflux ratio, T_{reb} and T_{ref} ,
- ...

1.6. Impact of various operating parameters on the separation efficiency

Usually when operating a conventional distillation column, the products flow rates are output parameters as well as the temperature profile. Such columns operate in an adiabatic way. Hence, it is important to understand the effect of some crucial parameters (feed composition, temperature of reboiler and reflux ratio) on the distillation performance in order to be able to optimize the whole process.

Regarding feed composition, the amount of the light component in the feed has a significant effect on the separation. An increase in the amount of light component in the feed leads to a purer distillate and residue since more vapor is generated, hence better mass transfer between both phases take place.

An increase in the reboiler temperature leads to the increase in the amount of vapor generated. Consequently, light components are driven off the liquid phase and purer products are obtained.

Finally, by increasing the reflux ratio, the amount of the light component in the distillate increases since more cold liquid is supplied externally to the top of the column. By flowing downwardly, this liquid will induce the condensation of the vapor flowing upwardly thanks to its low temperature. Hence, improving the efficiency of the separation and increasing the purity of the distillate. [4]

1.7. Distillation columns internals

The most encountered distillation columns are whether tray columns or packed columns [1,2]. In the case of tray columns, mainly three internal configurations exist: bubble-cap tray, sieve or perforated tray and valve tray. All these configurations aim principally to enhance the bubbling of the vapor phase in the liquid one. They are illustrated in **Figure 1-6**.

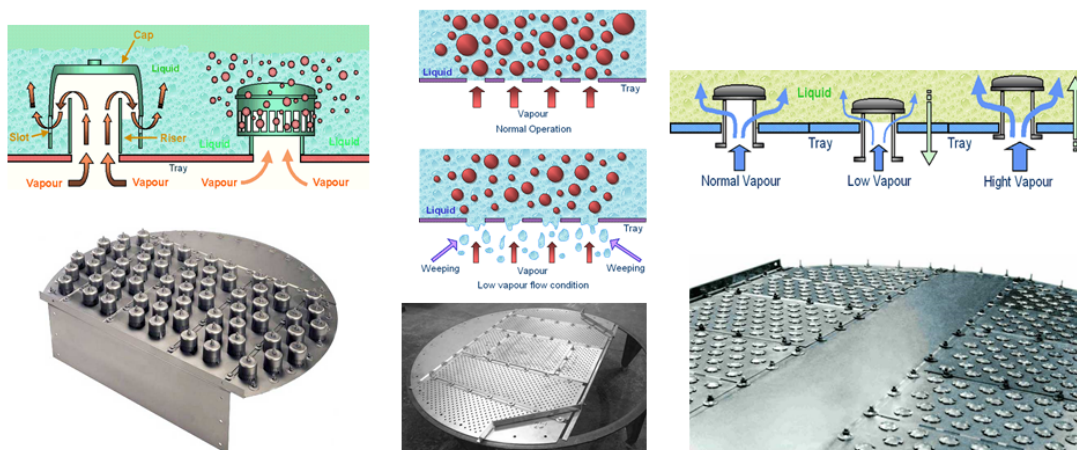


Figure 1-6 Different types of trays: (a) bubble-cap trays, (b) sieve or perforated trays and (c) valve trays [5].

The second type of columns is the packed ones that use random or structured packings instead of trays (**Figure 1-7**). These are wetting materials such as metal sheets that offer high contact area between both phases. The structured packings are organized in such a way that the packing resembles highly to a honeycomb thereby, enhancing the liquid spreading [6].

The choice between trays or packings depends mainly on several operating constraints such as flow rate range, allowable pressure drop, liquid holdup and many others.



Figure 1-7 Random and structured packings [7,8].

1.8. Conclusion

Distillation is a separation process based on the different boiling points of a miscible liquid mixture components. The liquid is driven downwardly inside a tower under the effect of gravity whilst the vapor travels upwardly. Both phases are in continuous contact throughout the column and mass transfer occurs. The vapor tends to vaporize the least boiling component from the liquid phase which aims, at its turn, to condense the high boiling component in the vapor phase. The distillate, least boiling component, is recovered at the top of the column while the residue, high boiling component, is collected as bottom product. In the case of a binary mixture, the McCabe-Thiele graphical methodology is usually used to compute the number of trays within a column. An empirical equation so-called Fenske's equation was given to estimate the minimum number of theoretical trays for a given separation.

The degree of freedom for classical distillation column was defined and a parametric study of some key variables was studied to understand their impact on the separation efficiency and to find out the optimum conditions. These variables were essentially the reboiler temperature, reflux ratio and the feed conditions.

From a chemical engineering point of view, distillation columns are limited to a minimum diameter and a certain range of flow rates, both for design and efficiency constraints. Such classical distillation columns are not always adapted to research purposes, for which the fluid's quantity is small. Indeed, as it can be seen from **Figure 1-8**, for the "miniplants" having a column's diameter that ranges between 30 to 50 mm, the impact of wall effects in terms of heat losses, wall flow, ... varies between 10 to 15% which is non-negligible. In this case, the distillation is no more adiabatic and the column's wall must be heated section-wise to minimize heat losses as much as possible to approach the adiabatic operation. It is reported that a nearly adiabatic operation can still be possible for a minimal diameter of 50 mm below which the experimental and simulated results do not match. Nonetheless, there is an increasing demand on reducing the column dimensions from laboratory-scale plants toward microplants, with flow rate down to 1 g/h. The main challenge is to achieve a column's size reduction while minimizing as much as possible the impact of wall effects [9] and overcoming the fact that capillary forces dominate gravity ones at this scale. Hence, developing small scale continuous distillations is possible and good separation performances are reachable, however the thermal efficiency is reduced. Therefore, continuous distillation downsizing requires more reflection.

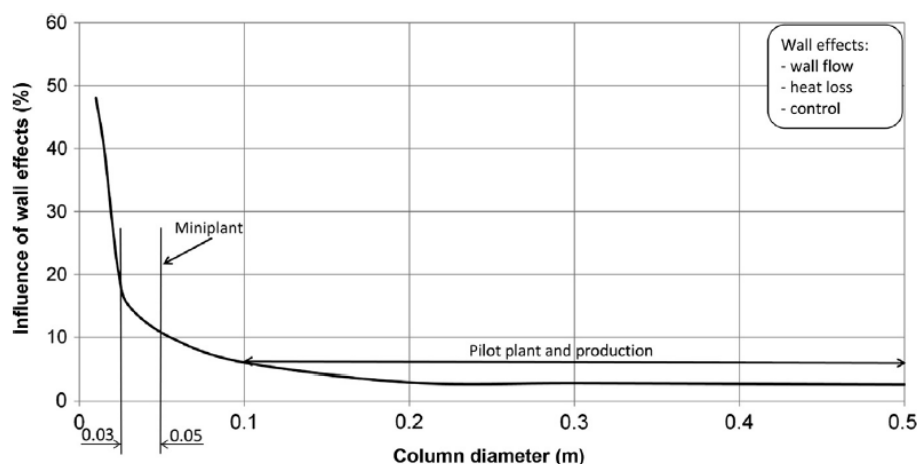


Figure 1-8 Graph showing the impact of the column wall (wall flow, heat loss and control) according to the column diameter [10].

2. Microdistillation

Microdistillations were previously known as small batch distillations that consist generally of a 50 mL flask much lower than the volume of the conventional columns (several liters). However, in these days, microdistillations refer to the reduced size batch or continuous distillations that treat lower feed volume or flow rate.

Following the miniaturization and the use of microreactors for continuous chemical processing, it has been noticed that there is no available continuous distillation tool, dealing with low flow rates in the range of mL/h, able to separate and analyze the low flow rates effluents of a pilot or production unit. Hence, when dealing with a gas-liquid effluent, the separation is usually performed by a single-stage flash, thus creating two streams. However, in this case, many products and impurities are split in the two streams and their amounts might be difficult to measure with usual analyses. This is for example the case of high throughput experimentation units at IFPEN, where a single flash separation is performed and gas chromatography is unable to quantify heavy compounds in the gas stream. As a result, mass balances never reach 100%. Being able to analyze precisely the different components would allow to access useful data, thus accelerating catalyst development.

Therefore, a new microseparation apparatus must be developed and designed. However, many technical barriers emerging from the miniaturization are difficult to overcome. Accordingly, adapting microprocess technologies in thermal separation processes constitutes a major challenge by virtue of required phase separation implicated.

Indeed, downsizing distillation faces some limitation related to the establishment of the gas-liquid counter-current flow since at the microscale, the effect of gravity and inertia forces fades in favor of surface tension forces. The governing forces could be determined based on a dimensionless number called Bond number (Bo). It is the ratio of gravitational to surface tension forces:

$$Bo = \frac{\Delta\rho g R^2}{\gamma} \quad (1-16)$$

where $\Delta\rho$ (kg/m^3) is the density difference between both phases, g (m/s^2) is the gravitational acceleration, R (m) is the radius of curvature of the gas-liquid interface and finally γ (N/m) is the surface

tension. If Bo is higher than 1, this means that gravity forces outweigh the capillary ones. However, in the opposite case, capillary forces are the dominant ones [11]. Thus, the classical gravity-based distillation methods are no more applicable. Alternative forces for driving the liquid phase and establishing the gas-liquid interface have to be considered.

As above mentioned, several objections are encountered while manufacturing a microscale distillation and have to be addressed. Establishing a controlled gas-liquid counter-current flow, managing the withdrawal of the residue and distillate products, the evaporation, the temperature as well as thermal losses, are a challenge at this scale as the surface to volume ratio is high.

Various strategies have been applied in the development of microdistillations since 1985 [12]. To monitor the liquid phase flow and establish a continuous gas-liquid interface, different driving forces were used to replace gravity ones. Capillary forces [12–25] were one of the possible alternatives. The first suggested microdistillation was based on capillary forces by adapting the heat pipe principle [12]. Afterwards, many inventions were realized by using wicks, nanopillars or even capillaries [23–27]. Wettability forces [27–31], centrifugal forces [28] and many others [29] have also been used as alternative forces to achieve microdistillation processes. In some cases, researchers tried to reduce the distillation size while maintaining overcoming surface forces by gravity forces [30–32]. Most of the investigated cases consists of on-chip microdistillation within which the microchannel dimensions fall between the milli- and the microscale in order to handle small flow rates.

Therefore, the main concepts in the microdistillation separation field are overviewed and discussed briefly in the next section. They will be divided in categories according to the type and size of the distillation process (batch, continuous of intermediate size and continuous on-chip microdistillation) and further subdivided according to the adapted driving force used to separate the gas-liquid flow. A scheme showing the proposed classification for the microdistillations is given in **Figure 1-9**.

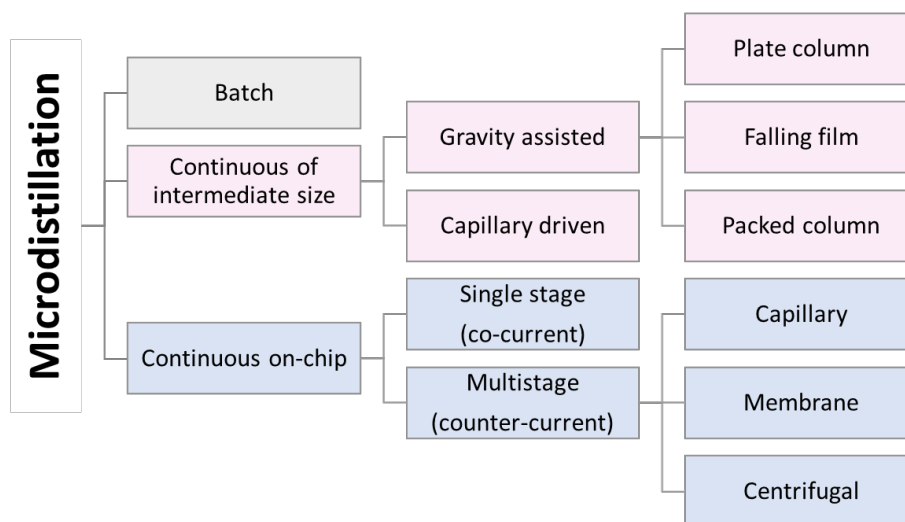


Figure 1-9: Scheme showing the classification of the various microdistillation concepts.

2.1. Batch microdistillation

In the studies presented hereafter, the aim of developing batch microdistillation process is essentially the extraction and quantification of a desired component from food samples. The concept consists of injecting a feedstock into the heating section of the channel along with a carrier gas. The mixture is then heated to a temperature above the boiling point of the target specie, causing it to vaporize. Thereafter, the flowing carrier gas will convey the emerging vapor toward a condensation channel where the temperature is cooled down to induce the condensation of the target specie that will be further quantified. The main goal behind this work was to achieve the quantification of specified species in various samples rather than the concept of on-chip microdistillation itself. Accordingly, the performances were illustrated by the percentage of recovery of the target specie. However, this factor is not sufficient to evaluate the distillation since the purity of the obtained products was not claimed.

PMMA-based microfluidic chips were manufactured using CO₂ laser ablation system. The microchips consist essentially of millifluidic channels, a serpentine channel, a heating zone, a cooling zone and a collection tank. The batch distillation occurs principally in the serpentine channel, where gravity ensures the two-phase separation.

This type of batch distillation was used by Ju *et al.* [33] to achieve the separation of sulfurous acid into sulfur dioxide and water, thus allowing the measurement of the SO₂ concentration using a spectrophotometer. The microchip was made of a single layer (**Figure 1-10**), and the heating and cooling were externally supplied to the chip. The distillation channel was 300 μm deep, 40 mm wide and 90 mm long. The percentage of SO₂ recovered using this apparatus was found to be around 94.6%.

Later, Dayao *et al.* [34] manufactured a microchip consisting of multiple layers of PMMA substrates bonded together (**Figure 1-11**). This particularity allowed the integration of the condenser and reboiler within the microchip. The distillation channel was a serpentine channel of 175 mm length and 4 mm x 4 mm cross sectional area. The concentration of recovered SO₂ was computed, after mixing it with H₂O₂, either by an alkali (NaOH) based titration method or by a paper-based detection method. The effect of different operating conditions on the distillation efficiency defined by the amount of recovered SO₂ was also studied. Accordingly, the optimal carrier gas flow rate, heating temperature, heating time and sample pH were found to be 25 mL/min, 130 °C, 25 min and 0.8, respectively. Under these operating conditions, the apparatus was able to achieve an average distillation efficiency of 90.5% in terms of recovered SO₂ for feeds having a SO₂ concentration ranging between 20 to 4000 ppm.

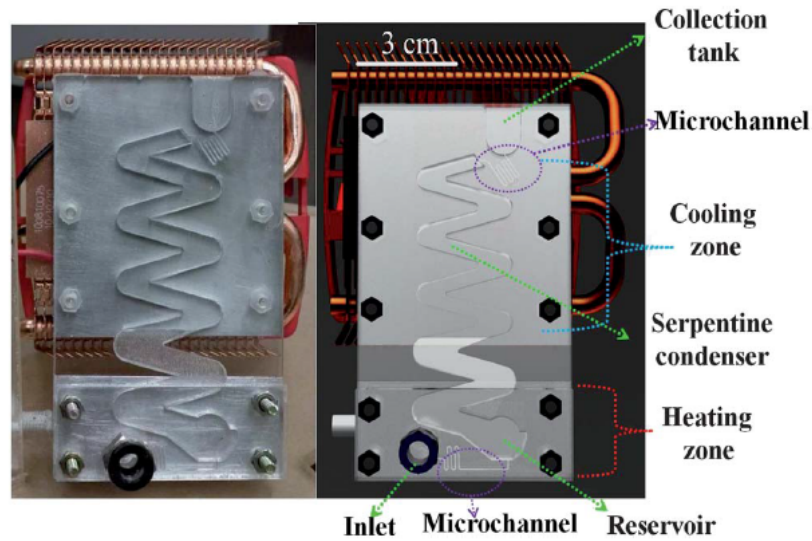


Figure 1-10: Microfluidic distillation chip assembly [33].

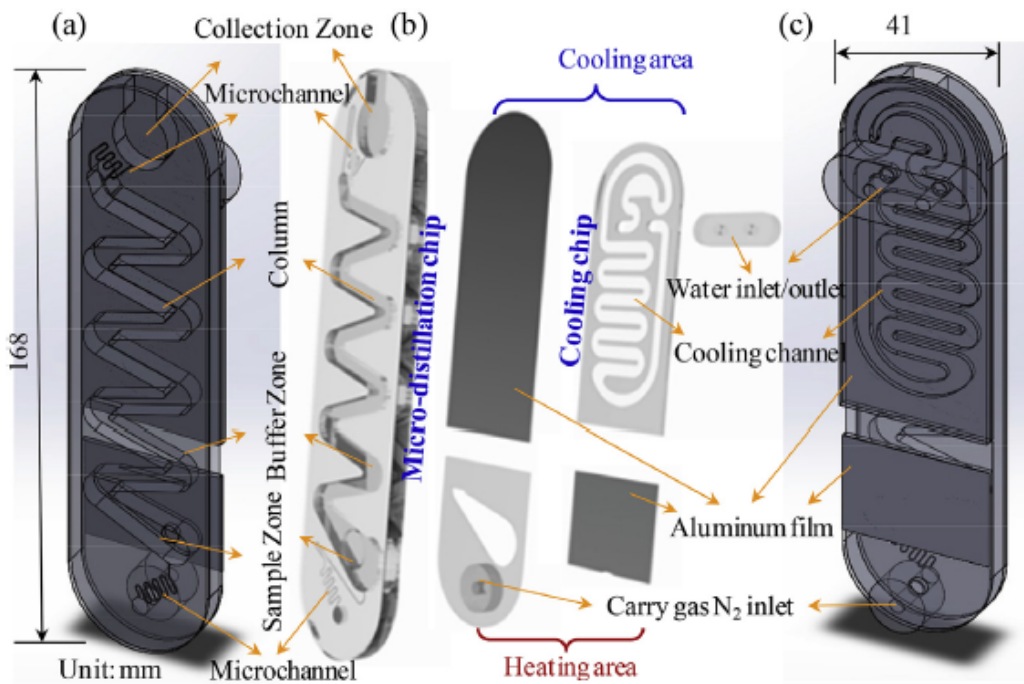


Figure 1-11: Dimensions of the different layers and channels of the microchip device [34].

Based on this principle as well, the detection of formaldehyde concentration in food products was also investigated by the same group of researchers [35,36]. In this case, the formaldehyde sample is injected into the channel and then mixed with high-pressure steam used as a heating source as well as a carrier gas. Two different multiple layers PMMA-based microchip designs were investigated.

The first one consists of 3 chained distilling chambers of 15 mL capacity [35]. The purpose of having three distilling chambers is not really clear since each was patterned on a PMMA substrate and were bonded together and there is no temperature difference between the three substrates (**Figure 1-12**). As aforementioned, it is the high-pressure steam that will cause the formaldehyde to vaporize; thus, the main objective behind these multiple distilling chambers is ambiguous. After condensation, the formaldehyde concentration was detected by conducting a colorimetric reaction with Fluoral-P

followed by a UV spectrophotometer measurement. It was proven experimentally that a 4-bar steam pressure led to a formaldehyde recovery percentage of 98%. Additionally, a Computational Flow Dynamics (CFD) simulation was done to evaluate the temperature profile and the steam flow field within the microdistillation chip. Particularly, the temperature profile of the cooling water and the sample steam within the microcondenser device was examined and illustrated. However, the temperatures of the various distillation chambers were neither studied nor mentioned.

The second one [36] consists of a single flash distillation zone having a thickness of 2 mm. The microchip assembly is shown in **Figure 1-13**. The recovered CH_2O is quantified using two different detection methods: AHTM (4-Amino-3-hydrazino-5-mercapto-1,2,4-triazole, $\text{C}_2\text{H}_6\text{N}_6\text{S}$) spectrometry method and a paper-based RGB (red green blue) intensity analysis method. Since the distillation time and steam flow rates are key parameters that impact directly the distillation efficiency, the researchers tried to find out the optimal conditions by conducting a parametric study. The highest formaldehyde recovery percentage was found to be 98.2% at a vapor stream rate of 0.4 mL/min and a distillation time of 10 min. Moreover, a calibration for each detection technique was done and it was found that a high linear relationship factor exists between the CH_2O concentration and the output signal of each technique. Finally, the performance of the suggested apparatus was evaluated by analyzing 21 commodity samples. The obtained results were then compared with results obtained from a commercial macroscale equipment for the same samples. The deviation of the microdistillation results from the commercial ones was found to be less than 4.3%. Additionally, this microdistillation apparatus has a lower detection limit of approximately 0.5 ppm.

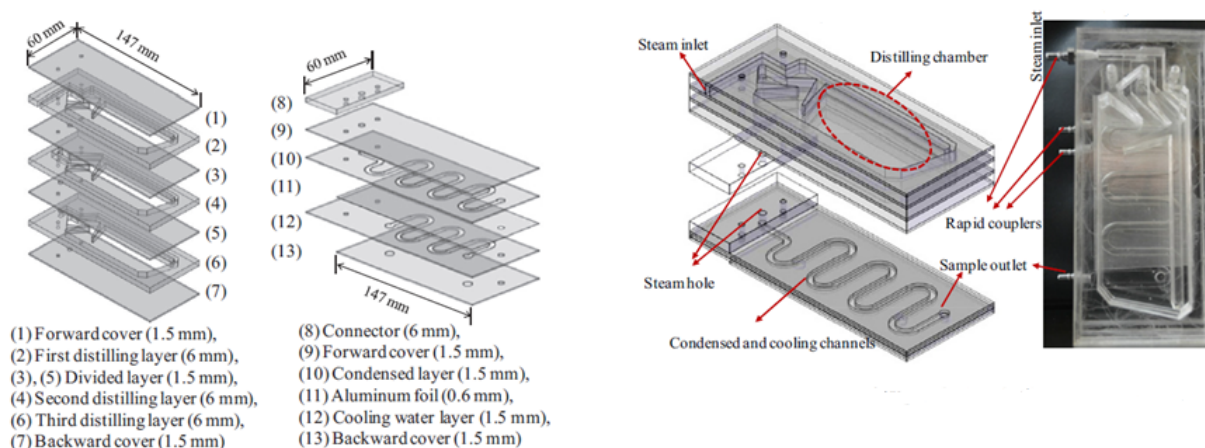


Figure 1-12: Schematic illustration of the various components of the microdistillation apparatus [35].

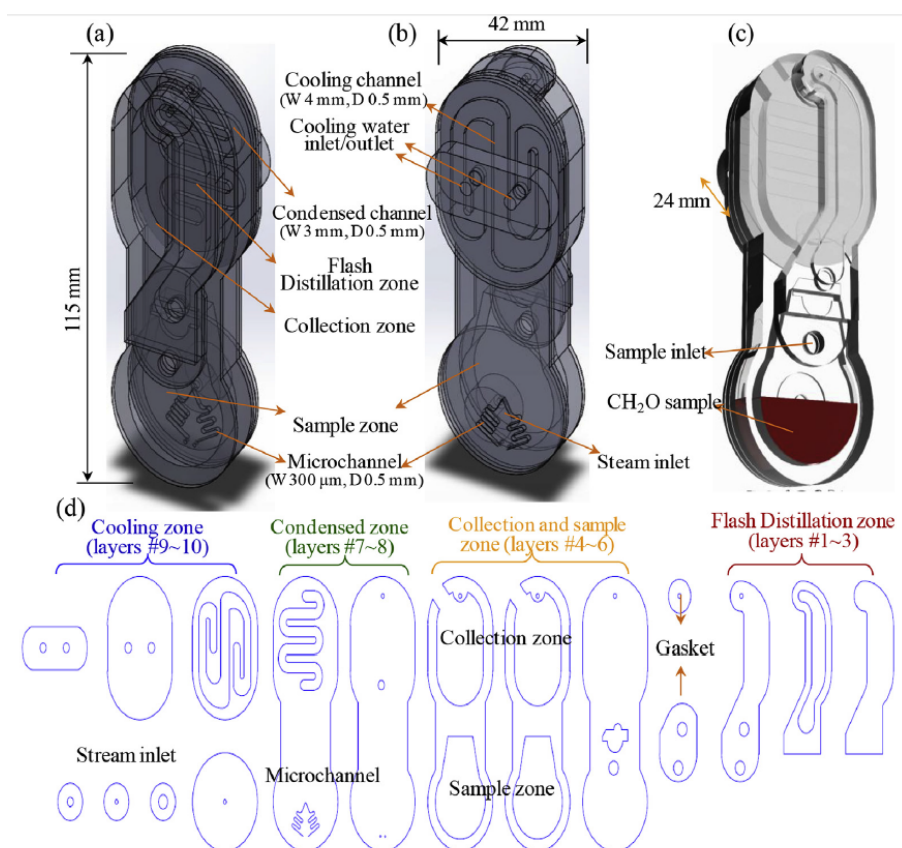


Figure 1-13: Schematic view of the different microchip components: (a) front view, (b) rear view, (c) front view illustrating the collection zone, and (d) structural elements [36].

The same principle was used to design a microchip for methanol quantification [37]. It is an integrated microfluidic chip (**Figure 1-14**) where the serpentine channel has a depth of 6 mm, a total length of 495 mm and a width of 4 mm in the upper region and 2.2 mm in the lower region. The device is designed in a way that each section of the channel (V-shaped or I-shaped) induces the distillation of the sample. According to the authors, it is equivalent to six separate batch distillations in series. The feedstock (methanol/ethanol/water solution) transported by the nitrogen flow undergoes evaporation followed by condensation cycles repeatedly in each section of the microchip. Therefore, the deionized water and part of the ethanol are condensed in the heating region thereafter recycled to the boiling region whereas the methanol remains gaseous and is then transported by the carrier gas toward the collection tank. It was shown experimentally by distilling ethanol/methanol/water solution for methanol concentration ranging from 300 to 800 ppm that this apparatus has an average distillation efficiency in terms of methanol recovery of 97.9%.

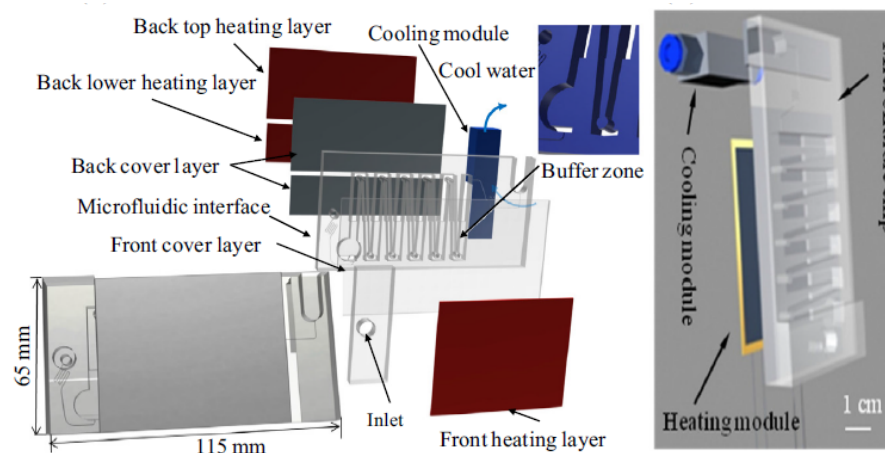


Figure 1-14: Microdistillation apparatus investigated by Wang *et al.* [37].

Another demonstration of microdistillation using low sample volumes was proposed by Giordano *et al.* [38]. In their device, the gas-liquid separation is reached using gravity forces; the volume of the distillation chamber is sized so that the gravity forces overweigh surface forces. A restriction in the top section, ending in a capillary channel where distillate flows out, helps contacting the vapor with the cold surfaces thus ensuring condensation and separation efficiency. 3D printing was used to manufacture and integrate such a device on a single PDMS chip (Figure 1-15). The chip also encompasses the elements encountered in a traditional flash distillation such as heating resistor, condenser, distillation flask and distillate collector. The volume of the distillation chamber was about 900 μL . A vertical temperature gradient was established from the bottom to the top of the distillation chamber thanks to the low conductivity of PDMS polymer. Thus, some of the generated vapor could condense at the wall of the distillation chamber and returns back to the liquid phase. The device was used to achieve the desalination of some samples as well as ethanol detection in alcoholic beverages. For the first aim, the device has succeeded to achieve high salt removal efficiencies for severe salinity conditions ($\text{NaCl } 600 \text{ mmol.L}^{-1}$) and high production rates (calculated based on the volume of distillate recovered after 1h of distillation). For the latter aim, their experimental results were in good agreement with those provided by gas chromatography. The performances of this device were not reported.

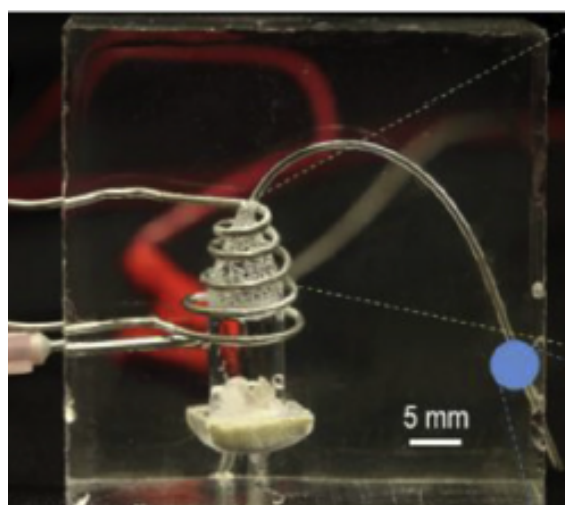


Figure 1-15: Principle of operation of the gravity-assisted distillation proposed by Giordano *et al.* [38].

Finally, a simple batch microdistillation apparatus was created by Mansfeldt *et al.*[39] by linking a heated sample vessel to a cooled absorption vessel via a capillary. The concept resides on heating the sample injected using a syringe pump and inducing its partial evaporation. The generated vapor is then transported via a capillary toward the absorption vessel where it condenses. The developed apparatus is shown in **Figure 1-16** and has been proved to be able to determine the total cyanide in soils. This device, compared to a conventional distillation apparatus used as an analysis laboratory method, appears to be advantageous because it achieves almost the same separation efficiency, even higher with lower input volumes (almost 10 mL for microdistillation instead of 100 mL for the standard distillation). Additionally, the effect of several parameters such as temperature, distillation time, sample volume, acid type and reducing agent on the microdistillation performance used for the determination of trace cyanide was studied by Chueachot and Chanthai [40].

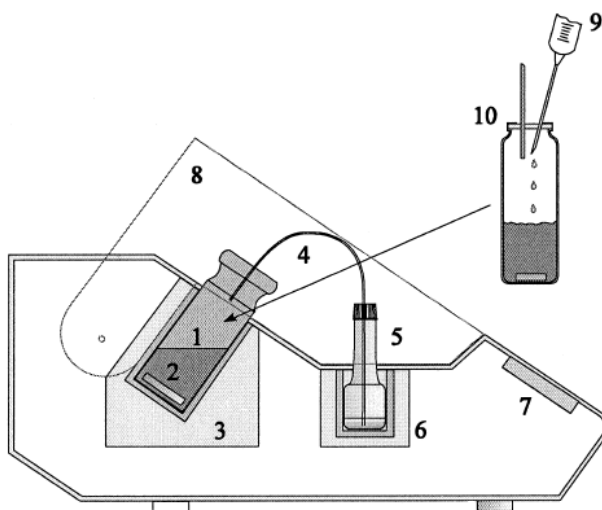


Figure 1-16: Microdistillation apparatus created by Mansfeldt and Biernath (sample vessel (1), frit (2), heater (3), capillary (4), absorption vessel (5), cooler (6), keyboard and display (7), protection hood (8), feed syringe pump (9), septum (10)) [39].

As a conclusion, all the presented designs were essentially based on the same general concept: injecting a feed inside an inlet reservoir, applying heat to the reservoir, thus inducing the vaporization of the light component. Some made use of a carrier gas to drive the gas phase and achieve the batch distillation, and gravity forces were always relied on as the driving factor to separate the vapor from the liquid phase. The purpose of this category of microdistillations is essentially the extraction and quantification of a desired component from food samples, herbs, *etc.* It is interesting to mention that in the cited cases, the reflux was not a controlled parameter but rather a resulting one. It was not quantified in any of these cases.

All these inventions and their principal characteristics as well as their performances are summarized in **Table 1-1**. The main advantage is that these devices require a small analysis volume whereas the main drawback is the use of a carrier gas, thus an additional gas-liquid separation step is required.

Table 1-1: Summary of the principle characteristics and performances of the different batch microdistillation approaches.

	Material	Distillation zone		Gas vector (if used)	Maximum Performance
		Dimensions	Chambers		
Ju <i>et al.</i> [33]	PMMA	D x W: 300 μ m x 40 mm	Single	carrier gas (N ₂ flow)	SO ₂ recovery 94.6%
Dayao <i>et al.</i> [34]	PMMA	D x W: 4 mm x 4 mm	Single	carrier gas (N ₂ flow)	SO ₂ recovery 90.5%
Liu <i>et al.</i> [35]	PMMA	Three 15 mL distilling chamber in series	Multi	high pressure steam	CH ₂ O recovery 98%
Hsu <i>et al.</i> [36]	PMMA	2mm thick	Single	high throughput steam	CH ₂ O recovery 98.2%
Wang <i>et al.</i> [37]	PMMA	D x W x L: 6mm x 4mm (upper)/ 2.2mm (lower) x 495 mm	Multi	carrier gas (N ₂ flow)	CH ₃ OH recovery 97.9%
Giordano <i>et al.</i> [38]	PDMS	900 μ L	Single	-	Not mentioned
Mansfeldt and Biernath [39]	Vessel	Vial of 10 mL of solution	Single	-	Not mentioned

2.2. Continuous microdistillation of intermediate size

This part is dedicated for the microdistillation of intermediate size (10 to 300 mL/h) operated in a continuous mode. Two main concepts could be adapted to achieve the distillation step:

- Gravity assisted microdistillation,
- Capillary driven microdistillation.

The first one makes use mainly of gravity forces in order to drive the gas-liquid counter-current flow, as in a conventional distillation column. Therefore, the idea is to create a design in which the gravity forces will conserve their main role and overweigh surface forces. The encountered designs based on this concept are listed in the gravity assisted microdistillation part.

The second concept is more complex and is highly inspired by the heat-pipe principle [12,16,18,20]. In a heat pipe, a pure liquid is vaporized when it is in contact with the hot interface. This vaporization step absorbs heat from the hot interface. Then, the generated vapor travels through the gas channel toward the cold interface where it is condensed, thus releasing heat. The condensed vapor joins the liquid phase and is further driven back to the hot end thanks to a specific packing that prevents mixing between the gas and the liquid phases. Such packing usually relies on capillary phenomena. Hence, a condensation-evaporation cycle is induced. This kind of device offers high heat flux, several times higher than heat conduction through copper. If the pure liquid is replaced by a binary mixture and the packing allows contact between gas and liquid phases, the same process will occur

along with a continuous mass exchange between both phases. The hot interface is the reboiler, while the cold interface is the condenser. Therefore, it resembles highly to a batch distillation process when operated at total reflux, with a temperature gradient from the reboiler to the condenser. In order to make it a continuous distillation, one inlet and two outlets channels must be placed. A noteworthy difference compared to the gravity assisted microdistillation type is that this kind of systems can operate horizontally since gravity forces are outweighed by capillary ones [12].

2.2.1. Gravity assisted microdistillation

2.2.1.1. Plate microdistillation column

A microcolumn based on gravitational forces which resembles highly to a conventional plate distillation column was proposed by Ziogas *et al.* [32]. It is a microrectification stainless steel equipment [32] that can be operated under batch, semi-batch or continuous conditions. It consists of a vertical plate column (**Figure 1-17**) equipped with a reflux condenser, a distillate drum and a bottom reboiler. It is possible to use mesh to ensure the liquid retention and to favor the two phases contact. Additionally, a certain liquid level was maintained at each plate thanks to the downcomer. Since the desired temperature profile was reached by using three heating cartridges inserted at different positions, the column is operated under non adiabatic conditions. Its performance was tested under batch conditions using acetone/n-butanol, toluene/o-xylene and i-octane/n-octane binary mixtures (total volume of 15 mL for each system). It was evaluated as well under continuous conditions using o-xylene/p-xylene mixture fed at 30 mL/h. A NTS of 12 and a height equivalent to one theoretical plate (HETP) of 10.8 mm were obtained for the batch distillation operation of i-octane/n-octane mixture at total reflux. This high separation efficiency is obtained thanks to a good temperature control and long duration of separation process (~3h). Moreover, an intensification of the mass transfer thanks to the high interfacial area between the liquid and the vapor was obtained under constant reflux. It was seen that the sieve plates were fully filled with liquid without reaching the flooding phenomenon under constant reflux. Additionally, it was claimed that the feed mixture has contributed to this high performance as i-octane and n-octane have almost the same heat of evaporation. The continuous distillation of an equimolar mixture of o-xylene/p-xylene at 30 mL/h under atmospheric and reduced pressure was also tested. The reflux ratio was managed by using a return valve at the top of the column. Therefore, the continuous distillation of an equimolar mixture of o-xylene/p-xylene (30 mL/h) under a reflux ratio of 7 gave a NTS of 12 and a HETP of 10.8 mm.

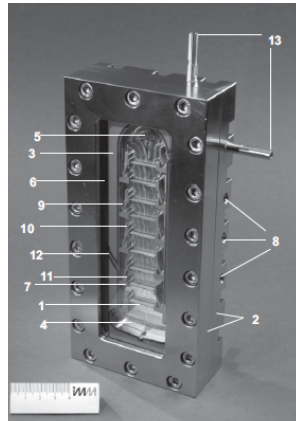


Figure 1-17: Different elements of a microrectification apparatus (plate (1), housing (2), plate inlay (3), column bottom (4) and top (5), viewing window (6), plate holder (7), heating cartridges position (8), downcomer (9), outlet (10) and inlet (11) weir, feed inlet channel (12), coolant inlet and outlet (13)) [32].

2.2.1.2. Falling film microdistillation column

The operating principle of the following microdistillation columns matches the falling film technology. A thin liquid film flows down the walls, whereas the vapor moves up to the top of the column. The distillation concept remains the same: evaporation followed by condensation with a counter-current two-phase flow enabled by gravitational forces.

Based on this principle, a microcontactor to separate binary mixtures was used by Kane *et al.* [31]. The device was made from microchannels etched on two heated vertical brass plates (2 mm thick, 9 cm wide and 18 cm long). Obviously, it is the use of these structured plates that will condition the liquid flow downward by gravity without being driven by the gas phase. In fact, the liquid flows in 72 straight microchannels (36 on both sides of the distillation chamber), each microchannel having a 200 μm depth, 1 mm width, and 150 mm length. It is important to note that there is no reflux nor reboiler implemented on this device: instead, a homogeneous heat flux is applied to both plates through electrical film heaters. As the feed injection is located at the top of the microchannel network, the principle is close to that of the stripping section of a classical distillation column. Since the feed is colder, a small temperature gradient can appear and generate an evaporation-condensation cycle inside the device. The bottom product was collected inside a small capacity which was drained using a peristaltic pump to avoid liquid accumulation, as illustrated in **Figure 1-18**. As for the gas phase, it is first heated when exiting the device to prevent condensation and backflow, and finally condensed for collection.

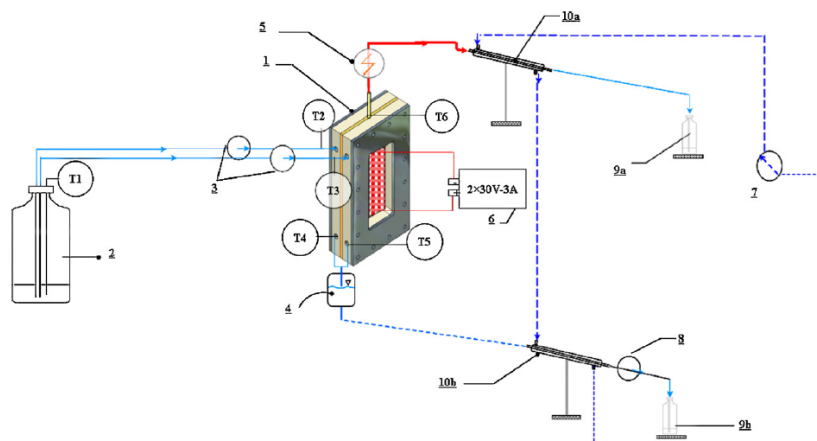


Figure 1-18: Experimental setup developed by Kane *et al.* [31] (1-microcontactor, 2-feed tank, 3-pumps, 4-bottom reservoir, 5-heater, 6-power supply, 7-cryostat, 8-peristaltic pump, 9a-distillate, 9b-residue, 10-condensers) [31].

The performances of the device shown in **Figure 1-19** were evaluated using a mixture of ethanol and n-propanol. The impact of feed flow rate (1-8 g/min) and electrical heating fluxes (2-5 kW/m²) on the separation performance was also studied. In the case of a distillation of 47.1 mol% ethanol/n-propanol mixture heated to 48.9°C and injected at a feed flow rate of approximately 1.55 g/min, the mole fractions of ethanol in the distillate and bottom product were 0.526 and 0.387, respectively. The performances in terms of NTS and HETP were not mentioned. Based on their results, the NTS was lower than 1, estimated using McCabe & Thiele diagram.

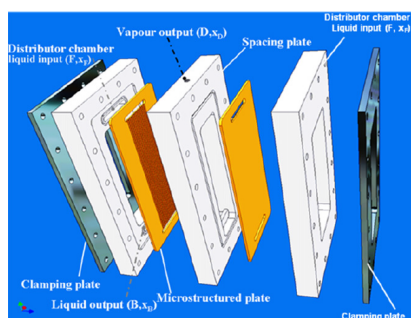


Figure 1-19: Schematic illustration of the microcontactor [31].

Exploring as well the falling film technology, Fink and Hampe [30] imagined a collimator column to separate a binary mixture of 32 mol% aqueous methanol fed at 10 mL/h under atmospheric pressure. The column is made up of polyvinylidene fluoride (PVDF) parts assembled together in order to offer an annular space for the liquid and vapor phases (**Figure 1-20**). Thanks to PVDF wetting properties, the liquid forms a thin film layer on the inner and outer surfaces of the annular space. Sintered metal elements are used in the feed and in the top section to ensure a suitable liquid spreading. The temperature gradient can be established by heating up the bottom of the column via a steel plate. Even if apparently built, performances of the system were unfortunately not evaluated or the results were not reported. Performances were estimated theoretically based on Kuhn and Jantzen model. The collimator column was found equivalent to 10 stages for a 16 mm inner diameter, a 19 mm outer diameter and a height of 40 mm. Authors also reported a 3 mL liquid holdup for the whole system.

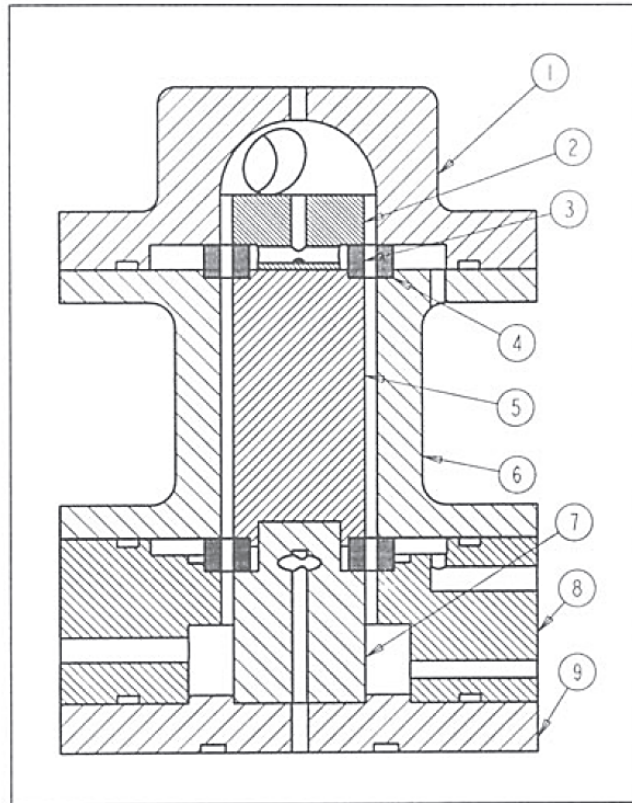


Figure 1-20: Collimator type column [30]. (1) and (2) outer and inner parts of the top, (3) and (4) sintered elements, (5) and (6) inner and outer parts of the enrichment section, (7) and (8) inner and outer parts of the stripping section and (9) bottom (heating plate).

2.2.1.3. Packed microdistillation column

Some made use of 3D printing to explore new routes of distillation intensification, thanks to the possibility to design and easily manufacture small structured devices. In this context, gravity forces are responsible for separating the gas and liquid phases. Two different distillation columns were investigated by Mardani *et al.* [41] using 3D printing. The chosen polymer was HTM140IV (high temperature mold material able to withstand to 140°C). The incorporation of different devices led to the recovery of the various functions of a conventional distillation column such as maintaining a constant rate of withdrawal and incorporating a reflux system, while minimizing the liquid hold up of the system. The first column is a one-block coiled-shape distillation column (10.8 cm (length) x 1.2 cm (width) x 0.4 cm (height)) illustrated in **Figure 1-21**.

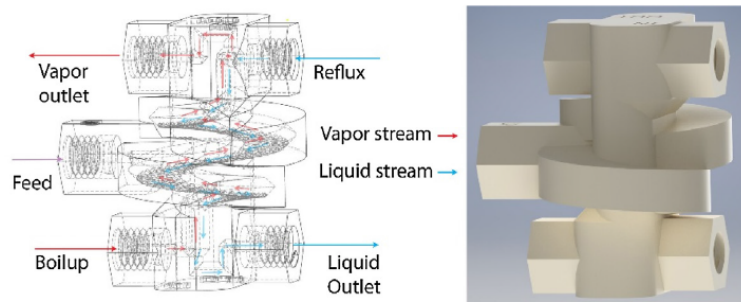


Figure 1-21: Schematic view (left) and 3D model (right) of the first design [41].

The second design (**Figure 1-22**) is a modular distillation column (11.2 cm (length) x 7.9 cm (width) x 15.1 cm (height)), more convenient since it allows adjusting some parts in order to optimize the distillation process without reprinting the whole column. This column was tested with stainless-steel spring packing and 3D printed random packing.

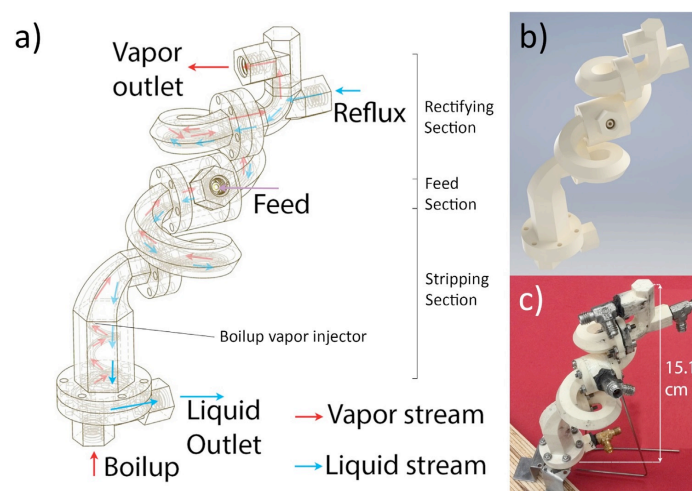


Figure 1-22: (a) schematic view, (b) 3D model and (c) the real modular microdistillation column obtained by 3D printing [41].

The distillation process is similar to that of the conventional column. The preheated feed was injected into the distillation column by using a syringe pump. The bottom product withdrawal was based on the communicating vessels principle, whereas the distillate was taken out by a micropump operating at constant flow rate. The reflux was not controlled: as the distillate flowrate was set, the excess liquid collected in the reflux drum was sent back to the column. This flowrate was however measured. Both products, residue and distillate, were analyzed using an online gas chromatography. Moreover, the whole system was operated under atmospheric pressure. It is interesting to mention that the whole column was insulated in order to make the operation adiabatic.

The evaluation of the column performance was done by separating a hexane-cyclohexane mixture. The one-block column was able to achieve a separation equivalent to a NTS of 0.5 during 1 hour of running. However, many inconveniences appeared by using this one-block system such as level control, plugging and leakage. Therefore, this design was disregarded and the second column configuration was evaluated. The modular distillation column was first tested without packing. It has achieved a separation equivalent to a HETP of 231 mm under total reflux. Once loaded with the stainless-steel packing, its separation efficiency was equivalent to a HETP of 74 mm under total reflux and of 95 mm with a reflux ratio of 4.6 and a feed flow rate of 53 g/h (based on distillate and residue flow rates). This column, loaded with 3D printed packing, achieved a separation equivalent to a HETP of 88 mm under total reflux conditions.

2.2.2. Capillary driven microdistillation

2.2.2.1. Principle

Up to now, all the presented microdistillation systems relied on gravitational forces to establish the gas-liquid counter-current flow inside the channel. For the capillary driven microdistillation category, a new principle that takes advantage of capillary forces is introduced. In these systems, the

liquid phase is driven by porous materials (metal foam, wick, *etc.*) where it moves preferentially through capillary action. The liquid flow from the condenser towards the reboiler occurs with a slight pressure drop mainly due to friction. On the other hand, the gas flow from the reboiler towards the condenser takes place with a slight decrease in the gas pressure. The small pore size of the porous materials induces the formation of a steady interface between the gas and the liquid phase. As this interface has a small curvature radius, a significant pressure difference between the gas and the liquid phase appears. This capillary pressure (ΔP_c) is given by the following Young-Laplace equation, assuming a pore having a circular cross section:

$$\Delta P_c = \frac{2\gamma \cos \theta}{r_p} \quad (1-17)$$

where γ (N/m) is the surface tension, θ is the contact angle between the gas-liquid interface and the solid surface of the pore and r_p (m) is the pore radius. A schematic view of the gas liquid interface with a spherical meniscus (radius R) is given **Figure 1-23**.

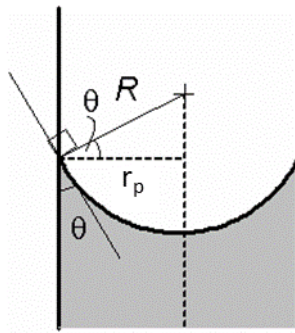


Figure 1-23: Schematic view of a gas-liquid interface in a narrow tube.

The contact angle θ varies between 0 and π , depending on the gas, liquid and solid composition. Three cases can be considered:

- If $\theta = \pi / 2$ (infinite radius of curvature) then $\Delta P_c = 0$ and the interface is flat. Beyond this value, the liquid can enter the gas phase.
- If $\theta \in [0; \pi/2[$, ΔP_c is positive and the liquid pressure is lower than that of the gas. Perfect wetting is obtained when $\theta = 0$, resulting in a radius of curvature equal to the pore diameter.
- If $\theta \in] \pi/2; \pi]$ ΔP_c is negative and the liquid pressure is higher than that of the gas. When $\theta = \pi$, ΔP_c is minimum

It has to be noted that in a straight pore, as represented on **Figure 1-23**, the interface slides inside the pore. This is for example the case of a vertical capillary dipping in a liquid, where the interface in the capillary rises under the action of both hydrostatic and capillary pressure (Jurin's law).

For a given system, the contact angle θ can vary slightly between an upper and a lower limit θ_{\min} and θ_{\max} . Given the Young-Laplace equation, this means the pressure difference between both sides of the interface can also vary. By considering a gas-liquid interface in a circular hole instead of a pore, the interface does not have the capability to slide. The contact angle θ will vary depending on the pressure difference between both sides, according to the Young-Laplace equation. Three configurations are possible depending on the pressure difference (**Figure 1-24**):

- $\Delta P < \Delta P_{C,min}$, i.e. $\theta > \theta_{max}$: the interface will break and the liquid phase will enter the gas side,
- $\Delta P > \Delta P_{C,max}$, i.e. $\theta < \theta_{min}$: the interface will break and the gas phase will enter the liquid side,
- $\Delta P_{C,min} < \Delta P < \Delta P_{C,max}$, i.e. $\theta_{min} < \theta < \theta_{max}$: the interface is stable

with:

$$\Delta P_{C,min} = \frac{2\gamma \cdot \cos\theta_{max}}{r_p} \quad (1-18)$$

$$\Delta P_{C,max} = \frac{2\gamma \cdot \cos\theta_{min}}{r_p} \quad (1-19)$$

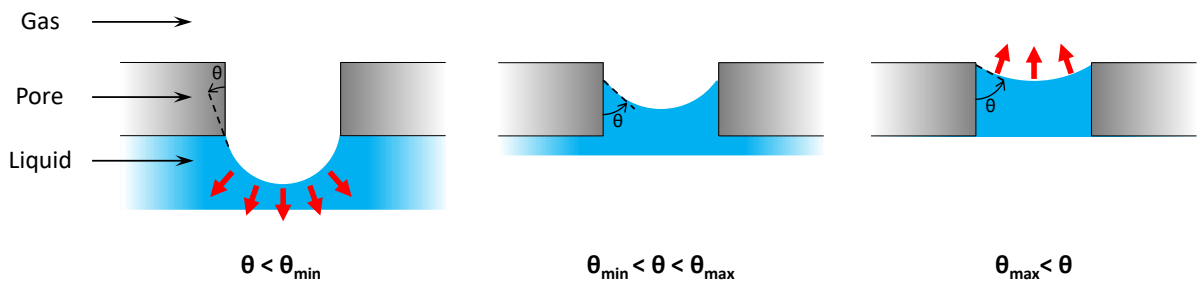


Figure 1-24 Different possible configurations according to the gas-liquid pressure difference.

This stability condition of the gas-liquid interface has to be fulfilled in each position of the channel in order to ensure a stable counter-current flow and a proper operation of the device. Particularly, in each position, the difference between the gas and the liquid pressure satisfies:

$$\Delta P_{C,min}(x) < P_G(x) - P_L(x) < \Delta P_{C,max}(x) \quad (1-20)$$

For simplification purposes, we will assume a wetting liquid with $\theta_{min}=0$ and $\theta_{max}=\pi/2$ for the following considerations.

Note that $\Delta P_{C,min}(x)$ and $\Delta P_{C,max}(x)$ can vary along the channel as the liquid phase composition will change, hence the x dependence. Both gas and liquid pressures inside the channel result from hydrodynamic conditions as they are flowing continuously and counter-currently. While the gas phase pressure will decrease on one side of the interface from the reboiler to the condenser, the liquid phase pressure will increase on the other side. The fact that the interface can have different radii of curvature depending on the location inside the microchannel is the key that allows establishing a gas-liquid counter-current flow.

Whilst capillary action is the main force that drives the counter-current flow in these systems, gravity still plays a role through the hydrodynamic pressure of the liquid phase. Consequently, operating a capillary microdistillation vertically or horizontally might affect its capacity.

These guiding principles were mentioned and taken into consideration in several works [12,17,21].

2.2.2.2. Wick based capillary network

The first manufactured capillary microdistillation based on the heat pipe principle was proposed by Seok and Hwang [12] in 1985 (**Figure 1-25**). Copper tubes were used for the reboiler and condenser while the central and adiabatic section was made of a glass tube (340 mm length and 10.5 mm internal diameter). The tube was lined with capillary wicks (fiber glass, 1.2 mm, held against the tube with an aluminum screen) that promote the formation of a thin liquid layer on the tube wall, whereas the gas flows in the core of the tube. The gas-liquid flow was similar to a counter-current annular flow.

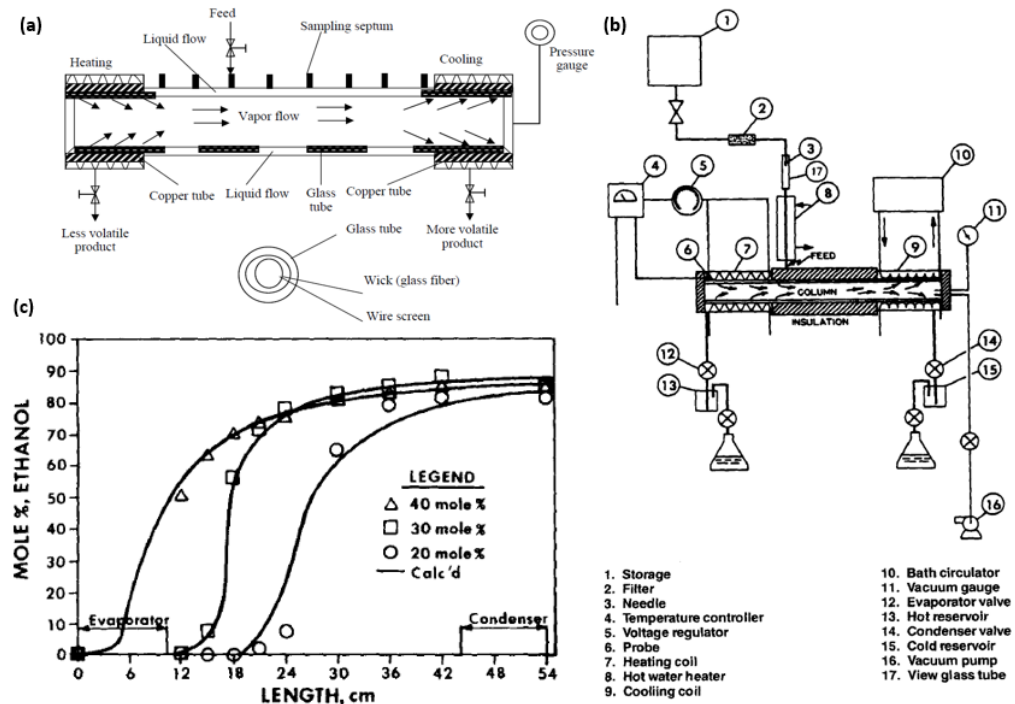


Figure 1-25: (a) Schematic view of zero gravity microdistillation device, (b) process scheme and (c) agreement between experimental results and calculated concentration profiles [12].

Product withdrawal was managed by using condenser and evaporator valves and opening them after reaching the steady state conditions. Both effluents were withdrawn in liquid state, and as the microdistillation was operated at atmospheric pressure, their flow rates resulted from the excess liquid inside the channel (capillary wicks have a constant liquid holdup). Products were collected into reservoirs of 6 cm³ capacity drained toward collectors once filled. According to the authors, these steps may not affect the operating process since the distillation is conducted under atmospheric pressure. The liquid phase was also sampled at different positions inside the channel to study the concentration profile (see **Figure 1-25**). The detailed process scheme is shown in **Figure 1-25, b**.

The performances of this microdistillation device were evaluated for various reflux conditions using two binary mixtures: ethanol/water and methanol/water with feed flow rate ranging between 18 and 24 mL/h. It was found that this device achieved a high degree of separation and the HETP was measured between 59 and 190 mm under total reflux. A numerical model, considering mass transfer between gas and liquid phases through height of a transfer unit (HTU) and Chilton and Colburn [42]

equation was solved to compute the composition profile inside the channel under total reflux. It was proven that the experimental and numerical results were in good agreement (**Figure 1-25, c**).

A similar microdistillation channel was patented by Velocys industry [17,21]. In fact, the patent addresses different applications with the same concept such as gas absorption, liquid-liquid extraction, and distillation being one of them. The device consists of one or several planar channels, lined with wicks or other porous materials on one or both end plates. The channel depth ranges from 0.1 to 1 mm, while width and length are not essential parameters. The preferred pore sizes in the wick materials ranges from 0.1 to 100 μm . It was also claimed that the thickness of the wick is an important parameter for processes where the liquid phase mass transfer is a limiting step. With thinner wicks, performances are enhanced (preconize thickness is 50-150 μm). These wicks could include or be replaced by microchannels ($D \times W$: 10-500 $\mu\text{m} \times 10$ -100 μm) that promotes liquid migration by capillarity. A schematic view of the microdistillation invention is displayed in **Figure 1-26**.

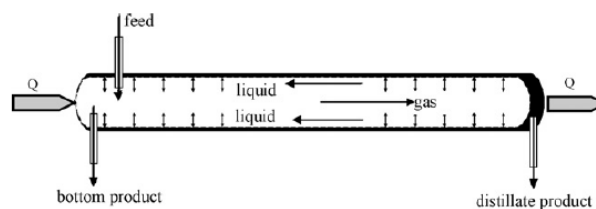


Figure 1-26: Schematic view of the planar microdistillation investigated by Huang *et al.* [18].

A microdistillation device based on this concept and having 15 channels provided with thin wicks (thickness between 0.1 to 1 mm) was used to produce a light (low sulfur content) JP-8 fuel feedstock for hydrodesulfurization (HDS) study [18,19]. The feed was pumped at flow rates between 1.5 and 3.5 g/min. The distillate was totally condensed and partially returned into the chip as it can be seen in **Figure 1-27** whereas the residue withdrawal was not mentioned. However, **Figure 1-27** shows that the residue is withdrawn by a pump. The possibility to use a pump to withdraw the liquid was mentioned in the patent [21]. A parametric study was considered to find out the optimal process conditions. Following this study, the low sulfur distillate for their study was produced at a 150 g/h feed flow rate, a 230°C JP-8 fuel feed temperature, and at a 4.3 reflux ratio. Experimentally, the sulfur content was reduced from 1300 ppmw to 329 ppmw in the distillate stream (sulfur species were concentrated in the residue). Compared to conventional batch distillation, they claimed performances were slightly better (332 ppmw sulfur content in the distillate) [18].

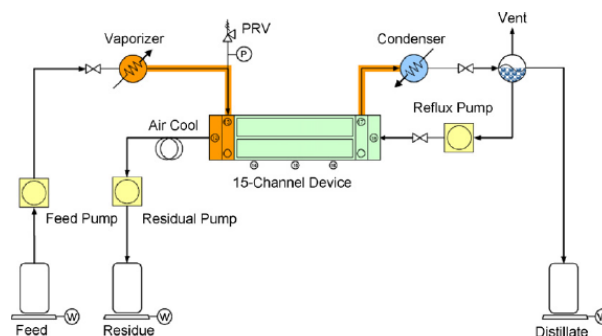


Figure 1-27: Diagram of the microchannel distillation apparatus implemented by Huang *et al.* [18].

As the device was operated under a JP-8 fuel feedstock, the NTS cannot be estimated with the classical McCabe-Thiele method applied for binary mixtures. The distillation efficiency in terms of HETP was numerically computed by using a ChemCAD model of a conventional distillation column fed with a vapor phase at the bottom and with no reboiler to approach as much as possible the real microdistillation conditions [19]. The target was to fit the experimental distillate composition by adjusting the NTS and the reflux ratio in the ChemCAD simulation. Using this approach, a 17.6 mm HETP was estimated, which represents good performances according to them given that commercial large-scale structured packings usually exhibit 30 cm HETP.

2.2.2.3. Metal foam based capillary network

Sundberg *et al.* [16] took advantage of the same principle by using metal foams as porous network. Three different microdistillations were modeled and manufactured with different metal foams positioned in various orientations. These devices were heated at one end and cooled using air or temperature-controlled water at the other end. A schematic view of the microdistillation device is shown in **Figure 1-28**. An equimolar mixture of n-hexane/cyclohexane was used to compare and test the separation efficiency of the different devices, with flow rates ranging from 0.15 to 2 mL/min in continuous operation. It should be noted that the foam was totally filled with liquid, and the liquid-vapor interface was only located at the surface of the metal foam. Reflux management was not mentioned in this work, but it appears that the reflux ratio is not controlled. **Table 1-2** summarizes the main characteristics and experimental results of the suggested devices. It can be deduced that the device 1B has the best separation efficiency. For this reason, it was tested in various inclinations and it was found that the horizontal orientation was the optimal one. The authors explained this result by gravitation forces dominance, which can be related to the rather high pore diameter compared to Velocys' patent [21]. Another proof of this high dependency to gravitational forces is that tilting the device toward the hot end highly increased the maximum liquid flow rate through the foam. Whilst exhibiting high porosity and low mean pore diameter, design 2 led to poor performances: in this foam type, porosity is not connected in the flow direction, thus hindering the liquid flow. Many difficulties have been encountered such as heat losses and lack of degasification due to the design (distillate is collected in liquid phase, thus any non-condensable will be trapped inside the channel). The first one was partially solved by fixing two temperature-controlled aluminum plates to both sides of the distillation device.

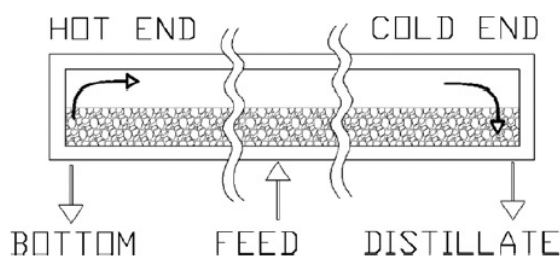
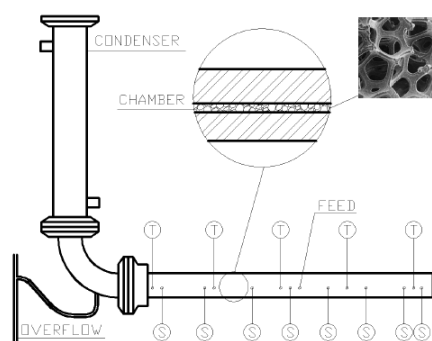


Figure 1-28: Sundberg *et al.* [16] distillation device.

Table 1-2: Characteristics and experimental results obtained at total reflux conditions for the various microdistillations [16].

Device	Internal dimensions (mm) (H*L*W)	Metal foam thickness	Specific surface area (m ² /m ³)	Porosity - Mean pore size	Orientation	NTS	HETP (mm)
1A	3.5*140*30	1.6 mm	5400	Over 95%, 0.4 mm	Horizontal	8.3	16.8
1B	3.5*140*30	2 mm	2800	Over 95%, 0.6mm	Horizontal	10.8	13.0
					Vertical	2.8	50.8
2	2*500*100	0.5 mm	15000	Max 97%, 0.15mm	Horizontal	9.9	50.5
3	5*290*30	3 mm	2800	Over 95%, 0.6mm	Horizontal	11.5	25.2

Later, the microdistillation of type 3 was improved by Sundberg *et al.*[15]. The improvement consisted mainly in the withdrawal of distillate via overflow at the vacuum elbow shown in **Figure 1-29** as well as eliminating the available open space above the foam (the total channel thickness is thus 3 mm, fully filled with metal foam). The latter one aims to force the vapor travel through the metal foam and to bubble into the liquid, thus enhancing the liquid-vapor mass transfer. The bottom product withdrawal was ensured by gravitation, and the overall liquid holdup of the channel was 40±5 mL. Aluminum plates were attached at both sides of the device for a better temperature control.

**Figure 1-29: Distillation device diagram (S stands for sampling connections and T for temperature measurements) [15].**

The same equimolar mixture of n-hexane/cyclohexane was used to evaluate the separation efficiency under total reflux. The experimental results obtained indicate a NTS of 18±2; equivalent to a HETP of 16 mm. The main drawback encountered is that the separation is principally taking place within the stripping section. This is potentially due to the vapor flow reduction near the condenser and the back mixing occurring from the holdup in the vacuum elbow.

Afterwards, Sundberg *et al.* [13] further updated this last design by implementing an accurate monitoring of the reflux and reboil flow rates. The planar, horizontal distillation channel (same as design 3 in **Table 1-2**) was totally filled with metal foam. Mass flow controllers were used to regulate the reflux and reboiler flow rates, while distillate and bottom product flow rates were controlled by liquid level sensors. This indicates the presence of gas-liquid separators at the condenser and reboiler sections of the device, even if it was not mentioned. Heat losses were compensated by the use of heated shell over the insulation layer. As for the conventional distillation, the feed is preheated and then injected into the microdistillation device to avoid the consumption of energy required to heat the feed to its bubble point.

The feed was injected at a rate of $1 \text{ cm}^3/\text{min}$, in the same order of magnitude as their previous work. Two binary (n-hexane/cyclohexane, methylformate/methanol) and one tertiary (2-methylbut-2-ene/ethanol/2-ethoxy-2-methylbutane) mixtures were distilled to evaluate the performance of the device shown in **Figure 1-30**. The distillation process was then simulated as a steady-state separation using Flowbat software based on Wilson model and Soave modification of Redlich–Kwong equation of state. Based on these results of n-hexane/cyclohexane and the experimental ones at total reflux, a HETP between 0.05 and 0.1 m was determined for this setup. A noteworthy observation is that this HETP continuously decreases with the gas load factor (in the range $0.02\text{-}0.1 \text{ Pa}^{1/2}$). Good agreement was found between the experimentally obtained concentration profile and the simulated one, while the temperature profiles were quite different. Bad positioning of thermocouples is however suspected, as the authors demonstrated that they managed compensating heat losses. The rather lower performances of this design compared to the previous one is attributed to the differences in the thicknesses (5 mm vs. 3 mm) and liquid stagnation at the bottom of the foam packing.

Eventually, authors also successfully implemented this updated microdistillation setup with a microreactor for the etherification of 2-ethoxy-2-methylbutane and recycle of unconverted reactant [14]. Additionally, this group of researchers has reviewed in 2012 the different microdistillation concepts existing at that time in the literature [43].

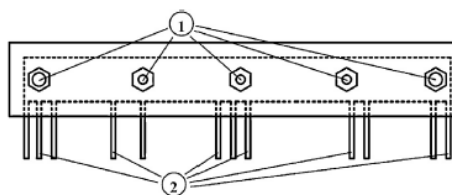


Figure 1-30: Schematic view of the distillation device showing the top (1) and the side (2) connections [13].

2.2.2.4. Stainless steel mesh capillary network

More widely, Tonkovich *et al.* [20] patented the principle of a microchannel distillation technology in 2009. It covers the use of different materials known as “wicking region”: sintered metal, metal screens, metal foams, wire mesh, polymer fibers, *etc.* Special geometries such as grooves were also considered to retain a thin liquid layer. The microchannel can either be equipped with condenser / reboiler or not, and can be parallelized, implemented in series, *etc.* It must be noted that the invention can be used vertically or horizontally. However, no clear indication was given regarding the typical size of the capillary network. They also referred to the use of a “pore throat”, placed at the outlet of the liquid channel and which acts as a liquid collector that prevents gas or vapor breakthrough. This material has a smaller pore diameter than the “wicking region”.

An example given in the patent is the separation of a hexane/cyclohexane mixture within a device that resembles to a stripping column [20] (a scheme of the setup is given **Figure 1-31**). The liquid channel is composed of a 72×72 stainless steel mesh, 2.9 cm wide, 14 cm high, and 0.36 mm thick, welded on one side of the channel. The “pore throat” is made of a $2.5 \text{ cm} \times 2.5 \text{ cm} \times 0.36 \text{ mm}$ fine mesh having a $25 \mu\text{m}$ pore diameter. As for the vapor channel, dimensions are 2.2 cm wide, 0.5 cm thick and 11 cm high. The liquid feed, injected in the top part of the device at 60.6 mL/h , was composed of 83.9 wt.% hexane at 65.7°C , while the vapor feed, composed of 8.5 wt.% hexane at 84.2°C , was injected at 60 mL/h in the bottom part (flow rate apparently measured in liquid phase even if not specified in the document). The device operates close to atmospheric pressure. A number of

theoretical stages of 10 across the system was determined according to outlet compositions and a ChemCAD simulation, giving a HETP of roughly $\frac{1}{2}$ " (12.7 mm).

Based on this microdistillation technology, Tonkovich *et al.* [17] imagined a methanol floating production, storage, and offloading plant (FPSO). For this special application, the microcolumn is operated under 48 bar for methanol-water separation. Six vertical microchannels assemblies (1.2 m (high) \times 1 m (wide) \times 3.9 m (long)) have to be used in series to reach the targeted separation, with temperatures ranging from 200 to 242°C and a HETP estimated to 1 cm.

The separation performances of the system were evaluated according to the principle proposed by Silva *et al.* [44] that relies on convection and diffusion times.

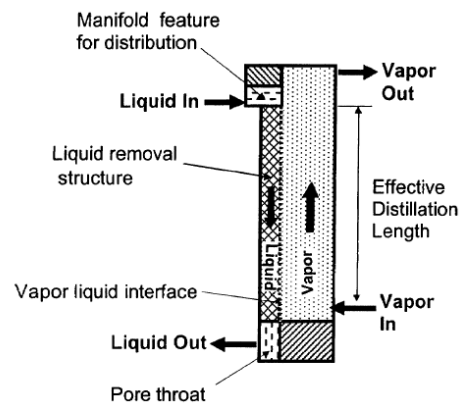


Figure 1-31: Schematic view of Tonkovich *et al.* microdistillation device [20].

2.2.3. Conclusion

All these listed setups belong to the “intermediate” size microdistillations operated in continuous mode, with flow rate typically ranging from 10 mL/h to 300 mL/h. In all these cases, the gas and liquid are flowing counter-currently. The proposed designs can be classified into two main types of microdistillations:

- Gravity assisted microdistillation: the liquid phase is driven by gravity forces as in the conventional distillation, and the size of the column is reduced as far as possible. In this category, we find the microrectification apparatus [32], the microdistillation based on the falling film technology where the surfaces could be smooth or structured [20,30,31] and the 3D printed modular microdistillation [41],
- Capillary assisted microdistillation [12–15,17–21,45], within which porous media are used to drive the liquid phase. This porous media consists of wicks, metal foams, meshes, *etc.*, and can be made up with different materials. Since the average pore size is usually of several hundreds of microns, both capillary forces and gravity ones play a major role in driving the liquid phase. As a result, these systems can be operated vertically as well as horizontally, and even in the absence of gravity. Moreover, these wetting structures intensify both mass and heat transfers between the two phases since they induce an increase of the interfacial area for a given microdistillation volume, which provides low HETP (sometimes down to 1 cm). However, the main issue with distillation downsizing is the heat losses. In many cases, the condenser and reboiler temperatures are fixed input parameters and the temperature profile is imposed and not thermodynamically

established. Thus, the microdistillation is operated in an isothermal mode; contrarily to the conventional column operation which is adiabatic.

Another challenge associated with the scale reduction is the management of the product withdrawal as well as the reflux. At this intermediate scale, the products may also be withdrawn according to the methods adapted in the classic distillation columns. Several ways of managing the residue withdrawal were mentioned in the previously listed microdistillations. They can be classified as follows:

- The liquid naturally leaves the area of gas-liquid contact (porous zone, grooves...) and arrives in a vessel, the volume of which is controlled (acting as a hydraulic guard to prevent the exit of the gas through this place). This method is mainly adopted from the classical columns [15,16,31,41],
- The liquid naturally leaves the area of gas-liquid contact and directly quits the device. Therefore, a direct exit from the contact area to the outside of the microdistillation exists [12],
- The liquid cannot exit naturally, thus requiring the use of a pump to withdraw the liquid to the outside of the microdistillation. As per the previous case, there is a direct exit from the contact area towards the outside of the microdistillation [20]. In this case, the flow rate is set by the operator.

The last two methods are dedicated for the intensified systems.

Concerning the reflux management, two main cases exist:

- Presence of a dedicated condenser, which condenses the gas phase. It can be either integrated within the device or added externally. In this way, the reflux can be controlled and cools down the microdistillation [13,15,18,20],
- Fixing the temperature at the cold region of the microdistillation instead of using a condenser. The reflux in this case is not controlled. There are two possible configurations:
 - the gas is evacuated from the device and constitutes the distillate [20],
 - there is an absence of gas phase and everything is condensed, thus part of the liquid is withdrawn [12].

Generally, in these cases, the distillate withdrawal was either done by venting the condenser section of the microdistillation [12,18,31] or fixing its flow rate [20,41]. Even though product withdrawal and reflux management display a great challenge that must be addressed, at this scale the reflux management can still be controlled in most cases.

The main characteristics and distillation efficiencies (HETP) of the various continuous intermediate size microdistillations are summarized in **Table 1-3**. The main advantage is that these devices are able to achieve distillation in continuous mode. However, the size reduction is not huge and these inventions are not really in the microscale range. From **Table 1-3**, it can be seen that among all the designs proposed in the literature, those based on capillarity (especially those designed by Sundberg *et al.* [9–12] and Tonkovich *et al.* [17,20]) are efficient in terms of HETP. Moreover, they offer more downsizing opportunities than the gravity based concept of Ziogas *et al.* [32]. Since the performance evaluation was not done under the same operating conditions (reflux ratio, pressure...), they cannot be compared and no judgement could be done. Indeed, the column designed by Tonkovich *et al.* [17,20] and mentioned within this work is a stripping one which requires gas injection at its bottom. Therefore, it could not be evaluated under total reflux, condition that gives the best performances. From

this point of view, it might have better separation efficiency than that implemented by Sundberg *et al.* [13–16] since its performance was evaluated under total reflux conditions.

Table 1-3: Summary of the principle characteristics and performances of the different continuous microdistillations of intermediate size.

	Material	Distillation zone dimensions	Gas-liquid counter-current driving phenomena	HETP (mm)	Reflux ratio	Flow rate
Ziogas <i>et al.</i> [32]	stainless steel	15 mL capacity	gravity	10.8	∞	30 mL/h
Kane <i>et al.</i> [31]	brass	2 x 36 vertical liquid channels D x W x L: 200 μ m x 1 mm x 150 mm	gravity	NM	NM	36-300 mL/h
Fink and Hampe [30]	metal	Annular falling film chamber. I.D. x O.D. x L: 16 mm x 19 mm x 40 mm	gravity	-	-	10 mL/h
Mardani <i>et al.</i> [41]	HTM140IV	H x W x L: 15.1 cm x 7.9 cm x 11.2 cm	gravity	73	∞	53 g/h
Seok and Hwang [12]	glass	I.D. x L: 10.5 mm x 340 mm	capillarity	59-190	∞	18-24 mL/h
TeGrotenhuis <i>et al.</i> [18,21]		D x W: 10-500 μ m x 10-100 μ m	capillarity	17.6	4.3	150 g/h
Sundberg <i>et al.</i> [13–16]	brass/ stainless steel	H x W x L: 3.5 mm x 30 mm x 140 mm	capillarity	13	∞	30 mL/h
Tonkovich <i>et al.</i> [17,20]	stainless steel	Liquid channel D x W x L: 1 mm x 2.9 cm x 14 cm Vapor channel D x W x L: 0.5 mm x 2.2 cm x 11 cm	capillarity	12.7	No external reflux	60 mL/h (vapor) 60.6 mL/h (liquid)

*NM stands for not mentioned

2.3. Continuous on-chip microdistillation

This part is dedicated to on-chip microdistillations devices. The distillation process remains the same as for the continuous microdistillations of intermediate size. The main difference resides in the abrupt scale reduction, making the distillation possible on microchips. Generally, all the principle elements of a conventional distillation column such as feed inlet, bottom and distillate outlets are encompassed within the same device. Therefore, by managing the continuous injection of the feed as well as the continuous withdrawal of both products, distillate and residue, a continuous on-chip microdistillation tool can be obtained.

These on-chip microdistillations operate continuously and can be divided into two groups. The first one is the single-stage (flash) microdistillation, which consists in vaporizing part of the feed, sometimes by using a carrier gas, and to separate the gas phase from the liquid phase. The second one is the multistage on-chip microdistillations, within which specific internals are used to establish a counter-current gas-liquid flow, thus developing more than one theoretical stage.

It is important to mention that some of the designs reviewed thereafter within the single-stage (flash) microdistillation category are technically "microevaporators" rather than microdistillation units.

In these cases, it is possible to operate below the bubble point(s) of the components or avoid liquid boiling by the use of a carrier gas. It is based on the stripping principle for a single-stage separation. Since the liquid does not achieve boiling, microevaporation techniques are simplest to monitor.

However, they will not be classified in here within a dedicated section since the classification was based on the separation performances of the device. They will be integrated within the same section as flash microdistillations.

2.3.1. Single-stage on-chip microdistillation

Prior to listing the different involved setups, it is essential to illustrate the concept of flash distillation. The flash microdistillation operation is achieved by partially vaporizing a feed in a microchannel. Sometimes, a carrier gas acts as a phase contactor to promote vaporization. The two-phase flow is then separated into liquid and vapor streams. The main challenge resides in the separation of these two streams, and this is what differentiates the proposed design. Thereafter, and if added, the vapor-carrier gas mixture separation is achieved by condensation and further gas-liquid separation.

A silicon-based microchannel shown in **Figure 1-32, left** was patented by Cypes *et al.* [46]. The details of the different configurations possible for the separation zone are shown in **Figure 1-32, right**. The microchannel is 500 μm wide and 280 μm deep. The design consists of two superimposed gas-liquid channels separated by a perforated plate. The liquid is fed into the channel *via* the liquid inlet port. Under the effect of high temperature, the liquid is partially vaporized and a gas-liquid equilibrium is reached. This section of the channel is the phase equilibrium zone. Thereafter, the two-phase flow are split into liquid and gas in a separation zone thanks to a capillary network connected to the liquid outlet port. This capillary network can be composed of several thousands of parallel capillaries (for example, capillaries with 10 μm x 70 μm cross section). By monitoring the pressure difference over these capillaries, the liquid is driven toward the outlet port through the capillary network while the gas is recovered from the gas outlet after condensation. The gas-liquid separation was allowed by keeping the pressure difference over the capillaries below 1 psi (6.89 kPa). Accordingly, a low dead volume solenoid regulated by a computer with two pressure differential transducers was used to control products flow rates. The condensed gas and liquid products are collected into different vials at atmospheric pressure and analyzed by gas chromatography.

The device was examined with two different feedstocks injected using syringe pumps: pentane/octane mixture (61 mol% pentane, flow rate: 30 mL/h, T_{heating} : 80°C) and crude oil (15 mL/h, T_{heating} : 200°C). For the first experiments, the results show that the molar fraction of pentane in the distillate and residue were 0.815 and 0.304, respectively. These results suggest a gas distillate carryover in the residue since the distillate composition corresponds to the one predicted by thermodynamic equilibrium while the residue composition is different and confirm a separation equivalent to a single-stage distillation. Moreover, the device was proven to be able to build the distillation curve of a crude oil by performing successive distillation tests at several temperatures. To achieve multistage distillation, multiple units could be connected in series with the product of the first unit being the feedstock of the subsequent one. Accordingly, the two previously distilled mixtures were

used to evaluate a multiple-flash process that seemed to be successful. Nevertheless, the guiding principles upon which the distillation unit was designed were not communicated.

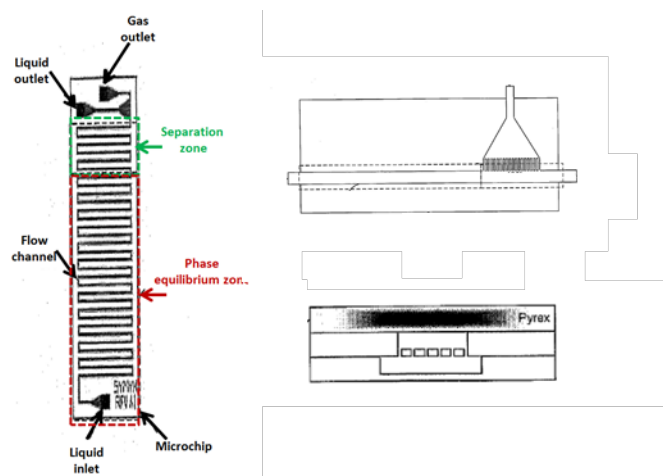


Figure 1-32: Schematic view of the microdistillation device (left) and its housing (right) [46].

Similarly to the prior discussed microdistillation, Hartman *et al.* [47] proposed a single flash on-chip distillation by combining capillary forces and segmented flow (**Figure 1-33**). A carrier gas enables the establishment of a cold segmented flow with the liquid feed before further heating in order to better control vaporization. A long channel was required to reach vapor-liquid equilibrium. The reason a long channel was used is because the volume of the vapor formed during boiling, above its boiling point, is orders of magnitude greater than the volume of the same component's condensed liquid phase. In those microfluidic systems that do not provide sufficient volume for the expansion of liquid into a vapor phase, it would not be theoretically possible to achieve vapor-liquid equilibrium on-chip at the operating temperatures and pressures. The microchannel dimensions were: 0.4 mm width and depth and 875 mm length. Then, a PTFE membrane (0.5 μm pore size) separator, through which only liquid can pass by means of capillary forces, was used to allow the two-phase flow separation. The pressure difference on both sides of the membrane was managed carefully to maintain a stable gas-liquid separation.

This step that extends from the feed injection till the two-phase separation is equivalent to a single-stage distillation [47]. In terms of product withdrawal, the vapor outlet is connected to a metering valve and 1000 μm internal diameter tubing fitted with a syringe needle, whereas for the liquid outlet there is no need for the metering valve. Both products were collected in different vials cooled with ice for further analysis. Equimolar mixture of methanol/toluene at 1.2 mL/h and dichloromethane/toluene were used to validate the feasibility of the device. For the first mixture, the molar fraction of methanol in the vapor and liquid were 0.79 ± 0.06 and 0.22 ± 0.03 , respectively. For the second mixture, the molar fraction of dichloromethane in the vapor and liquid were 0.63 ± 0.05 and 0.16 ± 0.07 , respectively. These experimental results were in full agreement with the phase equilibrium predictions. Moreover, this device was later implemented in a microchemical synthesis process requiring multiple reaction and separation steps [48]. As for the previous design of Cypes *et al.* [46], multiple distillation stages are possible by combining several of these one stage microdistillations in series.

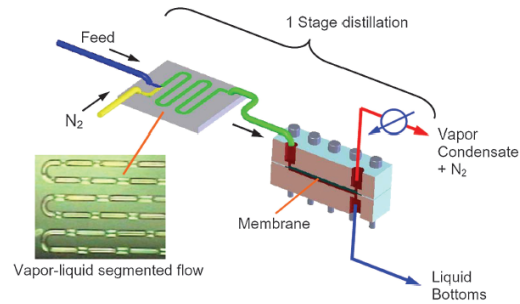


Figure 1-33: Single-stage microdistillation assembly designed by Hartman *et al.* [47].

Wootton *et al.* [49] studied a single-stage on-chip microdistillation system that used forced laminar gas-liquid flow. Chevron structures (width x depth: 100-500 μm x 50 μm) on the floor of the contact chamber force a laminar liquid flow and a steady gas-liquid interface, thus allowing the gas-liquid separation. Consequently, gas and liquid phases are flooding co-currently, side by side, facilitating their subsequent separation. The glass-based microdistillation device, shown in **Figure 1-34**, used a carrier gas (helium) to achieve this evaporative transport and is composed of three sections. The first one (section i) is a heated zone devoted for the gas-liquid streams contact and thermodynamic equilibrium. In this section the liquid is injected using a syringe or HPLC pump at a constant flow rate through numerous inlet channels, whereas the gas is injected in the central channel at constant pressure. After being mixed, the streams are split: the liquid with part of the carrier gas are recycled using HPLC pump and mixed with the feedstock and the vapor-saturated carrier gas flow is transported through a long channel (section ii) dedicated for condensation. In the last section (section iii), the liquid distillate is separated from the carrier gas by using a gas/liquid separator.

To evaluate the device, the separation of an equimolar mixture of acetonitrile/dimethylformamide at a rate of 4.5 mL/h and a heating temperature of 60°C was performed. The carrier gas was injected at a pressure of 25 psi. Withdrawal conditions of the carrier gas and condensate mixture were not mentioned but are rather managed at controlled pressure. The distillation results show a separation equivalent to 0.72 equilibrium stages and a residence time of the liquid in the contact chamber of 0.1 s. It was noted that the device can be further improved by linking an active cooling device to the condensation channel, thus reducing the evaporation of condensate by the carrier gas. The main difference compared to the previous cited single-stage microdistillation is the liquid recycling. This type of device is rather a microevaporator than a microdistillation since 60 degrees Celsius at 25 psi is well below the bubble point of both components in the mixture.

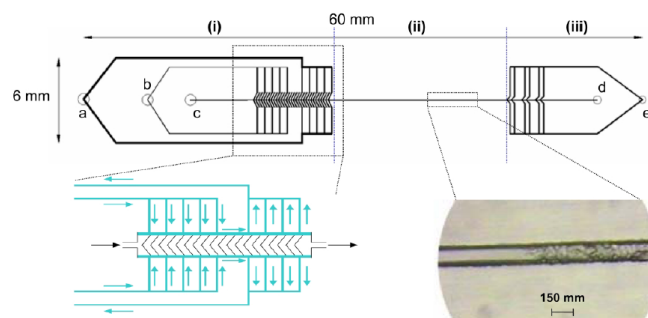


Figure 1-34: Drawing of a continuous laminar evaporation microdevice (black and blue arrows designate the carrier gas and liquid flow, respectively) [49].

Hibara *et al.* [27] designed a microfluidic distillation on a fused silica-based microchip by integrating nanopillars of 900 nm long, 900 nm wide and 250 nm deep. The microchip dimensions are illustrated in **Figure 1-35**. The main channel is made of a deep section (30 μm deep) devoted for the liquid phase, and a shallow part (10 μm deep) for the gas phase. The surface of this shallow channel is modified with fluoride resin in order to prevent liquid intrusion. This particular configuration allows the gas-liquid separation. In fact, the liquid flows through the 250 μm wide main channel at its bubble point and it partially vaporizes in the microchannel. The generated vapor flows alone in the shallow channel and is further condensed in the nanopillar area. Indeed, the low capillary radius (270 nm) in the nanopillar region induces a saturation pressure lower than that in the evaporative zone (Kelvin equation). Accordingly, condensation is promoted even if the temperature is kept the same. This device does not require the use of a carrier gas as the previously cited single-stage on-chip microdistillation apparatuses. Evaporation and condensation phenomenon were clearly seen by using pure water as fluid.

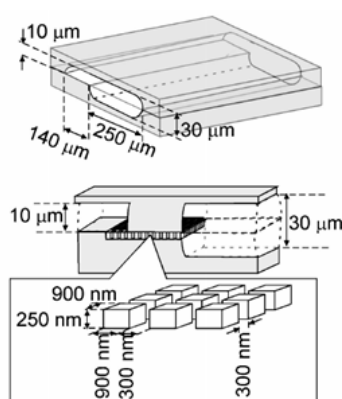


Figure 1-35: Illustration of the microchip distillation unit [27].

The device was examined by distilling a 9 wt% aqueous ethanol solution fed at 0.12 mL/h. The manner of injection and withdrawal of the different streams was not mentioned. The microchip temperature was mastered by a temperature controller.

As the recovered products volumes were very small, only the residue could be analyzed to evaluate the performance of this device (**Figure 1-35**). The analyzed volume was about 213 μL and the weight percentage of ethanol was almost 8.6%; claiming that somehow a distillation process took place. By assuming a total mass balance of 100%, the weight percentage of ethanol in the condensed phase was estimated around 19%. The researchers explained the poor separation by the absence of liquid reflux back to the heating zone. Therefore, it has to be optimized to achieve higher distillation efficiencies. However, from a critical point of view, a distillation could not be really proven based on the tested conditions: feed at 9 wt% ethanol separated into a residue at 8.6 wt% ethanol. The accuracy of the analytical method has not been communicated and therefore in the case where the measurement uncertainty is in the range of 0.5 wt% (which is not really high), the composition of the residue and of the charge will be identical and no separation would have taken place as the composition of the distillate is deduced from that of the residue. The method of analysis was not even specified. Therefore, further work and separation tests must be investigated to concretely prove the performances of the device.

A Foturan glass-based capillary module proposed by Stanisch *et al.* [26]. (**Figure 1-36**) was able to achieve a successful distillation of feeds with flow rates up to 600 mL/h. The main channel dimensions were 600 μm width, 200 μm depth and 56 mm length. The principle of operation is the same as for the aforementioned devices. A preheated partially vaporized mixture is fed into the channel. In this device no carrier gas is used. The two-phase flow is then transported through the main microchannel where 80 capillaries (H X W X L: 0.2 mm x 0.5 mm x 7.7mm) were oriented perpendicularly. These capillaries have the same function as that of the nanopillars: they allow liquid withdrawal as bottom product from the main channel by means of capillary forces. The vapor remains in the main channel and is recovered as condensate, thus achieving a gas-liquid separation.

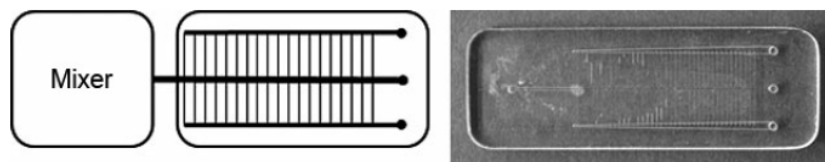


Figure 1-36: Capillary module for distillation purposes [26].

To test the efficiency and capability of this device, a mixture of ethanol and water was fed at 100°C into the microchannel using a HPLC pump. The main variable input parameters were the feed temperature and streams volume. The manner of controlling the microchip temperature, if done, was not mentioned nor the products withdrawal. The feed composition was in the range of 0.13-0.48 mol% of ethanol, and was fed at a flow rate varied between 300-1200 mL/h. Thereafter, water and ethanol contents were quantified using Karl-Fischer titrator and gas chromatography, respectively. After four distillation steps (the distillate of one step is used as feed for the next one), and starting from a 13% mole fraction feed, an ethanol mole fraction of almost 50% is reached in the final distillate. Since the capillary module was designed for a much lower gas-liquid ratio than the one applied here, backmixing occurred between the distillate and the residue, inducing a poor separation per pass. Indeed, the preheated mixture is injected into the main channel and the liquid is withdrawn from the side channels in the first section of the chip (**Figure 1-37, a**). If, at a certain moment, all the liquid was withdrawn; then the capillaries are no more filled with liquid. This situation will allow the slightly pressurized vapor to enter the capillaries and reach the side channels containing the withdrawn liquid (**Figure 1-37, b**). Consequently, backmixing can take place. Moreover, since the capillaries in the end section of the microchip are not yet filled with fluids; withdrawn liquid can pass from the side channels toward the main channel via these unfilled capillaries. In this case, both outlets are remixed (**Figure 1-37, c**). Therefore, further work aiming to optimize the distillation efficiency of the module and avoid the liquid backmixing has to be done. Furthermore, the effect of operating parameters such as temperature, pressure and capillary dimensions and number on the throughput was also investigated.

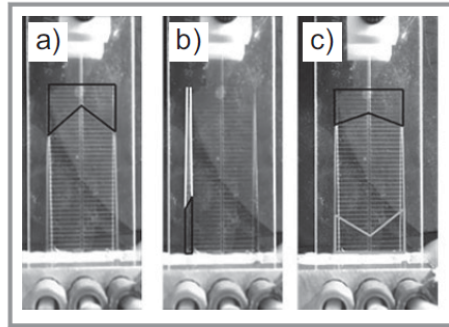


Figure 1-37: Possible back mixing phases within the capillary module [26].

Boyd *et al.* [29] explored a different way to achieve a single-stage separation on microchip, using bubbly assisted interphase mass transfer (BAIM). BAIM consists of supplying a small amount of heat near a gas-liquid interface of a captive gas bubble in a microchannel. This leads to a controlled interphase mass transfer through the bubble occurring with a minor change in the fluid temperature. Thereupon, this method can be used to achieve distillation without the use of high temperature, cooling agents or vacuum supply. In this paper, the microchannel assembly (**Figure 1-38**) consists of a poly(dimethylsiloxane) (PDMS) channel (width x depth x length: 30 μm x 5 μm x 10 mm) sealed to a glass substrate and covered with an array of gold nanoparticles (14.5 nm diameter and 46 nm spacing). The added heat was provided by focusing on the substrate a laser able to excite the gold nanoparticle arrays on the liquid side of the gas (air) - liquid interface (partially filled channel). Consequently, vaporization takes place at the heating point, vapor is generated through the gas-liquid interface and condenses 10–30 μm away. Therefore, the air bubble is trapped within the liquid phase and acts as a diffusion barrier across which condensation and vaporization occur. The maximum volume injected within the channel is few nanoliters.

As the liquid phase is evaporated and then condensed further away, this BAIM device was able to separate a mixture of deionized water, ethanol and dye into aqueous ethanol as distillate and dye as residue. The successful separation was proven by fluorescence detection techniques. Unfortunately, the exact composition of both products (distillate and residue) was not computed. Nevertheless, the feed flowrate was not controlled and this concept is unlikely to perform steady and reliable distillation.

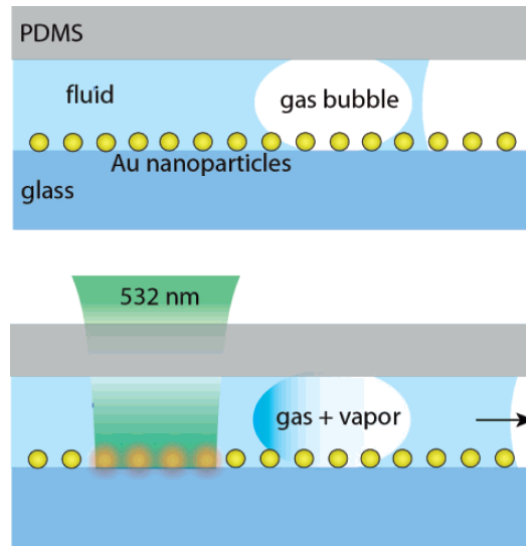


Figure 1-38: Bubble assisted interphase mass transfer concept [29].

All the aforementioned devices are interesting breakthrough regarding on-chip distillations. They can be divided into several categories based on the separation of the gas-liquid mixture:

- Pore or capillary network (Cypes *et al.* [46], Hartman *et al.* [47], Stanisch *et al.* [26])
- Shallow microchannel with modified surface (Hibara *et al.* [27])
- Forced laminar flow (Wootton *et al.* [49])
- Bubble assisted separation (Boyd *et al.* [29])

From the reported performances, the first category is the most efficient. However, as their design only allows one single theoretical stage, separation is poor. Even if several microdistillation units can be used in series to achieve multistage distillation, this would require manufacturing several of them, which might be expensive. For a better separation and an optimized chemical process, a counter-current configuration with reflux is more desirable.

2.3.2. Multistage on-chip microdistillation

This part concerns the on-chip microdistillations operating in counter-current gas-liquid configuration to improve the separation. Several designs were depicted in the literature and are reported bellow.

2.3.2.1. Counter-current capillary microdistillation

The principle is similar to that of the heat-pipe (see 2.2.2) with a drastic reduction in the channel dimensions. Since it is complicated to use foreign wicks, it is needed to design a space where the liquid will preferentially go based on capillary retention forces. This is generally provided by implementing arrays of micropillars along the walls of the microchannel. Other possible solutions exist such as the use of a porous membrane or centrifugal forces.

In this context, Lam *et al.* [22–25] studied several geometries. To design the microchips, the group of researchers proceeds according to the same aforementioned guiding principles (see section

2.2.2). The silicon-based microchips were provided with micropillars (20/40 μm diameter) to guide the liquid flow by capillarity inside the microchannel. The researchers have reviewed the gas-liquid separations in microchannel devices in 2013 [50].

The first suggested design consists of a straight channel provided partially with an array of micropillars having a diameter of 40 μm . The reboiler is integrated within the chip by heating one of its ends. The generated vapor leaves the micropillars toward the gas channel where it is further transported toward the other end. At this section of the channel (cooled with circulating water), the vapor condenses due to the temperature difference. The condensed vapor fills again the micropillars region and is guided toward the hot end by capillarity. No external reflux is supplied. As the chip is short, the reboiler and condenser are very close, and the thermal gradient along the channel is established naturally by thermal conduction through the silicon. Therefore, the microdistillation is inherently operating in isothermal conditions and is not adiabatic. The authors managed the withdrawal of the distillation products at fixed flow rates with syringe pumps.

Thereafter, various channel designs (straight, zig-zag, serpentine) were tested [24]. However, for very long channels, the pressure drop across the microdistillation increases, resulting in flooding. The liquid phase could not be restrained in the micropillars region since the long array of micropillars caused a high liquid pressure drop, resulting in condensation in the gas channel and formation of liquid slugs. The considered solution was first to widen the vapor channel in order to reduce the formation of liquid slugs, but this did not resolve the flooding problem. Therefore, it was suggested to reduce the liquid pressure drop by creating an empty liquid channel, separated from the gas channel by a single row of micropillars. Even though this latter solution was able to prevent flooding, no separation was detected since the residence time was too short. Hence, a compromise concerning the width of the liquid channel must be found to reduce the pressure drop without hindering performances. The implementation of micropillars arrays on both sides of the channel was able to solve the problem. The most efficient chip design is shown in **Figure 1-39**.

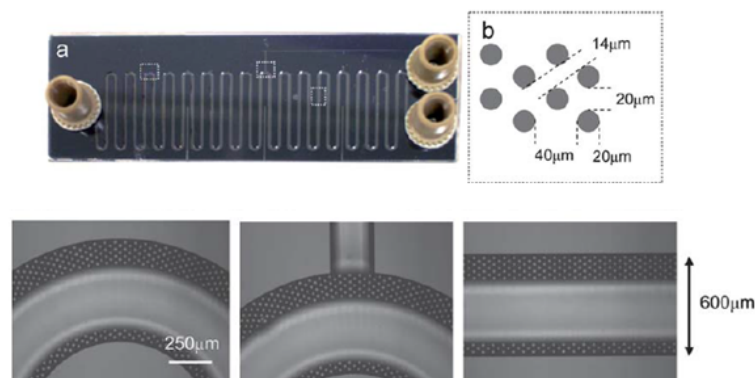
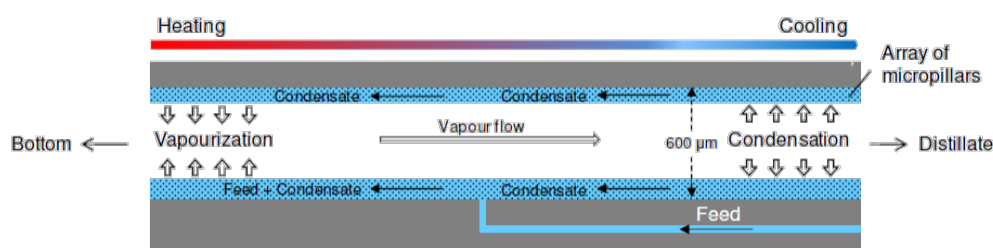


Figure 1-39: Design of the most efficient microdistillation conceived by Lam *et al.* [24].

The principle of operation is illustrated in **Figure 1-40**. The 400 mm long microdistillation was evaluated using three binary equimolar mixtures (acetone/water, methanol/toluene, and acetone/ethanol) under total reflux conditions. By analyzing the product concentrations and using McCabe-Thiele diagram, the distillation efficiency in terms of NTS and HETP was computed. As reflux was not measured, performances were estimated assuming total reflux. The most relevant results are summarized in **Table 1-4**.

Table 1-4: Distillation performances of chip 6 (400 mm long) using different binary mixtures and operating parameters [23,24].

Binary mixture	Feed flow rate (mL/h)	Distillate flow rate (mL/h)	Residue flow rate (mL/h)	T_{Heating} (°C)	T_{Cooling} (°C)	NTS	HETP (mm)
Acetone/water	0.15	0.12	0.03	90	42	3	133.3
				95		4	100
Methanol/toluene	0.15	0.11	0.04	110	52	3	133.3
Acetone/ethanol	0.15	0.84	0.66	76	32	4	100
	0.05	0.28	0.22			5.4	74


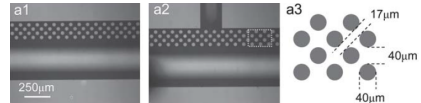

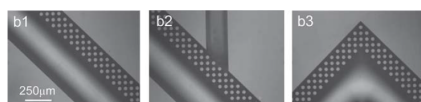
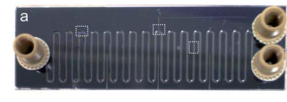
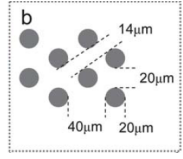

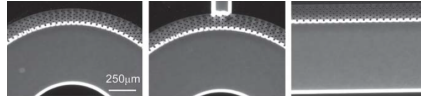

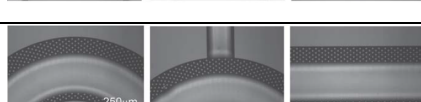
**Figure 1-40: Schematic view of the operation principle of the serpentine microchip distillation at the feed entry [25].**

Afterwards, the effects of various operating conditions (temperature, feed conditions, outlet flow rates) on the distillation of an acetone/ethanol mixture using the most efficient microchip were investigated [23]. It was found that the feed conditions have more pronounced impact on the separation in a microdistillation than in a conventional distillation column. Moreover, the purity of the distillate product decreases as the distillate flow rate increases because of lower liquid reflux. This result is similar to what happens in the conventional distillation columns, however there is a noteworthy difference: the distillate and feed flow rates are fixed, as well as the reboiler and condenser temperatures. This over-specification (**see section 1.5**) indicates that one or more parameters, for example temperature, are not really fixed.

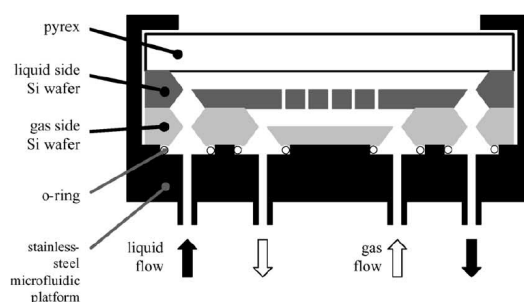
The case study of benzaldehyde/toluene separation using this microchip was examined [22]. Under the tested operating conditions, the distillation of a 35 mol% toluene/benzaldehyde mixture was equivalent to a NTS in the range of 0.9 to 2.7. It was found that 2 out of 6 cm (linear distance between both outlets, the total serpentine length being 400 mm) is the length devoted for the separation zone. It was also proven that Raman spectroscopy, infrared imaging camera and optical microscopy are efficient tools for *in situ* monitoring of microdistillations thanks to the transparency of the Pyrex substrate [22].

Since various configurations were studied and investigated, a summary of all of them is recapped in **Table 1-5**.

Table 1-5: Summary of the various investigated configurations with the associated performances [24].

Microchip designs	Internal configurations	Dimensions	HETP (total reflux)
		Width: 550 µm Length: 60 mm Depth: 300 µm	Not mentioned
		Width: 550 µm Length: 81 mm Depth: 300 µm	>81 mm (less than 1 stage observed)
 		Width: 600 µm Length: 400 mm Depth: 300 µm	Flooding - no separation
		Width: 800 µm Length: 400 mm Depth: 300 µm	Flooding - no separation
		Width: 600 µm Length: 400 mm Depth: 300 µm	Very short residence time - no separation
		Width: 600 µm Length: 400 mm Depth: 300 µm	74-400 mm

Cypes *et al.*, who also studied a single-stage on-chip microdistillation [46] (see section 2.3.1), have developed a counter-current microchannel for stripping purposes [51]. It is important to illustrate the differences between stripping and distillation process. Stripping is mainly a separation process through which a dissolved gas is removed from a liquid stream by a vapor stream flowing co or counter-currently. It involves the use of an external gas stream to achieve the separation contrarily to the distillation process that implies the integration of a reboiler and a condenser and no external gas stream.

**Figure 1-41: Cross section of the microfabricated stripping device [51].**

The microchip consists of two silicon and one Pyrex substrates. The vapor and liquid channels were etched each on a silicon substrate (100 mm diameter wafers) according to the standard silicon processing techniques. The dimensions of the liquid and vapor microchannels are length x width at the top (bottom) x depth: 3.35 cm x 920 (450) µm x 330 µm and the hydraulic diameter was about 415 µm. Both channels were separated by a perforated silicon layer acting as a membrane to promote gas-

liquid contact as shown in **Figure 1-41**. Indeed, the gas and liquid flow counter-currently and do not mix thanks to capillary forces generated by the 50 μm diameter perforations.

The performance of the device was evaluated by stripping toluene from water using dry nitrogen. The gas was injected using a rotameter and a pressure regulator at a fixed mass flux ranging from 1 to 5.6 $\text{g}/(\text{cm}^2 \cdot \text{min})$. Additionally, the liquid was injected counter-currently using a syringe pump at a fixed mass flux ranging between 16 and 80 $\text{g}/(\text{cm}^2 \cdot \text{min})$. Both products were withdrawn at atmospheric pressure. The toluene concentration was determined by gas chromatography.

The evaluation of this device in terms of recovery percentage of toluene was not communicated. However, the crucial parameter to judge a stripping column efficiency is the rate of removal of the volatile component. Series of equations were developed to allow the calculation of the overall capacity coefficient ($K_L a$) based on experimental data. This parameter could be predicted in packed tower column by using a power-law correlation that takes into account both fluids flow rates. Therefore, they supposed that it might work for their microstripping device. The correlation has the following form:

$$K_L a = c_1 G_l^{c_2} G_g^{c_3} \quad (1-21)$$

where G_l and G_g stands for the liquid and gas mass flux, respectively ($\text{g} \cdot \text{cm}^{-2} \cdot \text{min}^{-1}$) and c_1 , c_2 , and c_3 are constants. The values of these constants were obtained through a numerical fitting. It was claimed that compared to a conventional packed tower, this device exhibits higher overall mass transfer capacity thanks to the thin liquid film. The difference, as it can be seen from **Figure 1-42**, was almost one order of magnitude. Nevertheless, this device has some drawbacks such as high fouling risks and manufacturing costs.

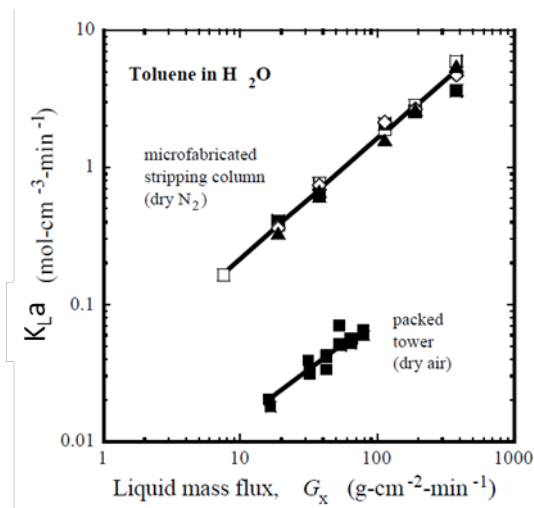


Figure 1-42: Evolution of the overall mass transfer capacity coefficient $K_L a$ as a function of the liquid mass flux for the microfabricated stripping device and a packed tower. The different symbols refer to different gas mass flux [51].

2.3.2.2. Counter-current membrane microdistillation

Another way to make gas and liquid flow counter-currently is to separate them with a porous membrane. In this case, the distillation process consists of feeding the device with a liquid that will be heated and partially vaporized. This feed will be in contact with the porous membrane. Then, either the generated vapor or the liquid travels through the membrane pores according to the membrane

characteristics (hydrophilic or hydrophobic). Therefore, thanks to the membrane, the channel is split into vapor and liquid channels. The liquid-vapor interface relies in the membrane pores where mass transfer takes place. The vapor phase movement can be managed by the use of a carrier gas or a vacuum driving force.

In this context, a vacuum membrane distillation (VMD) shown in **Figure 1-43** was designed by Zhang *et al.* [52,53]. It is a membrane made of a porous hydrophobic polytetrafluoroethylene (PTFE). Vacuum was established above the membrane to create a driving force and promote mass transfer across it. Since the membrane is hydrophobic, only the generated vapor can travel through it. The vapor moves in the opposite direction of the liquid under the effect of the vacuum pump. At that region, the vapor partially condenses in the membrane pores due to the low temperature controlled by cold water circulation. Hence, liquid and vapor flow counter-currently into channels of 72 μm deep and 1 mm wide each. The condensed vapor ends up joining the liquid channel as a reflux and travelling back toward the hot liquid outlet. Accordingly, an evaporation-condensation process occurs. Forming a vapor-liquid equilibrium through the membrane and the use of vacuum both make this study a micromembrane distillation rather than a microdistillation.

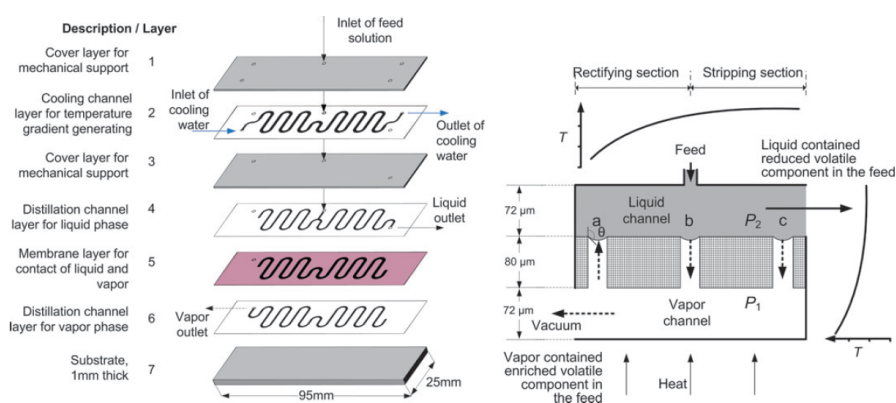


Figure 1-43: Different layers of the microchip (left) and the microdistillation process (right) [52,53].

The experimental set-up is exposed in **Figure 1-44**. The feed was injected using a syringe pump, while the liquid and vapor products were collected in microvials cooled by ice water and dry ice mixed with ethanol, respectively.

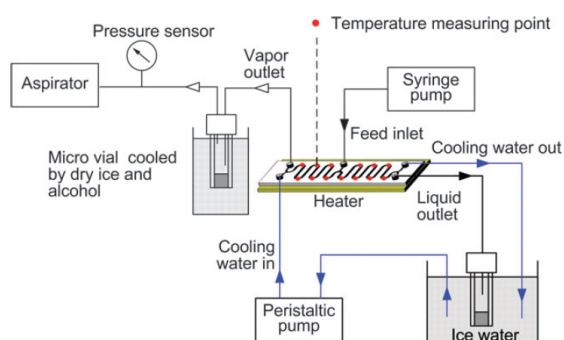


Figure 1-44: Experimental set-up of the vacuum membrane distillation process [52].

Various compositions of methanol/water mixtures were distilled using the VMD. The effects of heating temperature, cooling water flow rate, feed conditions and membrane pore size on the separation capability were studied. The results show a separation equivalent to 1.7 theoretical stages equivalent

to 153 mm HETP under optimum conditions (feed flow rate: 0.54 mL/h, T_{heating} : 95°C, cooling water flow rate: 13.2 mL/h, membrane pore diameter: 0.2 μm).

The major drawback of the device is its limited efficiency because of the temperature control. The temperature gradient was managed by circulating a cooling water stream in layer 2 and heating the chip *via* an underlying aluminum plate (**Figure 1-44**). This is somehow uncommon and complex since the temperature gradient is only controlled by the cooling water stream. The temperature of the vapor phase is nearly constant, whereas that of the liquid varies due to continuous heat transfer between the liquid and the cooling water channels. A better way to control temperature would have been to heat one end and to cool the other; thus controlling the temperature gradient across the chip and potentially achieving higher separation.

Adiche and Sundmacher [54] integrated the principle of sweep gas membrane distillation in microfluidics. The microseparator was made of two polycarbonate plates (**Figure 1-45**). On each plate, a 342 mm long rectangular microchannel of 677 μm hydraulic diameter was etched. A sweep gas is used to drive the vapor phase instead of vacuum, as for the previous example [52,53]. The carrier gas was nitrogen flowing at a rate of 600 NmL/min. The feed is injected using a microannular gear pump and is heated by an electrical micro heat exchanger. A microporous membrane is inserted between the two rectangular microchannels dedicated for the gas and liquid flows. Accordingly, the heated feed and the carrier gas can travel co or counter-currently through different microchannels, tangentially to the membrane. The nitrogen sweeps the permeate (the distillate) through the membrane pores outside the microseparator. The distillate is recovered in a sample tube submerged in a water ice-bath.

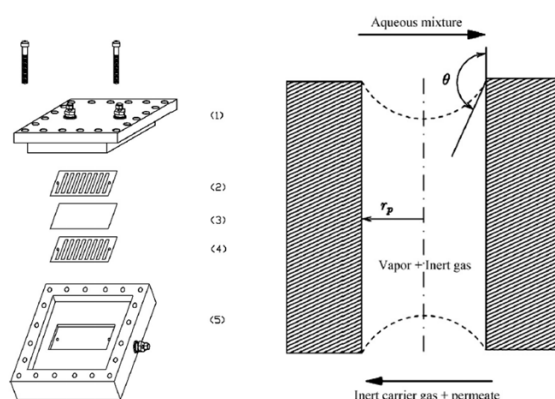


Figure 1-45: Different layers of the sweep gas membrane distillation (left) and the liquid-vapor gas membrane contactor (right) [54].

The device ability to process solutions with low to high methanol concentrations has been studied. The separation efficiency in terms of NTS or HETP was not communicated. It was mostly evaluated by a separation factor that expresses the preferential transport of the target specie as well as the permeate (distillate) flux.

Aqueous methanol solutions of various concentrations (5-70 wt% methanol) with flow rates up to 1800 mL/h were used to evaluate the performance of the device. These experimental tests have shown successful results with a methanol separation factor ranging from 2.5 to 5, depending on operating conditions. Furthermore, a parametric study (feed conditions, inert gas flow rate, and membrane type) has also been considered. The main drawback of this device is the use of carrier gas, thus requiring a gas/liquid separator to recover the distillate as a condensate.

Afterward, a mathematical model that takes into account the two-phase flow with the associated heat and mass transfer occurring inside the channel and across the membrane was coupled to a CFD approach. It was used to evaluate numerically the impact of the apparatus geometry on the separation performance [55]. The simulated results were in good agreement with the experimental ones. In addition, implementing baffles in the channel reveals great potential for the process intensification in terms of mass transfer enhancement.

2.3.2.3. Counter-current centrifugal microdistillation

Centrifugal force is another possible way to overcome microdistillation downsizing barriers. When opposed to the pressure gradient across the channel, these forces keep up phases' segregation into parallel counter-current flowing liquid and vapor. Consequently, the liquid is driven outward along the channel whereas the vapor is flowing inward under the effect of centrifugal acceleration.

MacInnes *et al.* [28] proposed a stripping distillation in a rotating spiral microchannel based on this above-mentioned principle (see **Figure 1-46**). The spiral channel (width x depth: 255 μm x 95 μm) within the glass-based microchip is connected to a central feed reservoir and two different collection vials for product withdrawal (**Figure 1-46, left**). The whole system is integrated within the rotating unit. Once the rotation is triggered, the feed is pumped from the reservoir into the microchip by centrifugal forces. An axisymmetric radial temperature profile across the channel was set using a heater and a cooling jet (**Figure 1-46, right**). Several parameters such as rotational speed and pressure gradient along the channel highly affect the phase contacting. The performances of this device were evaluated experimentally using an equimolar mixture of 2,2 dimethylbutane and 2 methyl-2-butene. The products recovered (condensed distillate and residue) in the different vials were analyzed using gas chromatography. The experimental results gave a NTS of 6.6 corresponding to a HETP of 5.3 mm at a rotating speed of 5000 rpm. In these conditions, the distillation time was found to be around 0.13 seconds per stage. Indeed, the diffusion time of a specie from the interface toward the adjacent liquid or vapor phase is an indication of how fast the separation can occur. It could be used as an estimation of the microdistillation performance based on the dimensions of the channel. For a 10 μm wide channel and a diffusion coefficient of 10^{-9} m^2/s , the diffusion time is estimated to be 0.1 s. This time corresponds to one theoretical stage since it is the time needed to have a uniform concentration of a specie over the distance of the channel. By comparing these results to those of previously cited multistage microdistillations, it appears that this centrifugal microdistillation device provides a better contacting time, a lower HETP, and a quicker separation.

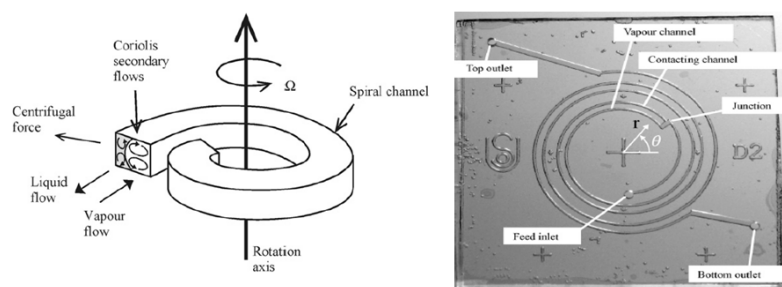


Figure 1-46: Schematic view of the phase contacting principle (left) and the centrifugal distillation device (right) designed by MacInnes *et al.* [28]

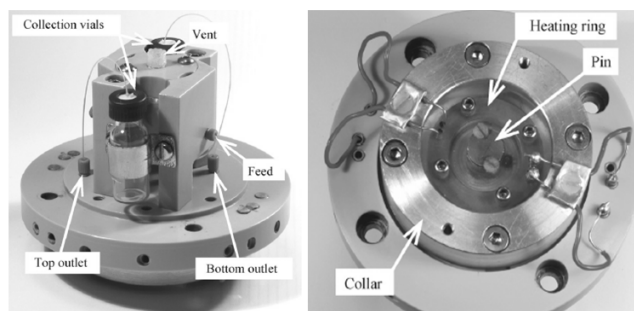


Figure 1-47 Top (left) and bottom (right) views of the base unit. [28]

2.3.3. Conclusion

Several groups of researchers managed to harshly reduce the scale of the distillation until it reaches approximately the micrometric range. All these previously mentioned designs can be classified mainly in two major categories according to the distillation procedure. It consists either of a single-stage or a multistage distillation.

The former mainly established co-current gas-liquid flow. Subsequently, the separation efficiency is limited to a single-stage separation. In this context, the challenge resides in the separation of the gas and liquid phases once the thermal equilibrium is reached. Porous membrane, capillary or microchannel network, forced laminar flow and surface functionalization could be used to induce a steady gas-liquid interface and allow this gas-liquid separation. In some case, a carrier gas could also be used to stabilize the flow pattern and promote vaporization.

Whereas the latter concept consists of settling a counter-current gas-liquid flow since it offers much more interesting performances from the separation point of view. However, this kind of flow is much more complex to implement compared to the co-current one. The complexity lies mainly in the handling of the gas-liquid interface because, in this situation, the pressure gradients of both fluids go in two opposite directions. To overcome all the barriers and achieve a counter-current on-chip microdistillation, capillary forces are widely used instead of gravitational forces to retain a constant liquid film within the microchannel. Centrifugal forces were used as well as they exhibit high potential, however they are difficult to operate. Depending on the principle used to force the gas-liquid counter-current flow, on-chip multistage microdistillations were classified into subcategories. Therefore, capillary, membrane and centrifugal on-chip microdistillations were encountered. It must be noted that both, capillary and membrane microdistillations, rely on capillary forces, the main difference being the design. In the first one, the capillary network is etched within the chip, while in the second one, it is provided by an external material that can in addition present some hydrophobicity.

A summary of all the main characteristics and performances of the different devices is important to be able to compare the several technologies within each category. Therefore, single-stage on-chip microdistillations are summarized in **Table 1-6** whereas multistage ones are listed in **Table 1-7**. Microchip materials are the same for both categories and the dimensions of the different microchannels fall in the micrometric range in terms of width and depth. In the tables, a distinction is made between porous membrane and capillary forces. In fact, porous membranes rely on the same principle, the difference being the membrane material that can be hydrophobic, and the smaller pore radius.

As it can be seen from **Table 1-6**, the microchips were principally based on capillary forces to achieve the gas-liquid separation. Several researchers revealed the possibility of obtaining a multistage distillation by connecting several single-stage on-chip microdistillation units in series with the product of the first unit being the feedstock of subsequent one. From **Table 1-7**, it can be noticed among all the evaluated microdistillation devices that the microchip based on centrifugal forces provide the lowest HETP; thus, the best separation efficiency. Among the capillary microdistillations, that of Lam *et al.* [22–25] was the only one able to achieve multistage separation equivalent to a HETP of 100 mm under total reflux.

By the reason of not being able to supply the reflux externally at such low flow rates, the reflux control turns out to be difficult to manage. For this reason, distillation performances are always evaluated assuming total reflux despite a continuous operation.

Table 1-6: Summary of the principle characteristics and performances of the different single-stage on-chip microdistillations.

	Microchip Material	Distillation zone dimensions	Gas-liquid interface generation	Flow rates
Cypes <i>et al.</i> [51]	Silicon	W x D: 500 μm x 280 μm	Capillary forces	15-30 mL/h
Hartman <i>et al.</i> [47]	PTFE membrane	W x D x L: 400 μm x 400 μm x 875 mm	Porous membrane	1.2 mL/h
Wootton and DeMello [49]	Chrome/Glass	W x D: 100-500 μm x 50 μm	Viscous forces	4.5-9 mL/h
Hibara <i>et al.</i> [27]	Fused silica	Liquid channel width: 250 μm	Capillary forces	0.12 mL/h
Stanisch <i>et al.</i> [26]	Glass	W x D x L: 600 μm x 200 μm x 56 mm	Capillary forces	300-1200 mL/h
Boyd <i>et al.</i> [29]	PDMS	W x D x L: 30 μm x 5 μm x 10 mm	Capillary forces	NM*

*NM stands for not mentioned

Table 1-7: Summary of the principle characteristics and performances of the different multistage on-chip microdistillations.

	Microchip material	Distillation zone dimensions	Gas-liquid interface generation	Flow rate	HETP* (mm)
Lam <i>et al.</i> [22–25]	Silicon	W x D x L: 600 μm x 300 μm x 400mm	Capillary forces	0.05-0.4 mL/h	74-400
Cypes <i>et al.</i> [51]	Silicon	W _{top (bottom)} x D x L: 920 (450) μm x 330 μm x 3.35 cm	Capillary forces	Liquid: 16-80 g/(cm ² .min) gas: 1-5.6 g/(cm ² .min)	-
Zhang <i>et al.</i> [52]	PTFE Membrane	W x D: 1 mm x 72 μm	Porous membrane	0.54 mL/h	144
Adiche and Sundmacher [53,54]	Polycarbonate	D _h x L: 677 μm x 342 mm	Porous membrane	up to 1800 mL/h	-
MacInnes <i>et al.</i> [28]	Glass	W x D: 255 μm x 95 μm	Centrifugal forces	non-computed	5.3

*HETP evaluated considering total reflux, even if estimated in continuous mode

2.4. Conclusion on microdistillation downsizing

There are 3 main categories of microdistillations which were briefly discussed within the previous section.

Batch microdistillations are essentially used to analyze and quantify target species in food products and herbs. These devices consist mainly of feeding the channel with a defined mixture. This feed is then heated to a specific temperature that causes the evaporation of the target specie which will be driven toward a collection tank by a carrier gas. The recovered condensate could then be quantified.

The second category is the continuous microdistillations of intermediate size (10 to 300 mL/h). These distillations do not fall within the microscale range. However, a size reduction from that of the laboratory scale has been achieved. Two main subcategories exist: gravity and capillary driven microdistillations. Since the microscale range is not reached, the researchers, in the first subcategory, tried to benefit from the gravity effect that is not overcome by capillary forces at this scale. Therefore, these inventions resemble highly to the conventional distillation columns. In the second subcategory, the principle of operation was mainly inspired from that of the heat-pipe. Wetting materials were implemented inside a channel to retain and drive the liquid phase. The microdistillation was operated principally under adiabatic conditions by heating one end and cooling the other one. Hence, a temperature gradient was established along the channel.

The last category and the most promising one is the continuous on-chip microdistillations. This category is further subdivided into single-stage and multistage on-chip microdistillations. It is a successful reduction of the distillation size to fit into the microscale range. The main elements of the distillation process were integrated within the chip. Two main types exist according to the established gas-liquid flow. It is either a co-current flow, thus limiting the distillation separation to a single-stage, or a counter-current flow, hence achieving a multistage separation. The co-current microdistillations principally make use of capillary forces to generate the gas-liquid separation once the thermal equilibrium is reached. The counter-current flow regime is much more interesting but is also complex to implement. It is established based either on capillary or centrifugal forces.

The most interesting microdistillation is that manufactured by Lam *et al.* [24] since it has been proved to achieve a separation equivalent to 4 or even 5 stages within a flow rate of 0.15 mL/h. Moreover, the dimensions of the channels fall exactly within the micrometric range. The feed was injected using a syringe pump into the silicon-based microchannel. Given that the microchip operates without gravitational force, the distillate and residue were withdrawn using syringe pumps at fixed flow rates. Controlling the outlet product flow rate aims principally to avoid flooding or weeping since it was apparently the only possible solution. Temperature gradient was established by heating one end of the microchip and cooling the other one. Hence, the microdistillation was operated under isothermal conditions contrarily to the classic distillation operation. However, these performances (HETP) seem rather low compared to intermediate size microdistillations reported in the literature : 74 mm compared to 12.7 mm for Sundberg *et al.* [13–16] or 13 mm for Tonkovich *et al.* [17,20] who used the same principle. This indicates that further developments may be possible to enhance performances of on-chip microdistillations.

3. Difference between distillation and microdistillation

To highlight the benefits of a microdistillation compared to a conventional distillation, a comparison between both separation processes with particular emphasis on separation forces, flow rates and HETP is recapped in **Table 1-8**. It allows a better understanding of the concept of each distillation method and illuminates the main differences.

Table 1-8 Comparison between conventional and microscale distillations.

	Conventional distillation	Continuous microdistillations					
		Intermediate size			On-chip		
		Plate	Packed	Heat pipe	Capillary	Membrane	Centrifugal
Flow rates	100 g/h-500 t/h	30 mL/h	53 g/h	9-120 mL/h	0.02-0.4 mL/h	0.18-0.72 mL/h	-
HETP (mm)	20-500	10.8	74-231	10-190	74-400	144-866	5.3

From **Table 1-8**, it can be remarked that microdistillation is able to provide promising separation efficiencies (in terms of HETP), better than the conventional distillation columns within a lower flow rate. On-chip microdistillations offer the possibility to operate under very low flow rates, but their performances can be improved, especially for the capillary on-chip microdistillations whose best HETP was measured at 74 mm.

It is necessary to point out the existence of several gaps that were either missed or not taken into consideration in distillation downsizing.

The liquid phase in such devices is continuous contrarily to conventional distillations. This continuity can induce the dispersion of the flow which decreases the separation efficiency. For example, if the liquid was perfectly mixed, then the species concentration is identical everywhere within the device thus, limiting the separation to a single-stage. This aspect was not mentioned in the literature, and has to be addressed in order to improve performances.

As microchips exhibit a high surface to volume ratio, heat losses are huge compared to the enthalpy carried by the fluids. Consequently, microchips can hardly be adiabatic. For microdistillation, both reboiler and condenser temperatures of the microchannels are fixed, and the microdistillation is operating under non-adiabatic conditions with an imposed linear temperature profile. However, from a thermodynamic point of view, and for a fixed pressure, the equilibrium composition of both phases is set by the temperature. Therefore, it means that the composition at each point of the microchannel is set by the temperature gradient. Thus, feed conditions and reflux should not impact the separation efficiency. Additionally, as explained before, in a classic distillation operation both products flow rates and temperature profile are output parameters. However, it seems to be different with on-chip microdistillations for which these parameters are rather input parameters. These two considerations suggest that even if the temperature gradient is set, the temperature inside the microchannel might not be the same, or that thermodynamic equilibrium is not reached, which offers some flexibility of operation. Otherwise, the microchip would not work.

Similarly to conventional distillations, liquid and gas mass transfer coefficients ($K_L a$) are crucial parameters to estimate the separation performance of microdistillations. Whilst sometimes mentioned when dealing with on-chip microdistillations, it was estimated in a single case. Nevertheless, it might be an essential parameter to enhance the separation and needs to be investigated.

Therefore, it is needed to study the hydrodynamics of the two-phase flow to better understand a capillary on-chip microdistillation and be able to enhance its performances. The distillation itself has

also to be investigated to not only determine its performances but also understand its particular behavior.

4. Conclusion

In this chapter, the need for developing a distillation column in the microscale range was mentioned. Distillation process remains one of the most efficient continuous separation process based on the relative volatility of the mixture components. Specifically used for large-scale volumes, its efficiency is high thanks to long-term experience inherently provided by the oil industry. However, recent advances in microscale processes have highlighted the need for separation downscaling. Indeed, despite the strong attention paid to the microfluidic domain, there exists a wide gap in the field of intensified and microstructured separators, especially for continuous purification of microreactor effluents. Driven by these considerations, it is necessary to design a continuous distillation tool, dealing with low flow rates below 1 mL/h, able to separate efficiently the low flow rate effluents of a microreactor.

The main challenge associated with microdistillation process development is that it cannot be based on gravity forces, which is the gas-liquid separation principle in conventional distillation column. Indeed, at the microscale, the effect of gravity fades in favor of surface forces, creating a major challenge that have to be addressed. Hence, new designs of vapor-liquid contactors based on gravity alternative forces have to be considered. Thus, a deep study of the most relevant previously developed microdistillation systems has been discussed. These devices were classified into categories according to the type of process (continuous or batch), channel size (intermediate size or on-chip), type of gravity-alternative forces and achieved performance (single or multistage). Each proposed device was illustrated, its operational principle was described and then its performance was displayed. The designs belonging to the same category were summarized in a table at the end of each section. A balancing of certain crucial performance parameters, mainly NTS and HETP, was carried out for most of the microdevices. Based on that, a statement can be done for selecting the most promising device that falls within the microscale range and is able to achieve a multistage separation.

It was figured out that the most advantageous and relevant microdistillations are those where the liquid-vapor separation was driven by capillary forces and were developed on-chip. The most promising microscale distillation system able to achieve a multistage separation per a single microchip based on capillary forces, was the one proposed by Lam *et al.* [24]. The reported performances seem however low compared to intermediate size microdistillations that are based on the same principle : HETP is worth 74mm for Lam *et al.* [24] versus 13 mm for Tonkovich *et al.* [17,20]. Better performances are expected and an in-depth study is required. Additionally, in such devices, withdrawal flow rates can be controlled, which is not applicable for the membrane microdistillation system or others and offers new ways to control the separation process. Therefore, the design proposed within this study will be inspired from that of Lam *et al.* [24].

In order to overcome the current limitations concerning microseparators and counter-current gas-liquid flow at the microscale, the objective of this PhD work is to design a continuous on-chip microdistillation tool based on capillary forces. The operating temperatures, pressures and flow rates have to range between 20-300 °C, 0-10 barg and 0.15 - 0.5 mL/h, respectively with expected separation performances of at least 10 theoretical stages. This tool must be then characterized through a

hydrodynamic study and distillation tests in order to relate the hydrodynamic parameters to the separation performances. To achieve this goal, several steps presented in the following chapters are required:

1. The first step is to build the guiding principles on which the design must rely. This will be introduced in the next chapter (**Chapter 2**). In fact, establishing a counter-current gas-liquid flow at the microscale is a challenge. By taking advantage of capillary forces, a counter-current gas-liquid flow configuration is possible. However, some requirements are essential to maintain a stable gas-liquid interface. Then, the microfabrication process to manufacture the newly designed microdistillations is presented.
2. The effect of hydrodynamic phenomenon on the separation efficiency must be considered and will be discussed in **Chapter 3**. Particularly, it is important to identify regions of local recirculations and dead volumes in the liquid phase that potentially hinder the separation efficiency. Hence, an attempt to measure the liquid dispersion in the liquid channel based on residence time distribution is presented.
3. Finally, the distillation performances of the chip are investigated through various operating conditions. The obtained results are presented in **Chapter 4**. These experiments are mainly intended to study the effect of the operational parameters on the distillation efficiency. Specifically, the impact of feed flow rate and composition, residue flow rate and heating temperature on the device performance are evaluated.

2. Chapter 2: Design and microfabrication

1. Introduction

This chapter presents a detailed description of the guiding principles used to design the microdistillation and to perform the microfabrication. An overview of the principal limitations is discussed focusing on the capillary one. Strategy employed for defining the design configuration is based on the conditions required to maintain a stable gas-liquid interface for a counter current flow. Once the guidelines are established, the different approaches for predicting the operating limits and performance of the microdistillation according to literature are briefly reviewed. Thereafter, the workflow followed within this study is displayed. Two main strategies were considered. The first one aims at reproducing a benchmark case, while the second one consists in suggesting an innovative design to achieve high separation performances. The different calculations are illustrated for each strategy. Finally, the microfabrication process used to manufacture the microchip is introduced, enumerated and concisely described.

2. General principles

To set the design guiding principles, we must first recall the principles of distillation at the microscale level. Given that the effect of gravity is outweighed by surface tension forces at the microscale, the distillation is mainly controlled by capillary pressures. The microchannel is made up of two specific areas. First, one area (micropillars) within which the liquid will be preferentially retained and then a second area (void section) in which the gas will be contained. Once the liquid mixture to be distilled is injected into the channel, it will fill the region made of microstructured patterns thanks to capillary forces. Thereafter, by applying a temperature gradient along the channel that ranges between the boiling temperatures of the pure components, the liquid will partially vaporize and the generated vapor will leave the liquid region toward the void section of the channel. Consequently, the vapor will be driven by the pressure difference toward the low temperature at the end of the channel, where it partially or totally condenses and joins back the liquid flow as a reflux. Accordingly, gas and liquid phases, each having a composition gradient along the channel, are flowing counter-currently. However, for a stable distillation operation, the presence of microstructured patterns is not sufficient to prevent the liquid from passing into the gas region or the opposite. A schematic view of the channel geometry is illustrated in **Figure 2-1**.

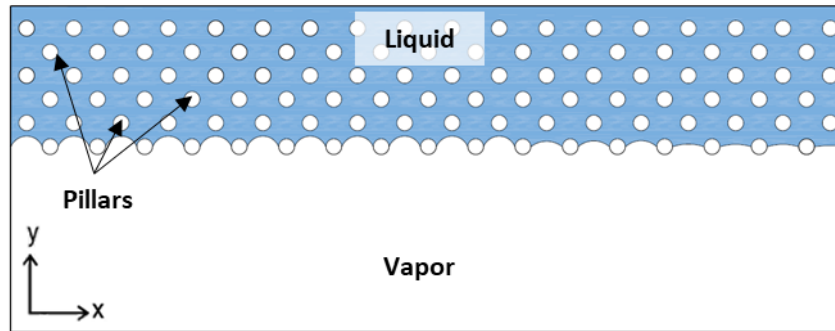


Figure 2-1 Schematic view of a channel partially filled with pillars to drive the liquid phase by capillarity.

To ensure proper operating conditions, a stable gas-liquid interface must be established. This is achieved by studying the pressure evolution of both phases at each location inside the channel. The liquid flow from the cold end toward the hot one through the microstructured region is accompanied with a liquid pressure drop. Similarly, the vapor flow from the hot end toward the cold one induces a slight vapor pressure drop. Since both fluids are flowing counter-currently, then pressure evolutions for the gas and liquid phases are in opposite directions. Indeed, a significant pressure difference between both phases, so-called capillary pressure (ΔP_c), appears because of the small radius of curvature in the area filled with microstructured patterns (**Figure 2-2**). This capillary pressure is given by Young-Laplace equation shown below (**equation 2-1**).

$$\Delta P_c = P_2 - P_1 = \gamma \left(\frac{1}{R_1} + \frac{1}{R_2} \right) \quad (2-1)$$

where P_2 is the pressure at the concave side of the interface and P_1 is that at the convex side of the interface. γ is the surface tension between the gas and liquid phases, R_1 and R_2 are the principal radii of curvature.

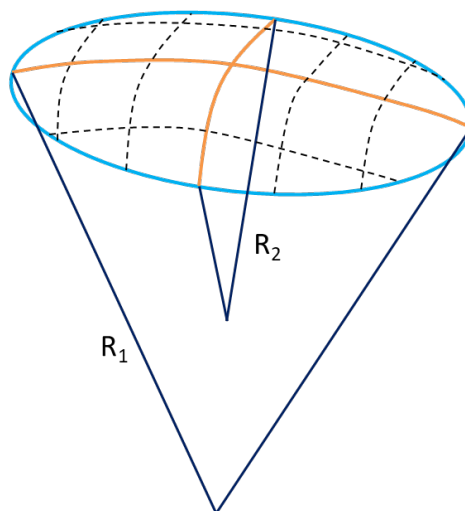


Figure 2-2 Schematic view of a gas-liquid interface relying between two micropillars.

From a geometrical point of view, the radii of curvature can range between two extreme values R_{\min} (minimum radius of curvature) and R_{\max} (maximum radius of curvature). These extreme values are linked to the properties of the wetting phase and of the solid. This translates into a capillary pressure ranging between two radicals: $\Delta P_{c,\min}$ and $\Delta P_{c,\max}$ that are function of the position inside the channel. Accordingly, the maximum and minimum capillary pressures are expressed as follows:

$$\Delta P_{c,\max}(\mathbf{x}) = \gamma(\mathbf{x}) \left(\frac{1}{R_{1,\min}(\mathbf{x})} + \frac{1}{R_{2,\min}(\mathbf{x})} \right) \quad (2-2)$$

$$\Delta P_{c,\min}(\mathbf{x}) = \gamma(\mathbf{x}) \left(\frac{1}{R_{1,\max}(\mathbf{x})} + \frac{1}{R_{2,\max}(\mathbf{x})} \right) \quad (2-3)$$

Three possible cases are encountered:

- $P_g(x) - P_l(x) > \Delta P_{c,\max}(x)$: the gas will infiltrate into the liquid phase and the gas-liquid interface is broken
- $P_g(x) - P_l(x) < \Delta P_{c,\min}(x)$: the liquid will enter the gas dedicated channel and the gas-liquid interface is broken
- $\Delta P_{c,\min}(x) < P_g(x) - P_l(x) < \Delta P_{c,\max}(x)$: a stable gas-liquid interface for a counter-current flow is maintained

Therefore, to maintain a stable gas-liquid interface for a counter-current flow, the third condition must be satisfied at each point within the channel. In other terms, the pressure difference between the gas and liquid phases at each location inside the channel must fulfill the following equation:

$$\Delta P_{c,\min}(\mathbf{x}) < P_g(\mathbf{x}) - P_l(\mathbf{x}) < \Delta P_{c,\max}(\mathbf{x}) \quad (2-4)$$

A model case of the device along with the evolution of the maximum and minimum capillary pressures as well as the gas-liquid pressure difference is illustrated in **Figure 2-3**.

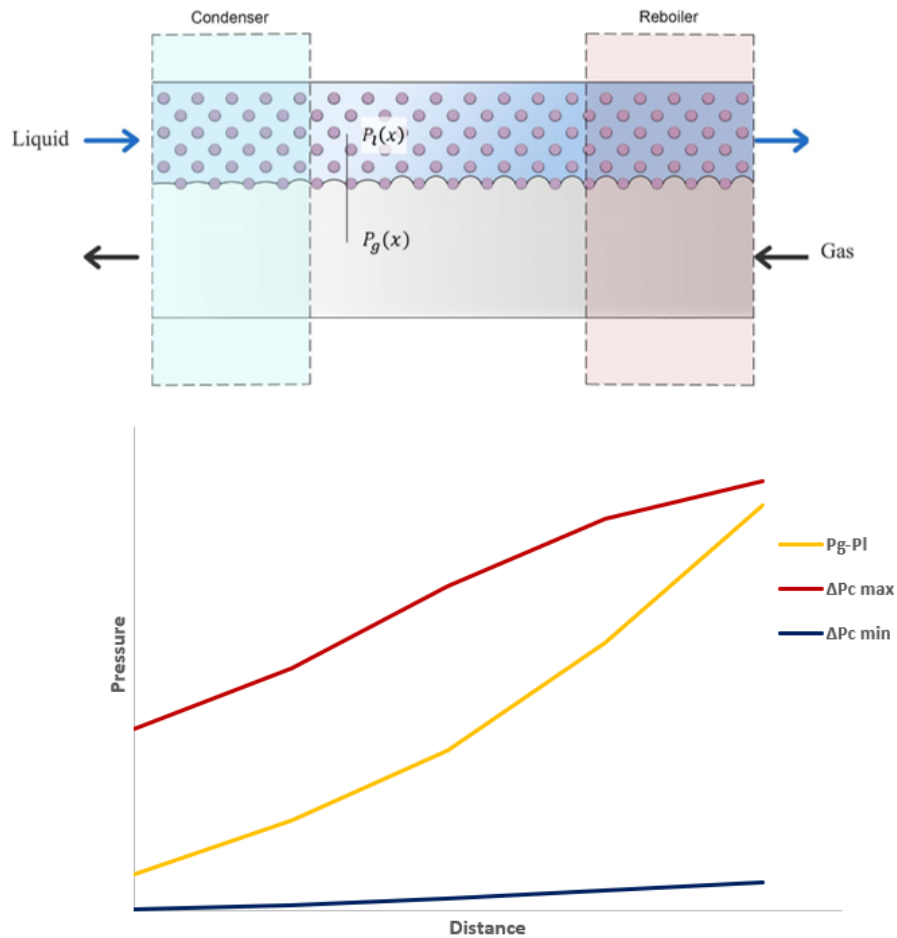


Figure 2-3 Schematic view of the pressure variation and stable interface condition in a counter-current two-phase flow.

3. Operating limit

As illustrated before, the capillary pressure depends mainly on the geometrical dimensions of the channel and the surface tension between the gas and liquid phases. The validity of the previously mentioned condition is based on the fluid pressure drops, which are directly linked to their flow rates and their physicochemical properties. Accordingly, an operating range of feed flow rates could be identified for which the condition of a stable interface is satisfied. In this context, the liquid and gas pressure drops could be calculated by integrating the pressure gradient along the channel of length L ($x=0$ at the condenser, $x=L$ at the reboiler) as follows:

$$\Delta P_l(x) = - \int_0^x \left(\frac{dP_l}{dx} \right) dx \quad (2-5)$$

and

$$\Delta P_g(x) = - \int_L^x \left(\frac{dP_g}{dx} \right) dx \quad (2-6)$$

Seok and Hwang [12] considered that in such miniaturized devices, the gas pressure drop is negligible and the only pressure drop to consider is the liquid one, which is mainly due to dynamic and frictional pressure drops. However, the dynamic component can be overlooked since the liquid velocity is very low. Consequently, the liquid pressure drop is restricted to the frictional one. Assuming that the

liquid driven in the wicks area complies with Darcy's law, an expression of the liquid pressure gradient can be obtained.

$$\frac{dP_l}{dx} = \frac{\mu_l Q_H M}{\rho_l K_p A_w h_{fg}} \quad (2-7)$$

where μ_l is the liquid dynamic viscosity, Q_H is the axial heat flow rate, M is the molecular weight, ρ_l is the molar density of the liquid, K_p is the wick permeability, A_w is the cross sectional area of the wick phase and h_{fg} is the latent heat of vaporization.

Accordingly, by combining **equations 2-5** and **2-7**, the liquid pressure gradient is expressed as follows:

$$\Delta P_l(x) = \int_0^x \left(\frac{\mu_l Q_H M}{\rho_l K_p A_w h_{fg}} \right) dx \quad (2-8)$$

The expression of the maximum capillary flow rate could be obtained for a flat interface and by considering that both radii of curvature are identical and equal to that of the wick. In this context, the maximum capillary pressure is:

$$\Delta P_{c,max}(x) = \frac{4\gamma}{D_{wick}} \quad (2-9)$$

where D_{wick} is the capillary diameter of the wick.

Consequently, the maximum heat flow rate for which the gas-liquid interface is maintained stable can be determined as:

$$\Delta P_{c,max}(x) = \Delta P_l(x) = \int_0^x \left(\frac{\mu_l Q_H M}{\rho_l K_p A_w h_{fg}} \right) dx \quad (2-10)$$

$$Q_{H,max} = \frac{4\gamma K_p A_w M}{D_{wick} \int_0^x \left[\frac{\nu_l}{h_{fg}} F(x) \right] dx} \quad (2-11)$$

where ν_l is the liquid kinematic viscosity, $Q_{H,max}$ is the maximum heat flow rate, and $F(x)$ is the distribution function of heat flow rate. Assuming that the heat is uniformly added to the evaporator and extracted from the condenser, the distribution function turns into:

- $F(x) = x/L_e$ at the evaporator
- $F(x) = 1$ at the adiabatic section
- $F(x) = (L-x)/L_c$ at the condenser

where L_e and L_c are the length of evaporation and condensation sections, respectively.

Therefore, the main conditions for designing a microdistillation tool are the same regardless the design of the device. The pressure difference between the gas and liquid must range between two extreme values of capillary pressure to maintain a stable interface. However, different strategies could be considered to estimate the pressure drop and define the possible assumptions for calculation simplifications and estimations, which are introduced in the next sections.

4. Additional considerations to take into account

The capillary barrier is a major concern in counter-current multistage distillations. However, entrainment, boiling, viscous and sonic limitations have also been previously highlighted in heat pipe

devices [56]. These limitations are mainly function of the thermal flux and the saturation pressure. They will be discussed thereafter.

4.1. Entrainment limitation

The first limitation concerns the liquid entrainment. In these devices, as liquid and vapor are flowing counter-currently within the same channel in two different regions, they are in continuous contact at the interface. If the velocity of the vapor flow reaches high values, the vapor forces out some liquid droplets from the liquid flow toward the vapor one, and the operation is no more stable. This is known as liquid entrainment which could be predicted based on Weber number. To avoid liquid entrainment, inertial forces must be dominated by interfacial forces which translates into a Weber number lower than 1 [57,58]:

$$We = \frac{\rho_g u_g^2 r_p}{\gamma} < 1 \quad (2-12)$$

Where ρ_g is the gas density, u_g the gas phase velocity, r_p the pore radius of the capillary structure, and γ the surface tension.

4.2. Boiling limitation

The second possible limitation is the boiling one. This case is encountered due to excessive vapor generation in the microstructured region. If it happens, a gas layer is stuck on the surface of the heating region and does not allow for fast heat conduction, preventing vapor generation, and leading to overheating of the device. This is known as the 'boiling crisis'.

This phenomenon can be encountered in heat pipes, where a pure compound is used and heated to a temperature above its boiling point. However, microdistillation devices deal with binary mixtures rather than pure compounds, and are less likely to face such limitation : the hot side temperature is higher than the boiling point of the light compound, but lower than that of the heavy one. Therefore, the heaviest compound will remain in its liquid state and total vaporization will not be reached.

Nonetheless, another problem may happen in such devices. The generation of gas bubbles within the liquid region at the heating section of the channel can disrupt the liquid flow. The generated gas bubble can remain trapped within the micropillar region and grow until it reaches the gas-liquid interface. It will then merge with the meniscus before leaving the microstructured region towards the void section of the channel. To avoid this issue, the vapor phase must be generated at the gas-liquid interface.

This means that the temperature must be at its maximum at the gas-liquid interface. This is not possible since the device is heated externally and the heat flow which allows evaporation comes from the hot wall and diffuses within the liquid film towards the gas-liquid interface. Accordingly, a thermal gradient exists across the liquid film thickness and the temperature for the liquid near the hot wall is greater than the temperature of the gas-liquid interface. This suggests that the vapor is not generated at the gas-liquid interface.

However, another phenomenon counterbalances this temperature gradient issue. Let's consider the nucleation of a bubble having a radius ' r_n '. Since the interface of this nucleation bubble is not flat and is rather curved, the pressure within the nucleation bubble is higher than the pressure of the liquid. If

the pressure within the nucleation bubble exceeds the bubble pressure of the liquid (at the local temperature of the liquid), condensation of the vapor trapped within the bubble occurs inducing a decrease in the bubble diameter. This diameter decrease induces pressure increase, thus a further diameter decrease, etc. Hence, the bubble will collapse. If initially the pressure in the nucleation bubble is lower than the bubble pressure of the liquid, the opposite phenomenon takes place and the bubble radius will increase. This initial pressure inside the nucleation bubble depends on the initial radius, and this nucleation radius r_n will depend on the existing impurities within the channel. It varies between 0.1 and 25 μm [57], and is rather approximated to 10 μm [58].

Thus, a criteria can be defined in order to ensure that the temperature gradient is small enough so that nucleation bubbles will only collapse in the liquid phase. In a heat pipe working with a pure compound, this criteria can be developed based on Clapeyron equation. Unfortunately, for the microdistillation case, the problem is more complicated because of the multicomponent mixture. In addition, the composition of the liquid might not be homogeneous through the depth of the liquid film. Moreover, for on-chip microdistillations, this phenomenon can take place over the entire length of the chip and not only at the heating section of the channel. This nucleation process in microdistillation devices is complex and could not be taken into consideration in the design. Only recommendations can be given to avoid this phenomena :

- Reduce the liquid film depth so that the temperature gradient from the hot surface to the gas-liquid interface is small,
- Limit the heat flux to avoid high temperature gradients across the liquid film.

4.3.Viscous limitation

Another constraint is the viscous limitation, which takes place in heat pipes operating at very low saturation pressure, specifically for fluids displaying a melting point near room temperature. In such cases, since pressure is reduced and gas velocity is high, the gas pressure in the heated area is not sufficient to overcome the viscous friction and drive the vapor flow towards the condenser. As a result, the boiling rate is limited. For a microdistillation device working at atmospheric pressure, this case is not expected.

4.4.Sonic limitation

The last limitation is the sonic one, encountered for the gas phase at low saturation pressure as well. It is rather related to the inertial pressure drop generated by the vapor flow. Due to the reduced pressure, this vapor flow can reach velocities near the sound ones [59]. Furthermore, high pressure and temperature gradients can be reached in the heating region leading to excessive superheating. Accordingly, an accurate control of the extracted heat flow must be done to avoid deterioration. This is mainly faced when dealing with high boiling fluids ($>300^\circ\text{C}$). As for the viscous limitation, the sonic limitation is not expected for microdistillations operating at atmospheric pressure or higher.

5. Performance estimation

After identifying the main principles that are essential to maintain and guarantee stable operation regime, it is needed to predict the performance of the device. There is no in-depth study nor a unique method to estimate the performance of the device.

Seok and Hwang [12] followed the concept of Chilton and Colburn [60]. The performance of a microdistillation is evaluated by the number of transfer unit (NTU) in the vapor phase instead of the number of theoretical plates. However, both parameters are very related. The number of transfer units needed to achieve a desired separation can be expressed as a function of the partial pressure of the most volatile component (p) or its mole fraction in the vapor phase (y') as follows:

$$NTU = \int_{p_1}^{p_2} \frac{dp}{\Delta p} = \int_{y'_1}^{y'_2} \frac{dy'}{\Delta y'} = \frac{K' a' P M_v H_{column}}{G_v} \quad (2-13)$$

where K' is the absorption coefficient, a' is the surface area of packing per unit of packed volume, P is the total pressure, M_v is the average molecular weight of the vapor stream, H_{column} is the height of the column and G_v is the mass velocity of the vapor.

MacInnes *et al.* [28] suggested the estimation of the performance of the device by computing the diffusion time (t_{diff}) for both phases. It is specified that the time required for a specie to diffuse from the gas-liquid interface toward the other edge of the channel is an illustration about how rapid the separation can occur. Accordingly, by assuming that the species transfer is done only by diffusion, the diffusion time is a prediction of the distillation time per stage. The diffusion time can be estimated according to the following equation:

$$t_{diff} = \frac{X^2}{D_{coeff}} \quad (2-14)$$

where X and D_{coeff} are the diffusion distance and coefficient, respectively.

Tonkovich *et al.* [17] proposed another method to estimate the height equivalent to a theoretical plate (HETP) by considering that the transfer is occurring through diffusion and convection. The convection time (t_{conv}) for each phase is the HETP divided by the fluid velocity (u). Then by setting that the characteristics times of each phase are equal, a first estimate of the HETP of each phase could be obtained:

$$t_{conv} = \frac{HETP}{u} \quad (2-15)$$

$$t_{diff,g} = t_{conv,g} \rightarrow HETP_g = \frac{u_g * X_g^2}{D_{coeff,g}} \quad (2-16)$$

$$t_{diff,l} = t_{conv,l} \rightarrow HETP_{liq} = \frac{u_l * X_l^2}{D_{coeff,l}} \quad (2-17)$$

where 'g' and 'l' designate the gas and liquid phases, respectively. Thereafter, both HETP, for the liquid and vapor phase must be equal. This is illustrated by **equation 2-18**.

$$\frac{u_g * X_g^2}{D_{coeff,g}} = \frac{u_l * X_l^2}{D_{coeff,l}} \quad (2-18)$$

Cypes and Engstrom [51] proposed the prediction of the device performance based on the overall capacity coefficient according to the equation of Chilton and Colburn [60] as illustrated below:

$$HTU = \frac{\dot{N}}{AK_x a} \quad (2-19)$$

where HTU is the height of each theoretical transfer unit, \dot{N} is the molar liquid flow rate, A is the cross-sectional area of the column and $K_x a$ is the overall capacity coefficient based on the liquid mole fraction.

All these approaches are useful to estimate distillation performances of a micro-device. However, the overall gas-liquid mass transfer coefficient is needed for some of them. In addition, they do not take into account the axial dispersion of the liquid within the microstructured region that can hinder performances. Thus, an in depth study of the hydrodynamics taking place within the microstructured region is essential to understand the behavior of the liquid phase. More specifically, the prediction of the overall gas-liquid mass transfer coefficient is essential as well as the residence time distribution of the liquid phase in the microstructured region.

6. Design and pressure drop calculation

6.1. Workflow

In the current study, binary mixtures having low boiling temperatures and moderate saturation pressure such as acetone-water have been considered. The expected fluid velocities remain very low in the range of mm/s. Hence, the device is not subjected to entrainment, boiling, viscous and sonic limitations. The predominant operating limitation is the capillary one. Consequently, the sizing and design of the device will mainly take into consideration the condition for maintaining a stable gas-liquid interface for a counter-current flow (**equation 2-20**). The procedure is based on suggesting the geometrical dimensions and verifying if the condition of a stable gas-liquid interface is validated. If this condition is not validated, new geometrical dimensions are suggested until it satisfies the condition illustrated in **equation 2-20**. Once validated, the estimation of the device performance based on the diffusion and residence time is done and the design is further tested experimentally.

$$\Delta P_{c,min}(x) < P_g(x) - P_l(x) < \Delta P_{c,max}(x) \quad (2-20)$$

The microstructured region is principally made of micropillar arrays. From a geometrical point of view, the capillary pressure can take two extreme values according to the radii of curvature (**Figure 2-2**).

The gas pressure decreases from the reboiler to the condenser, that of the liquid decreases from the condenser to the reboiler. When both pressures are equal, the capillary pressure approaches a minimum value, and the interface flattens. This is illustrated in **Figure 2-4** where the vapor flow flattens the interface at the condensation zone. For simplification purposes, the gas and liquid pressures are assumed to be equal at the condenser ($x=0$):

$$P_g(x = 0) = P_l(x = 0) \quad (2-21)$$

Accordingly, the minimum value of capillary pressure is obtained at the condenser ($x=0$) and is illustrated by the equation written below:

$$\Delta P_{c,min} \approx \Delta P_{c,min}(x = 0) = 0 \text{ (flat interface)} \quad (2-22)$$

Therefore, the pressure difference between the gas and the liquid at each position x inside the channel must be always higher than this minimum value of capillary pressure to avoid the passage of the liquid in the gas flow.

The maximum value of capillary pressure is obtained when the radii of curvature are set in a way that R_1 is equal to half the spacing between the micropillars (a_μ) and R_2 is equal to the micropillars height (H). This is displayed by **equation 2-23**. Surpassing this limit would break the gas-liquid interface and the gas would infiltrate into the liquid region.

$$\Delta P_{c,max}(x) = \gamma(x) \left(\frac{1}{a_\mu} + \frac{1}{H} \right) \quad (2-23)$$

Accordingly, maintaining a stable interface constraints a difference in the gas and liquid pressures ranging between $\Delta P_{c,min}$ and $\Delta P_{c,max}$.

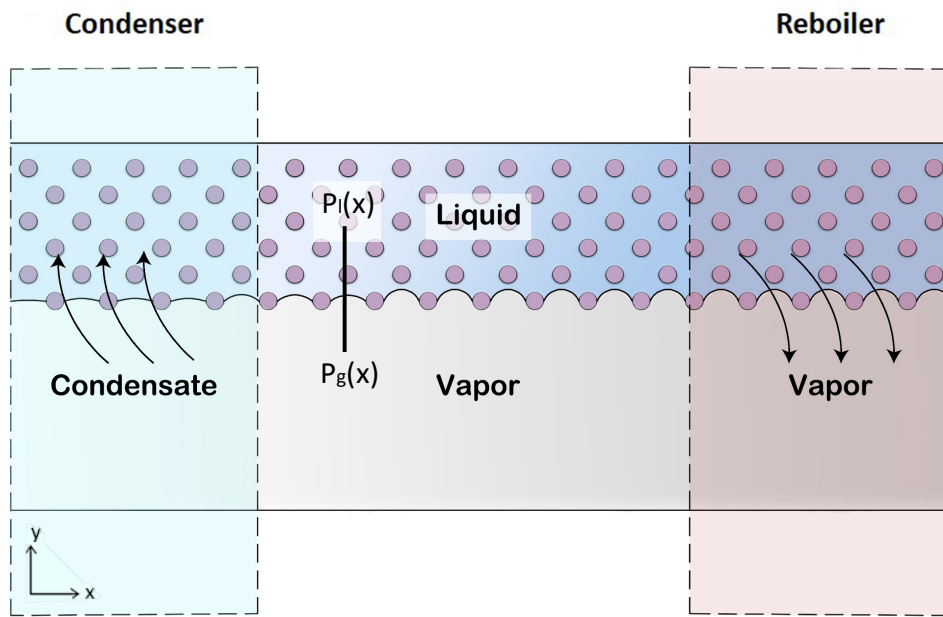


Figure 2-4 Schematic view of the evaporation-condensation cycle within the microdistillation.

Moreover, the pressure of the gas and liquid at each location inside the channel can be calculated according to the following expressions:

$$P_g(x) = P_g(x = 0) + \Delta P_g(x) \quad (2-24)$$

$$P_l(x) = P_l(x = 0) - \Delta P_l(x) - \rho_l(x) g x \sin \alpha' \quad (2-25)$$

where ρ_l is the liquid density, g is the gravitational acceleration and α' is the tilt angle with respect to the horizontal position of the device as shown in **Figure 2-5**.

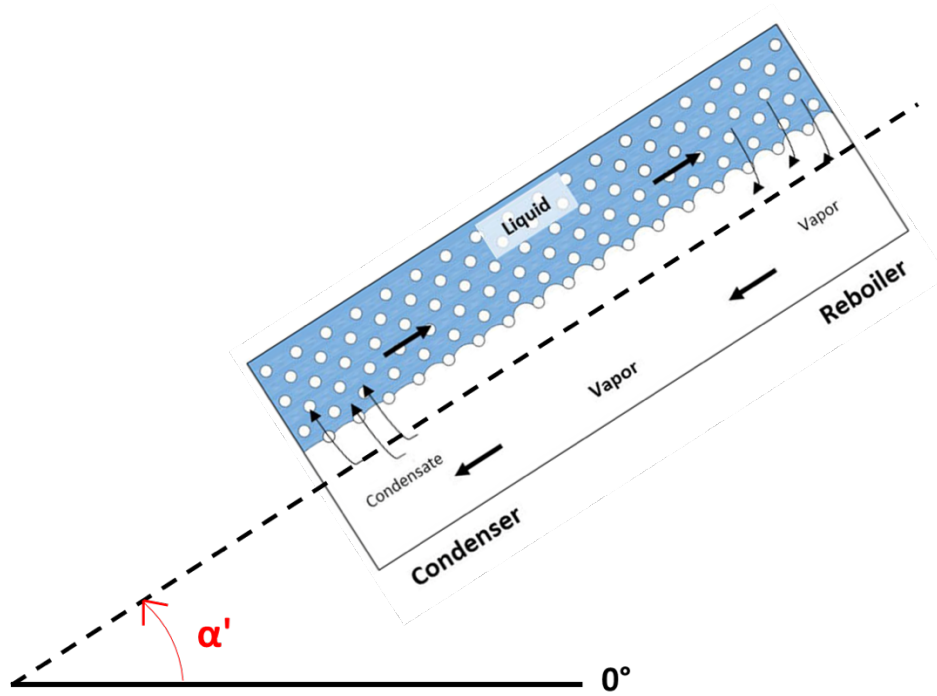


Figure 2-5 Schematic view of a tilted device and the corresponding tilt angle with respect to the horizontal position.

Subtracting equation 2-25 from equation 2-24 gives:

$$P_g(x) - P_l(x) = \Delta P_g(x) + \Delta P_l(x) = \Delta P_c(x) \quad (2-26)$$

Combining equations 2-20, 2-22, 2-23 and 2-26 gives the main condition to maintain a stable gas-liquid interface for a counter-current flow:

$$0 < \Delta P_g(x) + \Delta P_l(x) < \gamma(x) \left(\frac{1}{a_\mu} + \frac{1}{H} \right) \quad (2-27)$$

To verify the validity of equation 2-27, it is needed to predict ΔP_g and ΔP_l within the device.

6.2. Gas pressure drop

The gas pressure drop (ΔP_g) was estimated based on Hagen-Poiseuille flow through some non-circular cross-sections knowing that the channel is of trapezoidal cross section and the flow is laminar [61]. This model is well suited for Newtonian fluids, incompressible and laminar flows that are present here. ΔP_g can be deduced from the following equation:

$$Q_g = \frac{\Delta P_g h_g^3 L_g}{12 \mu_g} - \frac{16 \Delta P_g h_g^4}{\pi^5 \mu_g} \sum_{n=1}^{\infty} \left[\frac{1}{(2n-1)^5} \frac{(\cosh(\beta_n L_g) - 1)}{\sinh(\beta_n L_g)} \right]; \quad \beta_n = \frac{(2n-1)\pi}{h_g} \quad (2-28)$$

Where h_g and L_g are the gas channel's height and length, respectively.

6.3. Liquid pressure drop

The liquid pressure drop across a bank of tubes has been studied since 1978 [62]. Different shapes and arrangements of tubes so-called pin fins have been tested. The liquid pressure drop could be estimated as follows:

$$\Delta P_l = \sum_{N_{column}} \frac{f u_l^2 \rho_l}{2} = N_{column} * \frac{f u_l^2 \rho_l}{2} \quad (2-29)$$

where N_{column} is the number of columns of micropillars, f is the friction factor, u_l is the liquid velocity and ρ_l liquid density.

The issue relies in estimating the friction factor. Several correlations for predicting the friction factor have been suggested for a narrow range of geometrical dimensions and the majority deals with high Reynolds number. However, when operating outside the experimental conditions based on which the correlation was proposed, the numerical results deviate drastically from the experimental ones. The friction factor correlations for laminar single-phase flow within micropillars region of various arrangements (for moderate Reynolds number) are recapitulated in the **Table 2-1**. Other existing friction factor correlations covering a wider range of Reynolds number are also summarized in **Appendix A, Table A- 1**. A schematic view of an in-line and staggered arrangement of micropillars with the different geometrical parameters is illustrated in **Figure 2-6**. S_T , S_L and S_D stand for the transverse, longitudinal and diagonal pitches. W_d is the distance between the micropillar and the wall of the channel. d_μ is the micropillar diameter. d stands for the depth of the channel. Re_μ is the Reynolds number in the micropillar region, $u_{l,max}$ is the maximum liquid velocity, D is the hydraulic diameter of a micropillar, \dot{m} is the liquid mass flow rate, A_{min} is the minimum cross-sectional area of the channel, N_{row} is the number of rows of micropillars, $A_{\mu pillar}$ and $P_{\mu pillar}$ are the cross sectional-area and wetting perimeter of a micropillar, respectively. w_l is the width of the liquid channel provided with micropillars.

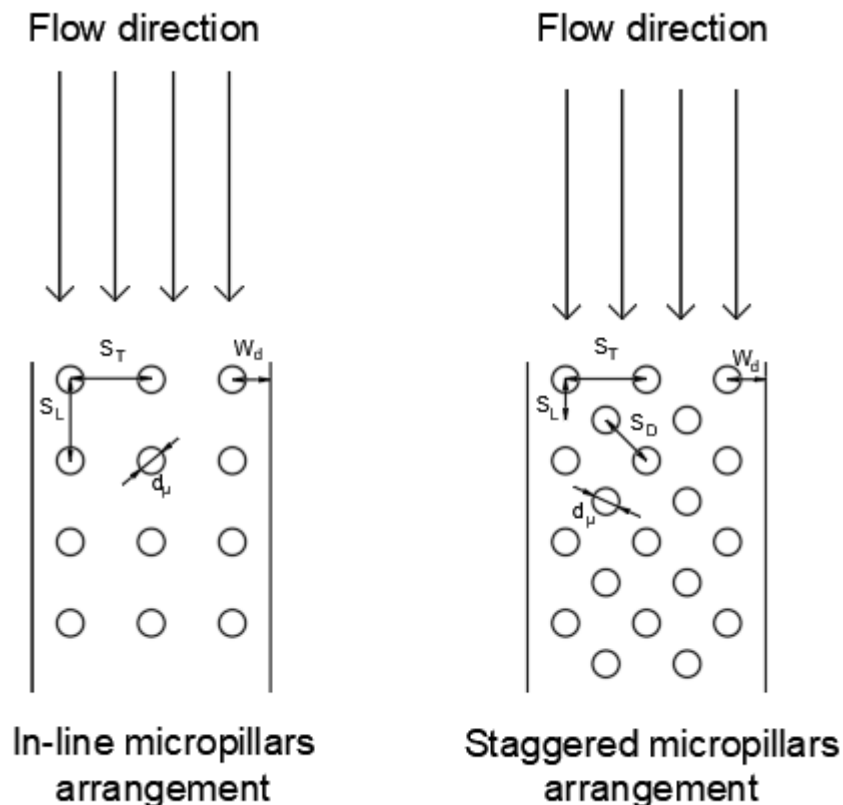


Figure 2-6 Schematic view of the in-line and staggered arrangements of micropillars with the main geometrical parameters.

Table 2-1: Friction factor correlations for laminar single-phase flow within micropillars region.

References	Range of validity	Friction factor correlation
Koşar <i>et al.</i> [63]	<u>Circular staggered micropillars</u> $\frac{H}{D} = \{1; 2\}$ $\frac{S_T}{D} = \frac{S_L}{D} = 1.5$ $5 < Re_\mu < 128$	$f = \frac{1739}{Re_\mu^{1.7}} \left(\frac{H}{D} + 1 \right)^{1.1} \left(\frac{S_T S_L}{A_{\mu pillar}} \right)^{-0.3} + \frac{345}{Re_\mu} \left(\frac{1}{\frac{H}{D} + 1} \right)^2 \left(\frac{S_T S_L}{A_{\mu pillar}} \right)^{-0.3}$ $A_{min} = \left(\left(\frac{w_l}{S_T} - 1 \right) * c + (S_T - D) \right) * H$ $c = \begin{cases} S_T - D & \text{if } S_T - D < S_D - D \\ S_D - D & \text{if } S_T - D > S_D - D \end{cases}$ with $S_D = \sqrt{\left(\frac{S_T}{2} \right)^2 + S_L^2}$
	<u>Circular in line arrangement</u> $\frac{H}{D} = 1$ $\frac{S_T}{D} = \frac{S_L}{D} = 1.5$ $5 < Re_\mu < 128$	$f = \frac{7259}{Re_\mu^{1.7}} \left(\frac{H}{D} + 1 \right)^{1.9} \left(\frac{S_T S_L}{A_{\mu pillar}} \right)^{-0.4} + \frac{54}{Re_\mu^{0.7}} \left(\frac{1}{\frac{H}{D} + 1} \right)^2 \left(\frac{S_T S_L}{A_{\mu pillar}} \right)^{-0.7}$
Prasher <i>et al.</i> [64]	<u>Circular staggered micropillars</u> $1.3 < \frac{H}{D} \leq 2.8$ $2 < \frac{S_T}{D} < 3.6$ $2.4 < \frac{S_L}{D} < 3.6$ $40 < Re_\mu < 1000$	All Re values (not so accurate) $f = 14 \left(\frac{H}{D} \right)^{0.724} \left(\frac{S_L - D}{D} \right)^{-0.442} \left(\frac{S_T - D}{D} \right)^{-0.245} Re_\mu^{-0.58}$ For $Re_\mu < 100$ $f = 679.28 \left(\frac{H}{D} \right)^{-0.64} \left(\frac{S_L - D}{D} \right)^{-0.258} \left(\frac{S_T - D}{D} \right)^{0.283} Re_\mu^{-1.35}$ For $Re_\mu > 100$ $f = 1.18 \left(\frac{H}{D} \right)^{1.249} \left(\frac{S_L - D}{D} \right)^{-0.7} \left(\frac{S_T - D}{D} \right)^{-0.36} Re_\mu^{-0.1}$
Gaddis and Gnielinski [65]	<u>Circular staggered and in-line tube banks</u> $Re_\mu \leq 10$	$f = \frac{280\pi \left\{ \left[\left(\frac{S_L}{D} \right)^{0.5} - 0.6 \right]^2 + 0.75 \right\}}{\left[4 \left(\frac{S_T}{D} \right) \left(\frac{S_L}{D} \right) - \pi \right] (c)^{1.6}} Re_\mu^{-1}$ where $c = \frac{S_T}{D} \text{ for in line arrangement and a staggered arrangement with } \frac{S_L}{D} \geq \frac{1}{2} \sqrt{2 \frac{S_T}{D} + 1}$

		$c = \frac{S_D}{D}; S_D = \sqrt{\left(\frac{S_T}{2}\right)^2 + S_L^2}$ for a staggered arrangement with $\frac{S_L}{D} < \frac{1}{2}\sqrt{2\frac{S_T}{D} + 1}$
Tullius <i>et al.</i> [66]	<p><u>Circular staggered micropillars</u></p> <p>$\frac{H}{D} = 1$</p> <p>$\frac{S_T}{D} = 2$</p> <p>$\frac{S_L}{D} = 2$</p> <p>$60 < Re_\mu < 1000$</p>	$f = 2.963 \left(\frac{S_L}{D}\right)^{0.2} \left(\frac{S_T}{D}\right)^{0.2} \left(\frac{H}{D}\right)^{0.18} \left(1 + \frac{d-H}{D}\right)^{0.2} Re_\mu^{-0.435}$

The parameters involved in most of the correlations illustrated in **Table 2-1** require the knowledge of the Reynolds number that can be estimated according to **equations 2-30, 2-31, 2-32** and **2-33**.

$$Re_{\mu} = \frac{\rho_l u_{l,max} D}{\mu_l} \quad (2-30)$$

$$u_{l,max} = \frac{\dot{m}}{\rho_l A_{min}} \quad (2-31)$$

$$A_{min} = H[(N_{row} - 1)(S_T - D) + (2W_d - D)] \quad (2-32)$$

$$D = \frac{4A_{\mu pillar}}{P_{\mu pillar}} = d_{\mu} \text{ (cylinders)} \quad (2-33)$$

It was stated by Gunda *et al.* [67] that micropillars arranged in-line offer higher flow resistance, hence more pressure drop than those having a staggered arrangement. To minimize the pressure drop, the micropillars were arranged in a staggered manner within this work. Two main strategies were used to estimate the pressure drop within the liquid region.

The first one was to test two of the abovementioned correlations for the prediction of the friction factor **Table 2-1**. The chosen correlations, which are the closest to the case studied within this work are those suggested by Prasher *et al.* [64], Koşar *et al.* [63], Gaddis and Gnielinski [65] and Tullius *et al.* [66].

The second one was to assume that the liquid flow is similar to the one flowing into a packed bed. Therefore, the liquid pressure drop (ΔP_g) can be estimated using Kozeny–Carman equations [68–70] (**equations 2-34**) and Ergun equations for laminar and incompressible flows [71] (**equations 2-35**).

$$\Delta P_l = \frac{u'_l \mu_l L_l K S^2 (1-\epsilon)^2}{\epsilon^3} \quad (2-34)$$

$$\Delta P_l = \left(151.2 \frac{\mu_l (1-\epsilon)^2}{D^2 \epsilon^3} u'_l \right) * L_l \quad (2-35)$$

where u'_l is the flux velocity in an empty channel (without the micropillars), L_l is the liquid channel's length, ϵ is the porosity, K is Kozeny constant that ranges between 3 and 6 and finally S is the specific surface area of the micropillars.

According to these calculations, a maximum feed flow rate can be defined. Exceeding this flow rate would break the gas-liquid interface. However, this condition is essential to have an operational system but is not sufficient.

All the devices mentioned thereafter are used in their horizontal orientation. Therefore, the gravitational pressure drop could be ignored.

6.4. Performance estimation

Before developing the device, a preliminary estimation of the separation performance must be done. Similarly to the approach proposed by Tonkovich *et al.* [17], performance estimation was based on the computation of the diffusion (t_{diff}) and residence time (t_{res}). In fact, each molecule in each phase must have sufficient time to diffuse from the interface toward the edge of the channel before leaving the channel (**Figure 2-7**). This translates into a ratio between the residence and diffusion time for both

phases that must be higher than 1 more preferably higher than 5 for a better separation. It is estimated using the following equation:

$$\tau = \frac{t_{res}}{t_{diff}} = \frac{V/Q}{X^2/D_{coeff}} \quad (2-36)$$

where V is the channel volume. In order to be representative of the order of magnitude of the diffusion coefficients, the gas and liquid diffusion coefficients were fixed at 10^{-5} and 10^{-9} m^2/s , respectively.

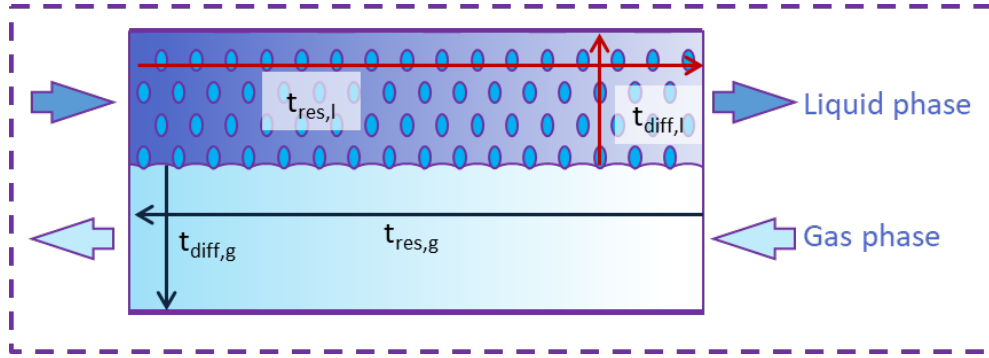


Figure 2-7 Schematic view of the concept on which the performance estimation was based for the gas and liquid phases.

6.5. Pressure drop calculation

6.5.1. General approach

It can be seen from the different correlations and equations that designing a microdistillation requires the knowledge of the fluids properties and fluid flow rates. Moreover, these parameters vary among the microdistillation. In order to take these constraints into consideration, a discrete approach is adopted: the microdistillation is divided into 5 sections, each corresponding to a theoretical tray. For each section, properties and flow rates are assumed constant. These data are provided by a ProII simulation using the NRTL model and considering a 5 theoretical plate column with a reboiler and a condenser.

The pressure drop of each section can then be calculated and summed to determine the total pressure drop of the gas and liquid phases. Consequently, the calculation of the pressure drops obtained by integration could be simplified and transformed into the summation per tray. The different sections of the microdistillation are illustrated in **Figure 2-8**. Thus, **equations 2-5** and **2-6** turn into **equations 2-37** and **2-38**, respectively.

$$\Delta P_l(x) = \sum_{j=0}^i \Delta P_{l,j} \quad (2-37)$$

$$\Delta P_g(x) = \sum_{j=i}^L \Delta P_{g,j} \quad (2-38)$$

In the next paragraphs, calculations were performed on different geometries. First, on the designs proposed by Lam *et al.* [24], whose performances are already known, in order to validate and adjust the proposed approach. Then, on a similar design suggested in this work, and finally on a new proposed design.

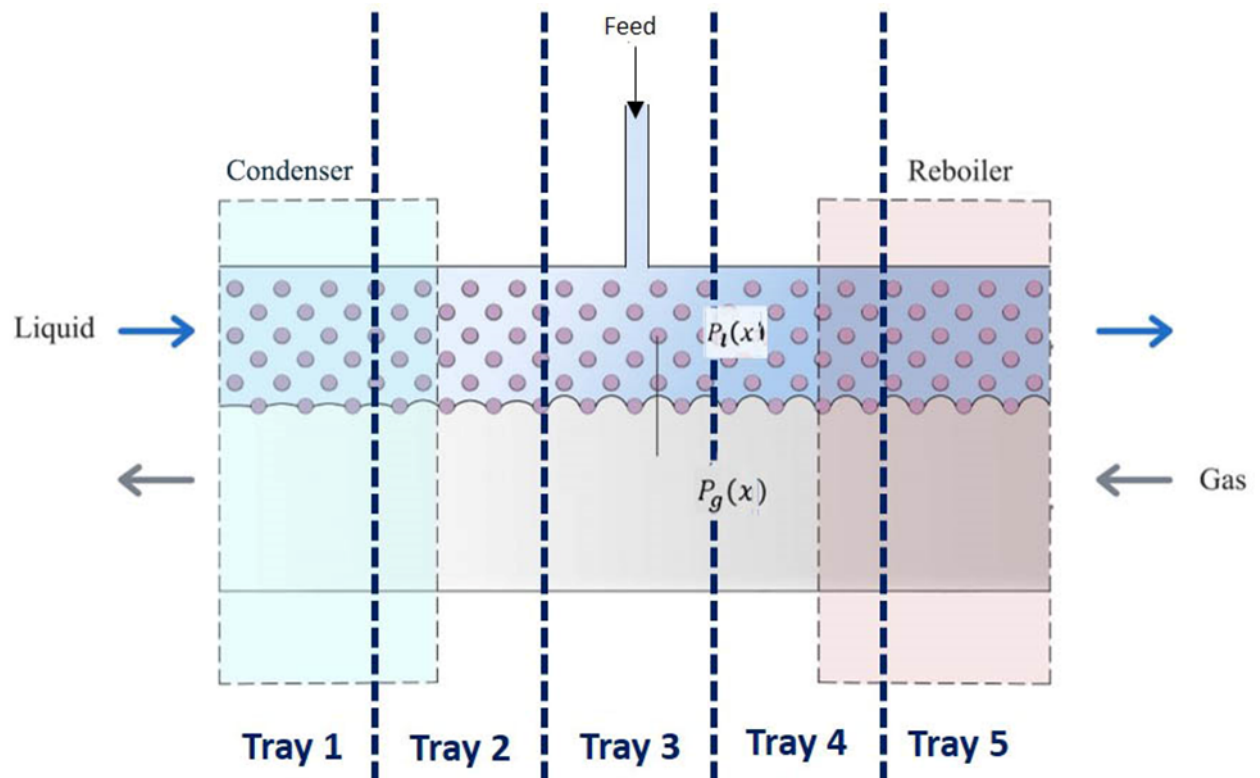


Figure 2-8 Schematic view of the different sections inside the microdistillation channel.

6.5.2. Fluid properties

Accordingly, a classic simulation of a distillation column having 5 theoretical trays (**Figure 2-8**), associated with a reboiler and a condenser, was adapted for estimating the physicochemical properties of both phases at the various involved operating conditions. The simulated case is an aqueous mixture of acetone (19 mol%) fed at 60°C and atmospheric pressure. The feed plate was number 3. The purity of both products was varied between 80 to 90 mol%. After converging, the results were collected and integrated in the design calculations. The maximum purity of both products for which convergence occurred was 88 mol%. This case is the most difficult one to achieve, hence requiring the highest separation performances. Therefore, this value was selected and the obtained results are illustrated in **Table 2-2**.

Table 2-2 Physicochemical properties of the fluids obtained from the simulation.

		Tray 1	Tray 2	Tray 3	Tray 4	Tray 5
Gas phase	Mass Flow rate (g/h)	6.41E-02	5.75E-02	6.04E-02	5.66E-02	-
	Density (g/cm ³)	1.96E-03	1.80E-03	1.80E-03	1.71E-03	-
	Pressure (bar)	1.01E+00	1.01E+00	1.01E+00	1.01E+00	-
	Molecular weight (g/mol)	5.33E+01	4.98E+01	4.97E+01	4.78E+01	-
	Dynamic viscosity (Pa.s)	8.60E-06	8.80E-06	8.80E-06	9.00E-06	-
Liquid phase	Mass Flow rate (g/h)	6.41E-02	3.16E-02	1.70E-01	1.66E-01	1.09E-01
	Dynamic viscosity (Pa.s)	2.59E-04	2.88E-04	3.81E-04	3.83E-04	3.93E-04
	Molecular weight (g/mol)	5.33E+01	4.74E+01	2.83E+01	2.78E+01	2.28E+01
	Density (Kg/m ³)	7.56E+02	7.66E+02	8.37E+02	8.41E+02	8.88E+02
Gas - liquid	Temperature (°C)	5.70E+01	5.83E+01	6.35E+01	6.36E+01	6.75E+01
	Surface tension γ (N/m)	2.48E-02	3.16E-02	5.33E-02	5.38E-02	5.89E-02

6.5.3. Benchmark case

The strategy followed within this work was first to reproduce a benchmark case. Among all the concepts published in the literature, the most promising capillary multistage distillation was that proposed by Lam *et al.* [24,25]. The designed microchips by Lam *et al.* [24], their internal configurations and their dimensions were illustrated in **Chapter 1 - section 2.3.2.1** and are summarized in **Table 2-3**. The Reynolds and Weber numbers for each design are recapitulated in **Table 2-4**. Weber number lower than the unity confirms that no liquid entrainment is expected (**see section 4.1**). Additionally, the low Reynolds values prove a laminar flow regime.

Table 2-3: Design, internal configuration and dimensions of the chips developed by Lam *et al.* [24,25].


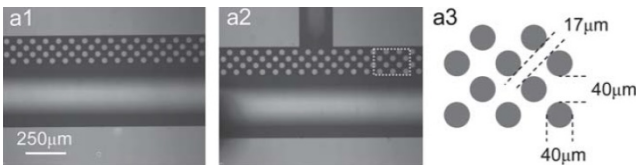
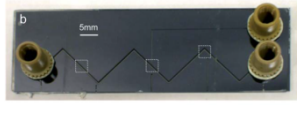

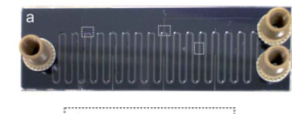
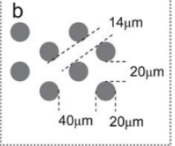
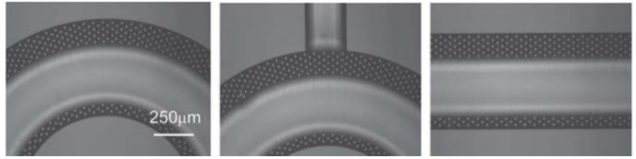
Microchips designs	Internal configurations	Dimensions
		Width: 550 µm Length: 60 mm Depth: 300 µm H/D: 7.5 $S_L/D: 1$ $S_T/D: 2$
		Width: 550 µm Length: 81 mm Depth: 300 µm H/D: 7.5 $S_L/D: 1$ $S_T/D: 2$
 		Width: 600 µm Length: 400 mm Depth: 300 µm H/D: 15 $S_L/D: 1.5$ $S_T/D: 2$

Table 2-4 Reynolds and Weber numbers calculated for the various designs proposed by Lam *et al.* [24,25] for a feed flow rate of 150 µL/h.

	Design	Tray 1	Tray 2	Tray 3	Tray 4	Tray 5
Re	Linear	0.131	0.058	0.235	0.229	0.147
	Zigzag	0.131	0.058	0.235	0.229	0.147
	Serpentine	0.029	0.013	0.051	0.050	0.032
We	Linear	0.007	0.006	0.004	0.004	0.004
	Zigzag	0.010	0.008	0.005	0.005	0.005
	Serpentine	0.009	0.007	0.005	0.005	0.005

The previously developed conditions are applied to the benchmark case. Concerning the correlation proposed by Prasher *et al.* [64], it is only valid for a ratio of $S_L/D > 3.6$ even from a mathematical point of view. Therefore, it won't be taken into account to predict the pressure drop of the liquid phase.

The conditions for a stable interface are generally validated as ΔP_c is always greater than the pressure difference between both phases predicted with most of the correlations for a flow rate of 150 µL/h (Figure 2-9, Figure 2-10, Figure 2-11). It is important to mention that ΔP_c is not constant since

it is a function of the surface tension that varies with the temperature and the composition. Moreover, the non-linearity of the ΔP_c curve is due to the feed injection in the middle of the channel. The linear, zigzag and serpentine designs are validated by all the correlations except for that of Koşar *et al.* [63] and Gaddis and Gnielinski [65]. In other terms, these designs would maintain a stable gas-liquid interface according to the Ergun, Kozeny Carman, Tullius *et al.* [66] equations. In fact, for all the designs proposed by Lam *et al.* [24,25], the H/D ratio is clearly greater than what the correlations have been established for. Even the S_L/D and S_T/D ratios do not fit in the range of feasibility of the correlation of Koşar *et al.* [63]. This explains the reason why the different correlation results are not in agreement with each other. Ergun and Kozeny-Carman models are more general, and probably more reliable in this case. However, no guarantee of accuracy can be admitted. It is important to mention that several researchers have tested the feasibility of the correlations summarized in **Table 2-1** and have noticed a high mean average error [66,72,73]. The pressure drops calculated with these correlations do not stick well with the experimental ones and could only be used for a specific range of dimensions. Moreover, the Reynold number is lower than unity which would not be valid except for the correlation of Gaddis and Gnielinski [65]. Despite the fact of having geometrical ratios out of the range of validity of the correlations, the results given by the correlations of Tullius *et al.* [66] and the models of Kozeny Carman and Ergun confirm that a condition of a stable interface is fulfilled. This is also applicable for the values obtained for the time constants shown in **Table 2-5**. For all the designs proposed by Lam *et al.* [24], the time constants for both phases are higher than 1, which means that the diffusion time is smaller than the residence time. Obviously, the serpentine channel presents the highest time constants since the channel is wider and longer. This translates into better separation performances as mentioned in **Chapter 1 - section 2.3.2.1**. Based on this previous discussion, the suggested model is able to predict based on the correlations of Tullius *et al.* [66] Kozeny Carman and Ergun if the design is theoretically operational or not. Hence, it will be adopted thereafter to estimate the liquid pressure drop and validate whether the developed designs are operational or not.

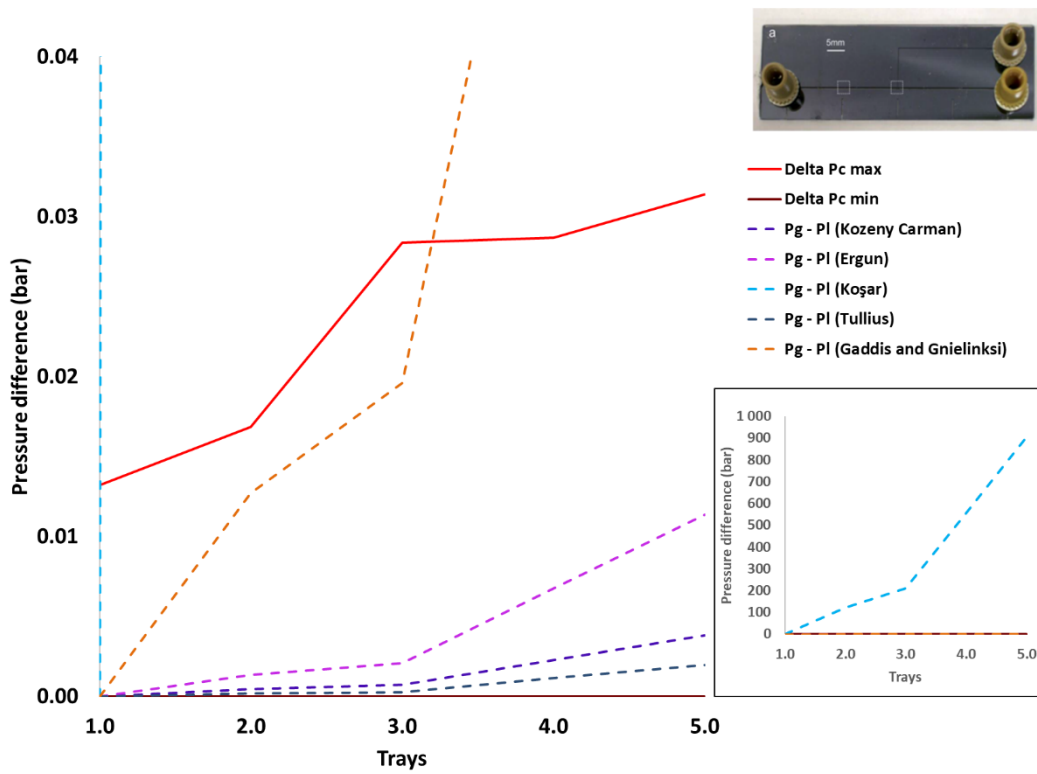


Figure 2-9 Graph showing the pressure difference between the two phases and the capillary pressure for 150 $\mu\text{L}/\text{h}$ all along the microchannel for the linear design proposed by Lam *et al.* [24].

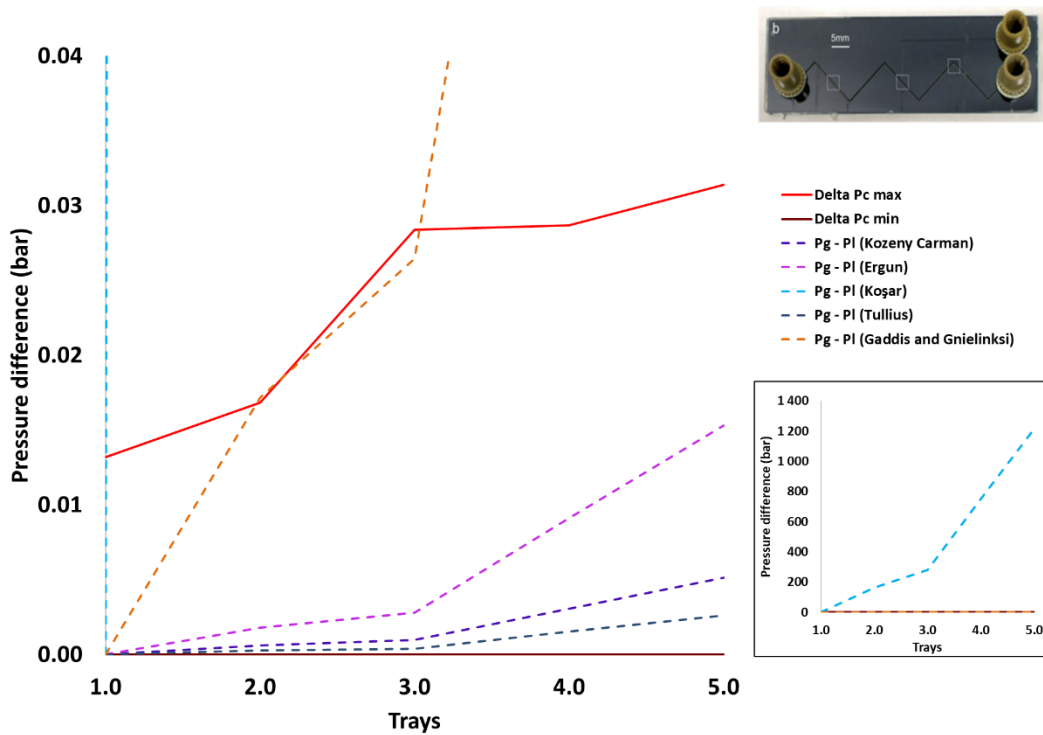


Figure 2-10 Graph showing the pressure difference between the two phases and the capillary pressure for 150 $\mu\text{L}/\text{h}$ all along the microchannel for the zigzag design proposed by Lam *et al.* [24].

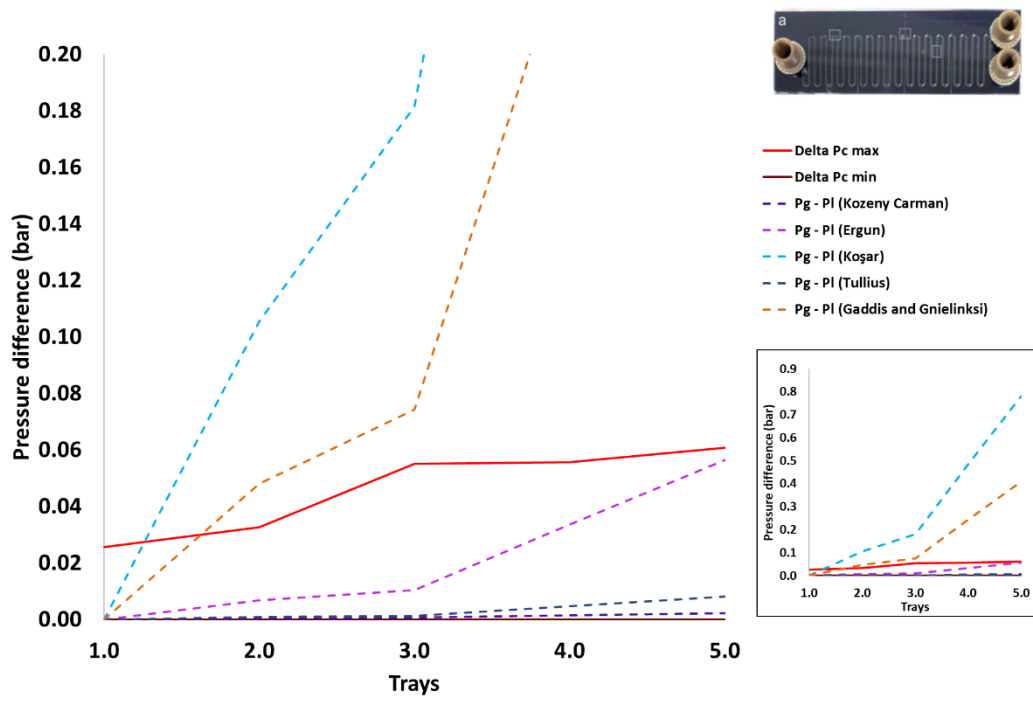


Figure 2-11 Graph showing the pressure difference between the two phases and the capillary pressure for 150 $\mu\text{L/h}$ all along the microchannel for the serpentine design proposed by Lam *et al.* [24].


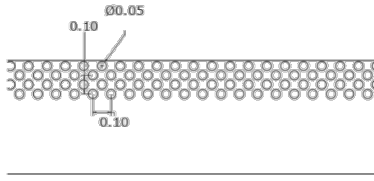

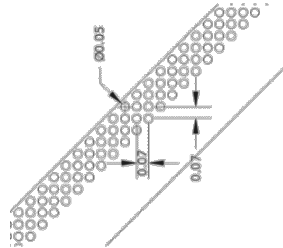
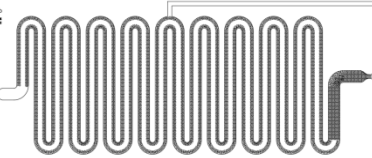
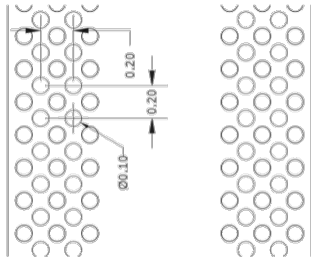
Table 2-5 Performance estimation of the different distillation channels proposed by Lam *et al.* [24].

		Linear	Zigzag	Serpentine
Vapor	Residence time (s)	0.790	1.067	5.268
	Diffusion time (s)	0.016	0.016	0.016
	τ	49.39	66.67	329.23
Liquid	Residence time (s)	45.484	61.404	491.452
	Diffusion time (s)	22.500	22.500	40.000
	τ	2.02	2.73	12.29

6.5.4. Suggested design (inspired from the work of Lam *et al.* [24])

The AutoCad drawings, internal configuration and dimensions of the proposed designs inspired from that of Lam *et al.* [24], are summarized in **Table 2-6**. *Chip a* is a linear channel provided with a single array of micropillar. The second chip is similar to the first one but with a zig-zag shape to increase the channel length for an expected better separation. *Chip c* consists of a wider channel lined with micropillars on both sides of the channel aiming at increasing the liquid holdup capacity.

Table 2-6: Design, internal configuration and dimensions of the chips inspired from the work of Lam *et al.* [24].

AutoCad drawing	Internal configurations	Dimensions
 <p style="text-align: center;">Chip a</p>		<p>Width: 610 μm Length: 60 mm Depth: 26 μm H/D: 0.52 S_L/D: 1 S_T/D: 2</p>
 <p style="text-align: center;">Chip b</p>		<p>Width: 550 μm Length: 77 mm Depth: 27 μm H/D: 0.54 S_L/D: 1 S_T/D: 2</p>
 <p style="text-align: center;">Chip c</p>		<p>Width: 1850 μm Length: 400 mm Depth: 25 μm H/D: 0.54 S_L/D: 2 S_T/D: 4</p>

In the current work, wet etching technique was used to produce the microchannel. Unlike Lam *et al.* [24], who employed dry etching techniques, the reachable channel depth turns out to be a limiting technical point. Dry etching *via* plasma leads to straight channels having a rectangular cross section. No limitation in terms of maximum depth exists since the etching is perpendicular to the surface of the wafer. Contrary to dry etching, a channel realized with wet etching is of a trapezoidal cross section. Thus, according to the width of the channel and the spacing of the micropillars, it exists a maximum depth where the micropillars base will merge. In fact, the maximum reachable depth for a center to center distance between the micropillars of 100 μm is 30 μm (specification to be detailed in the upcoming section). A higher depth can be etched by increasing the micropillar diameter and their spacing. However, the main parameter involved in the capillary action is the micropillar inter-distance. It must be as small as possible to increase the capillary effect.

A schematic view of the cross section, top view, and 3D model of a channel fabricated by dry and wet etching are illustrated in **Figure 2-12** and **Figure 2-13**, respectively.

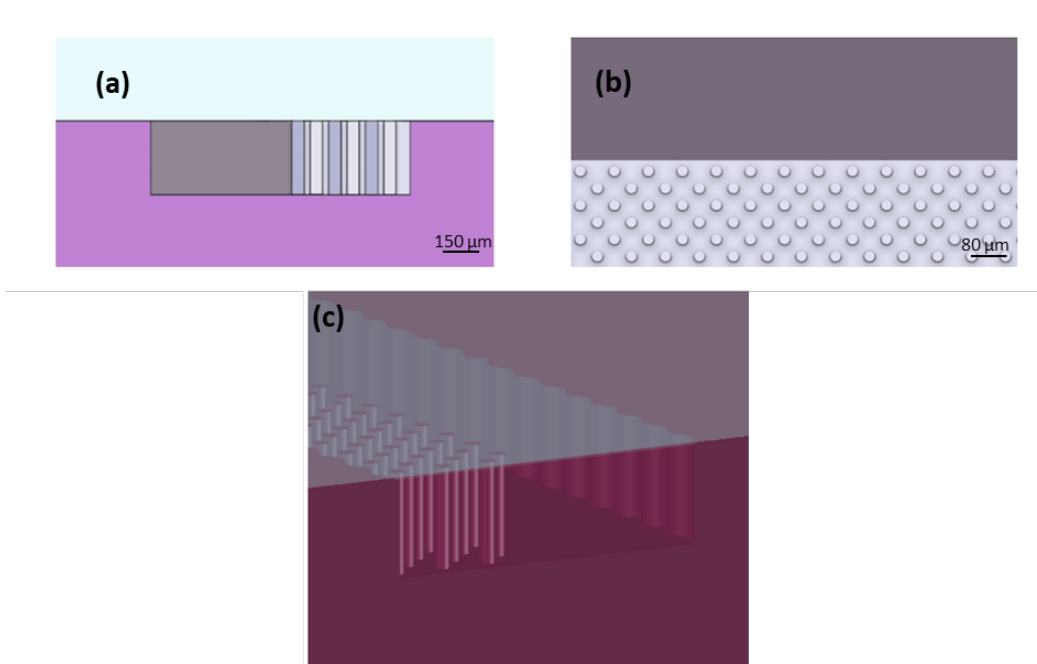


Figure 2-12 Cross section (a), top view (b), and 3D model (c) of a channel realized by using dry etching.

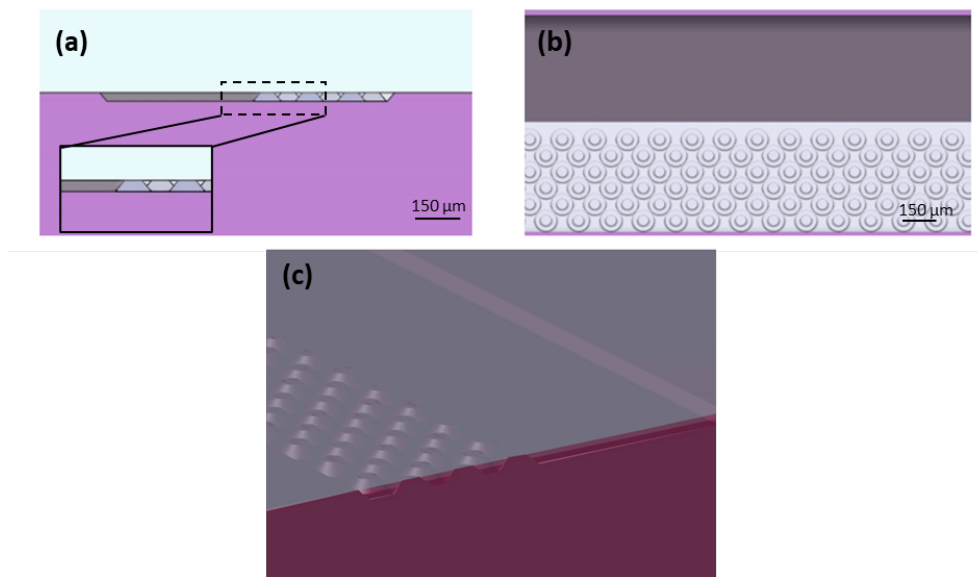


Figure 2-13 Cross section (a), top view (b) and 3D model (c) of a channel engraved by using wet etching.

Table 2-7 Reynolds and Weber numbers for the various designs proposed within the current work for a feed flow rate of 150 $\mu\text{L/h}$.

	Design	Tray 1	Tray 2	Tray 3	Tray 4	Tray 5
Re	Linear	1.261	0.559	2.263	2.202	1.413
	Zigzag	1.108	0.491	1.990	1.936	1.242
	Serpentine	0.127	0.056	0.229	0.223	0.143
We	Linear	0.426	0.338	0.220	0.218	0.211
	Zigzag	0.422	0.336	0.218	0.217	0.209
	Serpentine	0.029	0.023	0.015	0.015	0.014

However, as shown in the graphs below (Figure 2-14, Figure 2-15, Figure 2-16), the model suggests that all the designs initially created within this work, considering wet etching and truncated cones instead of pillars, are not able to satisfy the conditions for a stable interface according to all the used equations. ΔP_c curve intersects with all the gas-liquid pressure difference curves. It is because of the shallower depth compared to the designs of Lam *et al.* [24]. Indeed, the pressure drop of the gas is inversely proportional to the depth of the gas channel as shown in equation 2-34. Consequently, the smaller the depth of the channel, the higher the pressure drop per plate for the gas flow and the greater the risk of exceeding the capillary pressure and breaking the gas-liquid interface. Moreover, the designs proposed within this study failed to give a liquid time constant higher than 1 (Table 2-8). This means that the liquid phase does not have sufficient time to diffuse from the interface towards the edge of the channel before leaving the channel.

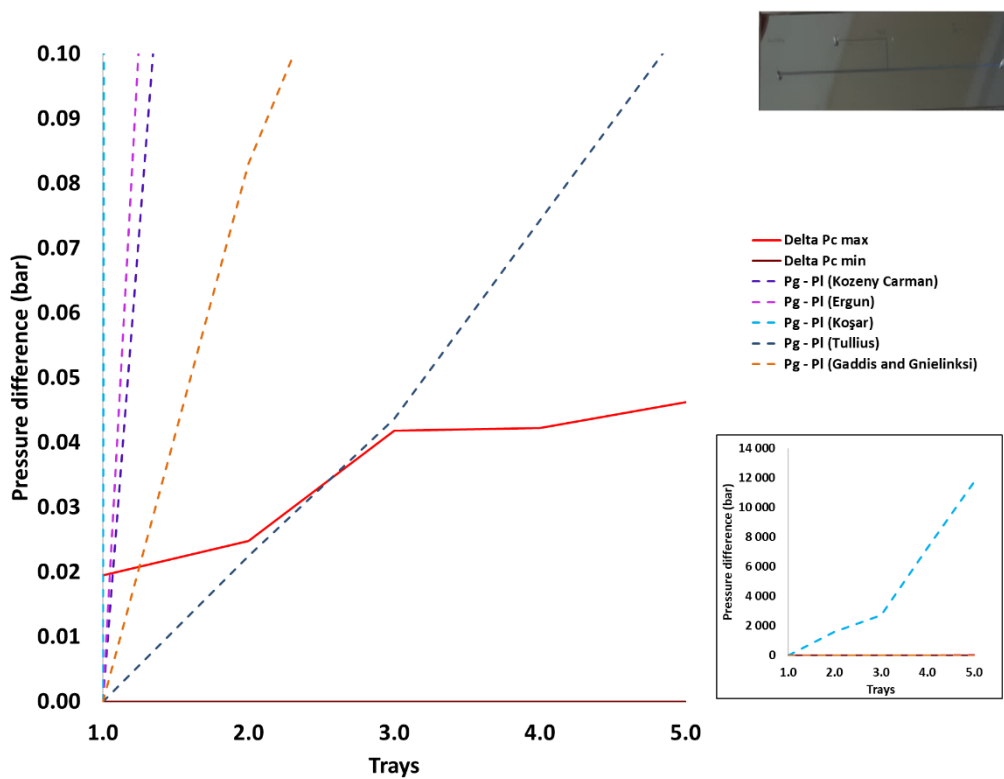


Figure 2-14 Graph showing the pressure difference between the two phases and the capillary pressure for the linear channel inspired from the literature (feed flow rate of 150 $\mu\text{L/h}$).

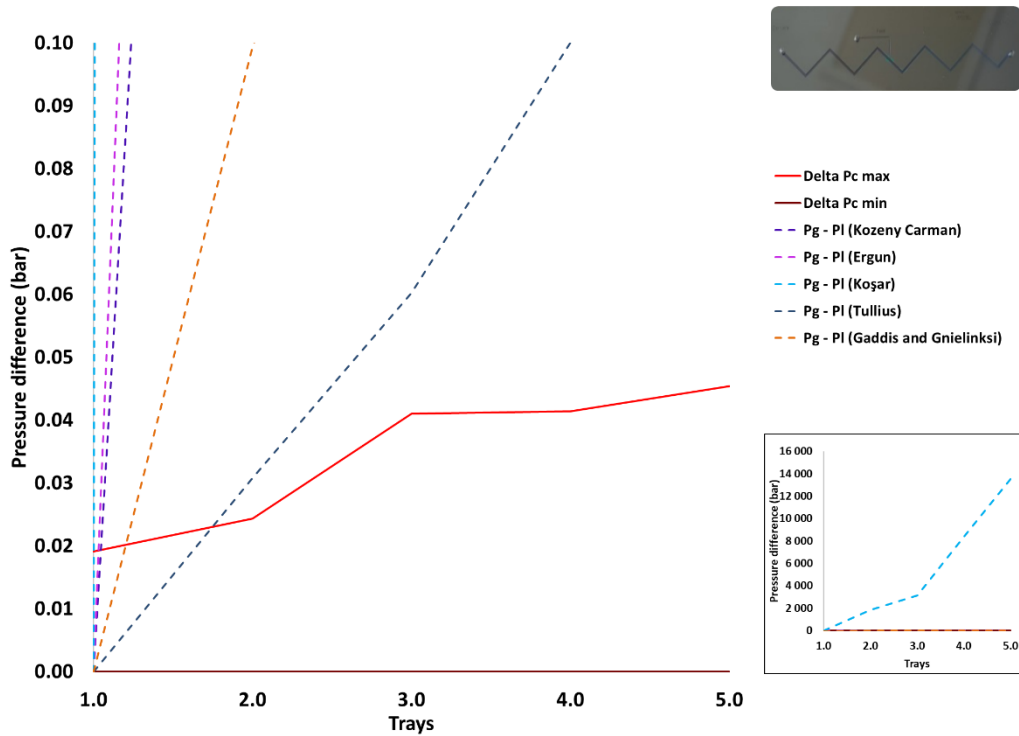


Figure 2-15 Graph showing the pressure difference between the two phases and the capillary pressure for the zigzag channel inspired from the literature (feed flow rate of 150 $\mu\text{L/h}$).

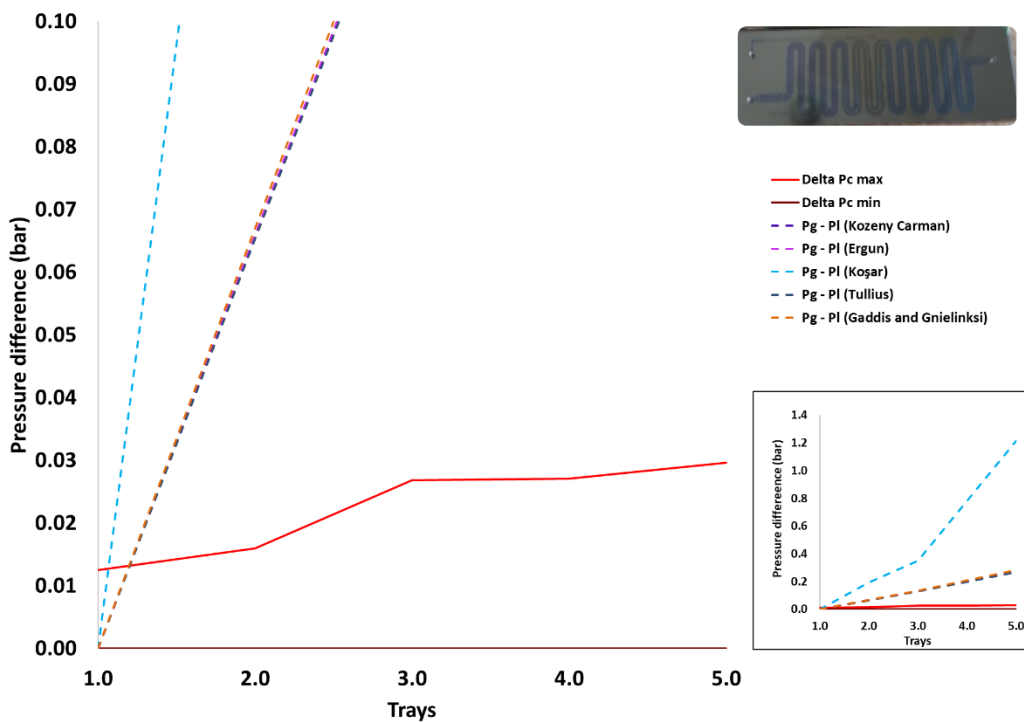


Figure 2-16 Graph showing the pressure difference between the two phases and the capillary pressure for the serpentine channel inspired from the literature (feed flow rate of 150 $\mu\text{L/h}$).

Table 2-8 Performance estimation of the different distillation channels suggested within the current work.

		Linear	Zigzag	Serpentine
Vapor	Residence time (s)	0.069	0.076	0.889
	Diffusion time (s)	0.016	0.011	0.056
	τ	4.23	6.81	15.80
Liquid	Residence time (s)	2.193	2.858	266.145
	Diffusion time (s)	42.025	46.225	1210.000
	τ	0.05	0.06	0.22

Unfortunately, for a wide range of channel dimensions and feed flow rates, it was not possible to find a single case that validates the previously illustrated conditions. Therefore, a new design able to be obtained with the current technology was developed.

6.5.5. New design

A new design was proposed to provide a high gain in the interfacial area between the gas and liquid aiming at reaching higher flow rates, while keeping the gas liquid pressure difference lower than the capillary one. The design consists of two superimposed gas-liquid channels rather than side by side. The liquid channel is provided with truncated cones of 50 μm diameter and spaced by 150 μm from center to center etched in a silicon wafer, whereas the gas channel was etched in a glass wafer (**Figure 2-17**).

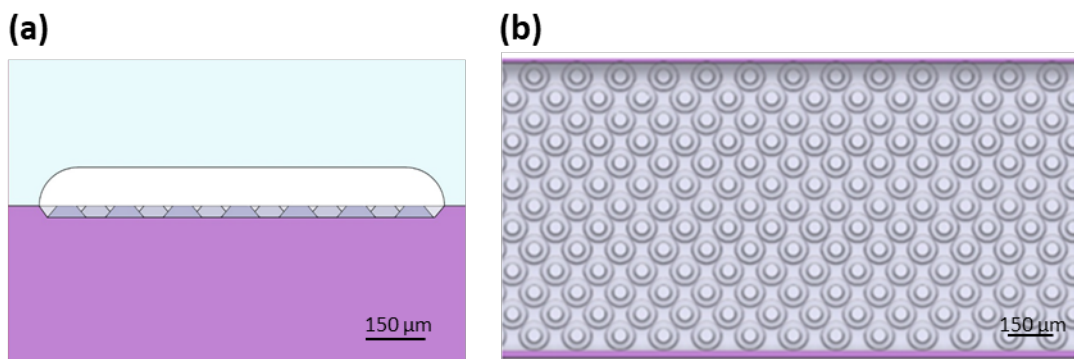


Figure 2-17 Cross section (a) and top view (b) of the new suggested design.

Both channels need to have the same length and approximately the same width but not necessarily the same depth. With this strategy, higher depth of channel could be achieved since the gas channel does not integrate micropillars. In this case, the gas-liquid interface is horizontal and no more vertical. The gain in interfacial area between both configurations for the channels dimensions of the benchmark case and those proposed in the current study is presented in **Table 2-9**. This proposed configuration offers a significant increase of the interfacial area compared to the literature design proposed by Lam *et al.* [24].

In the design proposed by Lam *et al.* [24], the gas-liquid interface is vertical and the vaporization is carried out from the side. The silicon pillars are very good heat conductor and provide the heat required to partially vaporize the liquid. However, within the current configuration the vaporization is achieved from above since the gas-liquid interface is horizontal. This is of high importance since in the

case of Lam *et al.* [24] it is probable that the thermal gradient in the liquid is low, because the liquid is heated on all sides by the silicon pillars that might be better for heat conduction than the liquid itself. On the other hand, in the current case the film thickness is low, so is the temperature gradient in the liquid. This allows to avoid the boiling limitation for both configurations.

Table 2-9: Gain in interfacial area for the proposed design compared to the literature one.

	Interfacial area (mm ²)		
	Side by Side (dry etching)	Superimposed (wet etching)	$Gain = \frac{Interfacial\ area\ superimposed}{Interfacial\ area\ side\ by\ side}$
Linear	18.0	36.6	2.0
Zigzag	24.3	42.4	1.7
Serpentine	240.0	740.0	3.1

By varying the feed flow rate and the channels' dimensions, a combination of geometrical variables that validates all the previous conditions was found. The suggested design is illustrated in **Figure 2-18**. The channel dimensions are summarized in **Table 2-10**.

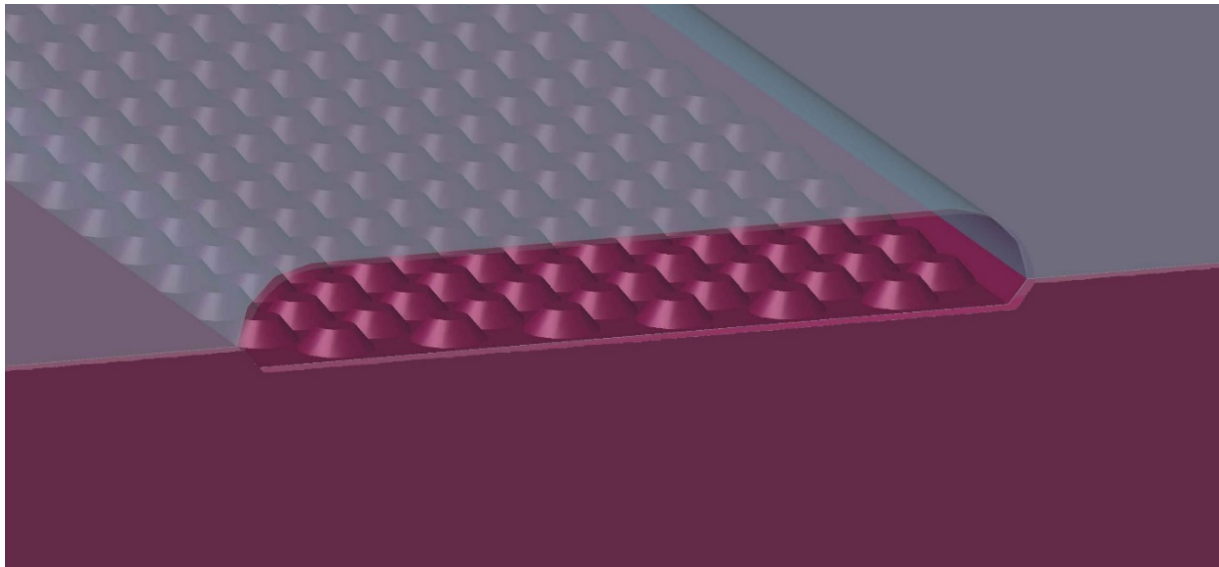


Figure 2-18 3D view of the two superimposed gas-liquid channels developed for the new design.

Table 2-10 Characteristics and dimensions of the proposed design.

Length	Width		Depth		Micropillar diameter	H/D	S _L /D	S _T /D
	Gas	Liquid	Gas	Liquid				
60 mm	1050 μm		100 μm	27 μm	50 μm	0.54	1.5	3

With this configuration the first and the second radius of curvature are equal to half the spacing between the micropillars. Since spacing is not equal, then the maximum spacing is taken into account which induces the minimum value of $\Delta P_{C_{max}}$. Additionally, since micropillars are not cylindrical, the wall

angle has to be considered when calculating $\Delta P_{c,max}$ (see **Figure 2-19**). Thus, this maximum capillary pressure is:

$$\Delta P_{c,max} = \frac{2\gamma \cos \delta}{a_\mu} \quad (2-39)$$

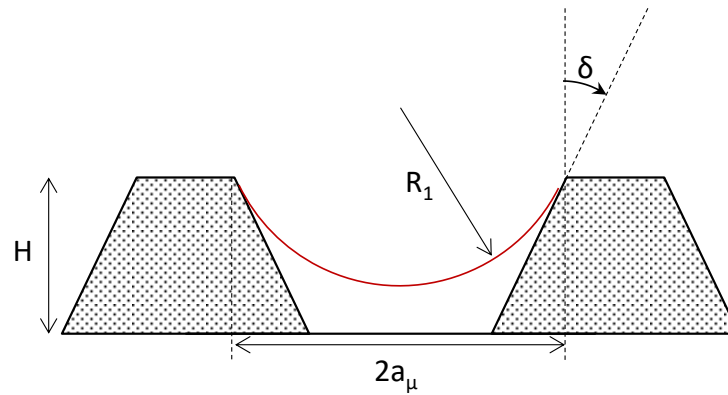


Figure 2-19 Gas-liquid interface relying between two truncated cone-shaped micropillars with the corresponding dimensions.

The estimated local pressures are shown in the graphs below (**Figure 2-20**, **Figure 2-21**, **Figure 2-22** and **Figure 2-23**) for various feed flow rates. The geometrical ratios of this design do not fit in the feasibility of all the correlations presented in **Table 2-1**, since the ratio H/D is lower than the unity. The S_T/D ratio fits only in the validity range of the correlation suggested Prasher *et al.* [64]. However, the Reynolds number as shown in **Table 2-11**, is out of the range of the Reynolds interval proposed by Prasher *et al.* [64]. Its maximum value is around 1 and this value does only fit in the range of validity of the correlation proposed by Gaddis and Gnielinski [65]. All the remaining correlations suggest at least a Reynolds number higher than 5.

In all cases, the correlation proposed by Koşar *et al.* [63] shows that the interface is not stable since the gas-liquid pressure difference intersects with the capillary pressure curve. The correlation proposed by Gaddis and Gnielinski [65] and Ergun model, failed to validate the condition of a stable interface for feed flow rates higher than 150 $\mu\text{L}/\text{h}$. However, all the other correlations show satisfying results for feeds flow rates up to 500 $\mu\text{L}/\text{h}$. Generally, from all these graphs, it can clearly be seen that the condition of a stable interface is validated for feed flow rates up to 500 $\mu\text{L}/\text{h}$. The corresponding times constants for both flow rates are presented in **Table 2-12** and show satisfying results. For all the tested feed flow rates, the time constants of both phases are higher than 5.

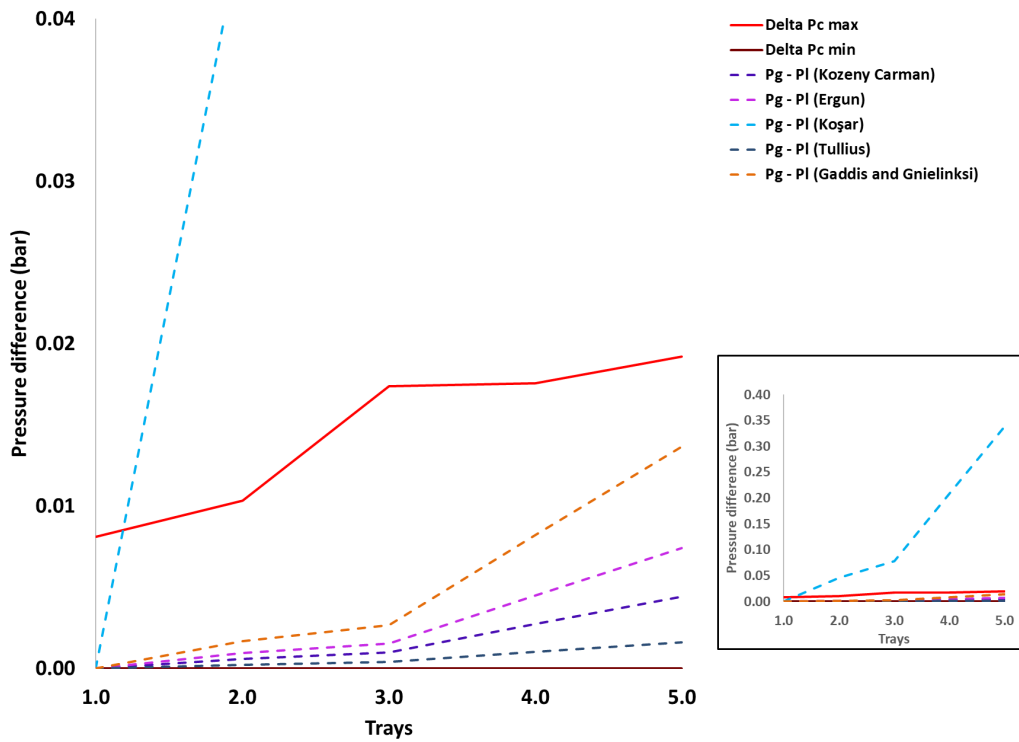


Figure 2-20 Graph showing the pressure difference between the two phases and the capillary pressure all along the microchannel for the proposed design at a feed flow rate of 150 $\mu\text{L/h}$.

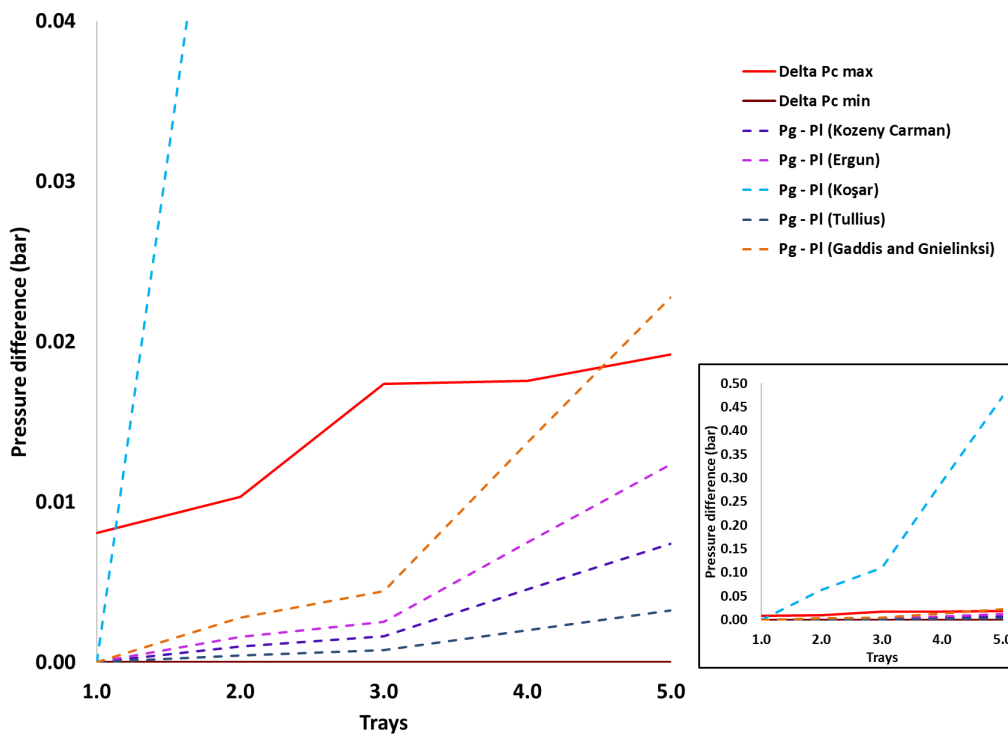


Figure 2-21 Graph showing the pressure difference between the two phases and the capillary pressure all along the microchannel for the proposed design at a feed flow rate of 250 $\mu\text{L/h}$.

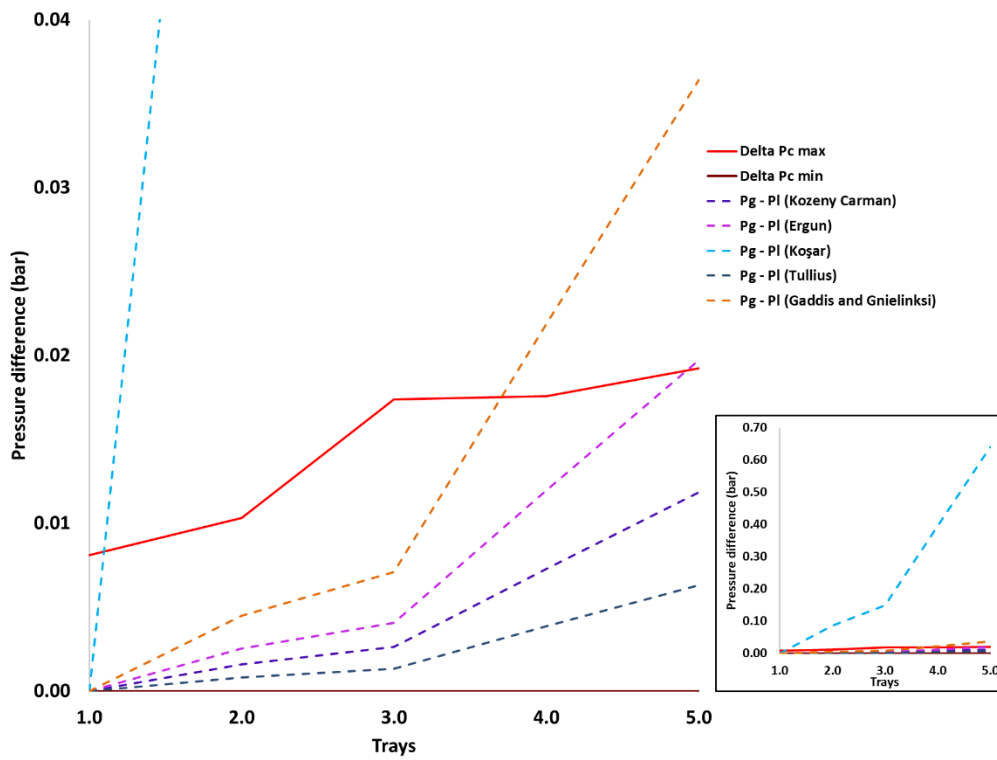


Figure 2-22 Graph showing the pressure difference between the two phases and the capillary pressure all along the microchannel for the proposed design at a feed flow rate of 400 $\mu\text{L/h}$.

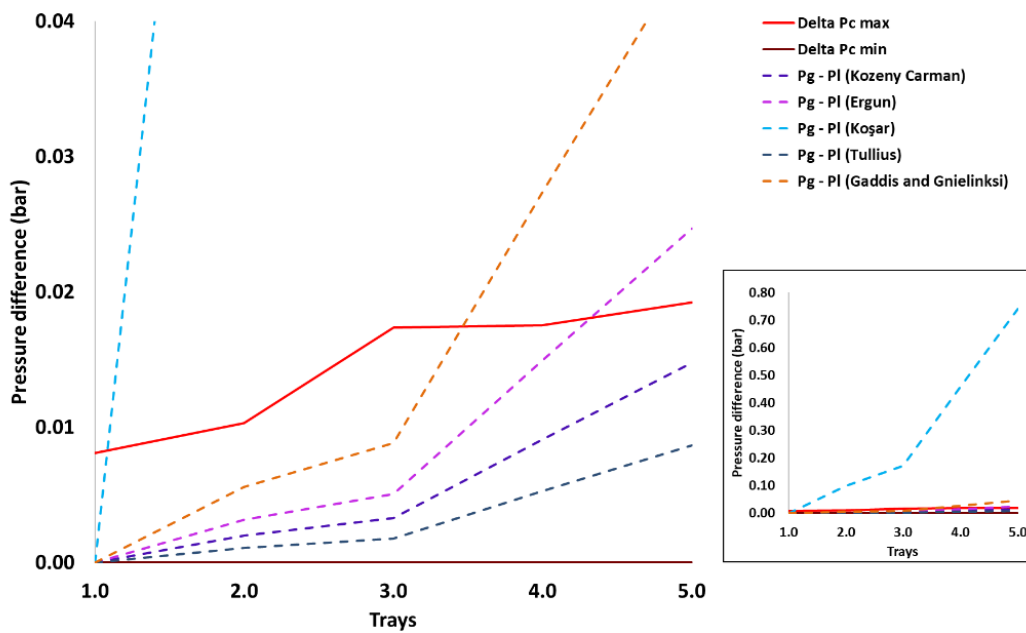


Figure 2-23 Graph showing the pressure difference between the two phases and the capillary pressure all along the microchannel for the proposed design at a feed flow rate of 500 $\mu\text{L/h}$.

Table 2-11 Reynolds and Weber numbers calculated for the superimposed gas-liquid design.

	Flow rate	Tray 1	Tray 2	Tray 3	Tray 4	Tray 5
Re	150 $\mu\text{L/h}$	0.181	0.080	0.324	0.316	0.203
	250 $\mu\text{L/h}$	0.301	0.133	0.541	0.526	0.338
	400 $\mu\text{L/h}$	0.482	0.214	0.865	0.842	0.540
	500 $\mu\text{L/h}$	0.602	0.267	1.081	1.052	0.675
We	150 $\mu\text{L/h}$	0.009	0.007	0.005	0.004	0.004
	250 $\mu\text{L/h}$	0.024	0.019	0.013	0.012	0.012
	400 $\mu\text{L/h}$	0.062	0.049	0.032	0.032	0.031
	500 $\mu\text{L/h}$	0.097	0.077	0.050	0.050	0.048

Table 2-12 Time constants for gas and liquid phases flowing in a superimposed channels configuration for various feed flow rates.

		150 $\mu\text{L/h}$	250 $\mu\text{L/h}$	400 $\mu\text{L/h}$	500 $\mu\text{L/h}$
Vapor	Residence time (s)	0.691	0.415	0.259	0.207
	Diffusion time (s)	0.001	0.001	0.001	0.001
	τ	691.39	414.83	259.27	207.42
Liquid	Residence time (s)	31.047	18.628	11.643	9.314
	Diffusion time (s)	0.729	0.729	0.729	0.729
	τ	42.59	25.55	15.97	12.78

Additionally, as shown in **Table 2-11**, all the calculated Weber numbers are lower than unity confirming that no liquid entrainment is expected.

Since the calculations demonstrate that the system is potentially functional, this 3D configuration was chosen to pursue this work. The design has been microfabricated for both hydrodynamic and microdistillation studies. For each study, two masks are needed: one for the liquid phase to be etched on a silicon wafer and the other for the gas phase to be etched on a glass wafer. In the next section, the microfabrication procedure is introduced.

7. Microfabrication

7.1. Introduction

Various microfabrication technologies exist and differ mainly by the type of the substrate and their manufacturing process. However, the choice of the microfabrication technology depends essentially on the goal of the study, more precisely on the chemical compatibility of the device with the selected solvents and the desired operating conditions in terms of pressure and temperature.

Polymer-based microdevices are the most encountered because of a low microfabrication cost compared to other technologies. The most considered polymers are the poly(dimethylsiloxane) (PDMS) or the poly(methylmethacrylate) (PMMA). However, these devices have very low chemical compatibility and do not resist to high pressure and temperature conditions ($p < 0.2 \text{ MPa}$, $T < 100^\circ\text{C}$) [74,75].

A better chemical compatibility is obtained by developing microdevices from glass/glass or silicon/Pyrex (Si/Pyrex) substrates. The former withstand pressure and temperature conditions up to 10 MPa and 150°C, respectively [76,77]. The main drawback is the low heat transfer efficiency under high temperatures. Oppositely, the latter system resists to high pressure and temperature conditions ($p < 20$ MPa and $T < 400^\circ\text{C}$) and offers high heat transfer performances [78–82].

Since chemical compatibility and temperature control are critical parameters in distillation processes, the chosen system is obviously made of Si/Pyrex substrates. Accordingly, the Si/Pyrex microfabrication technology will be detailed in this chapter.

7.2. Materials

7.2.1. Wafers

The wafers used to manufacture the microdistillation are made of two types: silicon and Pyrex. They are all purchased from the BT Electronics company.

Silicon wafers are 1000 ± 25 μm thick and have a diameter of 4 inches. The surface (both sides) of these wafers is coated with a 500 nm thick PECVD-grown silica layer.

Pyrex wafers are 2000 ± 50 μm thick and are coated with a 20 nm thick chrome layer covered by a 100 nm thick gold layer on both sides which will be used as protective layers during the etching process.

7.2.2. Chemicals

All the characteristics of the considered reagents are shown in **Table 2-13**.

Table 2-13: Reactants' specifications

Product Name	Company	Composition	Comments
MICROPOSIT™ S1818™ Positive Photoresist	Dow	Propylene glycol methyl ether acetate	
Microposit™ MF-319	Dow	TMAH, water, polyalkene glycol	
Tetramethylammonium hydroxide (TMAH)	Sigma aldrich	TMAH, water	25 wt.% in water
Buffered oxide etch (7:1)	VWR	Ammonium fluoride, hydrofluoric acid	
Sulfuric acid	EMSURE	Sulfuric acid	95-97 % purity
Hydrogen peroxide	Scharlau	Hydrogen peroxide	35% v/v
Triton X-100	Sigma aldrich	Polyethylene glycol tertoctylphenyl ether	Laboratory grade
Isopropanol	Alfa Aesar	Isopropanol	>99 % purity
Acetone	Xilab	Acetone	
Ethanol	Xilab	Ethanol	96 % purity
Gold etching	Sigma aldrich	Potassium iodide iodine	>99.0% 99.999% trace metal basis
Chrome ETCH 18	Dow		
HF		Hydrofluoric acid	40%

7.2.3. Instruments

All the involved instruments in the microfabrication process are summarized in **Table 2-14**.

Table 2-14: Instrument's specifications.

Instrument name	Company	Function	Comment
POLOS200 spin coater + vacuum pump	SPS-Europe incorporation	Spin coating	
UV-KUB 2	Kloé	Exposure and masking system	Insolation wavelength of 365 nm Resolution of 2 µm
Fisherbrand™ Isotemp™ Advanced Stirring Hotplate	Fisher Scientific	Wet etching	
Sandblaster	Arena C60	Drill inlet and outlet holes	
Oven	Nabertherm P300 model	Oxidation	heating capacity up to 1200°C
Eurotherm temperature controller + electrical tension system	Eurotherm +Bfi OPTILAS	Anodic bonding	home-made anodic bonding system
Die saw IsoMet™ 4000	Buehler	Cutting	

7.2.4. Si/Pyrex based microdevices

A schematic view of the microfabrication process based on silicon etching is illustrated below (**Figure 2-24**). It consists of three main steps: photolithography, chemical etching and finally reoxidation and anodic bonding.

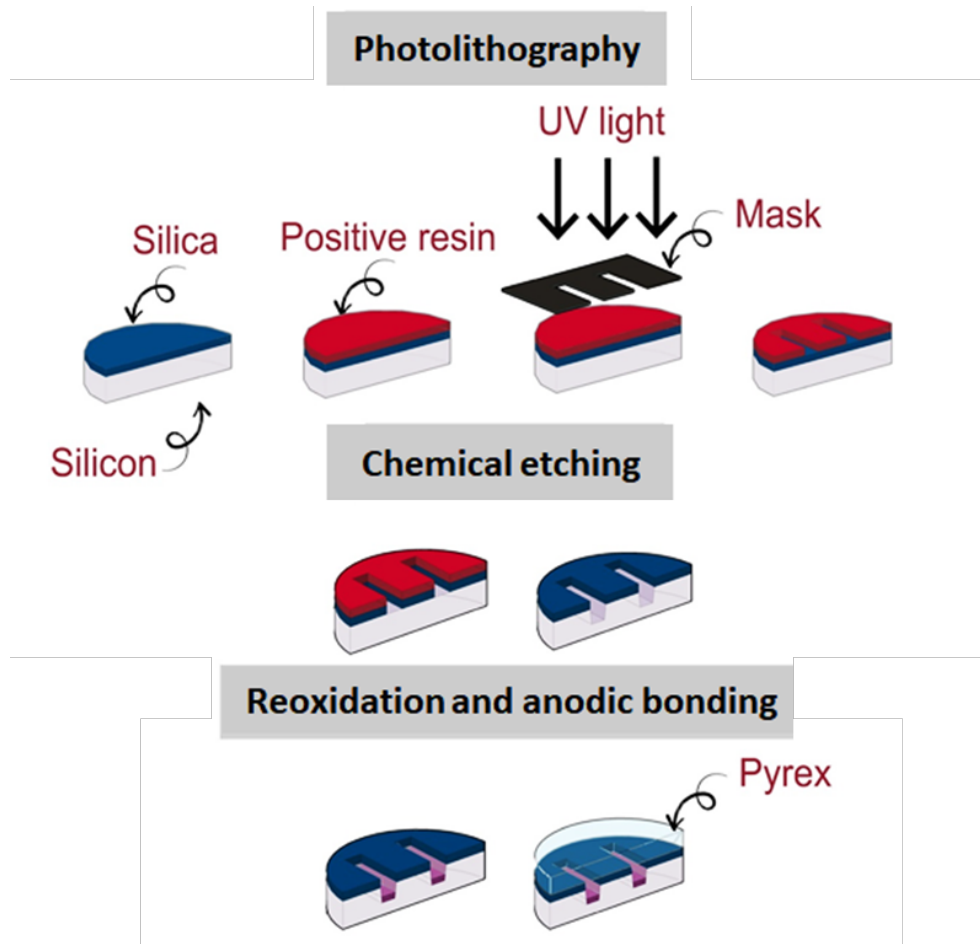


Figure 2-24 Different steps of a Si/Pyrex microfabrication process.

7.2.5. Silicon wafer preparation

Step 1: Photolithography

The SiO₂-coated silicon wafer must be well cleaned with isopropanol and ethanol then dried to eliminate any dust particles that could potentially alter the photolithography process. Consequently, a positive photoresist, is spread uniformly on one side of the wafer by using a spin coater and a vacuum pump. This photoresist is highly sensitive to ultraviolet radiation. A spin speed of 1200 rpm at a ramp of 500 rpm/s during 30 s leads to the deposition of a 4 μm thick film of photoresist. The wafer is then placed during 5 min on a hot plate, previously heated to a temperature of 115°C, aiming at rigidifying the created layer by eliminating the amount of solvent remaining in the photoresist. Consequently, the desired pattern is printed on the photoresist layer by shining a UV light source through an optical plastic mask stick to a transparent support. The used UV device is a UV-KUB 2 that emits light at a wavelength of 365 nm during 45 s. The pattern on the mask is designed using AutoCad 2018 software.

Development is then made by immersing the wafer in a solution of developer for a fixed duration (approximately 30 s). The developer dissolves the positive exposed photoresist that will be further eliminated by rinsing with a developer solution. Thereafter, the wafer is rinsed with deionized water, dried and finally baked during 6 min at 115°C for both, excess solvent removal and film hardening. In this work, the photoresist is MICROPOSIT™ S1818™ Positive Photoresist and its associated developer is Microposit™ MF-319.

Step 2: Chemical etching

At this stage, the desired pattern can be clearly observed on the wafer since the resin is only covering the areas that do not have to be etched. Thereafter, the wafer, placed in a Teflon crystallizer, is exposed to a buffered oxide etching HF solution that selectively removes the exposed oxidized silicon. This step must be done delicately since HF have to be deposited only on the zones to be engraved. Once done, the wafer is rinsed abundantly with deionized water. The remaining resin is then removed using acetone. The wafer is then washed with ethanol and eventually dried with compressed air.

Finally, the wafer must be etched. To do so, it is placed in an etching solution bath previously heated and constantly agitated. This technique is known as wet etching. The solution etches selectively silicon and the etching rate is not the same for all the crystalline planes [83]. Hence, the obtained pattern has a trapezoidal cross-section. Based on **Figure 2-25**, the width of the channel at a fixed depth can be estimated by assuming that the angle between the silicon crystal planes <100> and <111> is worth 54.7° ($w_{bottom} = w_{top} - \frac{2*d}{\tan(54.7^\circ)}$). This etching technique is known as an “anisotropic wet etching”. It is necessary to mention that in some cases, the etching depth is limited because of this technique. For example, if the top width is 100 μm, then the maximum allowed depth is around 50 μm. In this work, the chosen etching solution is a tetramethylammonium hydroxide (TMAH) (25 wt.% water) with one drop of Triton X100 surfactant that decreases the etching rate but leads to a more uniform and clean etching process. Etching time depends on the desired depth as well as the etching rate that controlled by the bath temperature. For a temperature of 84°C, the etching rate is about 28 μm/h. The etched depth is then measured using a mechanical profilometer instrument (Veeco).

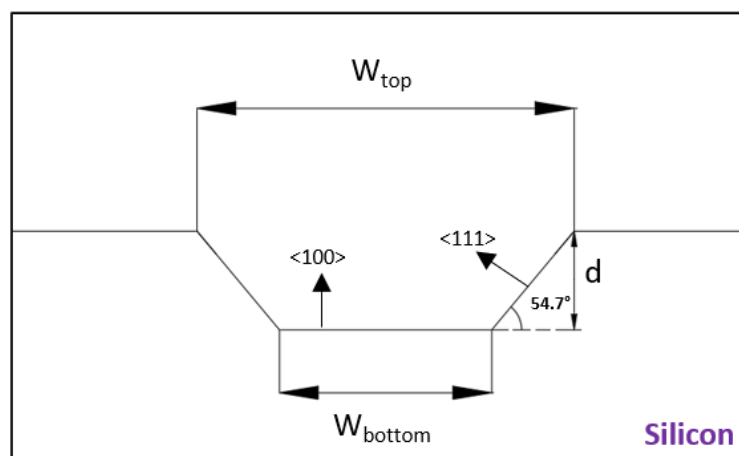


Figure 2-25 Microchannel's cross sectional view on a silicon substrate.

It is interesting to mention that multilayered structures could be obtained by oxidizing the etched wafer and repeating the previously detailed process with an accurate alignment of the photomask.

7.2.6. Pyrex etching

The Pyrex etching process is similar to the silicon one. In fact, the first three steps (spin coating, photolithography and development) are the same as for the silicon wafer. However, the parameters of the insolation must be adjusted to stick with the Pyrex thickness. The different steps of the process are illustrated in **Figure 2-26**. After the developing and heating step, the gold and chromium layer underlying the previously removed resin must be eliminated. The gold is removed by using a gold etching solution made of 4 g of potassium iodide, 1 g of iodine and 40 mL of deionized water. The gold etching solution is deposited on the wafer with a pipette. The etching time is of approximately 5 mins. Thereafter, the wafer is rinsed with deionized water and dried with compressed air. The chromium layer is then removed by putting drops of the chromium etching solution on the wafer during 5 mins. The wafer is then rinsed again with deionized water and dried with compressed air.

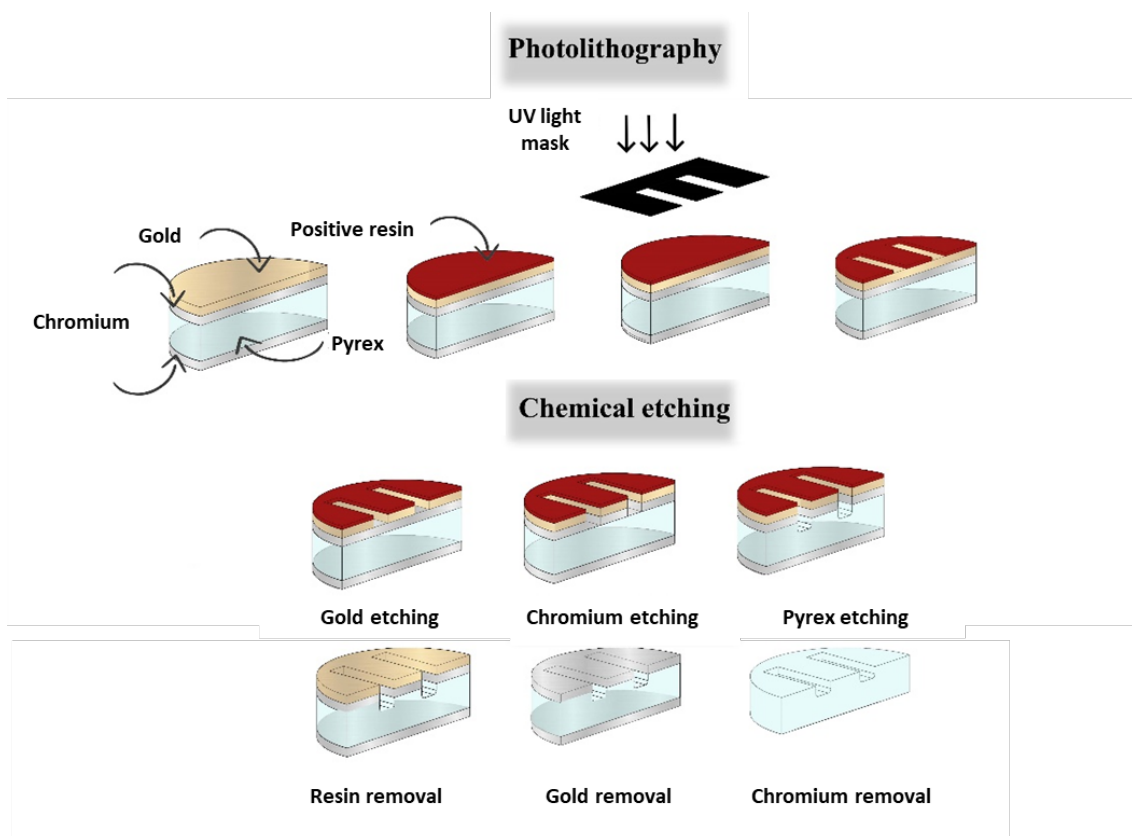


Figure 2-26 Pyrex etching process.

At this stage, the glass must be etched. It is achieved by using a 40% concentrated hydrofluoric acid (HF). After putting on the appropriate safety coverall, gloves and face shield for HF, the wafer is placed in a Teflon crystallizer. The HF solution is set on the desired region and the etching is done at a rate of 1 $\mu\text{m}/\text{min}$ approximately. As for the silicon etching process, the reaction time depends on the needed depth. Additionally, the etching rate is highly sensitive to the HF concentration. The wet etching of glass by hydrofluoric acid is an isotropic process. The resulting microchannel has rounded sidewalls. A schematic cross section of a glass etched microchannel is shown in **Figure 2-27**. Once finished, the wafer is abundantly rinsed with water. The resin is then eliminated by rinsing the wafer with acetone

and water. Thereafter, the gold and chrome layers on both sides are removed by immersing the wafer in the gold and chrome etching solution consecutively for 15 mins each. The wafer is rinsed with water and dried with compressed air between the removal of gold and chrome layers. The etched depth can be measured using a mechanical profilometer instrument.

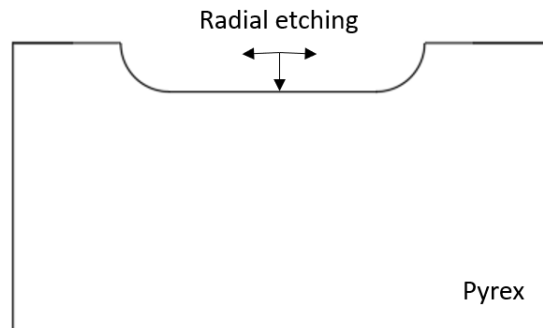


Figure 2-27 Microchannel's cross sectional view on a glass substrate.

Step 3: Sandblasting, oxidation, and anodic bonding

The inlets and outlets are drilled on the silicon wafer using a sandblasting machine under a pressure of 6 bar.

Thereafter, the silicon wafer is oxidized to ensure similar wetting properties of the final microchannel. The oxidation process consists in placing the wafer in an oven that will be heated up to 1000°C during 40 min, then the wafer will remain at 1000°C for 3 h with a continuous injection of water at a rate of 1 mL/h to saturate the atmosphere of the oven with water vapor. Consequently, the oven temperature gets back to the ambient temperature within 10 h. A well-done oxidation is confirmed by an obvious change of the wafer's color, which is associated with the growth of approximately a 200 nm thick silica layer.

Finally, a glass wafer is bonded to the silicon one by anodic bonding. To do so, both wafers must be well cleaned. This is done by dipping each wafer in a piranha solution composed of 35 mL of sulfuric acid and 15 mL of hydrogen peroxide during 15 min. The reaction, which takes place when the two solutions are mixed, is highly exothermic. Stirring at the beginning is required to improve the mixing of the two solutions and results in a better cleaning.

Once cleaned, both wafers are rinsed with deionized water and ethanol and then dried. A drop of water is deposited on the middle of each wafer and they are then aligned and pressed together. This step is known as pre-bonding. Then, these wafers are placed between two plates heated to 400°C (**Figure 2-28**). Once the temperature is well stabilized, the heating is stopped and an electrostatic field is applied step wisely between the wafers. In fact, the applied voltage is increased by 100 volts at a time from 250 till 1250 volts, when the electric current is stable. From a safety point of a view, the electric current should not exceed, in any case, 8 mA. Once done, the electrical voltage is shut down and the wafers are again heated to 400°C. This process is repeated 3 times to guarantee a successful bonding. Finally, the wafer stack is cooled down.

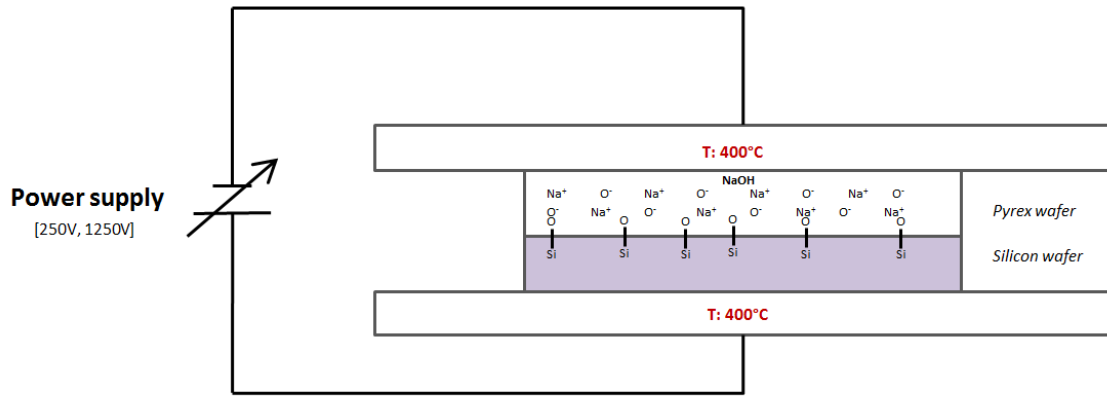


Figure 2-28 Schematic view of the anodic bonding system.

Step 4: Cutting

The last step consists in cutting the wafer into chips by using a die saw, hence the microchips (Figure 2-29) are ready to be used in the experimental setup.



Figure 2-29 Microchip illustration of the innovative desing.

The different dimensions of the chips developed within this work are recapitulated in Table 2-15.

Table 2-15 Dimensions and cofigurations of the different chips designed within this study.

	Dimensions
<p><u>Configuration 1:</u></p>	<p>Width: 1000µm</p> <p><u>Gas channel</u></p> <p>Length: 8 cm</p> <p>Depth: 100 µm</p> <p><u>Liquid channel</u></p> <p>Length: 8 cm</p> <p>Depth: 27 µm</p> <p><u>Injection line:</u></p> <p>Width: 1000 µm</p> <p><u>Micropillars</u></p> <p>Diameter: 50 µm</p> <p>Spacing: 150 µm</p>
<p><u>Configuration 2:</u></p>	<p>Width: 1000µm</p> <p><u>Gas channel</u></p> <p>Length: 6 cm</p>

<p style="text-align: center;">Liquid mask for distillation experiments, 1000μm width</p>	<p>Depth: 100 μm <u>Liquid channel</u> Length: 8 cm Depth: 27 μm <u>Injection line:</u> Width: 1000 μm <u>Micropillars</u> Diameter: 50 μm Spacing: 150 μm</p>
<p><u>Configuration 3:</u></p>	<p>Width: 1000μm <u>Gas channel</u> Length: 6 cm Depth: 100 μm <u>Liquid channel</u> Length: 8 cm Depth: 27 μm <u>Injection line:</u> Width: 75 μm <u>Micropillars</u> Diameter: 50 μm Spacing: 150 μm</p>

7.3. Packaging and connections

Once the chips are ready to be used, they must be connected to the injection and withdrawal pumps. For Si/Pyrex systems, many types of connections are possible such as nanoport fixed with epoxy glue, capillary tubes and many others. However, the device is designed to distill chemical mixtures of high boiling temperatures. Therefore, the main limitations of using the nanoport fixed with epoxy glue is the chemical incompatibility of the glue with a wide range of chemical products mainly acetone, and the low temperature resistant. Moreover, both connections methods (nanoport and capillary tubes) are irreversible: once connected to the chip, they cannot be isolated anymore. The goal was to handle a compact packaging method that is thermal and chemical resistant. The solution is the use of compression parts, that consists of two pieces holding one edge of the chip and bolted together. The sealing between the chip and the compression parts is obtained by using O-rings sealing. The compression parts can be made of several material according to the operating conditions of the target application. They can be easily connected and disconnected to the chip. The possible connections are shown in **Figure 2-30**.

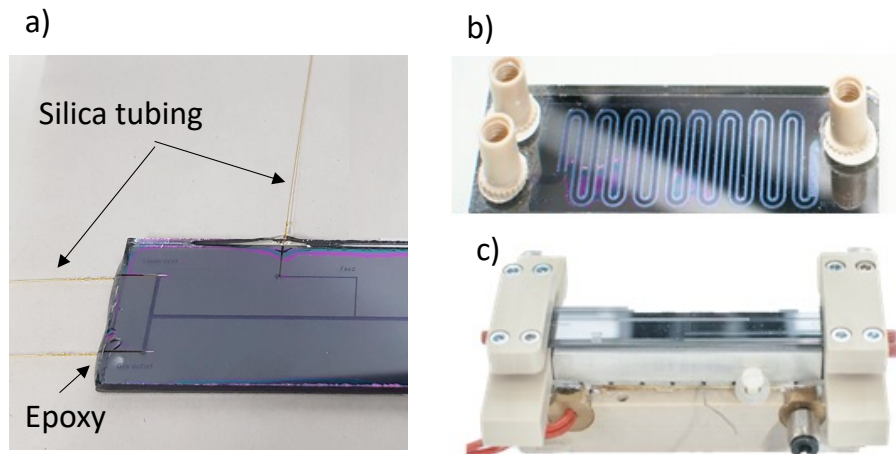


Figure 2-30: Microchip's connections ((a) silica tubing, (b) nanoport, (c) compression parts).

8. Conclusion

The design principles when dealing with counter-current gas-liquid flows in microchannels were exposed within this chapter. The challenge relies in maintaining a stable interface for a counter-current gas-liquid flow. It consists of having, at each location inside the channel, a gas-liquid pressure difference ranging between a minimum and a maximum value of capillary pressure. Accordingly, a range of operating conditions, more specifically, a maximum feed flow rate above which the gas-liquid interface would be broken, could be defined. The different strategies for the determination of the operating conditions and the estimation of the device performances published in the literature were briefly reviewed.

The gas pressure drop within this work was estimated based on Hagen-Poiseuille equation. Concerning the liquid pressure drop in the micropillar region, several researchers have tried to establish a correlation for the prediction of the friction factor. Some of these correlations were reviewed in this chapter along with their operating range. Consequently, the liquid pressure drop within this study was estimated based on several of these correlations.

The fluid properties were obtained from a case study run using the Pro II software and the different simulation results were illustrated. The primary results concern a benchmark case that presents promising distillation performances. Inspired from the channels' geometry, an innovative design made of two superimposed gas-liquid channels was suggested. The numerical applications in terms of pressure drops and time constants have shown successful results. To experimentally prove these simulation results, the microdistillation was then microfabricated.

As in the current case, the microchannel is designed to be used in distillation which is a thermal separation process; thus, the chip must be characterized by a good heat transfer and a broad chemical compatibility. Therefore, the device was chosen to be manufactured using Si/Pyrex systems. Hence, the Si/Pyrex microfabrication process was described briefly. The device is connected to the experimental setup by using compression parts that are compatible with wide range of chemical products, withstand high temperature and are reusable.

The next chapter will deal with the experimental work on studying the hydrodynamics of the liquid flow within the developed chips.

1. Introduction

Along with the development in the field of microfluidics and the complexity of the designed systems, it is necessary to understand the fluid mechanics taking place within a newly design microchip. Particularly, it is important to determine the dispersion of the liquid within the micropillars region, the presence or absence of liquid dead volumes, preferential paths, as well as the gas-liquid mass transfer coefficients within the developed microdistillation. These hydrodynamics results must be related to the separation performance of the device in order to optimize the design.

To do so, experimental measurements allowing flow visualization and characterization are performed. Residence time distribution (RTD) is the chosen technique to get insights in two-phase flows within a microdevice. It is one of the most precious tools to study the continuous flow systems.

2. RTD measurement methodology

Residence time distribution measurements are used to characterize the overall flow behavior of a reactor [84]. Two different types of fluid reactor models are mainly identified by RTD measurements. The first one is the plug flow model assumed in a tubular-shape reactor (PFR) whereas the second one is the perfect mixing model in continuous stirred tank reactors (CSTR). In the former, the fluid molecules exit the reactor exactly the same way they enter into it, without any mixing with those in front and behind. In the latter, once the fluid is fed into the reactor, it is instantly perfectly mixed so that the composition of the fluid at the outlet and within the reactor are the same. These two models happen only in ideal reactors. In real cases, the model deviates from the ideality and the reactor is rather considered as real reactor. The residence time distribution curves for the different flows are illustrated in **Figure 3-1**.

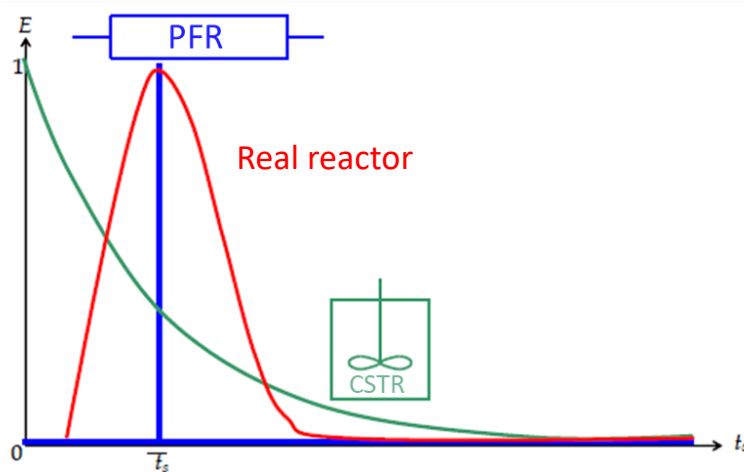


Figure 3-1 Residence time distribution curves for the various reactor types.

Additionally, RTD theory enables the determination of the axial dispersion within the system when considering plug flow behavior. Thus, the most suitable geometry to a defined application can be selected based on RTD measurements.

The principle of operation consists of feeding the microdevice with a defined volume and concentration of a non-reactive tracer. The tracer output signal is then recorded at the outlet of the microdevice. The inlet and outlet RTD curves for the two different types of tracer injection are illustrated in **Figure 3-2**. By measuring this signal, the residence time distribution is established, and the axial dispersion can be computed. A noteworthy information is that the tracer should not alter the physical properties of the fluid (equal density, equal viscosity) or the hydrodynamic conditions.

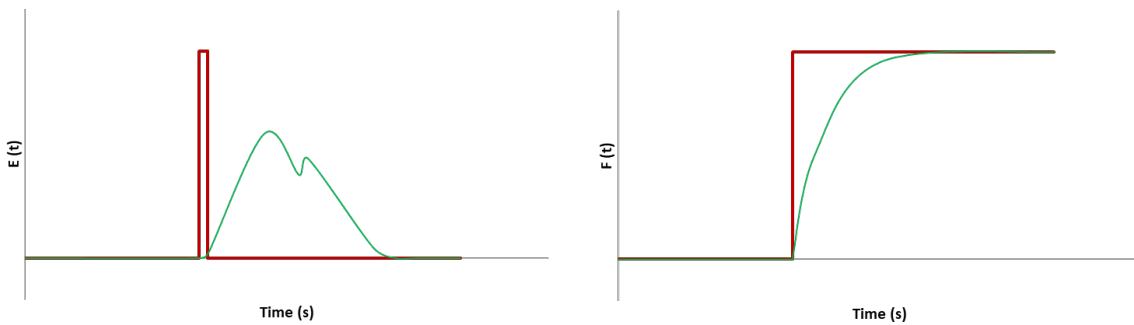


Figure 3-2 Inlet (red) and outlet (green) curves for a pulse (left) and a step (right) RTD measurement.

For a pulse signal, the distribution function $E(t)$ is defined as follows:

$$E(t) = \frac{C(t)}{\int_0^{\infty} C(t) dt} \quad (3-1)$$

$$\mu_n = \int_0^{\infty} t^n E(t) dt \quad (3-2)$$

where C stands for the liquid concentration.

However, when dealing with a step function instead of a pulse one, a new function is defined which is the cumulative RTD function denoted $F(t)$. This function can be calculated as follows:

$$F(t) = \frac{C(t)}{C_{\infty}(t)} \quad (3-3)$$

The relation between a step function and the cumulative function is illustrated below:

$$E(t) = \frac{dF(t)}{dt} \quad (3-4)$$

These functions have the usual properties of distribution functions, specifically the distribution moments. These moments denoted ' μ ' are recapitulated in **Table 3-1**. The first order moment is related to the mean residence time, whereas the second order moment is related to the variance.

Table 3-1 Moments of the dirac and step residence time distribution functions [84].

Moments of order	Dirac/pulse function	Step function
n	$\mu_n = \int_0^{\infty} t^n E(t) dt$	$\mu_n = \int_0^{\infty} nt^{n-1} (1 - F(t)) dt$
1	$\mu_1 = \int_0^{\infty} t E(t) dt$	$\mu_1 = \int_0^{\infty} (1 - F(t)) dt$
2	$\mu_2 = \int_0^{\infty} t^2 E(t) dt$	$\mu_2 = \int_0^{\infty} 2t(1 - F(t)) dt$

The variance σ^2 between the inlet and outlet can be estimated based on the equation below:

$$\sigma^2 = (\mu_2 - \mu_1^2)_{in} - (\mu_2 - \mu_1^2)_{out} \quad (3-5)$$

Consequently, the residence time of the liquid ($t_{res, in \rightarrow out}$) the Peclet number ($Pe_{in \rightarrow out}$) and the axial dispersion coefficient ($D_{ax, in \rightarrow out}$) between the inlet and outlet can be computed as follows:

$$t_{res, in \rightarrow out} = \mu_{1, out} - \mu_{1, in} \quad (3-6)$$

$$Pe_{in \rightarrow out} = 2 * \frac{t_{in \rightarrow out}^2}{\sigma^2} \quad (3-7)$$

$$D_{ax, in \rightarrow out} = \frac{U_i * d'}{Pe_{in \rightarrow out}} \quad (3-8)$$

where d' is the distance between the inlet and outlet and U_i is the superficial inlet velocity.

3. Experimental setup

A special design of the distillation chip was developed to investigate the RTD experiments. It consists only of a single liquid channel etched on the silicon wafer, without neither the lateral injection line nor the gas channel (**Figure 3-3**). This configuration was chosen to study the liquid dispersion and residence time within the micropillar region and avoid the passage of the liquid into the gas channel.

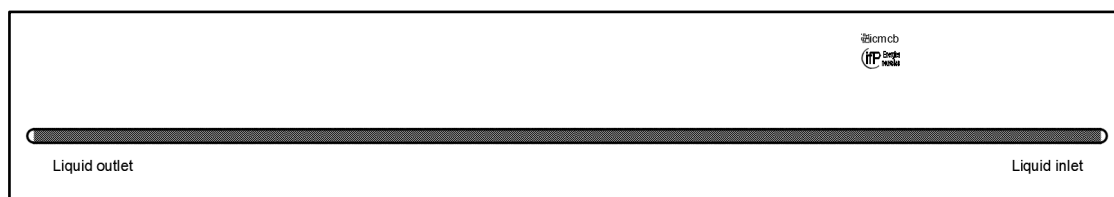


Figure 3-3 Mask used to manufacture the chips dedicated for the RTD experiments.

A preliminary study was carried out to define the suitable method for the RTD experiments. To determine the RTD within a controlled volume, pulse or step experiment could be used. The first one requires the injection of a small volume (~1% of the reactor volume) of concentrated tracer at the inlet of the reactor. The second type of experiments consist of abruptly changing the concentration of the tracer at the inlet of the reactor from 0 to C_0 (maximum concentration of the tracer). Since the volume of the channel is 1.2 μL , using pulse experiments seems to be complicated and not reproducible because of the injection of a very small amount of tracer. Therefore, step experiments are chosen for the current study.

The first approach was to attempt residence time distribution experiments with the setup illustrated in **Figure 3-4**, with probes for inlet and outlet signal acquisition positioned in the connecting capillaries. However, it appeared that the cumulated dead volume is 48 μL , much higher than the microchip volume (1.2 μL). Detailed explanation of the total inlet and outlet dead volumes is summarized in **Table 3-2**. This high dead volume is detrimental for RTD measurements as the contribution of all these elements will interfere.

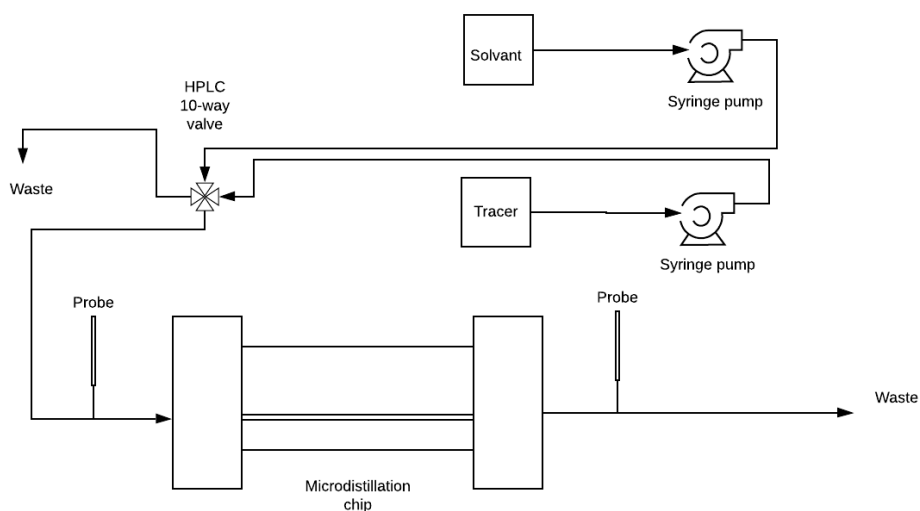


Figure 3-4 Flow diagram of a step RTD experiment with detectors placed at the inlet and outlet of the channel.

Table 3-2 Volume of the equipment involved in the RTD experiment.

	Inlet dead volume			Volume of the distillation channel	Outlet dead volume		
	T-junction	Capillary (~2 cm long)	compression part		compression part	Capillary (~2 cm long)	T-junction
	3 μL	1 μL	20 μL	~1.2 μL	20 μL	1 μL	3 μL
Total	24 μL			~1.2 μL	24 μL		

To get rid of the dead volume effect, signal acquisition must be recorded inside the channel (*i.e.* at the inlet and outlet). Since the microdevice is based on Si/Pyrex, then an optical access is possible thanks to the transparency of the Pyrex substrate. Therefore, Raman microscopy could be used to record the signal of the tracer at the inlet and outlet of the channel based on step experiments as illustrated in **Figure 3-5**. A real photograph of the experimental setup is illustrated in **Figure 3-6**.

Considering the fact that the tracer must have similar physicochemical properties as the solvent, the chosen solvent-tracer system is deionized water-ethanol. The ethanol was provided by VWR and has a purity of 99.94%.

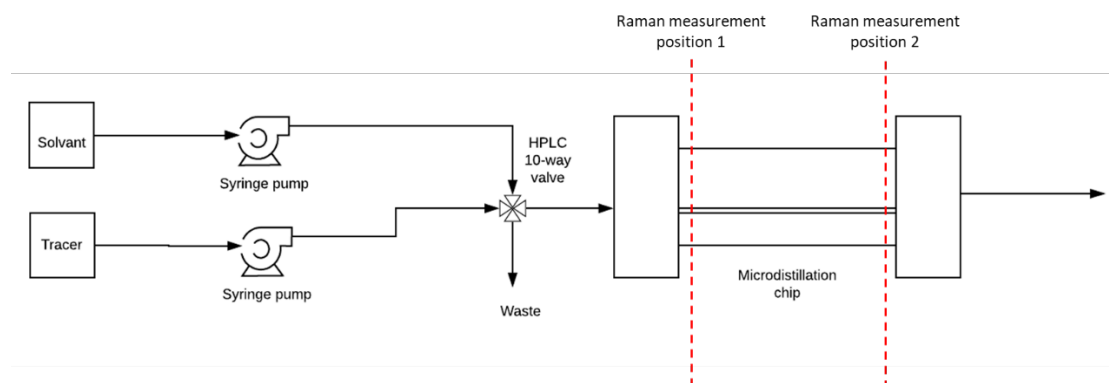


Figure 3-5 PID diagram of a step RTD experiment using Raman microscopy.

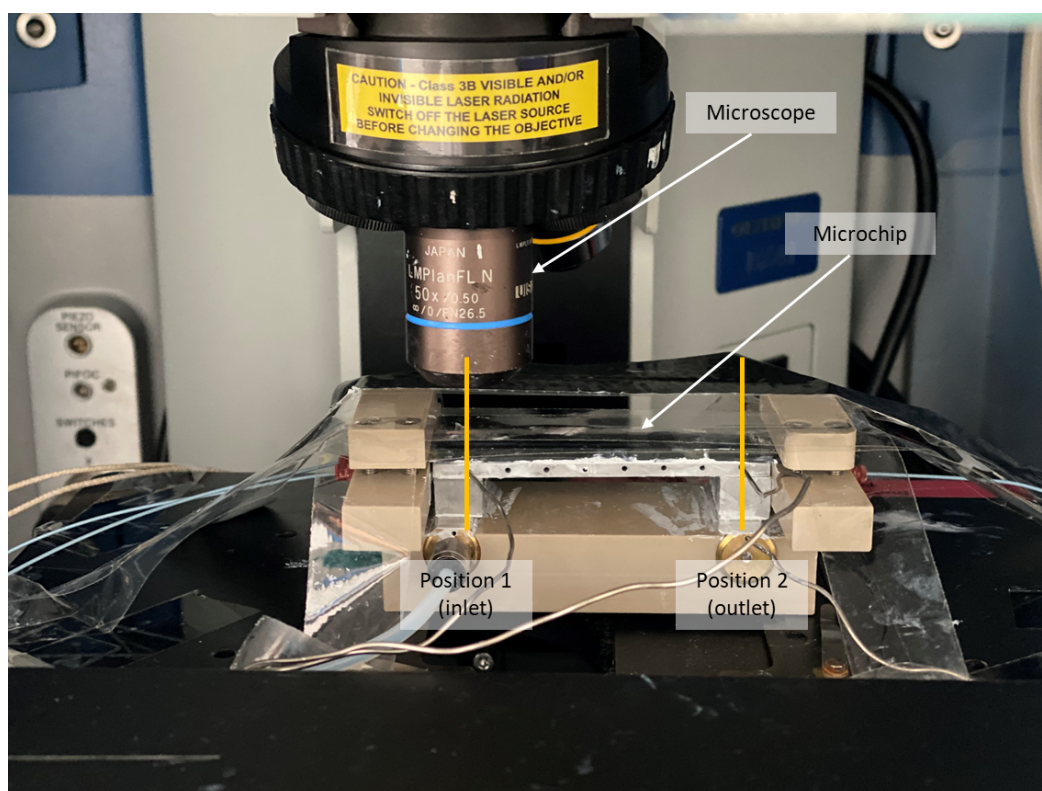


Figure 3-6 Experimental setup developed for the RTD experiments.

4. Tracer analysis by Raman spectroscopy

The principle of operation of Raman spectroscopy is briefly discussed in **Appendix B**.

Green laser with a wavelength of 532 nm is used as emitting source within the flowing experiments. The used Raman spectrometer is Raman Aramis spectrometer (Horiba Jobin Yvon).

The ethanol has two different bands at two different wavelengths ranges ($840\text{--}900\text{ cm}^{-1}$ and $2700\text{--}3100\text{ cm}^{-1}$). However, the signature of water appears between 3000 and 3700 cm^{-1} and interfere with the ethanol band consisting of 3 different peaks at $2700\text{--}3100\text{ cm}^{-1}$. Therefore, to avoid the interference of the water band with that of ethanol, data treatment based on ethanol band in the range of $840\text{--}900\text{ cm}^{-1}$ was chosen.

Regarding the data treatment, Plugim software, developed within IFPEN, was used. The Raman spectra at $t=0$ and $t=\infty$ are illustrated in **Figure 3-7** and **Figure 3-8**, respectively. It consists of three main steps:

1. Crop of the spectra between $700\text{-}1800\text{ cm}^{-1}$,
2. Justifying the baseline (Baseline Length 500, Smooth filter 4, Filter factor 0.25),
3. Integrating the peak of ethanol between $840\text{ and }900\text{ cm}^{-1}$ (Integration Minima tolerance: 0.25, Smooth filter: 5, Local continuity: 2, Number of peaks: 1, $840\text{-}900$) (**Figure 3-9**).

Thereafter, either the intensity or the area of this peak, rid of noise, are related to the ethanol concentration and can be considered for plotting the RTD curves.

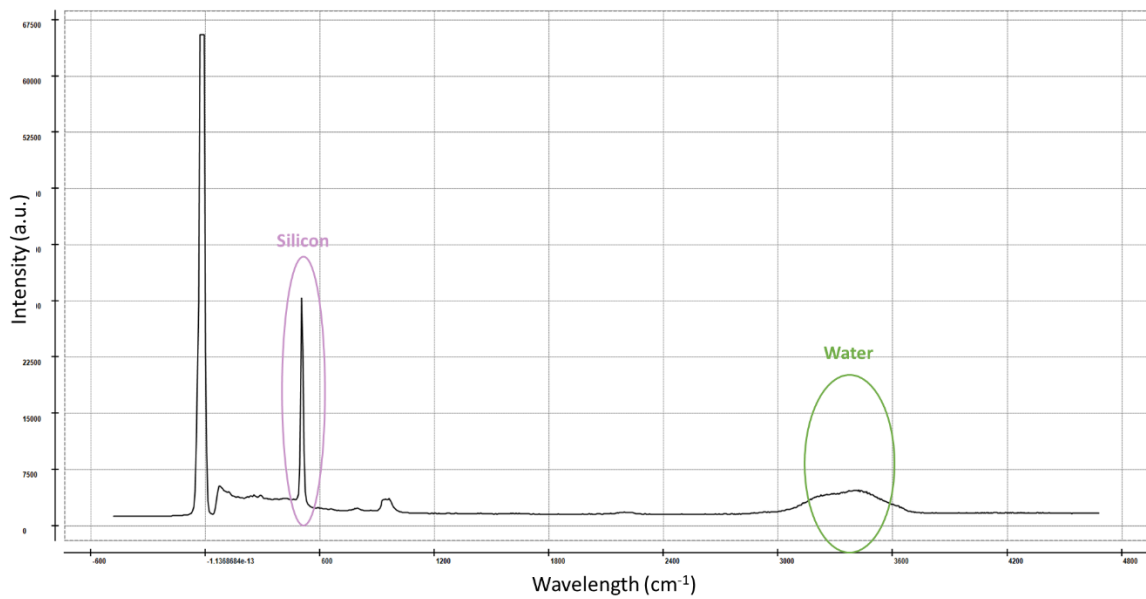


Figure 3-7 Water spectrum measured with Raman spectrometer.

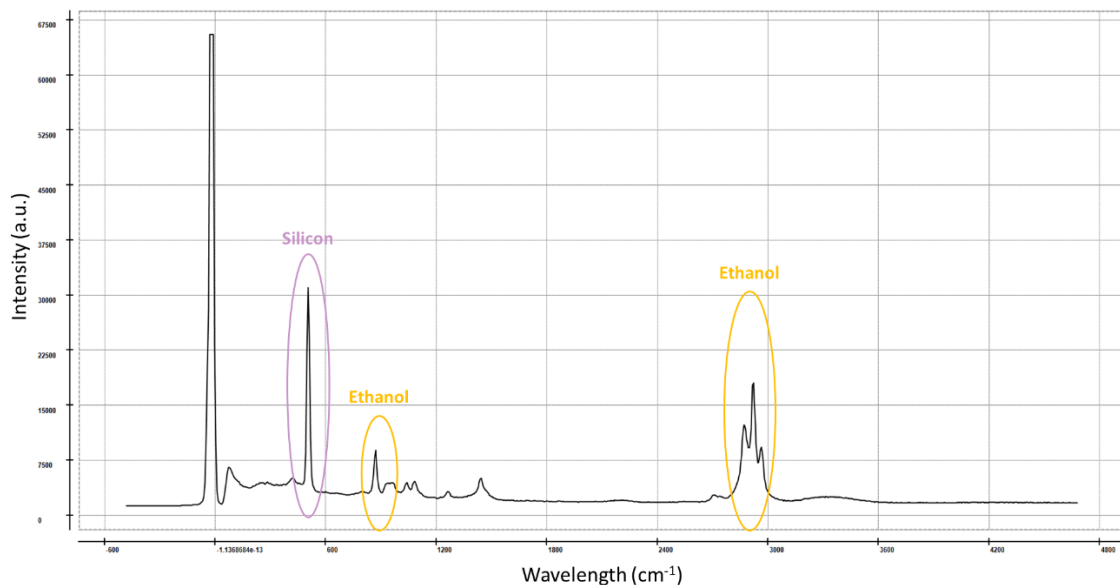
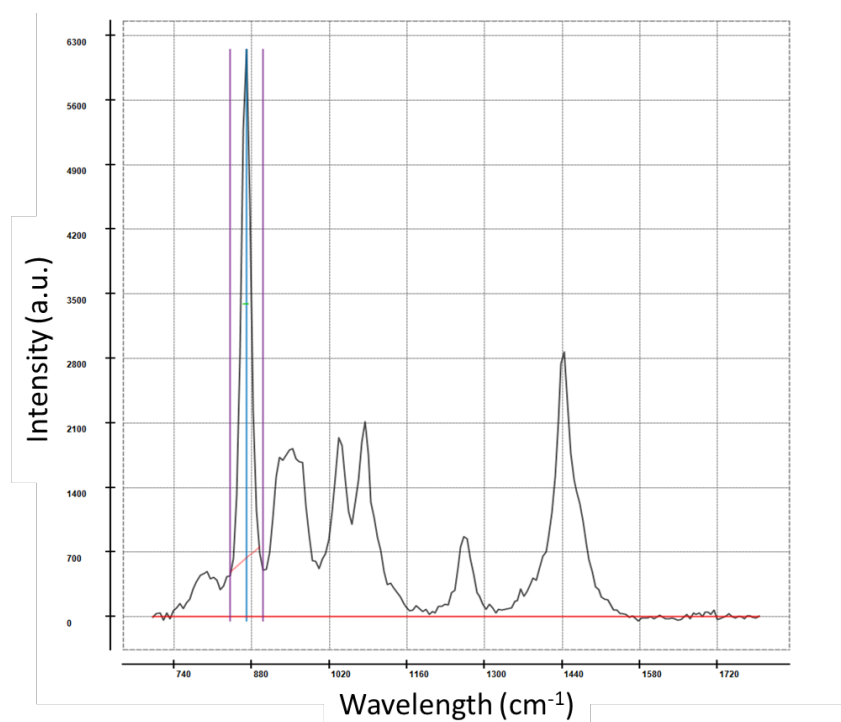


Figure 3-8 Ethanol spectrum measured with Raman spectrometer.

Figure 3-9 Baseline correction, crop and integration of the ethanol peak between 840 and 900 cm⁻¹.

5. Experimental procedure

The water and ethanol pumps operate under continuous injection mode. Firstly, water is injected into the system at a given flowrate, while the ethanol flow is driven toward the waste outlet at the same flow rate. Once both flow rates are steady and water has replaced all the liquid inside the microdevice, the position of the HPLC valve shown in **Figure 3-5** is switched with an actuator and Raman acquisition started ($t=0$). Accordingly, water is directed toward the waste outlet, whereas ethanol is injected inside the channel. Raman measurements at positions 1 and 2 are recorded within two similar independent experiments. Several flow rates were tested: 50, 100, 250, 500 and 1000 $\mu\text{L/h}$. The obtained results are recapitulated within the next section.

Raman microscope records spectra every 0.8 s at a given position in the microchannel (representing a volume of 56 nL injected in the device for a flow rate of 250 $\mu\text{L/h}$). Each spectrum is interpreted as described in the previous section, thus giving an intensity or an area curve of the ethanol peak as a function of time designated $C(t)$. The signal that corresponds to 100% of ethanol fed into the system is denoted $C_{\infty}(t)$. Different positions inside the channel were chosen and tested.

Each measurement was repeated at least 5 to 10 times in order to be able to reduce the confidence interval.

6. Results and discussion

The series of measurements presented within this section correspond to the middle position of the channel in the Y direction. For each position, measurements are performed at the beginning and at the end of the microchannel (61 mm between the two locations) as shown in **Figure 3-10**.

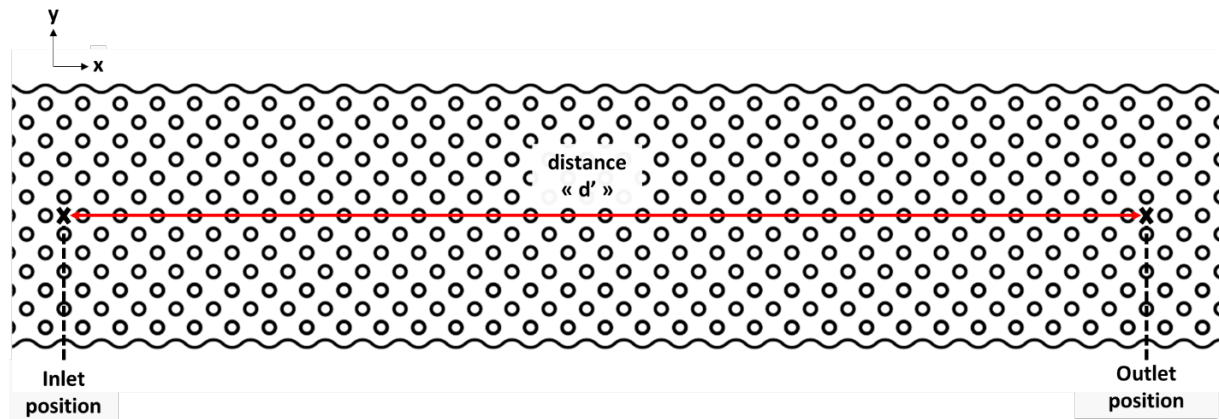


Figure 3-10 Schematic view of the inlet and outlet positions of the channel where the Raman measurement was done.

6.1. Data treatment of a typical case

The example of an experiment at $1000 \mu\text{L/h}$ is presented below. The Raman was focused on the upper part of the channel between four micropillars as indicated by the red cross shown in the figure below (**Figure 3-11**). The plots of $F(t)$ as a function of time for the inlet and outlet measurements recorded several times are illustrated in **Figure 3-12 (left)**. As it can be seen, results present some dispersion. Therefore, the mean value of $F(t)$ for the different inlets and outlets curves is represented in **Figure 3-12 (right)**. By doing the derivative of the $F(t)$ signal, the distribution function $E(t)$ is obtained. The inlet and outlet distribution curves are illustrated in **Figure 3-13**. From these curves, it can be clearly seen that the perturbation starts exiting the system before being fully entered.

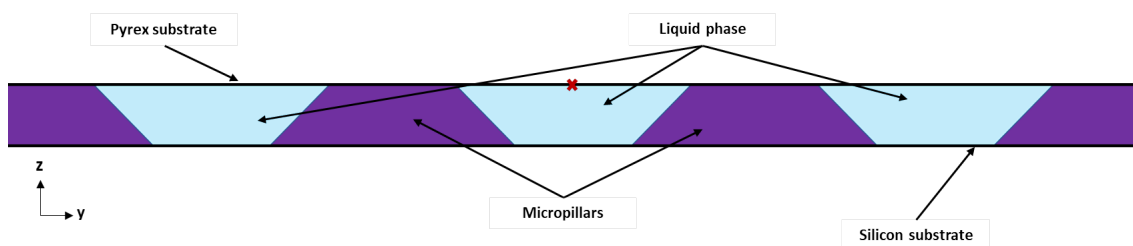


Figure 3-11 Cross-sectional view of the microchannel illustrating the position of the first recorded RTD experiments.

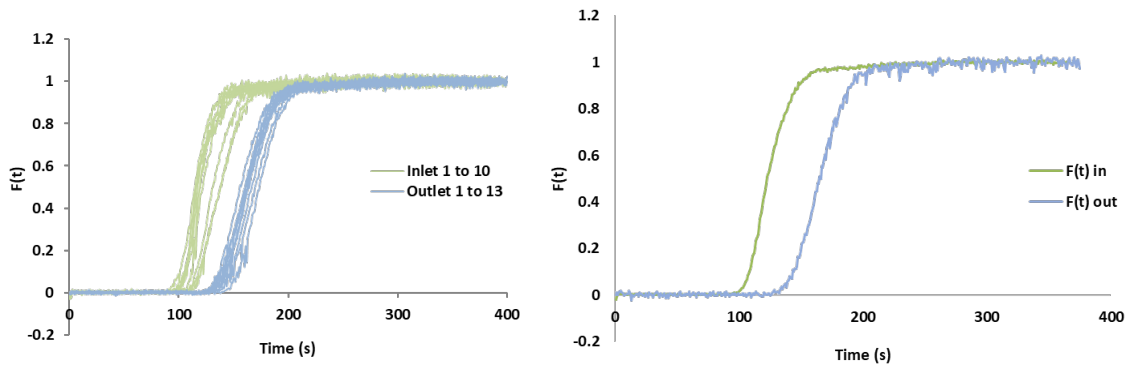


Figure 3-12 Plot of $F(t)$ at the inlet (green) and outlet (blue) of the reactor for each experiment (left) and the corresponding mean value (right) for a feed flow rate of $1000 \mu\text{L/h}$.

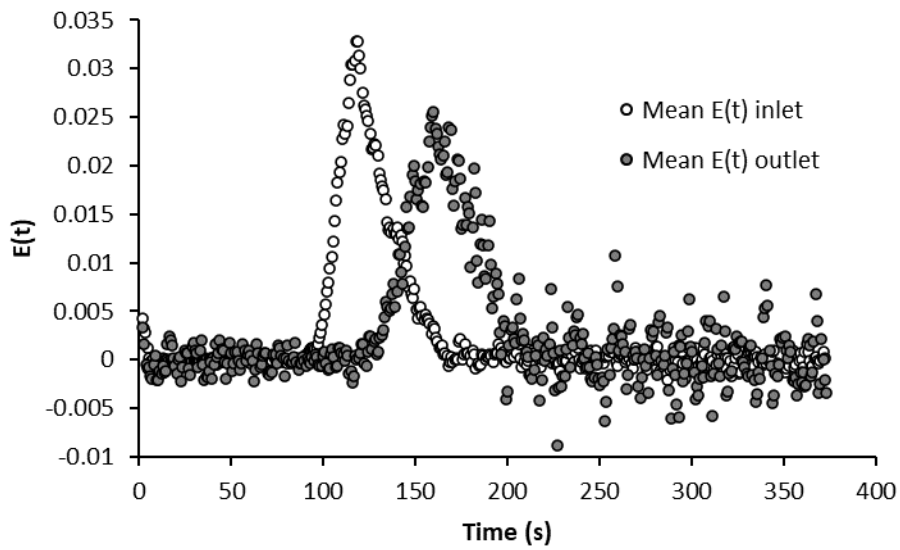


Figure 3-13 Plot of the RTD curve for a feed flow rate of $1000 \mu\text{L/h}$.

The results of the first and second moments calculated according to the equations mentioned in **Table 3-1**, are recapitulated in **Table 3-3**. For the different inlet and outlet tests, a mean value was calculated along with the standard deviation and the confidence interval (C.I.) calculated based on student law (95%).

Table 3-3 First and second moments for the different recorded distribution functions at the inlet and outlet of the reactor and their corresponding standard deviation and C.I. values for a feed flow rate of 1000 $\mu\text{L/h}$.

		μ_1 (s)	Mean Value	Standard deviation	C.I.	μ_2	Mean Value	Standard deviation	C.I.
Inlet	Test 1	121.5	126.6	8.6	6.2	15364	16641	2361	1689
	Test 2	121.7				15357			
	Test 3	120.4				14929			
	Test 4	121.6				15141			
	Test 5	117.3				14298			
	Test 6	124.6				16014			
	Test 7	123.3				15512			
	Test 8	134.6				18750			
	Test 9	141.0				20604			
	Test 10	140.1				20435			
Outlet	Test 1	175.8	166.8	4.4	2.7	31424	28428	1505	909
	Test 2	171.6				30186			
	Test 3	168.2				28991			
	Test 4	163.1				27333			
	Test 5	160.0				26165			
	Test 6	163.7				27426			
	Test 7	165.5				28095			
	Test 8	165.2				28035			
	Test 9	165.7				27163			
	Test 10	165.7				28245			
	Test 11	164.3				27877			
	Test 12	165.9				27955			
	Test 13	173.5				30671			

Based on the mean values of the residence time, Peclet number and axial dispersion coefficient are calculated according to **equations 3-6, 3-7 and 3-8**, respectively. The obtained values are given in **Table 3-4**. As observed for this case of measurement, a high discrepancy was found between the theoretical (calculated based on the liquid flow rate and the volume of the liquid channel) and experimental residence time. Therefore, the RTD along the channel depth has to be investigated in order to avoid the impact of bad positioning of the Raman (focusing near a non-slip condition) and to check if the flow pattern has the expected laminar profile.

Table 3-4 RTD results obtained for a feed flow rate of 1000 $\mu\text{L/h}$.

Flow rate	Inlet outlet distance (m)	Residence time (s)		C.I.	Peclet	Axial dispersion coefficient (m^2/s)
		Theoretical	Experimental			
1000 $\mu\text{L/h}$	0.0612	4.7	40.2	6.9	768.478	1.2E-06

6.2. Measurement of the RTD as a function of the depth of the channel

The evolution of the residence time distribution as a function of the channel depth is investigated for flow rates of 250 $\mu\text{L/h}$ and 500 $\mu\text{L/h}$. Acquisition points Z_1 to Z_5 are evenly distributed

within the depth of the channel, z_1 and z_5 being located $2\ \mu\text{m}$ away from the upper and lower boundaries of the channel, respectively. The different positions are illustrated in the figure below (**Figure 3-14**). The values of the first moment for both tested flow rates at the different positions along with the standard variation are illustrated in **Figure 3-15**. The different measurement characteristics for both flow rates are summarized in **Table 3-5**. For the flow rate of $250\ \mu\text{L/h}$, the time taken to reach the outlet position was longer than that for the inlet position, whereas concerning the $500\ \mu\text{L/h}$ flow rate, the result was totally the opposite. However, for $500\ \mu\text{L/h}$, a longer residence time was obtained for z_1 and z_5 due to the impact of the non-slip conditions. The expected parabolic profile is observed.

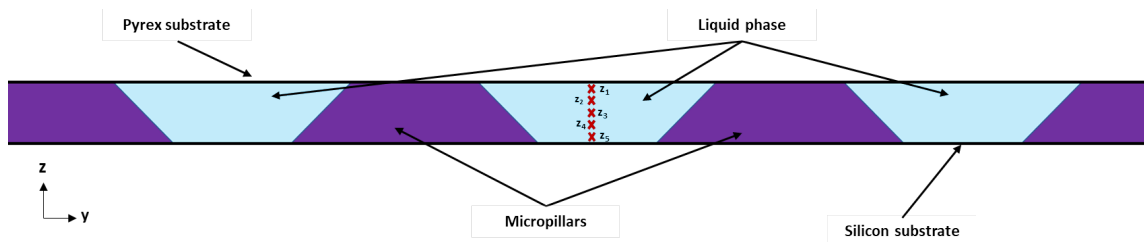


Figure 3-14 Cross-sectional view of the microchannel illustrating the different positions for the RTD measurements.

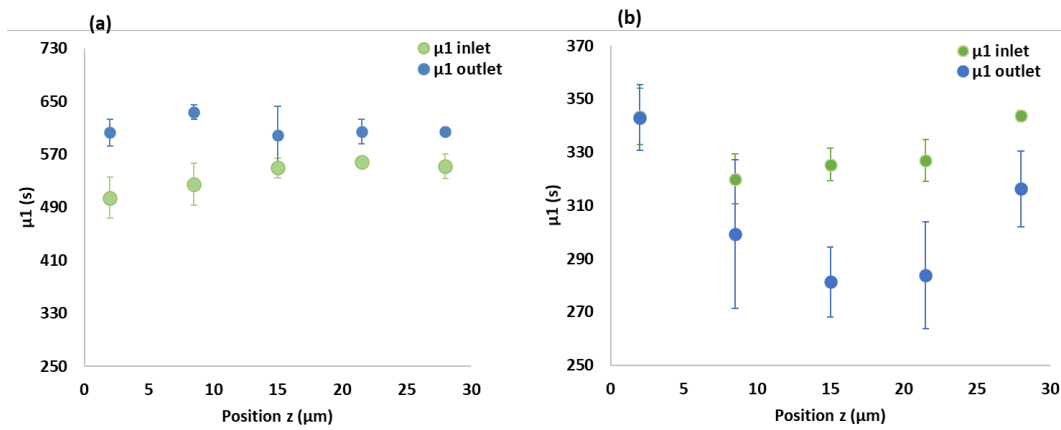


Figure 3-15 First moment of the cumulative function for a flow rate of $250\ \mu\text{L/h}$ (a) and $500\ \mu\text{L/h}$ (b) at different depths inside the channel.

Table 3-5 Number of tests, first and second moments and the corresponding confidence intervals for flow rates of 250 and 500 $\mu\text{L/h}$ at the inlet and outlet position within the channel.

Flow rate	Position (z)	Position (x)	Tests	μ_1			μ_2		
				Mean value	Standard deviation	C.I.	Mean value	Standard deviation	C.I.
250 $\mu\text{L/h}$	z1	Inlet	3	504.5	31.2	77.5	2.86E+05	3.50E+04	8.71E+04
		Outlet	5	603.2	20.4	25.3	3.66E+05	2.37E+04	2.94E+04
	z2	Inlet	3	525.0	31.1	77.4	2.79E+05	3.28E+04	8.14E+04
		Outlet	5	634.0	11.2	13.9	4.03E+05	1.36E+04	1.68E+04
	z3	Inlet	3	549.6	14.5	36.1	3.05E+05	1.58E+04	3.92E+04
		Outlet	3	599.6	43.0	106.9	3.62E+05	5.15E+04	1.28E+05
	z4	Inlet	3	559.3	4.2	10.5	3.16E+05	4.58E+03	1.14E+04
		Outlet	3	604.5	18.1	44.9	3.68E+05	2.17E+04	5.39E+04
	z5	Inlet	3	552.4	18.9	46.9	3.08E+05	2.10E+04	5.21E+04
		Outlet	3	605.0	6.0	14.8	3.68E+05	7.63E+03	1.90E+04
500 $\mu\text{L/h}$	z1	Inlet	5	343.6	10.6	19.7	1.20E+05	7.15E+03	8.86E+04
		Outlet	5	343.1	12.4	58.3	2.33E+05	7.04E+04	9.99E+04
	z2	Inlet	5	320.0	9.3	21.4	1.04E+05	6.05E+03	1.10E+05
		Outlet	5	299.3	27.8	34.9	1.96E+05	3.71E+04	4.61E+04
	z3	Inlet	5	325.4	6.0	12.9	1.34E+05	5.98E+04	1.01E+05
		Outlet	5	281.3	13.2	33.8	1.69E+05	1.08E+04	4.29E+04
	z4	Inlet	5	326.9	7.9	13.0	2.38E+05	1.11E+04	7.70E+04
		Outlet	5	283.8	20.0	36.1	1.72E+05	2.64E+04	4.92E+04
	z5	Inlet	5	343.7	2.0	15.0	2.60E+05	3.07E+03	1.07E+05
		Outlet	5	316.3	14.1	25.9	2.12E+05	2.10E+04	3.28E+04

It is interesting to note that the reproducibility issues seem to be flow rate dependent: confidence intervals are significantly lower for 250 $\mu\text{L/h}$ than for 500 $\mu\text{L/h}$. Moreover, the average residence time sticks much better with the expected value estimated based on the feed flow rate and the volume of the liquid channel (9.4 s for 500 $\mu\text{L/h}$ and 18.8 s for 250 $\mu\text{L/h}$). However, the puzzling results obtained for 500 $\mu\text{L/h}$ suggest that there might be some bypass inside the microchannel, and that these bypasses depend on the liquid flow rate. Indeed, this z profile, and all the RTD measurements performed in this study, are limited to the center of the channel only (see **Figure 3-10**). A full mapping of the microdevice would provide useful data to better understand the flow pattern or to reveal an experimental issue that has not been identified until now.

Since the C.I. is very high compared to the residence time and given the high discrepancy depending on where the measurement is done in the microchannel, the “local” measurement approach is not the ideal one to access the global residence time distribution. This last one was not feasible because of the high dispersion generated by the whole system that might have induced, as well, lots of uncertainties. Instead, it was decided to rely on a CFD study that will be presented in the next paragraph.

7. Simulation of the liquid flow within the micropillars

A CFD case was investigated using the Autocad model of the microdevice. Consequently, the numerical case is close to the real one from a geometrical point of view. This work was done by Alexis Tourbier, a PhD student at IFP Energies Nouvelles with the OpenFOAM software. Openfoam is an open source CFD software based on a finite volume method for the discretization and solving of fluid mechanics equations. Navier Stokes and a passive scalar transport equations were used to study the liquid flow within the microchannel. The set of **equations 3-9** was used to predict the pressure and velocity profiles within the channel based on the mass conservation and momentum balance equations of an incompressible isothermal fluid. To solve this set of equations, the Simple algorithm was considered. Thereafter, the first and second moments for the residence time distribution functions were computed based on **equation 3-10** and **equation 3-11**, respectively.

$$\begin{cases} \nabla \cdot \mathbf{u}_l = 0 \\ \frac{\partial \rho_l \mathbf{u}_l}{\partial t} + \nabla \cdot (\rho_l \mathbf{u}_l \mathbf{u}_l) = -\nabla p_l + \nabla \cdot \Sigma + \rho_l \mathbf{g} + S_v = 0 \end{cases} \quad (3-9)$$

where Σ stands for the viscous stress tensor and, S_v is an external volumetric source.

$$\frac{\partial \mu_1}{\partial t} + \nabla \cdot (\mathbf{u}_l \mu_1) = \nabla \cdot (D_{ax} \nabla (\mu_1)) + S_v \quad (3-10)$$

$$\frac{\partial \mu_2}{\partial t} + \nabla \cdot (\mathbf{u}_l \mu_2) = \nabla \cdot (D_{ax} \nabla (\mu_2)) + S_v + 2\mu_1 \quad (3-11)$$

S_v in all the cases is considered equal to zero since no external source is added to the system.

All the equations were used for Newtonian fluids and the boundary conditions were considered as no-slip conditions. The relative pressure of the fluid at the outlet of the channel was fixed to zero. At the channel walls, the pressure flux was considered constant. The simulation was based on the injection at $t=0$ of ethanol at 20°C, with a channel previously filled with water. The considered diffusion coefficient of ethanol in water is $1.24 \cdot 10^{-9} \text{ m}^2/\text{s}$. The mesh was designed to ensure an accurate evolution of the velocity and pressure profiles within the channel. This leads to a mesh of 24 million cells for a 5 mm long channel. Therefore, the simulation was done for a section of the channel rather than the entire length of the real device to avoid exceeding of the computational capacities. Different flow rates were simulated. Convergence was reached after 600-1000 iterations. The mesh independency was verified by monitoring the liquid flow rate. Finally, the results were refined close to the wall of the channel.

The evolution of the first moment, Peclet number, second moment of the cumulative function and pressure as a function of the distance of the channel are illustrated in **Figure 3-16**. A high linear relationship exists between each of these parameters and the distance travelled. Hence, the value of these parameters for the whole microdistillation device could be obtained by extrapolation. CFD results are displayed in **Table 3-6**.

The theoretical residence time are slightly higher than the simulated one because of the estimated void fraction based on the truncated cone. The first and second moments profile all along the channel length are illustrated in **Figure 3-17**. This profile was taken at a depth of 15 μm away from the top boundary for a feed flow rate of 250 $\mu\text{L}/\text{h}$. In addition to that, the residence time profile in the y direction is also displayed in **Figure 3-18** at different positions of the channel (x).

Calculated Peclet number are high and denote a plug flow behavior for the considered micropillar arrangement. This is of particular interest since it indicates very low backmixing due to the liquid flow. Thus, no improvements are expected from this aspect of the microdistillation regarding global performances.

The calculated ΔP is however much higher than the one predicted using the considerations adopted in **Chapter 2**. This highlights the need for a better approach to estimate this parameter in order to design devices that work effectively. However, this ΔP is calculated for a “closed” microchannel, with no slip in its upper part, which is not fully representative of the real microdistillation device. As a result, the expected pressure drop is smaller. The velocity and pressure profiles within the channel for a flow rate of 250 $\mu\text{L/h}$ at a depth of 15 μm from the bottom of the channel is displayed in **Figure 3-19, top**.

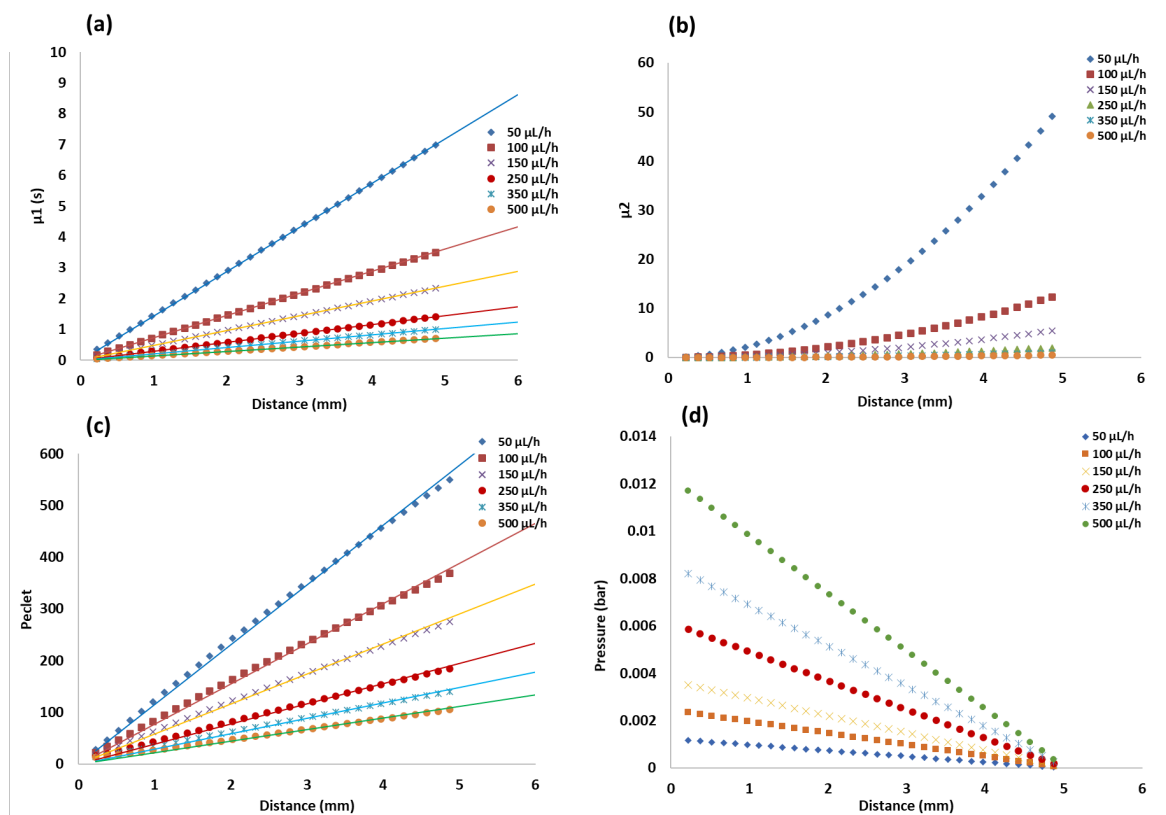


Figure 3-16 Plot of the first moment (a), second moment (b), Peclet number (c) and pressure (d) as a function of the distance in the channel for various flow rates.

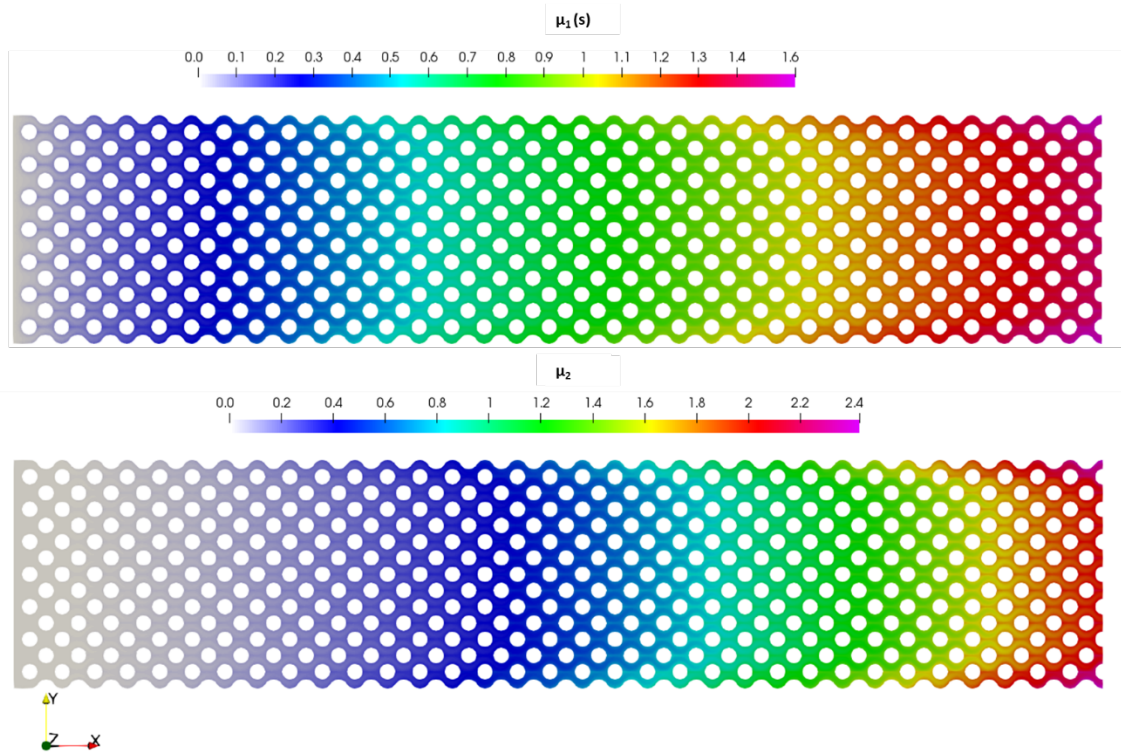


Figure 3-17 First and second moments profile for a 5 mm length channel at a depth of 15 μm from the bottom of the channel and a flow rate of 250 $\mu\text{L/h}$.

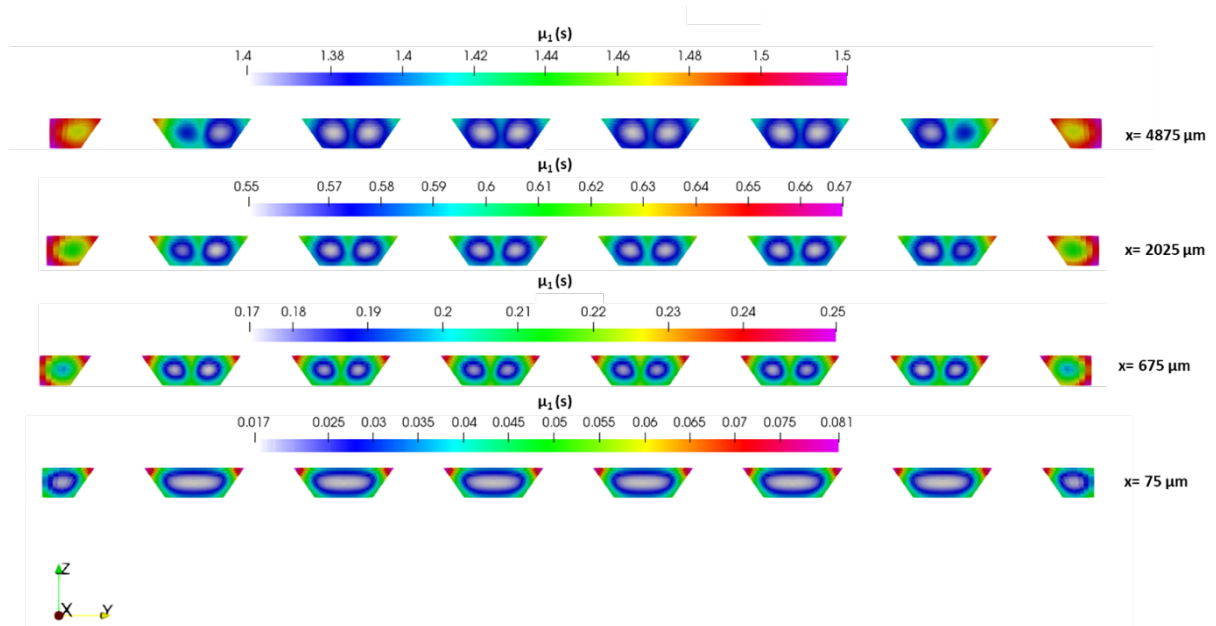


Figure 3-18 Residence time profile of the liquid at various sections of the channel in the x direction for a flow rate of 250 $\mu\text{L/h}$.

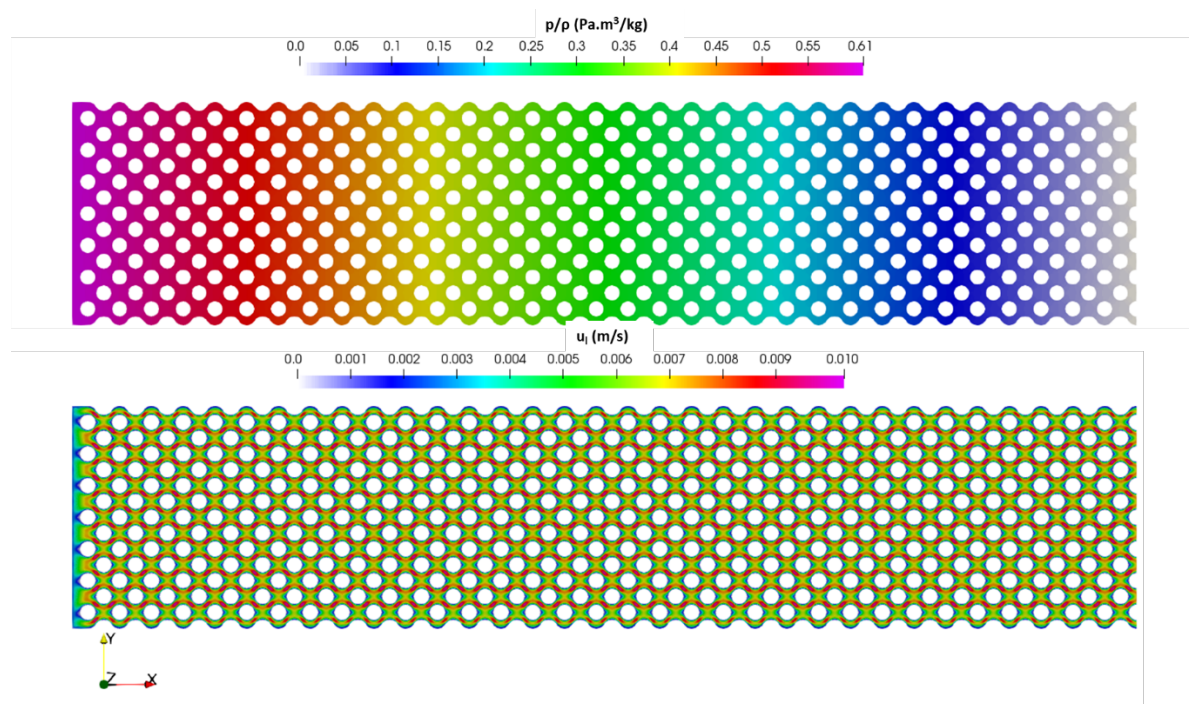


Figure 3-19 Pressure and velocity profiles within a 5 mm long channel for a flow rate of 250 $\mu\text{L/h}$ at a depth of 15 μm from the bottom of the channel.

Table 3-6 CFD and theoretical results obtained for various liquid flow rates within a 6 cm long channel filled with the micropillars.

Flow rate ($\mu\text{L/h}$)	Simulated residence time (s)	Theoretical residence time (s)	Peclet	D_{ax} (m^2/s)	Simulated ΔP (mbar)	Theoretical ΔP (mbar)		
						Ergun	Kozeny-Carman	Tullius <i>et al.</i> [66]
50	86.3	99.9	6929.4	6.31E-09	14.0	2.8	1.4	0.4
100	43.2	50.0	4656.9	1.88E-08	27.9	5.6	2.8	0.9
150	28.9	33.3	3476.4	3.78E-08	41.9	8.3	4.2	1.5
250	17.3	20.0	2337.7	9.22E-08	69.8	13.9	7.0	2.9
350	12.4	14.3	1784.9	1.70E-07	97.7	19.5	9.8	4.7
500	8.7	10.0	1341.2	3.24E-07	139.6	27.8	14.0	7.7

An additional parameter that is usually adopted by conventional distillations in order to predict their performances is the overall mass transfer coefficient. This is also the case of microdistillations. Consequently, experimental measurement is essential to mitigate the complexity of the hydrodynamic phenomena occurring within the channel and to optimize the separation. However, a preliminary study is required to confirm the feasibility of the experimental measurement of this parameter.

8. Mass transfer coefficient

The majority of the work carried out in literature was dedicated to co-current flows [85–88]. It mainly considers the co-injection of a gas and liquid via a ‘Y’, ‘T’, or ‘Cross-shaped’ junction and then either the gas or the liquid phase is analyzed. However, counter-current configurations are complex to

establish at the microscale and the measurement of the material transfer coefficients within these channels was little discussed.

To confirm that the coefficient could be measured experimentally, a theoretical approach should be developed. Let's consider a two-phase system made of water and N₂/CO₂ (1-2%) mixture. A schematic view of the two-phase flow within a section of the microchannel is illustrated in **Figure 3-20**. The equation used to estimate the material transfer coefficient for a counter-current flow is expressed by the following equation:

$$\frac{K_L a^* L}{u_L} = \ln \left(\frac{c^{eq} - c_{CO_2}^{in}}{c^{eq} - c_{CO_2}^{out}} \right) \quad (3-12)$$

where $K_L a$ is the volumetric mass transfer coefficient, L is the channel length, u_L is the superficial velocity of the liquid phase, c^{eq} is the equilibrium concentration and $c_{CO_2}^{in}$ and $c_{CO_2}^{out}$ are the concentrations of CO₂ in the entering and exiting liquid flows, respectively.

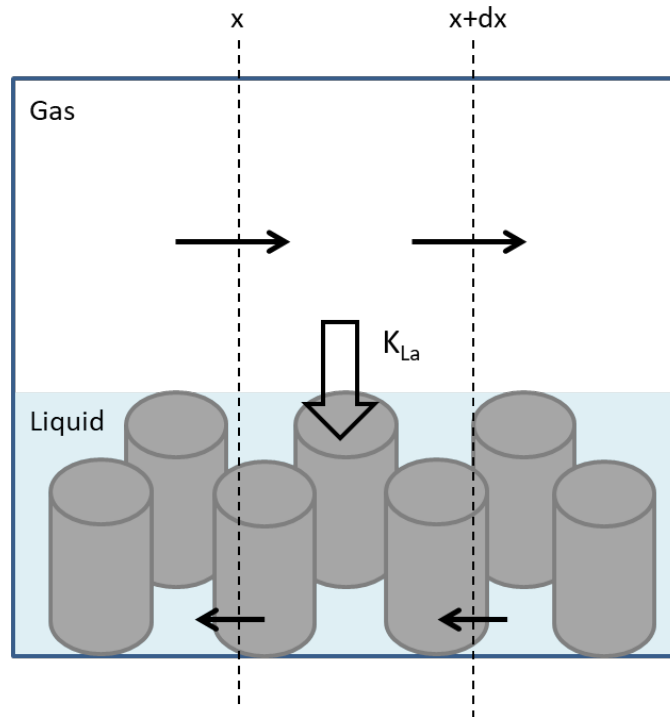


Figure 3-20 Schematic view of transfer phenomena between the gas and liquid phases.

By assuming that the liquid fed into the channel is without CO₂, then $c_{CO_2}^{in}$ is considered null. Based on **equation 3-12** and to be able to estimate the material transfer coefficient $c_{CO_2}^{out}$ must be different from c^{eq} . A good measurement of the material transfer coefficient requires a low ratio of $\frac{K_L a^* L}{u_L}$ otherwise, a length of the channel, which is not involved in the diffusion phenomena (reaching equilibrium before the end of the channel), would be considered in the calculation and leads to wrong results. Accordingly, the superficial velocity must be high. Hence, a minimum K_L must be estimated. The diffusion time from the gas-liquid interface towards the liquid channel wall is estimated around 0.56 s based on a diffusion coefficient and distance of 0.0016 mm²/s and 30 μm, respectively. If only diffusion phenomena were considered, then the diffusion time is worth $1 / K_L a$. Consequently, the minimum K_L is estimated around $2.3 \cdot 10^{-4}$ m/s. However, the liquid residence time for a flow rate of 250 μL/h or 400 μL/h is 20 and 12

seconds, respectively. This is relatively high compared to the diffusion time and the liquid will directly reach the equilibrium concentration. Therefore, in a large section of the channel, no diffusion will occur while considering the entire length of the channel in the calculation of the $K_L a$.

An enhancement factor exists if a chemical reaction is taking place. This means that the diffused CO_2 within the liquid phase is consumed by the chemical reaction that is taking place. Therefore, an accelerated diffusion of CO_2 is induced to reach equilibrium. The enhancement factor was mentioned by Hegely *et al.* [89]. If the kinetics of the chemical reaction were fast, then its contribution can be neglected, and the acceleration factor tends to the unity.

Since within the current work, the residence time is much higher than the diffusion time; then the physical absorption/desorption phenomena is not feasible to predict K_L . Chemical reaction must be considered. However, the K_L will certainly be larger than in the calculation because the estimated one is only limited by the molecular diffusion in the liquid film. The movements of the liquid can only increase the K_L in relation to this limit. Accordingly, more absorption will occur and the change in CO_2 concentration in the gas may be important and could not be neglected.

The conditions seem favorable for the investigation of $K_L a$ experimental measurement. It is required to study the variation of K_L according to the gas and liquid flow rates. It is also essential to check the amount of CO_2 in the exiting liquid. It must remain lower than 20 wt%, otherwise uncertainties are introduced. However, because of experimental complications and time restrictions it was not possible to do these measurements.

9. Conclusion

In this chapter was discussed the hydrodynamic characterization of the chip. In order to study the liquid dispersion within the micropillar region, an experimental setup was developed to measure the residence time distribution. The injection of a tracer according to a step function was chosen due to the low volume of the chip ($\sim 2 \mu\text{L}$). Raman microscopy was selected to investigate the RTD. Measurements at the inlet and outlet of the chip were recorded independently. However, reproducibility issues were encountered, and a further investigation was initiated. Local characterizations were performed at different depths inside the microchannel, revealing a high variation of the residence time pattern depending on the position and on the flow rate. The same discrepancy is expected when performing measurements at a different lateral position, but this work could not be done within this study. Consequently, it is concluded that the local RTD approach adopted here is not suitable for the needs of the study, and that the global RTD approach is more representative. Nevertheless, this last one was not attempted since high dispersion of the results was also expected. Another possible alternative to study the fluid mechanics taking place within the device is the Microparticle Image Velocimetry (μPIV). It allows the computation of the local and mean velocity field by cross-correlating the experimentally recorded images. Preliminary μPIV experiments were conducted and the obtained local velocity field is illustrated in **Figure 3-21**. However, these tests were done using microchannels partially filled with micropillars. Due to time constraints, further experiments could not be carried out.

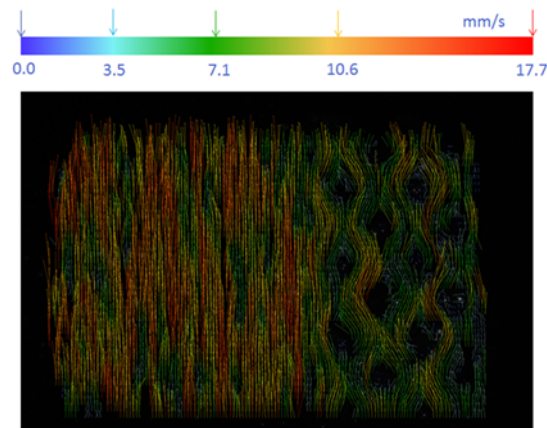


Figure 3-21 Local velocity field obtained for an injection and withdrawal flow rate of 108 $\mu\text{L/h}$.

Eventually, a CFD work gave some insight of the hydrodynamic behavior of the microchip. A plug flow behavior of the liquid phase is expected, which is of particular interest for microdistillation performances. Concerns are raised regarding the pressure drop across the bank of micropillars, as the predicted value using CFD is two orders of magnitude higher than the one estimated using correlations adopted in **Chapter 2**.

4. Chapter 4: Microdistillation experiments

1. Introduction

Distillations experiments are conducted on the proposed devices in order to determine their performances under various conditions (flow rate, temperature, feed composition). In this chapter, the materials, equipment and developed distillation setup are presented. Thereafter, the experimental procedure is detailed along with the experimental results. The impact of feed flow rate, residue to feed flow rate ratio, heating temperature and feed composition on the performance of the microdistillation are also studied and overviewed within this chapter. Finally, *in situ* monitoring of distillation experiments using Raman microscopy was investigated.

2. Experimental setup

The experimental setup, developed specifically for microdistillation experiments, enables an accurate temperature control of the chip and allows a precise quantification of distillation products.

2.1. Fluids

The considered binary mixture is composed of acetone and deionized water. The acetone is provided by VWR and has a purity higher than 99.5%.

2.2. Microchip assembly

A specific assembly was designed to hold the microdistillation during experiments and to connect its inlet and outlet ports to other equipment. A schematic view of this assembly is shown in **Figure 4-1**.

It consists of a peek block within which are inserted two copper tubes. In the first tube, a heating cartridge is inserted to heat up the system to a target temperature. Water circulation is ensured through the second tube to cool down the system. Two aluminum blocks (23 mm long, 10 mm wide, 9 mm high) rest each on a copper tube without being in direct contact with the peek block. An aluminum plate (69 mm long, 23 mm wide, 3 mm thick) is placed on the top of these aluminum blocks. Therefore, a temperature gradient is established inside the aluminum plate from the hot end toward the cold one. Height drillings (small holes) are evenly spaced on the side of the aluminum plate for temperature measurement purposes.

All these elements (copper tubes, aluminum block, aluminum plate) are assembled together using thermal paste to favor heat conduction, and, somehow, to glue them together. Indeed, all these parts are not assembled in a solid way and are just stacked. Most of the time, pressure is applied on compression parts for better heat conduction.

The purpose of the compression parts is to connect the injection and outlet channels of the microdistillation to other equipment. It was presented in **Chapter 2 - section 7.3**. Pictures of these parts are presented on **Figure 4-2**. The lower element of each compression part is provided with small

internal channels (drilled), one end being connected to the chip thanks to silicon o-rings, the other one to capillary tubing thanks to standard 6-32 microfluidics ports. The upper and lower elements of each compression part are screwed together and clamp the microdistillation to ensure o-rings tightness.

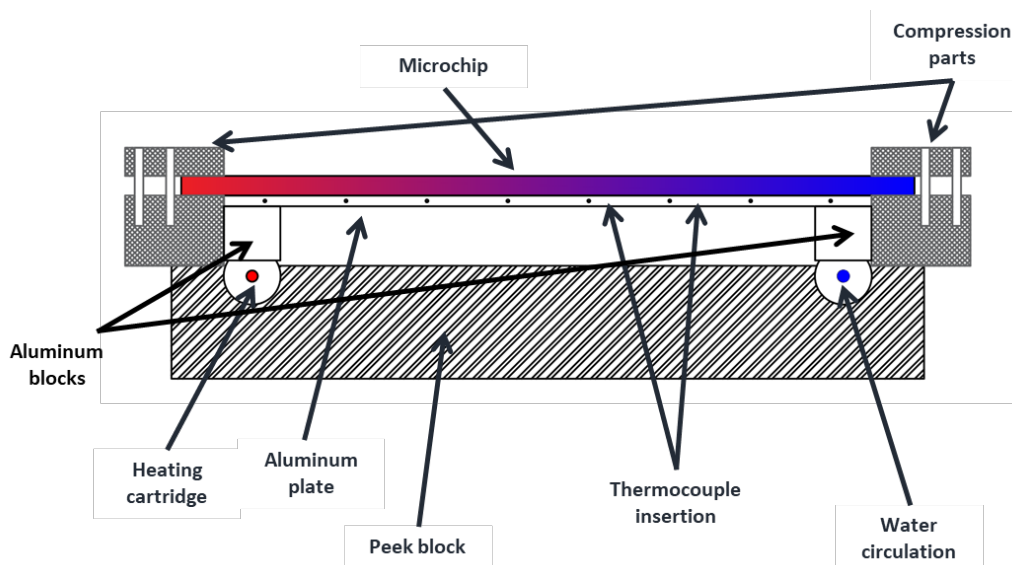


Figure 4-1 Front view of the experimental device.

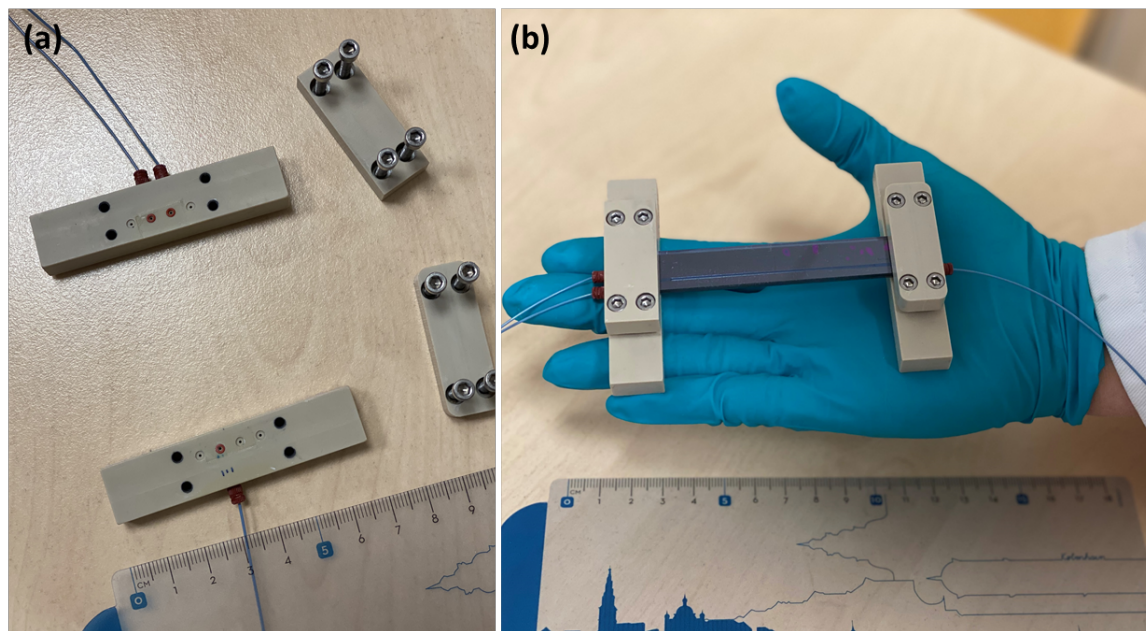


Figure 4-2 (a) Detailed photograph of the different parts of the compression pieces and (b) the packaged chip.

2.3. Distillation experimental setup

The flow diagram of the experimental setup is shown in **Figure 4-3**. Two syringe pumps are used to continuously prepare the binary mixture to be distilled. The mixture is then injected inside the chip through the compression parts. The residue is withdrawn at a fixed flow rate with another syringe pump, whereas the distillate outlet is "free". This means that the microdistillation is operating at atmospheric pressure (given that the pressure drop in the outlet capillary is small).

All syringe pumps are PHD Ultra™ 4400 Harvard programmable syringe pumps with 8 mL Harvard

syringes. They are able to inject and withdraw at constant flow rates from 30 nL/min to 13 mL/min. For the present application, syringe o-rings are made of FFKM (Kalrez) for chemical compatibility purposes.

Samples are collected in HPLC vials. Needles are used to inject samples through septum directly inside the vials. Another needle connects each vial to the atmosphere, thus avoiding vial pressurization and maintaining a stable back pressure for the microdistillation. Accordingly, sample losses due to vaporization in air are minimized.

A nitrogen bottle is also connected to the chip for leak-tightness tests. As it can be seen in **Figure 4-3**, either the binary mixture or the gas is fed into the system.

The heating of the microdevice is realized by a heating cartridge controlled using an Eurotherm regulator (EPC 3016) whereas the cold end temperature was controlled by circulating glycol water set by a cryostat (Julabo F2S).

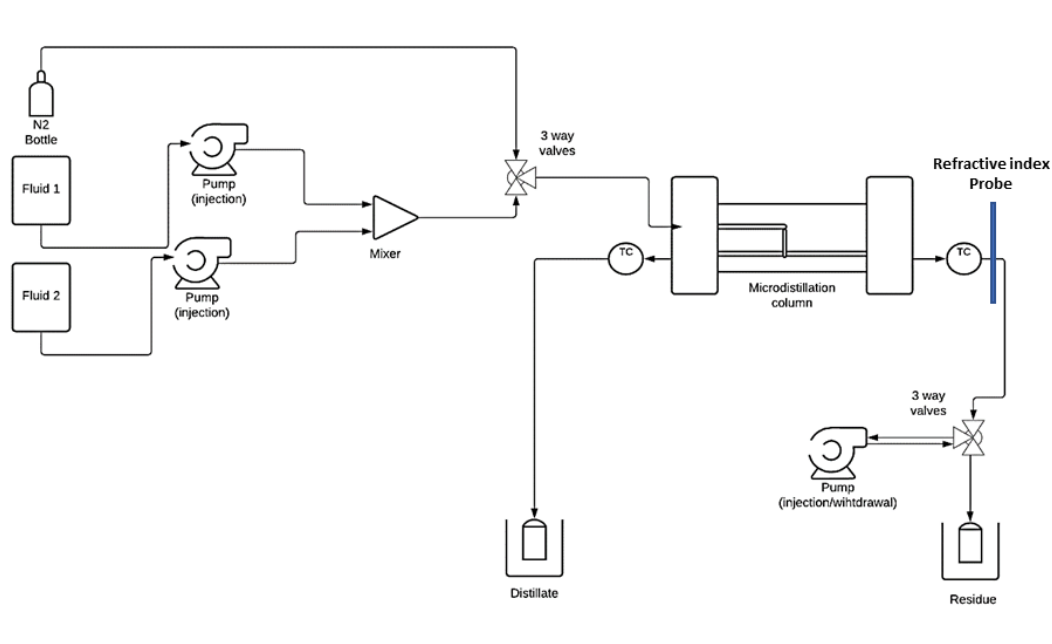


Figure 4-3 Process flow diagram of the distillation setup.

A photograph of the device is shown in **Figure 4-4**. In this photo are shown all the aforementioned equipment used for the distillation experiment. Raman spectroscopy was also used during distillation experiments.

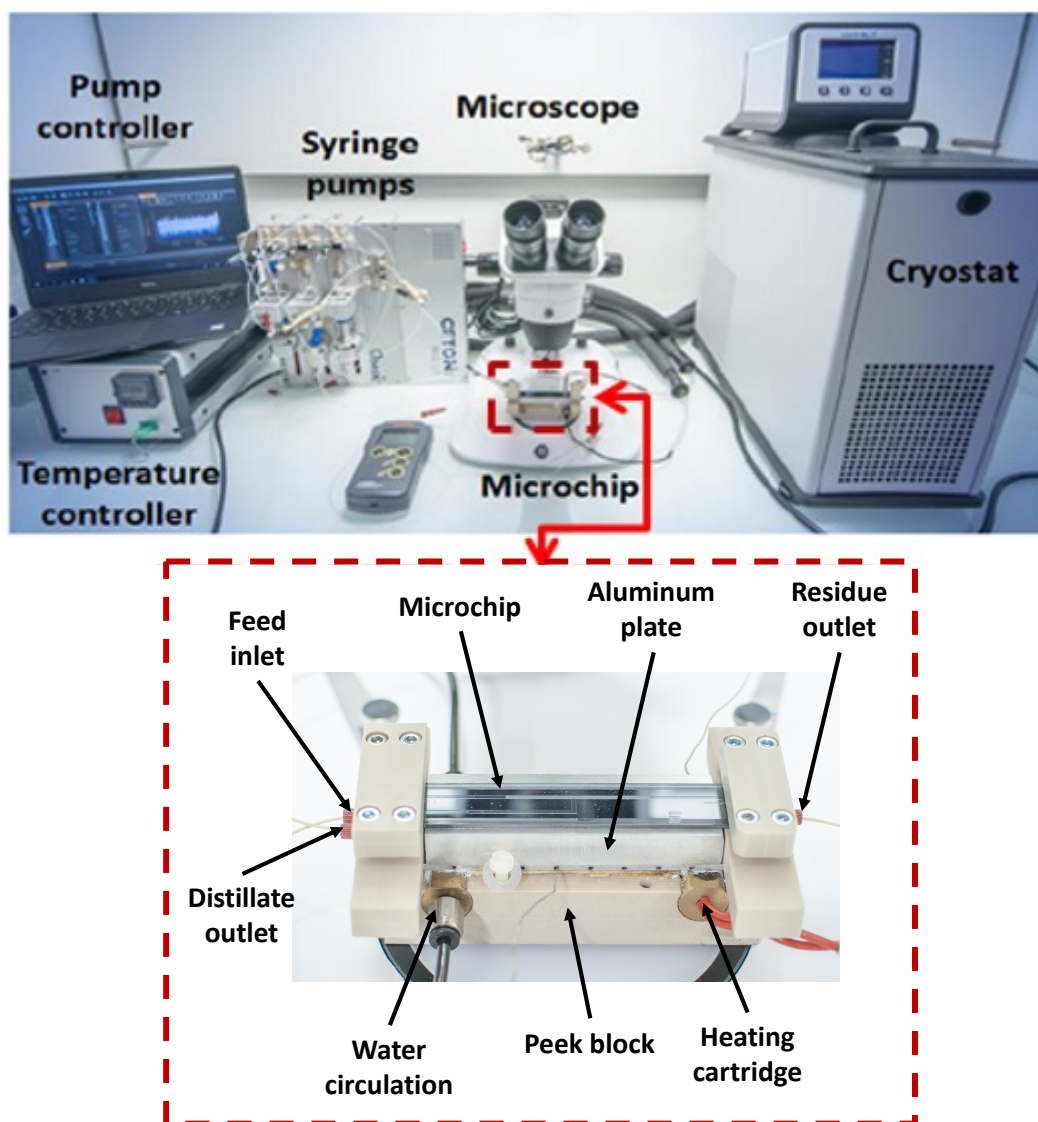


Figure 4-4 Real photo of the developed experimental setup.

2.4. Thermal profile

2.4.1. Thermocouple inserted in the aluminum plate

The temperature profile established across the chip and measured via thermocouple insertions is shown in **Figure 4-5**. By setting the reboiler temperature at 90°C and the condenser temperature at 57°C, a nearly linear temperature gradient was obtained.

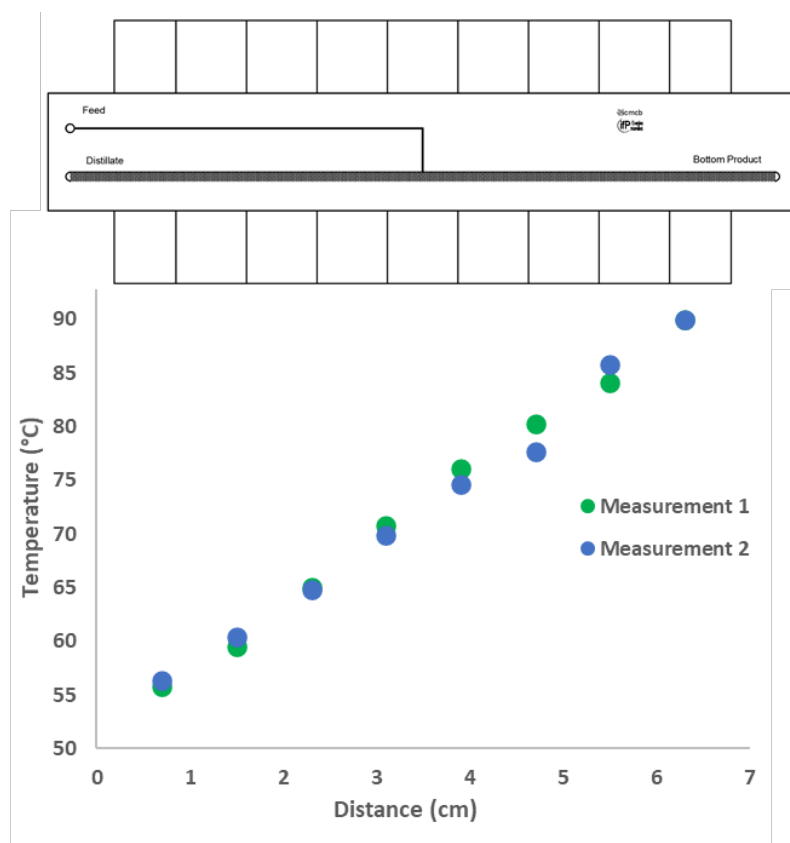


Figure 4-5 Temperature profile measured *via* thermocouple insertions.

2.4.2. Thermal camera

An infrared thermal camera (Infratec) was used to check the thermal profile of the system. The principle of operation relies on detecting the heat released by the system and converting it into an electronic signal which will be further processed to generate an image [90]. For a bottom set at 95°C and a condenser temperature at 58°C, the obtained temperature gradient is illustrated in **Figure 4-6**. Two different images were taken and shows a slight deviation from the real case because of the materials reflectance. To get rid of that, black scotch tape was used to cover the distillation channel. Thereafter, two other images were taken and are those illustrated in the bottom of **Figure 4-6**. The temperature gradient within the aluminum plate ranges between 45 and 90°C. The temperature near the feed injection is around 65°C. The outlet capillaries and the corresponding products do not appear in the different displayed images. This confirms that the products are almost recovered at room temperature. These images were taken during an ongoing distillation test.

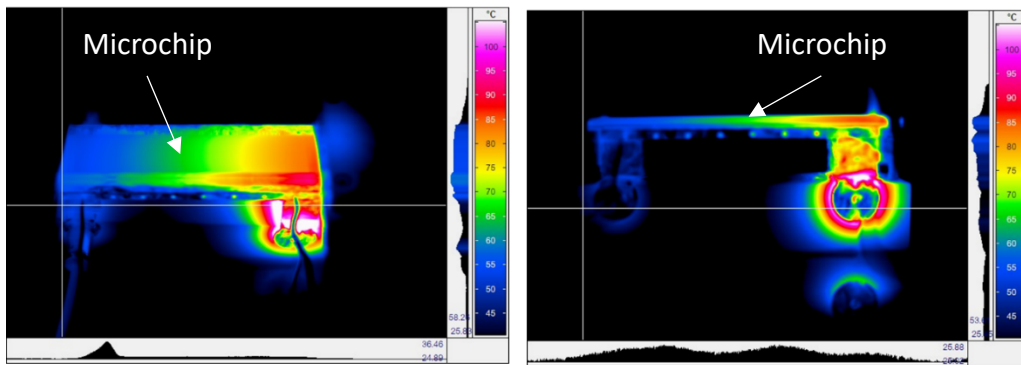


Figure 4-6 Temperature profile obtained by Infrared thermal camera.

A comparison between the theoretical temperature profile (56-95 °C) and that measured by infrared camera is illustrated in **Figure 4-7**. A slight deviation from the theoretical profile is observed. This is attributed to a slight temperature fluctuation induced by the hood ventilation since the system is not thermally isolated.

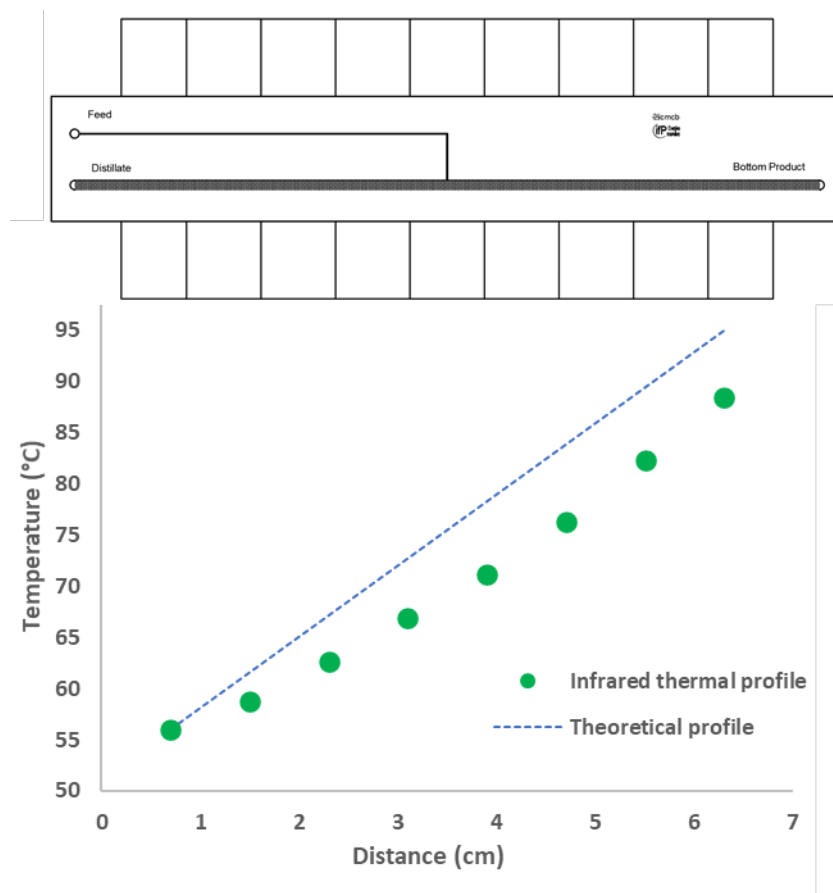


Figure 4-7 Temperature profile obtained by infrared thermal camera.

3. Experimental procedure

3.1. Distillation experiments

Before doing any experiment, a leak test is performed to check the tightness of the system. To do so, the system is pressurized at 5 barg and the pressure loss after few hours is noted. By estimating the volume of the system, the leak flow rate in NmL/h is calculated. Thereafter, this value is compared to the minimum feed flow rate that will be used within the experiments. The adopted criteria to consider the system tightness is that the leak to feed flow rate ratio must be lower than 0.1%.

Each distillation experiment is conducted within a working day. Dealing with low flow rates usually implies slow stabilization, and long experiment to gather enough sample volume for further analysis. Therefore, a tight procedure consisting of 3 main phases was adopted:

1. **Cold phase:** the binary mixture is fed at the desired flow rate at ambient temperature. The residue is withdrawn at fixed flow rate, whereas that of the distillate is free. This phase extends for 1 hour to drive the remaining gas (air) out of the channel (**Figure 4-8** and **Figure 4-9**) and ensure that the composition inside the channel is that of the feed.
2. **Heating phase:** the temperature gradient is settled along the channel. This phase lasts 1 hour to ensure that the thermal gradient is stable and that compositions at the channel outlet reach a steady state. When increasing temperature, a gas phase starts to appear (**Figure 4-10**).
3. **Distillation phase:** The gas and liquid flows are appropriately settled during this phase. Hence, quantification of the distillation experiment is done within this phase. Accordingly, samples are recovered after this phase for further delocalized analysis. The duration of this phase is 4 hours.

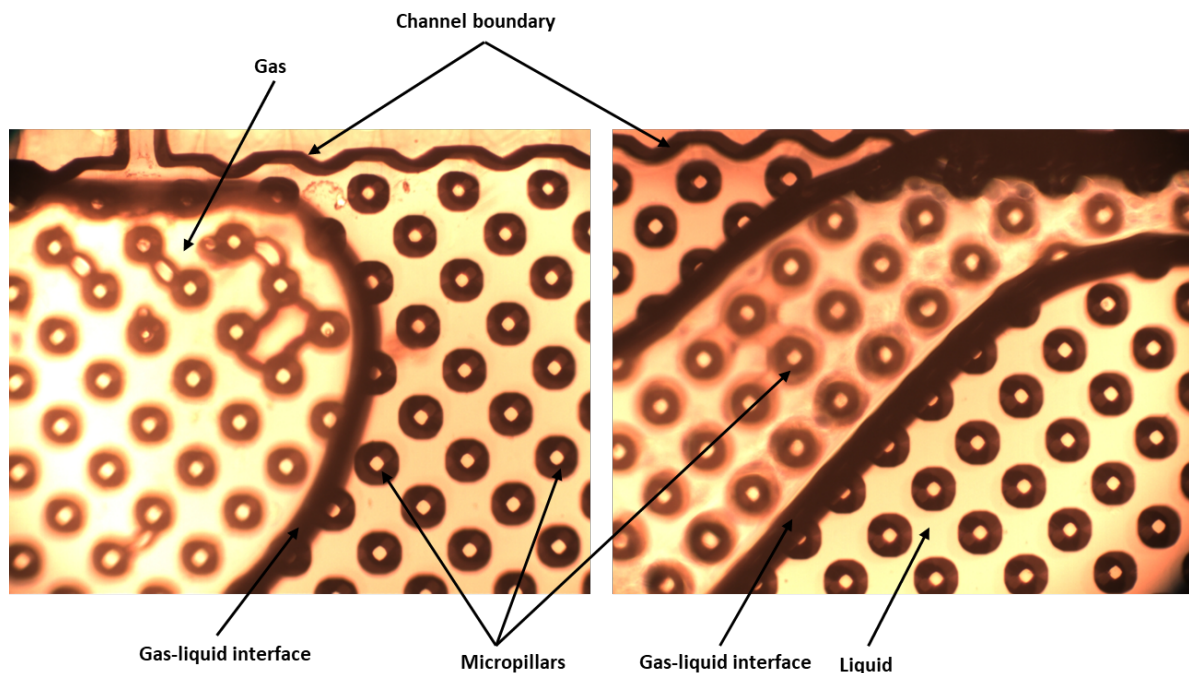


Figure 4-8 Microscopic image of the distillation channel filled with gas and liquid.

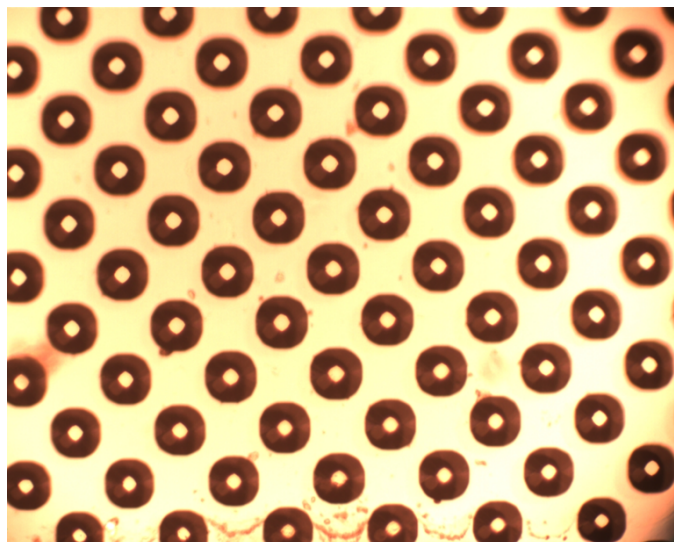


Figure 4-9 Microscopic image of the channel completely filled with liquid.

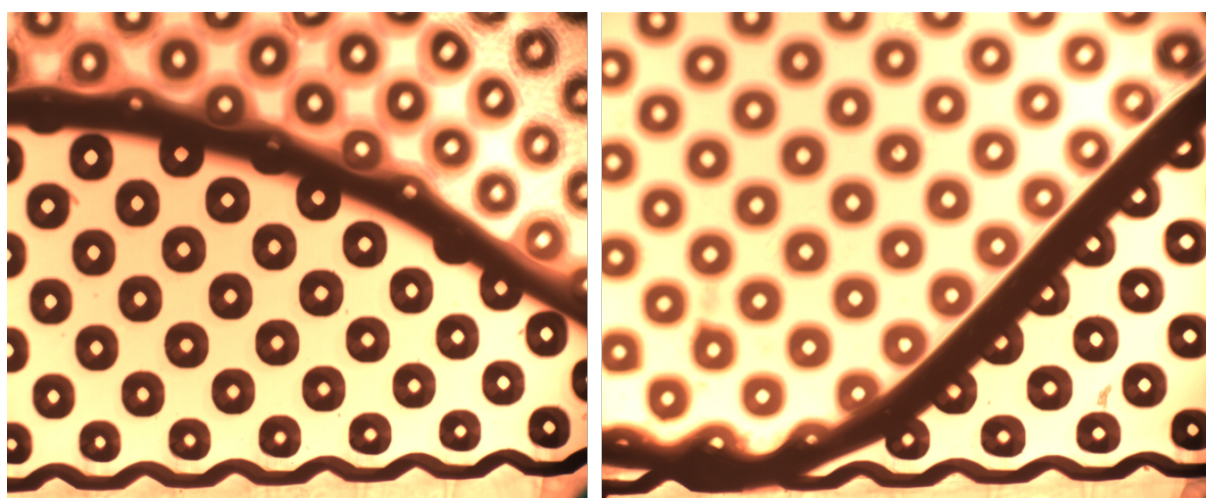


Figure 4-10 Microscopic image of the channel in the heating phase.

3.2. Mass balance

Prior to the start of each experiment, the feed syringes are purged via an outlet connected to the atmosphere in order to avoid the presence of air bubbles which may appear from one day to another due to a slight relaxation of the syringes. The syringe dedicated for the residue withdrawal is filled with 150 μL of air at a rate of 150 $\mu\text{L}/\text{min}$ before each phase to ensure a stable withdrawal rate. This was proven by preliminary tests before starting the distillation experiments and was encountered especially with low flow rates.

Vials for products recovery are weighed before and after each phase. Consequently, the mass balance of each test was calculated based on the feed flow rate and the mass of the recovered products and their composition. This allows calculation of the global mass balance of each phase as well as the mass balance with respect to each component. The experimental results considered are only those having a mass balance between 95 – 105%.

3.3. Sample characterization

To be able to evaluate the performance of the microdistillation in terms of separation efficiency, it is essential to analyze quantitatively the collected products.

Ex-situ characterization was investigated based on Gas Chromatography (GC). It is an analytical technique used to identify qualitatively and quantitatively the composition of a given sample. The apparatus is an Agilent 7890B provided with a HP-Pona column and a Flame Ionization Detector (FID). A precise volume of the liquid sample (0.25 μ L) is vaporized and mixed with the carrier gas (Helium) in a hot injector. Separation is performed on the 50 m long HP-Pona column while quantification is given by the FID. The FID is a convenient detector for organic compounds but needs a calibration when dealing with oxygenates, and is not suited for water [91]. Thus, only acetone is quantified. Ethanol is used as an internal standard and is added in a known weight concentration to the sample before it is injected.

4. Results and discussion

4.1. Experimental conditions

First distillation experiments were dedicated for the proof of concept. Once proven, the device will be used to study the impact of the various operating parameters on the separation efficiency.

Various microdistillation chips were fabricated. They all rely on the same design with a slight modification according to the experimental result. Three main chips were designed:

1. Configuration 1: gas channel completely superimposed over the whole length (~8 cm) of the liquid channel. A problem with withdrawing products in the gas phase was encountered since the two channels were superimposed until the end. Therefore, a second configuration is required,
2. Configuration 2: a shortening of the separation channel by superimposing the gas channel only on part (~6 cm) of the liquid channel has been considered. The problem was solved but the gas-liquid interface near the feed injection breaks up continuously,
3. Configuration 3: a narrowing of the feed injection line from 1000 μ m to 75 μ m, without increasing the pressure drop is considered. This is the design within which all the tests presented thereafter are done.

A noteworthy information is that from a thermodynamic point of view, if the reboiler and condenser temperatures are fixed, then a single composition of residue and distillate exists, disregarding the feed flow rate. This point was discussed in **Chapter 1 - section 3** and is well explained based on the acetone-water equilibrium curve shown in **Figure 4-11**. This was not the case for this microdistillation tool for which the product purities vary even if the reboiler and condenser temperatures were fixed. Additionally, based on the total and partial mass balances equation previously presented in **Chapter 1 - section 1.2**, the products flow rates are uncontrolled output parameters for fixed feed conditions since the products composition are thermodynamically fixed. However, it was proven by Lam *et al.* [23] that the microdistillation can be operated at various outlets flow rates and does not achieve the same separation even for a fixed temperature gradient.

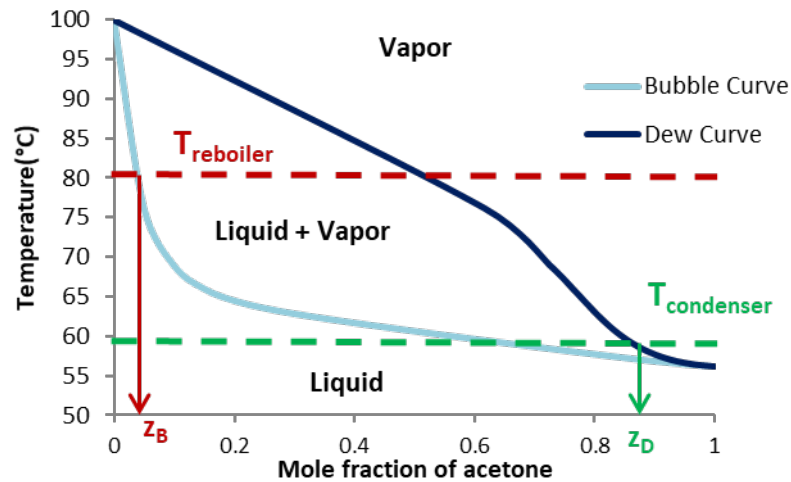


Figure 4-11 Vapor-liquid equilibrium curve of acetone water mixture at 1 atm.

The experimental plan was proposed to study the effect of feed flow rate, composition, residue flow rate and heating temperature on the performance of the developed tool. The tested feed flow rates are 200, 250 and 300 $\mu\text{L}/\text{h}$. The volumetric residue to feed flow rate ratio ranges between 0.3 and 0.6. However, the thermodynamic ratio is around 0.5. The composition of the feed varies between 0.35 and 0.75 acetone volumetric fraction. The tested distillation experiments are summarized in **Table 4-1**. A noteworthy information is that these tests are not presented in the same chronological order as they were realized.

Table 4-1 Distillation experiments conditions.

	Test Label	Feed conditions		Residue flow rate $\mu\text{L}/\text{h}$	Volumetric residue to feed flow rate ratio	Bottom temperature ($^{\circ}\text{C}$)
		Flow rate $\mu\text{L}/\text{h}$	Acetone mol%			
Feed and residue flow rate	Run_1A & B	200	20	60	0.3	90
	Run_2	250	20	75	0.3	90
	Run_3	300	20	90	0.3	90
	Run_4A & B	200	20	80	0.4	90
	Run_5A & B	250	20	100	0.4	90
	Run_6A & B	300	20	125	0.4	90
	Run_7 A to E	200	20	100	0.5	90
	Run_8A to D	250	20	125	0.5	90
	Run_9A & B	300	20	150	0.5	90
	Run_10A & B	200	20	120	0.6	90
	Run_11A to D	250	20	150	0.6	90
	Run_12A & B	300	20	180	0.6	90
Temperature	Run_13	250	20	128	0.5	95
	Run_14	300	20	154	0.5	95
	Run_15	250	20	145	0.6	80
Composition	Run_16	250	12	176	0.7	90
	Run_17	250	42	65	0.3	90

The different experimental results and the mass balances for the various distillation tests are summarized in **Appendix C** in **Table C-1** and **Table C-2**, respectively.

4.2. Preliminary results

The first distillation tests were monitored by a refractive index probe placed at the residue outlets. This probe was not calibrated but allows the on-line monitoring of the distillation experiment qualitatively. Note that the refractive index of a binary mixture is a linear combination of the composition of the mixture and the refractive indices of the pure compounds. In addition, the refractive index of acetone at room temperature is higher than that of water. Hence, by following the evolution of the refractive index curve of the residue, it is possible to predict whether the product is depleted or enriched in acetone and whether the distillation phase is stable or not. The on-line monitoring of two different distillation experiments is illustrated in **Figure 4-12**. Concerning the graph at the left of **Figure 4-12**, the distillation test (Run_5B) was triggered from another test resulting in a low refractive index at $t = 0$. Then, during the cold phase, the refractive index increases until reaching a stable value corresponding to that of the feed and confirming that the entire volume of the chip and capillaries has been renewed. This makes it possible to confirm that one hour of cold phase is sufficient for all the old volume to be evacuated. Once the heating is started, a change in refractive index at the residue level is noticed almost 20 minutes after the start of this phase. The refractive index drops until it reaches a plateau. This plateau is reached almost 1 hour after the start of this phase. Accordingly, the duration of the heating phase was set to one. Finally, the distillation phase is started for 4 hours. It can clearly be seen that the index has been stable throughout this phase. However, this was not the same result encountered with another test (Run_6A) in which the refractive index does not stabilize, and huge fluctuations are encountered. The reason for these fluctuations is not perfectly clear but could be related to the inadequacy of the operating conditions with a stable operation.

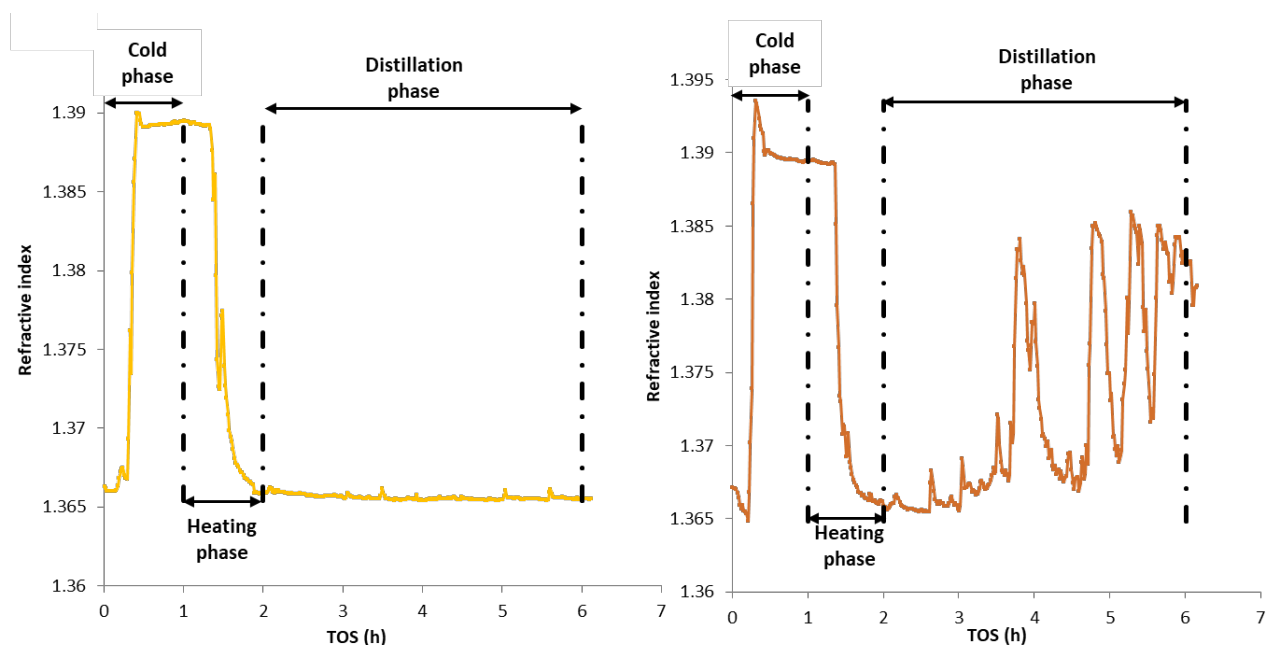


Figure 4-12 Refractive index online analysis of distillation experiments denoted Run_5B (left) and Run_6A (right).

4.3. Distillation results

The entire parametric study has been investigated with different chips having the same design. The results for the different flow rates, composition and temperature are summarized below.

It should be noted that an aging of the microdistillation was observed. Indeed, it has been observed that the performance of all devices drops with the number of tests undergone. And that even for the chip manufactured within the same batch, different results were obtained for the same operating conditions. Therefore, performances are compared for the same microchip at the same age, when possible.

The representation of the device performance in terms of distillate and residue acetone mole fraction for all the tested conditions are reviewed within the next paragraphs. Since the established reflux was not known, the estimation of NTS for all the distillation tests was done under total reflux conditions based on McCabe-Thiele method as shown in **Figure 4-13**.

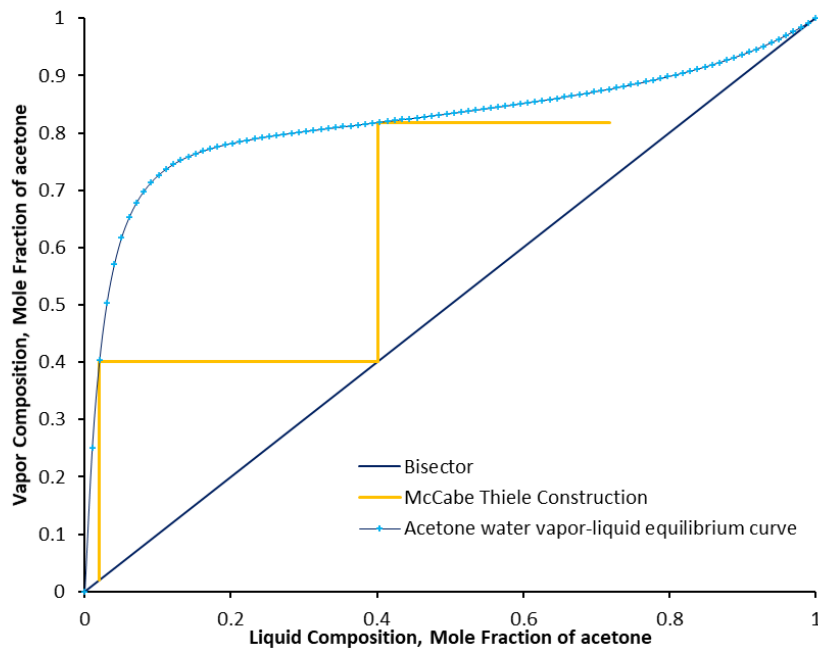


Figure 4-13 Estimation of the NTS of Run_8C based on McCabe-Thiele method under total reflux conditions.

4.3.1. Effect of feed and residue flow rates

The experimental results obtained for the effect of feed and residue flow rates on the separation efficiency are summarized in **Table 4-2**.

Table 4-2 Effect of feed and residue flow rates on the separation of 50 vol% acetone-water mixture at a heating temperature of 90°C.

Test label	Feed flow rate ($\mu\text{L/h}$)	Volumetric residue to feed flow rate ratio		mol% of acetone		NTS
		Theoretical	Experimental	Distillate	Residue	
Run_1A	200	0.3	0.2	34%	2%	0.9
Run_1B	200		0.2	14%	54%	-
Run_2	250		0.3	35%	2%	0.9
Run_3	300		0.2	28%	2%	0.7
Run_4A	200	0.4	0.4	46%	2%	1.2
Run_4B	200		0.3	11%	50%	-
Run_5A	250		0.4	45%	2%	1.2
Run_5B	250		0.4	48%	1%	1.3
Run_6A	300		0.4	39%	5%	0.6
Run_6B	300		0.2	31%	2%	0.7
Run_7A	200	0.5	0.4	66%	2%	1.6
Run_7B	200		0.4	32%	11%	0.3
Run_7C	200		0.4	32%	12%	0.3
Run_7D	200		0.4	53%	2%	1.4
Run_8A	250		0.4	55%	3%	1.2
Run_8B	250		0.4	9%	47%	-
Run_8C	250		0.5	72%	2%	1.8
Run_8D	250		0.5	40%	8%	0.5
Run_9A	300		0.3	36%	2%	0.8
Run_9B	300		0.5	30%	13%	0.3
Run_10A	200	0.6	0.5	71%	4%	1.5
Run_10B	200		0.6	38%	10%	0.4
Run_11A	250		0.5	71%	6%	1.3
Run_11B	250		0.4	12%	33%	-
Run_11C	250		0.5	46%	13%	0.5
Run_12A	300		0.5	36%	13%	0.4
Run_12B	300		0.5	13%	26%	-

Effect of feed flow rate

Let's consider the volumetric residue to feed flow rate ratio of 0.5 since it corresponds to the thermodynamic ratio obtained by the simulation of the distillation test using Proll. The acetone mole fraction in the distillate and residue for several feed flow rates is displayed in **Figure 4-14**. A decrease in the acetone mole fraction of the distillate is remarked with the increase of feed flow rate whereas that of the residue increases. This could be related to the residence time and mass transfer between both phases. As the feed flow rate increases, the residence time decreases and the mass transfer rate remains the same, hence a poorer separation occurs. As previously discussed in **Chapter 2 – section 6.4**, the performance estimation could be based on the time constant which is the ratio between the residence and diffusion time. By increasing the feed flow rate, the diffusion remains constant whereas the residence time decreases. Hence, a lower time constant is obtained and a poorer separation is achieved. The evaluation of the number of theoretical stages (NTS) based on McCabe Thiele method

are labelled on the previously illustrated graph. The performance of the device in terms of NTS, decreases with the feed flow rate, for a fixed residue to feed flow rate ratio.

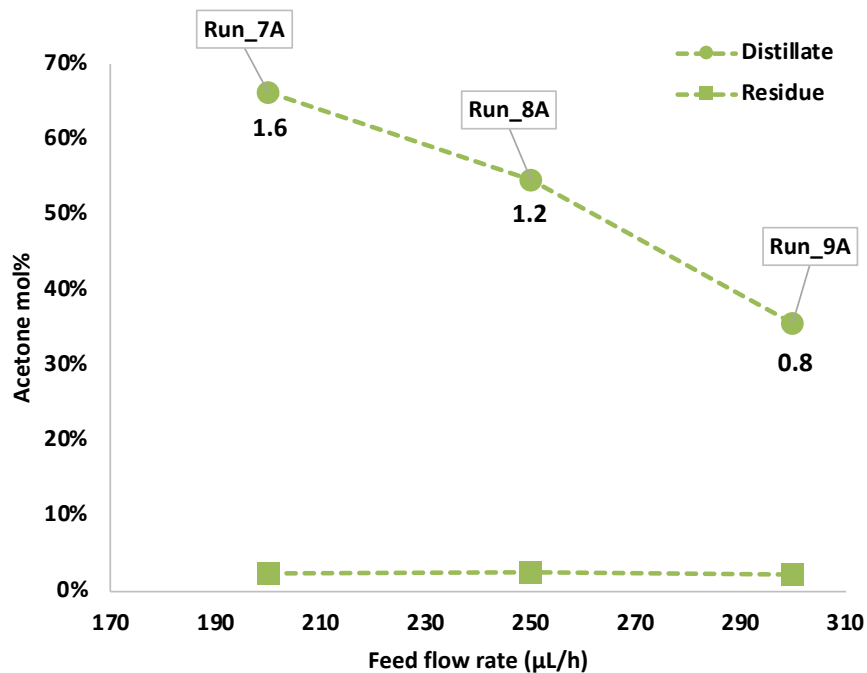


Figure 4-14 Impact of feed flow rate on the distillate and residue acetone mole fraction for a residue to feed flow rate ratio of 0.5. The labels of each point correspond to the calculated NTS.

Figure 4-15 displays the variation of products acetone mole fraction as a function of the feed flow rates for a fixed volumetric residue to feed flow rate ratio (0.3, 0.4 and 0.6). The trend was the same for all the examined ratios. The impact of fixed residue to feed flow rate ratio will be further discussed within the next paragraph. The gas-liquid mass transfer appears to be a limiting factor towards better performance. The same result was also obtained with the tool developed by Lam *et al.* as illustrated in Figure 4-16 [23]. It should be noted that the presented results within this paragraph are obtained with a chip that maintains its performance.

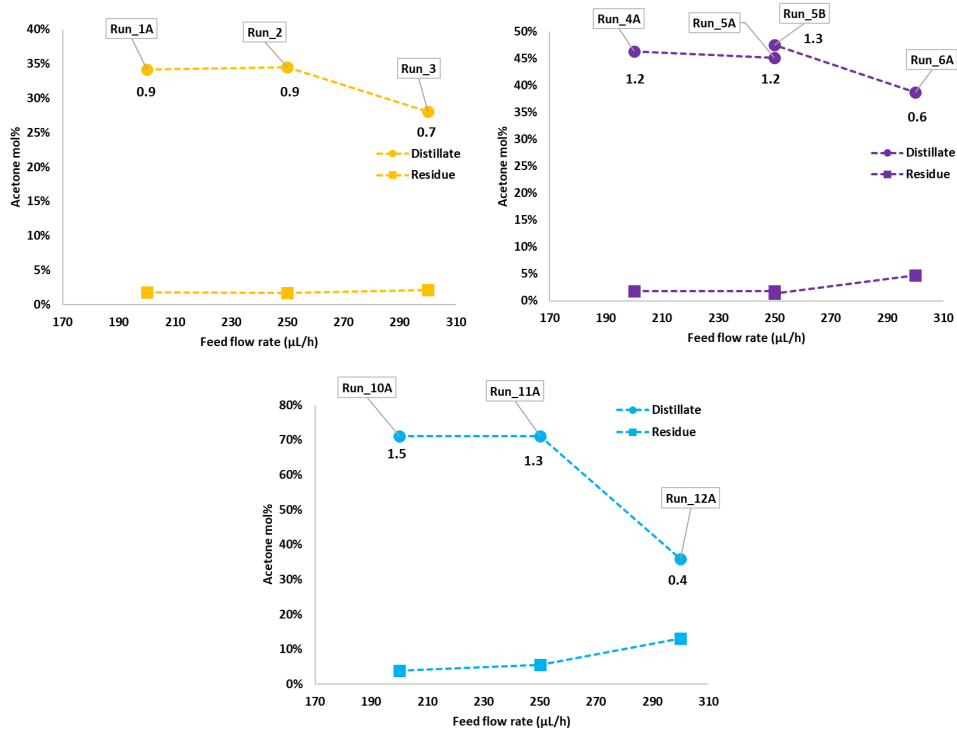


Figure 4-15 Impact of feed flow rate on the distillate and residue acetone mole fraction for a residue to feed flow rate ratio of 0.3 (yellow), 0.4 (purple) and 0.6 (blue). The labels of each point correspond to the calculated NTS.

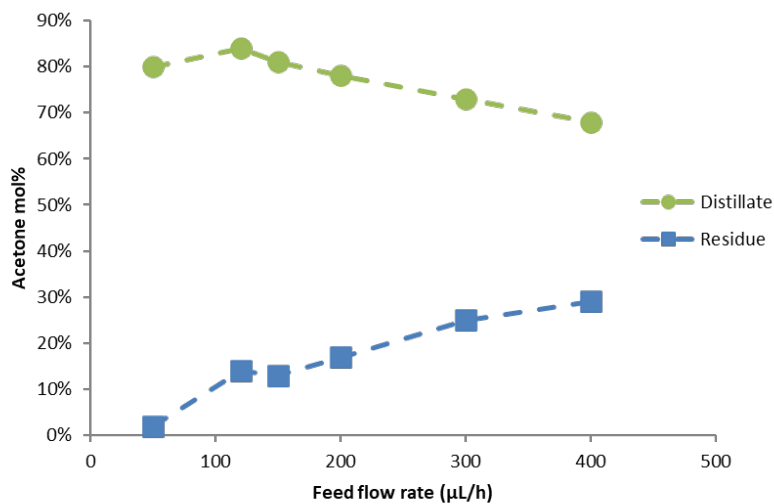


Figure 4-16 Graph showing the variation of the distillate and residue compositions as a function of the feed flow rate [23].

Effect of residue flow rate

As illustrated in the different graphs below (Figure 4-17) for several flow rates, separation by distillation has been observed for different residue to feed ratios for the same temperature gradient. This device was able to distill mixtures at several residue withdrawal flow rate for a fixed feed flow rate. Hence, a window of operating range exists rather than a single operating point. Additionally, the

experimental products purities are different from the thermodynamic ones suggesting the possibility of not reaching thermodynamic equilibrium. Another possible explanation is the difference between the measured temperature and the exact temperature of the fluid within the channel. The trend is monotonic for the three tested flow rates: better separation at higher residue to feed flow rate ratio. As observed in **Figure 4-17**, the purity of the distillate increases whereas that of the residue decreases with increasing residue flow rate for a fixed heating and cooling temperatures. This observation is in good agreement with the results obtained by Lam *et al.* [23] and is the same for the conventional distillation systems. Indeed, when the residue flow rate is increased, less high boiling components exist through the distillate, resulting in a purer distillate product. However, depending on the target of the separation, more precisely the purity of the desired product, the residue flow rate can be chosen.

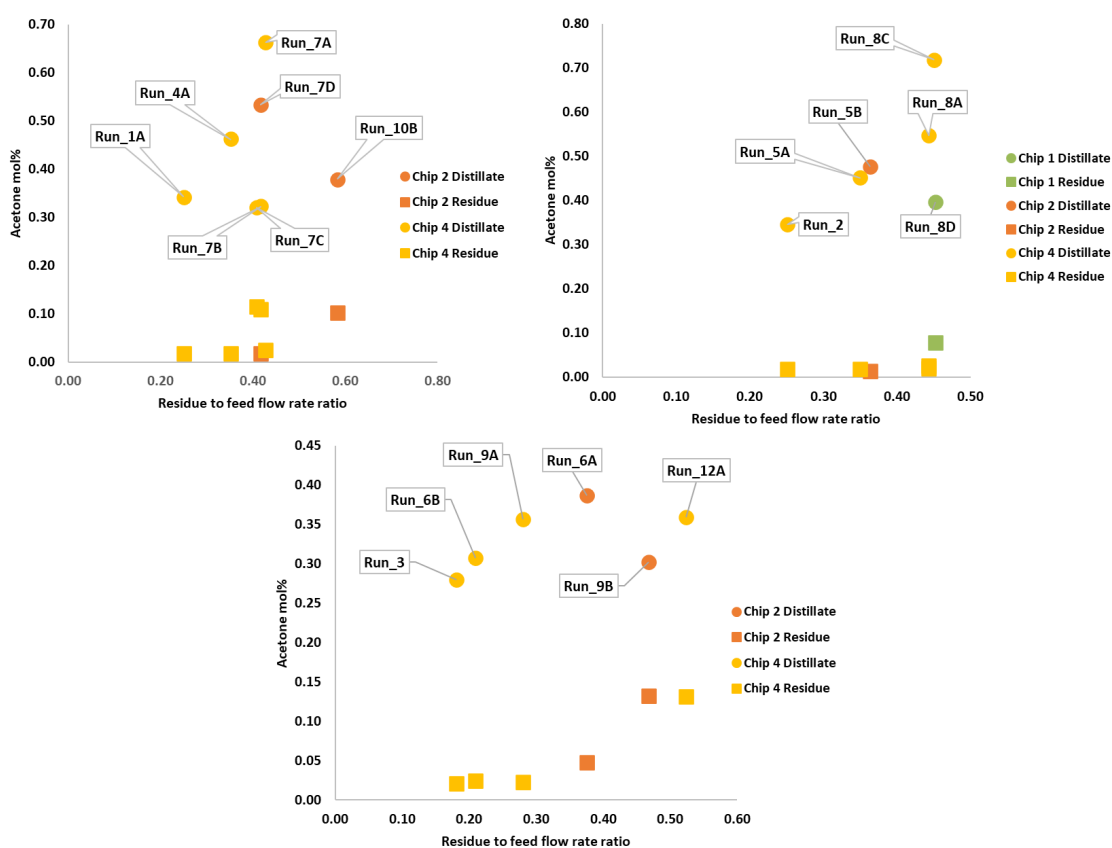


Figure 4-17 Impact of residue withdrawal flow rate on the distillate and residue composition for a feed flow rate of 200 $\mu\text{L/h}$ (top left), 250 $\mu\text{L/h}$ (top right) and 300 $\mu\text{L/h}$ (bottom).

Generally, the amount of acetone in the residue or distillate for a fixed residue to feed flow rate ratio are nearly the same for all the tested flow rates below a residue to feed flow rate ratio of 0.4 as observed in **Figure 4-18**. A clear explanation of the two different trends of acetone mole fraction in the distillate as a function of the residue to feed flow rate ratio does not exist. It might be the resultant of the aging of the microdistillation, which will be further discussed in a dedicated paragraph, or the result of an operation at high residue to feed flow rate ratios. Additionally, these tests were not all conducted with the same microchips. Even if the microchips were fabricated within the same batch, their performances are not identical.

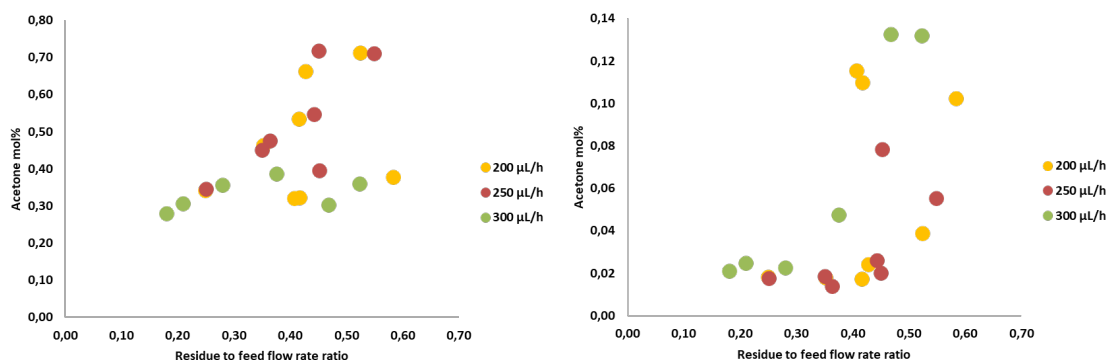


Figure 4-18 Distillate (left) and residue (right) purities as a function of the residue to feed flow rate ratio for feed flow rates of 200, 250 and 300 $\mu\text{L/h}$.

4.3.2. Effect of the reboiler temperature

The effect of heating temperature on the separation performance was studied for feed flow rates of 250 and 300 $\mu\text{L/h}$. The results are summarized in **Table 4-3**. The imposed volumetric residue to feed flow rate ratios were calculated based on the thermodynamic equilibrium diagram of acetone water, mass balances equations and the reboiler and condenser temperatures. However, as for the previous tests the experimental residue to feed flow rate ratios were arbitrary and different from the theoretical ones. Hence, the separation efficiency is not only impacted by the heating temperature but also by the residue to feed flow rate ratios. The variation of the mole fraction of acetone in the distillate and residue products as a function of the heating temperatures is illustrated in **Figure 4-19**. For the feed flow rate of 250 $\mu\text{L/h}$, the mole fraction of acetone in the distillate increases with heating temperature. However, for the reboiler temperature of 95°C, the decrease of acetone mole fraction is rather the result of the low experimental residue to feed flow rate ratio than the heating temperature. An increase in the reboiler temperature increases the generated vapor and the internally established reflux. Thus, inducing better separation. To better understand the effect of heating temperature, the residue to feed flow rate ratio must be fixed. For the feed flow rate of 300 $\mu\text{L/h}$, the mole fraction of acetone in the distillate increases with both reboiler temperature and residue to feed flow rate ratios. However, it is not possible to clearly understand the effect of heating temperature since other parameters are also varying.

Table 4-3 Effect of heating temperature on the separation of 50 vol% acetone-water mixture.

Test label	Feed flow rate ($\mu\text{L/h}$)	volumetric residue to feed flow rate ratio		mol% of acetone		Bottom temperature ($^{\circ}\text{C}$)	NTS
		Theoretical	Experimental	distillate	residue		
Run_15	250	0.6	0.5	35.4%	12.1%	80.2	0.4
Run_8C	250	0.5	0.5	71.8%	2.0%	89.8	1.8
Run_13	250	0.5	0.2	26.7%	1.5%	95.3	0.8
Run_14	300	0.5	0.5	45.8%	6.7%	95.0	0.6
Run_9A	300	0.5	0.3	35.7%	2.3%	89.7	0.8

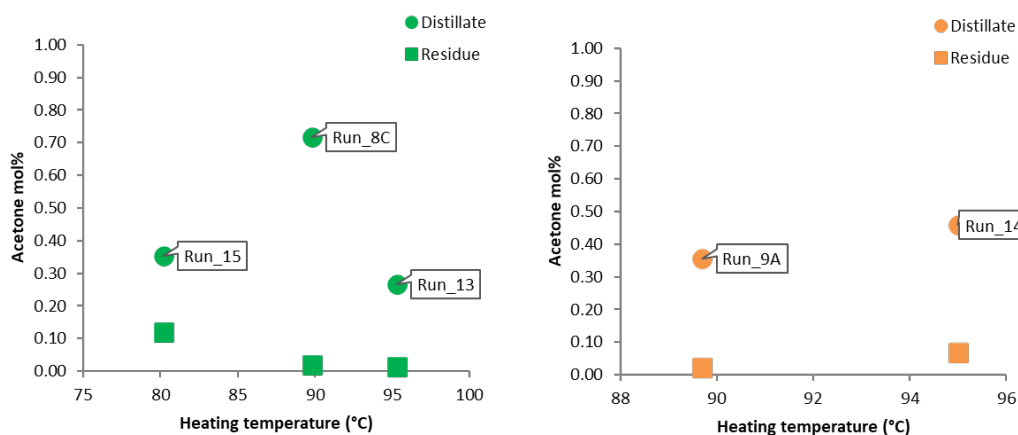


Figure 4-19 Graph showing the variation of the distillate and residue compositions as a function of the heating temperature for a feed flow rate of 250 µL/h (green) and 300 µL/h (orange).

4.3.3. Effect of feed composition

Finally, the effect of feed composition on the separation efficiency was considered. The increase in the light component in the feed results in a better separation and higher NTS. However, the performance of the Run_8C are better than that of Run_17. This might be related to the fact that both tests were done with two different microchips.

Table 4-4 Impact of feed composition on the separation performance for a feed flow rate of 250 µL/h and a heating temperature of 90°C.

Test label	Feed flow rate (µL/h)	Compositon in acetone		volumetric residue to feed flow rate ratio		mol% of acetone		NTS
		%vol	%mol	Theoretical	Experimental	distillate	residue	
Run_16	250	0.35	0.12	0.7	0.6	0.2	0.1	0.3
Run_8C	250	0.50	0.20	0.5	0.5	0.7	0.0	1.8
Run_17	250	0.75	0.42	0.3	0.2	0.6	0.1	0.8

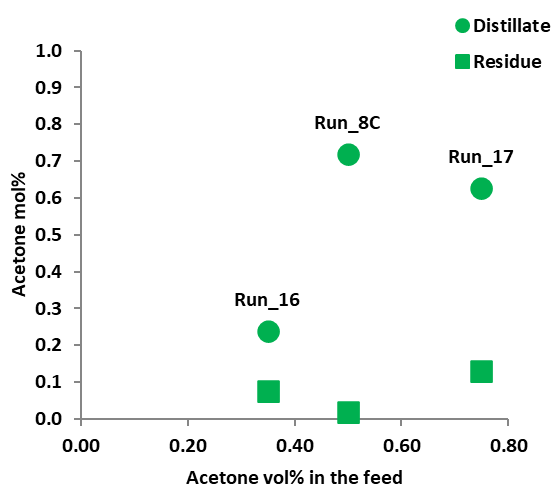


Figure 4-20 Graph showing the variation of the distillate and residue compositions as a function of feed composition for a feed flow rate of 250 µL/h and a heating temperature of 90°C.

4.3.4. Overall performances

The overall performances of the microchip are evaluated in terms of NTS per meter. These results are displayed in **Figure 4-21**. The NTS/m for the proposed design ranges between 4.6 and 29.3. The minimum value was obtained for Run_9B which corresponds to a feed flow rate of 300 $\mu\text{L/h}$ and a time constant of 21. The maximum value (29.3 stages/m) was obtained for Run_8C which was done with a newly manufactured chip. The feed flow rate and time constant in this test were 250 $\mu\text{L/h}$ and 26, respectively. These performances are better than those obtained by the most promising capillary microdistillation published in the literature. The separation within this study was almost 30 stages/m, whereas that of Lam *et al.* was of 15 stages/m [23]. It can be claimed that the proposed parameter (residence to diffusion time ratio; see **Chapter 2, section 5**) succeeds to predict the distillation performance for a newly manufactured device. However, once the performances are hindered the obtained results are far away from the predicted ones.

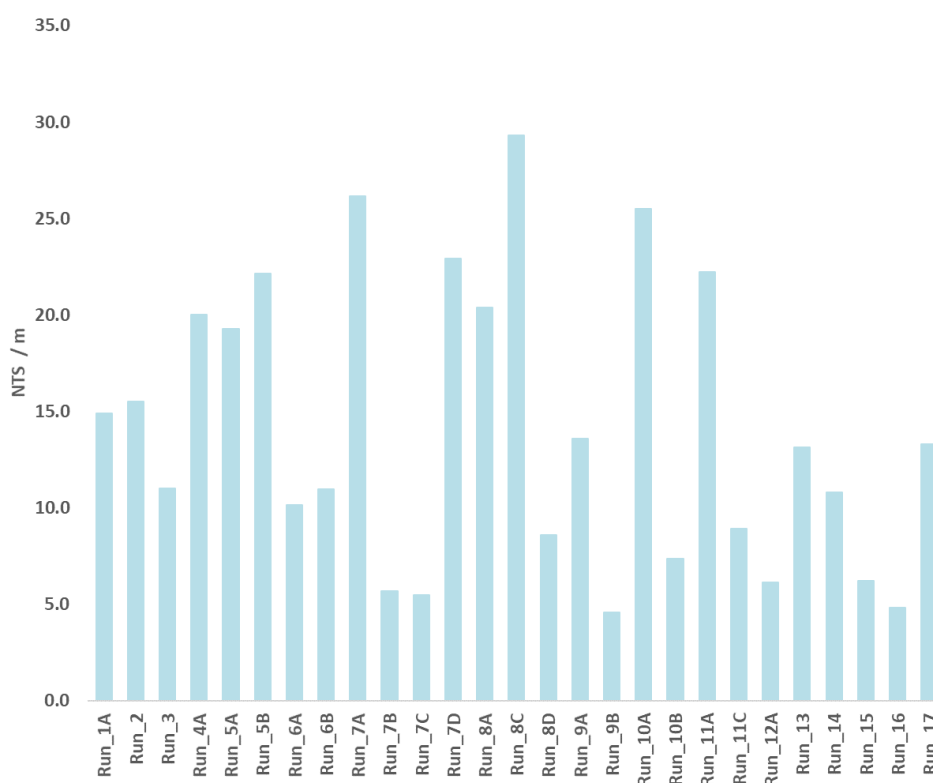


Figure 4-21 NTS per m for the various distillation tests.

Another parameter resulting in performance degradation is the number of undergone distillation tests. As aforementioned, this might be related to the change in wettability properties of the silicon micropillars region hence a decrease in the allowed capillary pressure. Repeatability has been proven in the case of consecutive distillation tests. However, if the repeatability test is performed after conducting several distillation tests with the same microchip, the results were found to be no more reproducible and separation performances decrease. Effectively, this is due to the aging of the microchannel. This is proven by the graph shown below (**Figure 4-22**). For example, run_7D was firstly done (as before mentioned, the experiments labelling was not done in a chronological order). Thereafter, Run_7A was investigated with a different microchip and has shown better performances than Run_7D. One week later, Run_7B and Run_7C were conducted. Run_7B and Run_7C displayed almost the same results, with lower separation efficiency compared to Run_7A. Accordingly, the

results were not the same even though they were investigated at the same experimental conditions (Run_7A to C). This result was also obtained for Run_8A, Run_8C and Run_8D. Run_8C was done with a different chip than Run_8D followed by Run_8A 10 days later. Run_9A and Run_9B were done with two different chips and the obtained results are close.

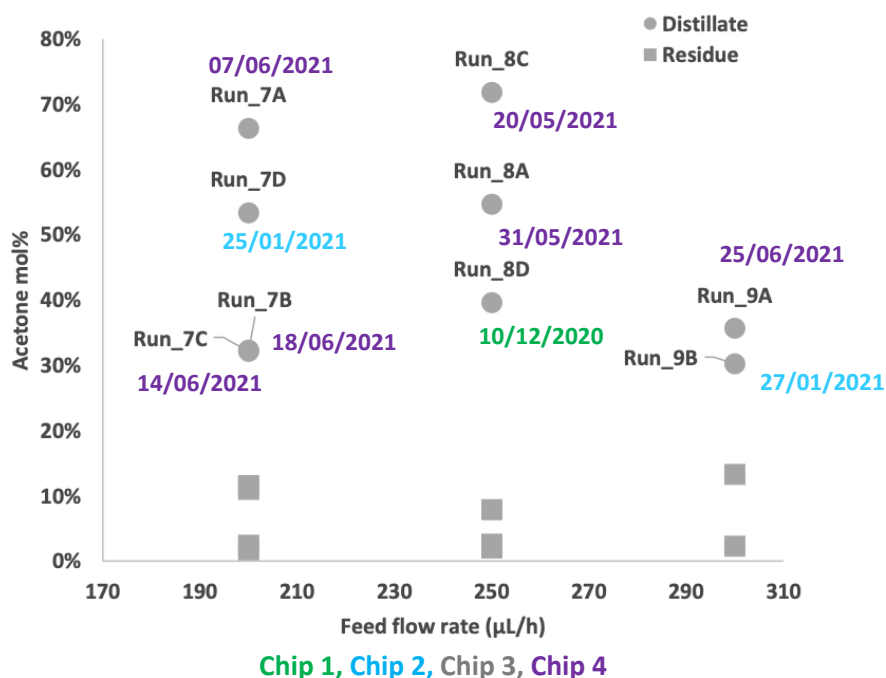


Figure 4-22 Graph showing the aging of the microdistillation.

5. In situ monitoring of distillation experiments using Raman spectroscopy

In situ monitoring was attempted using Raman microscopy in order to access the composition profile of the liquid phase while distillation is performed. The challenge is to measure the acetone concentration regardless the local temperature in the distillation chip. To do so, a calibration work was first carried on.

Prior to the calibration work, it is interesting to illustrate the acetone and water spectra. It can be seen from **Figure 4-23** that acetone has 5 different bands in Raman spectroscopy. However, the acetone band around 1700 cm^{-1} is the chosen one because it has the highest intensity among the acetone bands that does not interfere with the water band. Hence the spectra were treated using Plugim as follows:

1. Crop between 1118 cm^{-1} et stop 4829 cm^{-1} ,
2. Justifying the baseline (Baseline PCS, Baseline Length 300, Smooth filter 5, Filter factor 0.25),
3. Integrating acetone and water peaks.

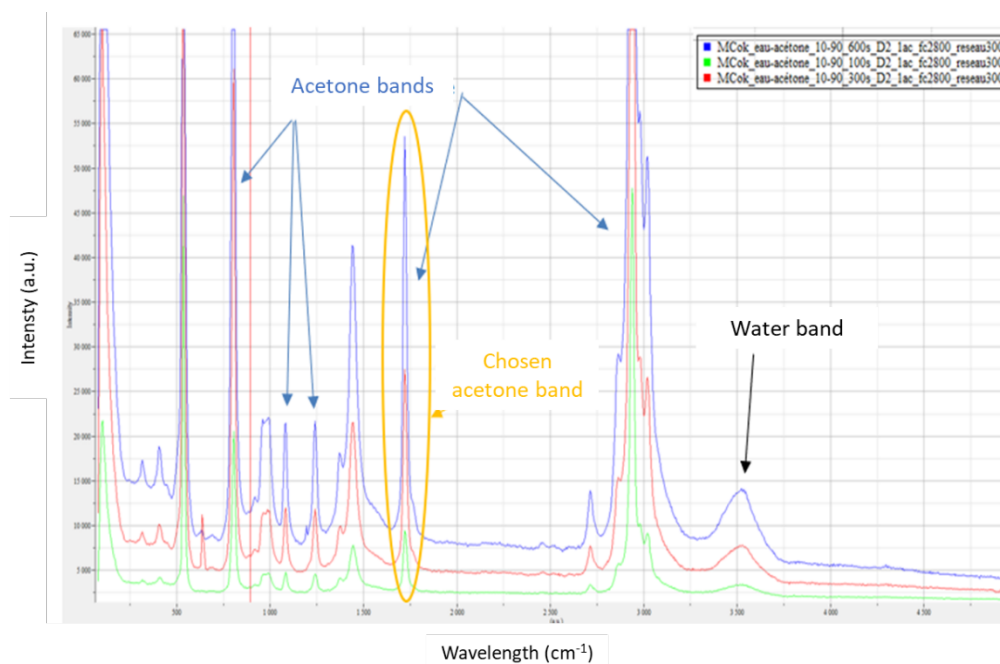


Figure 4-23 Acetone and water signature in Raman spectroscopy.

5.1. Calibration curves

A calibration curve is needed in order to track the evolution of the liquid phase composition with the microdistillation. Additionally, temperature effect was also studied. To establish this calibration curve, different acetone water mixtures were fed into the system at different temperatures. Then, the signal was recorded for all these mixtures. A plot of the intensity of acetone to water bands ratio as a function of the amount of water in the mixture is illustrated in **Figure 4-24** (left). It can be observed that the Raman signal for mixtures at room temperature (RT), 40°C and 60°C are fairly superimposable indicating that the temperature does not have a significant impact on the ratio of acetone to water intensity bands. **Figure 4-24 (right)** displays the plot of the logarithm of acetone to water intensity ratio as a function of the water content. A high linear relationship factor exists between the logarithm of the ratio of acetone to water intensity bands and the composition of the mixture. As aforementioned, no significant difference was found between the results at different temperatures for the same composition. Hence, the calibration curve was generalized for all the temperatures. This calibration curve is illustrated in **Figure 4-25**.

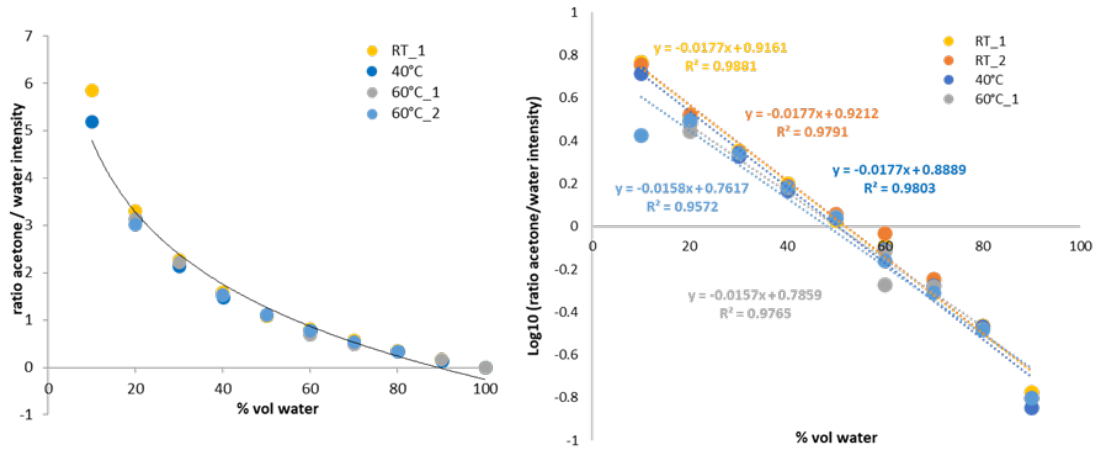


Figure 4-24 Plot of the acetone to water intensity ratio and its logarithm as a function of the water composition for several temperatures.

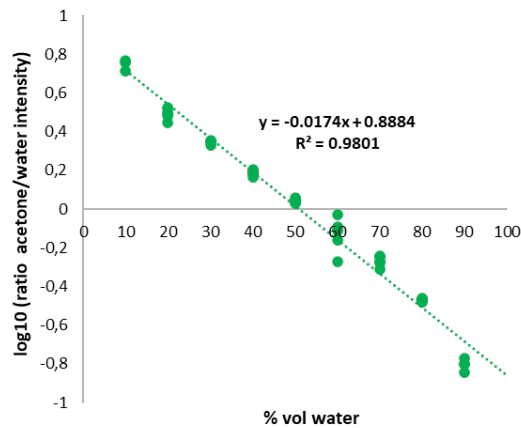


Figure 4-25 Linear correlation between the logarithm of acetone to water intensity ratio and the amount of water regardless of the mixture temperature.

5.2.Composition profile

Two distillation experiments were monitored *in situ*. The results are shown in **Figure 4-26**. GC results of the distillate and residue are also displayed on the same graphs. For the test labelled Run_7B, two different Raman measurements were done through the distillation phase. The profile composition of the liquid film within the channel is illustrated and shows a decreasing acetone amount from the condenser towards the reboiler. It can be noted that the GC results are slightly different from the composition of the liquid at both ends. A noteworthy information is that the distillation experiment is not stable during the distillation phase. The distillate and residue products are recovered for 4 hours and quantified thereafter, whereas the Raman measurements are instantaneous measurements inside the channel. The instability of the distillation phase was proven by a refractive index detector used for qualitative online analysis. The plot on the refractive index as a function of time on stream (TOS) is illustrated in **Figure 4-12** and shows that for some experiments the distillate was fully stable, whereas for others the distillation phase was not stable at all.

Moreover, the Raman measurements were focused at the edge of the channel due to the complexity of the system and the superimposed gas-liquid configurations. Concerning Run_11C, GC results are closer to the composition profile measured by Raman spectroscopy. It is also remarked for both tests that the separation does not take place through the entire distillation channel. As it can be observed, the composition is nearly constant 2 cm away from the residue outlet. This result was also obtained by Foerster *al.* [22] who found that the separation occurs only in a section of the distillation channel.

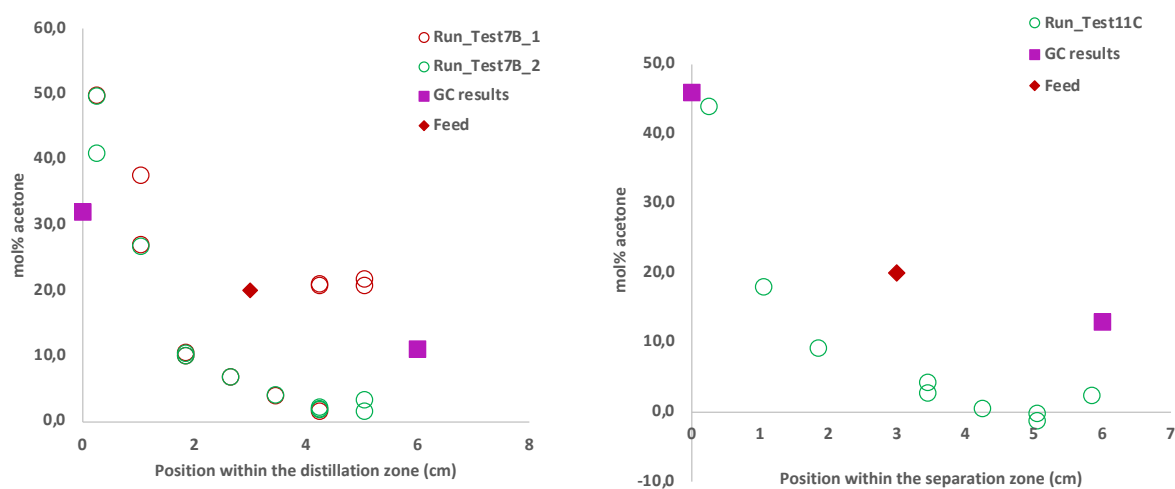


Figure 4-26 Composition profile within the chip measured with Raman spectroscopy for the conditions of the test denoted Run_Test7B (left) and Run_Test11C (right). $x=0$ and 6 are the condenser and reboiler locations, respectively.

The confidence intervals of the calculated amount of water based on the established calibration curve for Run_7B are recapitulated in **Table 4-5**. It can be clearly seen the confidence interval for all the measurements was less than 4.5 which is acceptable since it is within the measurement uncertainty.

Table 4-5 Difference for the concentration profile obtained based on the different calibration curves.

Position (cm)	Max water intensity	Acetone intensity (1700 cm^{-1})	Acetone to water intensity ratio	vol% of water	Standard deviation	C.I. 95%
0.25	2711	9472	3.5	19.8	3.4	4.2
0.25	3024	8254	2.7	26.0	3.0	3.7
1.05	8675	13517	1.6	40.0	2.2	2.7
1.85	22199	11456	0.5	67.6	1.0	1.2
1.85	13946	6938	0.5	68.5	1.0	1.2
2.65	12858	4576	0.4	76.8	1.1	1.4
3.45	21266	5381	0.3	85.4	1.5	1.8
4.25	17053	3257	0.2	92.4	1.9	2.3
4.25	22284	4369	0.2	91.7	1.8	2.3
4.25	24130	4474	0.2	93.1	1.9	2.4
5.05	13816	3177	0.2	87.7	1.6	2.0
5.05	28550	5166	0.2	93.7	1.9	2.4

6. Conclusion

The distillation performance of the newly developed microdistillation tool was evaluated within this chapter. A setup devoted to performance estimation of the microdistillation was built and validated. Despite stabilization and microchip aging issues, a parametric study was successfully conducted on the proposed design. Effects of feed flow rate, residue flow rate, feed composition and heating temperature on the separation efficiency of the developed tool were investigated.

An interesting result is the decrease of the separation efficiency with the feed flow rate for a fixed residue to feed flow rate ratio. This result is mainly related to the reduced residence time with the increase of feed flow rate and was anticipated. Hence, insufficient mass transfer between the gas and liquid phases is emphasized, which gives an insight into how to improve global performances.

Another noticeable result is the ability to adjust the residue flow rate while setting the condenser and reboiler temperatures. This is enabled by the continuous liquid phase within the microdistillation and offers new paths to adjust global performances. This parameter cannot be controlled with conventional distillation since the reboiler and condenser temperatures set products composition and flow rates. For microdistillation, it seems that either the thermal or the thermodynamic equilibrium is not yet reached inside the channel. It was found that the purity of the distillate increases and that of the residue decreases when increasing the residue to feed flow rate ratio. Since the products are withdrawn in the liquid phase, then increasing the ratio will induce a higher liquid withdrawn from the residue outlet and less high boiling component. Therefore, a purer distillate is recovered at high residue to feed flow rate ratio for a fixed feed flow rate.

The impact of heating temperature and composition on the separation efficiency were not clear since other parameters have been varied along with the reboiler temperature or the composition, specifically the residue to feed flow rate ratio. However, it seems that an increase in the reboiler temperature enhances the vapor generation and increases the internal reflux within the channel. Hence, better separation is obtained and a distillate richer in the low boiling component is recovered. Moreover, when the amount of low boiling component is increased in the feed, the amount of generated vapor near the reboiler is increased inducing a higher reflux and a better separation.

Finally, *in situ* monitoring of distillation experiments was investigated thanks to Raman spectroscopy. A calibration curve was established by plotting the logarithm of the intensity of acetone to water band as a function of the mixture composition in terms of water. Consequently, the composition profile of two distillation tests were recorded as a function of the distance within the channel. A good agreement was found between the analyzed products by GC and the composition measured by Raman spectroscopy at the outlets of the channel, even if instabilities of the distillation were noted. In fact, GC results are averaged over 4 hours while those measured by Raman spectroscopy are instantaneous. Raman spectroscopy showed that for the tested conditions, distillation occurs across two third of the microchannel.

Aging issues were encountered. This resulted in deteriorating performances over time (with the number of undergone tests), which made the parametric study quite complex. This phenomenon is not yet understood, and can be related to modification of surface interaction inside the microchip. One of them had been dried overnight under vacuum to try to investigate the issue, but unfortunately after this procedure the chip was plugged and unable to perform any distillation test.

Conclusion and perspectives

Conclusion

Classical distillation columns used in separation processes are generally large in size, therefore limiting their use to semi- or industrial processes. Hence, they are not always adapted to multiple-step continuous synthesis processes or research purposes, for which the fluids quantities and flow rates are small. Consequently, there is an increasing need for robust microdistillation units able to operate with lower fluid volumes at mL.h⁻¹ flow rates, which could be connected to the outlet of a small-scale pilot plant or research prototypes.

The main challenge associated with this kind of microdistillation process development is that it cannot be based on gravity forces anymore, which is the gas-liquid separation principle in conventional distillation column. Indeed, at the microscale, the effect of gravity fades in favor of surface forces. Thus, new designs of vapor-liquid contactors have to be considered. Capillary forces and many others are gravity alternative forces for driving the liquid phase and establishing the gas-liquid interface.

Based on this context, a state of art was done to review all the microdistillations that have been proposed and manufactured until now. They could mainly be divided in three categories, namely: (i) batch microdistillations, (ii) continuous microdistillations of intermediate size and (iii) continuous on-chip microdistillations.

The former ones were carefully reviewed in **Chapter 1 - section 2.1**. The continuous microdistillation of intermediate size either still operate with gravity forces or makes use of capillary forces to drive the liquid phase. However, in both cases they fail in reaching the desired low flow rates (typically 5 to 30 mL.h⁻¹). At this scale, especially for the gravity assisted microdistillations, most of the conventional distillation technologies remain applicable. The reflux management can still be controlled and products withdrawal was either done by liquid level control. Oppositely, on-chip microdistillation provide ways towards proper separation at low to ultra-low flow rates (0.01 to 1 mL.h⁻¹). In this later concept, the driving force of the separation process is commonly based on capillary forces. According to literature, different teams have succeeded to reduce abruptly the distillation scale toward the micrometric range by designing an on-chip microdistillation within which all the main elements of the distillation column were integrated. The microchips integrate either nanopillars or capillaries that retain the liquid phase and drive it away from the distillation zone or makes use of centrifugal forces or a membrane to separate the two-phase flow. In some other cases, multistage on-chip distillation was proven.

From all the aforementioned inventions, the most promising systems are the ones that achieve a multistage distillation in the micrometric range, such as the ones proposed by Lam *et al.* . [24]. They consist in micrometric distillations implemented on Si/Pyrex chips, where the reflux could be controlled indirectly by managing the products withdrawal flow rates. The design initially developed in this thesis was inspired from this proof of concept. However, most microdistillation studies have been reported without deep understanding of the hydrodynamic taking place within the chip; while

the comprehension of the two-phase flow is essential to relate the hydrodynamic behavior to the distillation performance.

To address these technical and fundamentals limitations and get deep insight into microdistillation processes, this PhD work had the following main objectives:

- i) to establish the design principle of an on-chip multistage distillation channel,
- ii) to develop a continuous counter-current on-chip capillary microdistillation tool and
- iii) to characterize its hydrodynamic behavior and evaluate its distillation performances.

To do so a theoretical approach was developed to guarantee that a counter-current gas-liquid flow is able to be established within the proposed design. The dimensions of the microdistillation were fixed in a way to satisfy the conditions of a stable gas liquid interface ($0 < P_g - P_l < \Delta P_c$) and guarantee sufficient time for the separation. Reproducing the concept demonstrated by Lam *et al.* [24] with our technology was not possible because of the used etching technique. Therefore, an optimized design aiming to increase the interfacial contact between both phases has been proposed. It allows to operate at high flow rates up to 500 $\mu\text{L/h}$, while maintaining a stable interface and insuring the required operational conditions.

The manufacture of the prototype has been outlined using AutoCad 2018. The silicon/Pyrex microfabrication process was selected to fabricate the microdistillation thanks to the coupling of the optical access through the Pyrex side and the thermal conductivity of silicon. The microfabrication process was carefully detailed, however it was transpired to be more complicated than expected. The execution of double etching on silicon for a channel provided with micropillars of 50 μm in diameter and 130 μm in depth turned out to be complex. Therefore, the double etching is replaced by a single etching of the silicon wafer for the liquid channel and another etching of the Pyrex wafer for the gas channel. The microdevice was made of a 27 μm deep liquid channel provided with micropillars (50 μm diameter) and a 100 μm deep gas channel. Subsequently, the two substrates are perfectly superimposed and bonded together. Once manufactured, the microchip is implemented in an experimental setup thanks to the use of compression parts.

Concerning the hydrodynamic characterization of the chip, an experimental setup was developed to study the residence time distribution of the liquid within the micropillar region for several flow rates. The RTD measurements were based on Raman spectroscopy and the step injection of a tracer. The measurements were done at the inlet and outlet of the chip by two independent experiments. Each measurement was repeated several times to reduce as possible the confidence interval and verify the results repeatability. However, reproducibility problems were identified because of the high variation of the residence time with respect to the position of the measurement and flow rate. These results indicate that the local RTD measurement is not appropriate to characterize the dispersion within the developed microdistillation tool and the global RTD approach might be more representative. However, high dispersion of the results was also expected (high dead volumes). Therefore, μPIV measurements were suggested to record the local velocity profile and study the fluid mechanics within the microdistillation channel. Additionally, a theoretical approach confirms that $K_L a$ measurement experimentally is possible. This is of high importance, since the volumetric mass transfer coefficient could be used to predict the microdistillation performance. Moreover, a CFD work has proven a plug flow behavior of the liquid phase and estimated a pressure drop within the device that is higher than the one predicted within the correlations presented in **Chapter 2**.

To measure the microdistillation performances, a specific experimental setup was developed that allows the application of a controllable temperature gradient on the chip (57°C-90°C) thanks to a combination of heating cartridges and a cooling bath generating a thermal gradient on an aluminum plate contacted with the silicon side of the microdistillation device. The injection and withdrawal were managed using Harvard programmable syringe pumps. The effects of operating parameters on the separation performance were also studied. It was found that the separation efficiency decreases with the increasing flow rate. This agreed with the time constant of the liquid phase, criterion chosen to estimate the performance. Contrary to conventional distillation columns, the residue flow rate was adjustable for a fixed thermal gradient and different performances were obtained. This was allowed by the continuous liquid film retained in the micropillar region. However, the amount of acetone in the distillate and residue was different from the thermodynamic one revealing the possibility of not reaching equilibrium. The mole fraction of the low boiling component in the distillate increases with the residue to feed flow rate ratio since more high boiling component is withdrawn from the residue outlet. The impact of heating temperature and feed composition on the separation performance was not clear because of the variation of several operating parameters simultaneously. However, the interpretation for both parameters is the same. An increase in the reboiler temperature or the amount of light component in the feed results in a higher amount of generated vapor. Hence, a higher reflux is established internally and a better separation is achieved.

Finally, *in situ* monitoring of distillation experiments with Raman spectroscopy was achieved. The composition profile within the microchannel of an ongoing distillation test was measured. A good agreement was found between the GC analysis and Raman results. This technique revealed that part of the microdistillation does not serve for distillation since the liquid composition is almost constant.

Perspectives

Concerning the design of the microdistillation channel, it is required to accurately measure the pressure drop within the microdistillation channel and suggest new designs for which the pressure drop is minimized as much as possible to prevent flooding. Additionally, interfacial area and mass transfer must be maximized while minimizing as much as possible the liquid film thickness (reducing liquid diffusion time) to enhance the separation efficiency of the microdistillation.

Measurement of mass transfer coefficients and the presence of liquid or gas backmixing are of high importance and have not been addressed in the literature yet. These are critical parameters directly linked to the performance of the device.

A better control of the temperature gradient imposed across the separation zone could be achieved *via* thin films thermocouples inserted within the microdistillation chip. Consequently, a temperature profile that sticks better with the adiabatic one could be obtained and better understanding of the phenomena governing the separation efficiency could be achieved. Unlike conventional distillations, microdistillations operate under imposed temperature gradient. Within this study, it was shown that the obtained compositions of the residue and distillate were different from the thermodynamic ones. A hypothesis was suggested that the temperature profile within the fluid is not that measured by thermocouple insertions. Hence, by accurately measuring the temperature profile, it could be proven if the distillation is only governed by thermodynamic equilibrium at the microscale or other possible phenomena interferes in the separation process at the microscale. Another hypothesis is that mass transfer is insufficient to reach the thermodynamic equilibrium.

In the case of a multicomponent mixture to distill, several distillation microchips could be used in series to achieve the separation of the mixture into its pure compound. However, this remains expensive due to the number of required devices and could be avoided by considering later withdrawal of effluents. Hence, complex mixtures could be separated into several different effluents to get closer to the operation of a conventional distillation column and achieve an efficient multicomponent separation process at the microscale.

Finally, the device must be tested under real conditions. Ideally two cases will be studied. The first one is the distillation of the effluents leaving the oligomerization reactors in IFPEN. This is an operation carried out at ambient pressure with a mixture composed of oligomers ranging from butenes to decenes with some heavy components diluted in a solvent (cyclohexane or xylene). The second case will be the separation of the effluents leaving IFPEN hydrotreatment unit.

References

- [1] A. Gorak and E. Sorensen, *Distillation: Fundamentals and Principles*, Elsevier Reference Monographs, s.l., 2014.
- [2] W. L. McCabe, J. C. Smith, and P. Hariott, *Unit Operations of Chemical Engineering*, 1956.
- [3] A. G. Loshchev, C. A. Cardona, and Y. A. Pisarenko, "Degrees of freedom analysis for a distillation column," *Theoretical Foundations of Chemical Engineering*, vol. 44, no. 5, pp. 686–697, 2010.
- [4] J.-C. CICLE, "Distillation. Absorption - Contrôle et régulation," 2615 V2, 1999.
- [5] W. S., "Distillation Internals: Trays and plates," 6/1/2020, http://www.wermac.org/equipment/distillation_part2.html.
- [6] "Distillation Column: Column Internals, Bubble cap trays, Valve trays, Sieve trays, Structured packing," 1/25/2020, http://www.wermac.org/equipment/distillation_part2.html.
- [7] Labbe Process equipment, "Internal and packing of columns: Labbe Process equipment," 7/3/2019, <https://www.labbe-france.fr/en/distillation-column/internals-of-columns/>.
- [8] Sulzer Chemtech, "Structured Packings: for Distillation, Absorption and Reactive Distillation," 5/12/2017, https://www.sulzer.com/-/media/files/products/separation-technology/liquid_liquid_extraction/brochures/structured_packings.ashx.
- [9] L. S. Hartmut Schoenmakers, "Chapter 10: Laboratory distillation and scale-up,".
- [10] L. Deibele, R. Goedecke, H. Schoenmakers, "Investigations into scale up of laboratory columns with different internal fittings," vol. 1997, May 1997.
- [11] S. Li, M. Liu, D. Hanaor et al., "Dynamics of Viscous Entrapped Saturated Zones in Partially Wetted Porous Media," *Transport in Porous Media*, vol. 125, no. 2, pp. 193–210, 2018.
- [12] D. R. Seok and S.-T. Hwang, "Zero-gravity distillation utilizing the heat pipe principle (Micro-distillation)," *AIChE Journal*, vol. 31, no. 12, pp. 2059–2065, 1985.
- [13] A. T. Sundberg, P. Uusi-Kyyny, K. Jakobsson et al., "Control of reflux and reboil flow rates for milli and micro distillation," *Chemical Engineering Research and Design*, vol. 91, no. 5, pp. 753–760, 2013.
- [14] A. T. Sundberg, P. Uusi-Kyyny, and V. Alopaeus, "The use of microplants in process development— Case study of etherification of 2-ethoxy-2-methylbutane," *Chemical Engineering and Processing: Process Intensification*, vol. 74, pp. 75–82, 2013.
- [15] A. T. Sundberg, P. Uusi-Kyyny, K. Jakobsson, et al., eds., *Development and modeling of micro distillation column*, 2010.
- [16] A. T. Sundberg, P. Uusi-Kyyny, and V. Alopaeus, "Novel micro-distillation column for process development," *Chemical Engineering Research and Design*, vol. 87, no. 5, pp. 705–710, 2009.
- [17] A. L. Tonkovich, K. Jarosch, R. Arora et al., "Methanol production FPSO plant concept using multiple microchannel unit operations," *Chemical Engineering Journal*, 135S, S2-S8, 2008.
- [18] X. Huang, D. King, F. Zheng et al., "Hydrodesulfurization of JP-8 fuel and its microchannel distillate using steam reformat," *Catalysis Today*, vol. 136, 3-4, pp. 291–300, 2008.
- [19] F. Zheng, V. Stenkamp, W. TeGrotenhuis, et al., eds., *Microchannel Distillation of Jp-8 Jet Fuel for Sulfur Content Reduction*, 2006.
- [20] A. L. Tonkovich, W. W. Simmons, L. Silva et al., *Distillation process using microchannel technology*, Jul. 8, 2005.
- [21] W. TeGrotenhuis and V. Stenkamp, *Conditions for fluid separations in microchannels, capillary-driven fluid separations, and laminated devices capable of separating fluids*, Apr.5, 2005.
- [22] M. Foerster, K. F. Lam, E. Sorensen et al., "In situ monitoring of microfluidic distillation," *Chemical Engineering Journal*, vol. 227, pp. 13–21, 2013.
- [23] K. F. Lam, E. Sorensen, and A. Gavriilidis, "Towards an understanding of the effects of operating conditions on separation by microfluidic distillation," *Chemical Engineering Science*, vol. 66, no. 10, pp. 2098–2106, 2011.
- [24] K. F. Lam, E. Cao, E. Sorensen et al., "Development of multistage distillation in a microfluidic chip," *Lab on a chip*, vol. 11, no. 7, pp. 1311–1317, 2011.

- [25] K. F. Lam, E. Sorensen, and A. Gavriilidis, eds., *On-chip microscale distillation for acetone-water separation*, 2010.
- [26] B. Stanisch, T. Wellsandt, and J. Strube, "Development of Micro Separation Technology Modules. Part 2: Distillation," *Chemie Ingenieur Technik*, vol. 87, no. 9, pp. 1207–1214, 2015.
- [27] A. Hibara, K. Toshin, T. Tsukahara et al., "Microfluidic distillation utilizing micro–nano combined structure," *Chemistry Letters*, vol. 37, no. 10, pp. 1064–1065, 2008.
- [28] J. M. MacInnes, J. Ortiz-Osorio, P. J. Jordan et al., "Experimental demonstration of rotating spiral microchannel distillation," *Chemical Engineering Journal*, vol. 159, 1-3, pp. 159–169, 2010.
- [29] D. A. Boyd, J. R. Adleman, D. G. Goodwin et al., "Chemical separations by bubble-assisted interphase mass-transfer," *Analytical chemistry*, vol. 80, no. 7, pp. 2452–2456, 2008.
- [30] H. Fink and Hampe M., "Designing and Constructing Microplants," *Microreaction Technology: Industrial Prospects*, pp. 664–673, 2000.
- [31] A. Kane, H. Monnier, D. Tondeur et al., "Capability of a falling film microstructured contactor for the separation of binary mixtures," *Chemical Engineering Journal*, vol. 167, 2-3, pp. 455–467, 2011.
- [32] A. Zogas, V. Cominos, G. Kolb et al., "Development of a Microrectification Apparatus for Analytical and Preparative Applications," *Chemical Engineering & Technology*, vol. 35, no. 1, pp. 58–71, 2012.
- [33] W.-J. Ju, L.-M. Fu, R.-J. Yang et al., "Distillation and detection of SO₂ using a microfluidic chip," *Lab on a chip*, vol. 12, no. 3, pp. 622–626, 2012.
- [34] L. A. N. Dayao, C.-C. Liu, S.-Y. Hsu et al., "Multifunctional microchip-based distillation apparatus II - Aerated distillation for sulfur dioxide detection," *Analytica chimica acta*, vol. 1071, pp. 44–52, 2019.
- [35] C.-C. Liu, Y.-N. Wang, L.-M. Fu et al., "Micro-distillation system for formaldehyde concentration detection," *Chemical Engineering Journal*, vol. 304, pp. 419–425, 2016.
- [36] S.-Y. Hsu, C.-C. Liu, C.-E. Yang et al., "Multifunctional microchip-based distillation apparatus I - Steam distillation for formaldehyde detection," *Analytica chimica acta*, vol. 1062, pp. 94–101, 2019.
- [37] Y.-N. Wang, C.-C. Liu, R.-J. Yang et al., "Microfluidic distillation chip for methanol concentration detection," *Analytica chimica acta*, vol. 912, pp. 97–104, 2016.
- [38] G. F. Giordano, L. C. S. Vieira, A. L. Gobbi et al., "Gravity-assisted distillation on a chip: Fabrication, characterization, and applications," *Analytica chimica acta*, vol. 1033, pp. 128–136, 2018.
- [39] T. Mansfeldt and H. Biernath, "Determination of total cyanide in soils by micro-distillation," *Analytica chimica acta*, vol. 406, no. 2, pp. 283–288, 2000.
- [40] R. Chueachot and S. Chanthai, "Spectrophotometric Determination of Trace Cyanide in Fruit Wines by the Catalytic Reaction of Ninhydrin following Micro-distillation," *Oriental Journal of Chemistry*, vol. 30, no. 1, pp. 119–131, 2014.
- [41] S. Mardani, L. S. Ojala, P. Uusi-Kyyny et al., "Development of a unique modular distillation column using 3D printing," *Chemical Engineering and Processing: Process Intensification*, vol. 109, pp. 136–148, 2016.
- [42] T. H. Chilton and A. P. Colburn, "Distillation and absorption in packed columns: A convenient design and correlation method," 1935.
- [43] A. T. Sundberg, P. Uusi-Kyyny, and V. Alopaeus, "Microscale distillation," *Russian Journal of General Chemistry*, vol. 82, no. 12, pp. 2079–2087, 2012.
- [44] L. Silva, R. Arora, A. Tonkovich, T. Hickey, ed., *High mass transfer efficiency with integrated heat transfer*.
- [45] H. J. Hwang, K. He, S. Gray et al., "Direct contact membrane distillation (DCMD): Experimental study on the commercial PTFE membrane and modeling," *Journal of Membrane Science*, vol. 371, 1-2, pp. 90–98, 2011.
- [46] S. H. Cypes, S. Bergh, and Hajduk D., *Microscale flash separation of fluid mixtures*, Sep.14, 2006.
- [47] R. L. Hartman, H. R. Sahoo, B. C. Yen et al., "Distillation in microchemical systems using capillary forces and segmented flow," *Lab on a chip*, vol. 9, no. 13, pp. 1843–1849, 2009.

- [48] R. L. Hartman, J. R. Naber, S. L. Buchwald et al., "Multistep microchemical synthesis enabled by microfluidic distillation," *Angewandte Chemie (International ed. in English)*, vol. 49, no. 5, pp. 899–903, 2010.
- [49] R. C. R. Wootton and A. J. DeMello, "Continuous laminar evaporation: micron-scale distillation," *Chemical communications (Cambridge, England)*, no. 3, pp. 266–267, 2004.
- [50] K. F. Lam, E. Sorensen, and A. Gavriilidis, "Review on gas–liquid separations in microchannel devices," *Chemical Engineering Research and Design*, vol. 91, no. 10, pp. 1941–1953, 2013.
- [51] S. H. Cypes and J. R. Engstrom, "Analysis of a toluene stripping process: a comparison between a microfabricated stripping column and a conventional packed tower," *Chemical Engineering Journal*, vol. 101, 1-3, pp. 49–56, 2004.
- [52] Y. Zhang, S. Kato, and T. Anazawa, "Vacuum membrane distillation on a microfluidic chip," *The Royal Society of Chemistry*, no. 19, pp. 2750–2752, 2009.
- [53] Y. Zhang, S. Kato, and T. Anazawa, "Vacuum membrane distillation by microchip with temperature gradient," *Lab on a chip*, vol. 10, no. 7, pp. 899–908, 2010.
- [54] C. Adiche and K. Sundmacher, "Experimental investigation on a membrane distillation based micro-separator," *Chemical Engineering and Processing: Process Intensification*, vol. 49, no. 4, pp. 425–434, 2010.
- [55] A. Lautenschleger, E. Y. Kenig, A. Voigt et al., "Model-based analysis of a gas/vapor-liquid microchannel membrane contactor," *AIChE Journal*, vol. 61, no. 7, pp. 2240–2256, 2015.
- [56] Alain BRICARD and Serge CHAUDOURNE, "Caloducs," B 9 545.
- [57] P. Nemeč, A. Čaja, and M. Malcho, "Mathematical model for heat transfer limitations of heat pipe," *Mathematical and Computer Modelling*, vol. 57, 1-2, pp. 126–136, 2013.
- [58] J. Bonjour, F. Lefèvre, V. Sartre et al., "Systèmes diphasiques de contrôle thermique - Thermosiphons et caloducs," 2010.
- [59] A. Bricard and S. Chaudourne, "Caloducs,".
- [60] T. H. Chilton/A. P. Colburn, "Distillation and Absorption in Packed Columns A Convenient Design and Correlation Method," *Industrial and engineering chemistry*, vol. 27, no. 3, 1935.
- [61] J. Boussinesq, "Mémoire sur l'influence des frottements dans les mouvements réguliers des fluides," *Journal de mathématiques pures et appliquées*, vol. 13, no. 2, pp. 377–424, 1868.
- [62] M. K. Chyu, "Heat transfer and pressure drop for short pin-fin arrays," vol. 112, no. 4, pp. 926–932, 1990.
- [63] Ali Koşar, Chandan Mishra, and Yoav Peles, "Laminar flow across a bank of low aspect ratio micro pin fins," *Journal of fluids engineering*, vol. 127, pp. 418–430, 2005.
- [64] R. S. Prasher, J. Dirner, J.-Y. Chang et al., "Nusselt number and friction factor of staggered arrays of low aspect ratio micropin-fins under cross flow for water as fluid," *Journal of heat transfer*, vol. 129, 2007.
- [65] Gaddis Edward Shafik, Gnielinski Volker, "Pressure drop in cross flow across tube bundles," *International Chemical Enigneering*, vol. 25, no. 1, 1985.
- [66] J. F. Tullius, T. K. Tullius, and Y. Bayazitoglu, "Optimization of short micro pin fins in minichannels," *International Journal of Heat and Mass Transfer*, vol. 55, 15-16, pp. 3921–3932, 2012.
- [67] N. S. K. Gunda, J. Joseph, A. Tamayol et al., "Measurement of pressure drop and flow resistance in microchannels with integrated micropillars," *Microfluidics and Nanofluidics*, vol. 14, 3-4, pp. 711–721, 2013.
- [68] J. Kozeny, ed., *Ueber kapillare leitung des wassers im boden*, 1927.
- [69] P.C. Carman, "Fluid flow through granular beds," *Transactions, Institution of Chemical Engineers, London*, vol. 15, pp. 150–166, 1937.
- [70] P.C. Carman, *Flow of gases through porous media.*, Butterworths Scientific Publications, London, 1956.
- [71] Sabri Ergün, Fluid Flow Through Packed Columns, *Chemical Engineering Progress*, Vol. 48, 1952, "Fluid flow through packed columns," *Chemical Engineering Progress*, vol. 48, 1952.

- [72] J. Mita and W. Qu, "Pressure drop of water flow across a micro-pin-fin array part 1: Isothermal liquid single-phase flow," *International Journal of Heat and Mass Transfer*, vol. 89, pp. 1073–1082, 2015.
- [73] A. M. Siu-Ho, W. Qu, and F. Pfefferkorn, eds., *Hydrodynamic and thermal characteristics of single-phase and two-phase micro-pin-fin heat sinks*, 2007.
- [74] N. K. Karadimitriou, M. Musterd, P. J. Kleingeld et al., "On the fabrication of PDMS micromodels by rapid prototyping, and their use in two-phase flow studies," *Water Resources Research*, vol. 49, no. 4, pp. 2056–2067, 2013.
- [75] M. Kim, A. Sell, and D. Sinton, "Aquifer-on-a-chip: understanding pore-scale salt precipitation dynamics during CO₂ sequestration," *Lab on a chip*, vol. 13, no. 13, pp. 2508–2518, 2013.
- [76] M. Sohrabi, A. Danesh, D. H. Tehrani et al., "Microscopic mechanisms of oil recovery by near-miscible gas injection," *Transport in Porous Media*, vol. 72, no. 3, pp. 351–367, 2008.
- [77] N. K. Karadimitriou, V. Joekar-Niasar, S. M. Hassanizadeh et al., "A novel deep reactive ion etched (DRIE) glass micro-model for two-phase flow experiments," *Lab on a chip*, vol. 12, no. 18, pp. 3413–3418, 2012.
- [78] E. R. Murphy, T. Inoue, H. R. Sahoo et al., "Solder-based chip-to-tube and chip-to-chip packaging for microfluidic devices," *Lab on a chip*, vol. 7, no. 10, pp. 1309–1314, 2007.
- [79] R. M. Tiggelaar, F. Benito-López, D. C. Hermes et al., "Fabrication, mechanical testing and application of high-pressure glass microreactor chips," *Chemical Engineering Journal*, vol. 131, 1–3, pp. 163–170, 2007.
- [80] S. Marre, A. Adamo, S. Basak et al., "Design and packaging of microreactors for high pressure and high temperature applications," *Industrial & Engineering Chemistry Research*, vol. 49, no. 22, pp. 11310–11320, 2010.
- [81] S. K. Luther and A. Braeuer, "High-pressure microfluidics for the investigation into multi-phase systems using the supercritical fluid extraction of emulsions (SFEE)," *The Journal of Supercritical Fluids*, vol. 65, pp. 78–86, 2012.
- [82] S. Marre, Y. Roig, and C. Aymonier, "Supercritical microfluidics: Opportunities in flow-through chemistry and materials science," *The Journal of Supercritical Fluids*, vol. 66, pp. 251–264, 2012.
- [83] R. Edwin Oosterbroek, J. W. (Erwin) Berenschot, Henri V. Jansen, A. Jasper Nijdam, Grégory Pandraud, Albert van den Berg, and Miko C. Elwenspoek, "Etching methodologies in <111> - oriented silicon wafers -," *Journal of microelectromechanical Systems*, vol. 9, no. 3, pp. 390–398, 2000.
- [84] J. Villiermaux, *Génie de la réaction chimique: conception et fonctionnement des réacteurs*, Lavoisier TEC & DOC, 1993.
- [85] S. Kuhn and K. F. Jensen, "A pH-sensitive laser-induced fluorescence technique to monitor mass transfer in multiphase flows in microfluidic devices," *Industrial & Engineering Chemistry Research*, vol. 51, no. 26, pp. 8999–9006, 2012.
- [86] H. Niu, L. Pan, H. Su et al., "Flow pattern, pressure drop, and mass transfer in a gas-liquid concurrent two-phase flow microchannel reactor," *Industrial & Engineering Chemistry Research*, vol. 48, no. 3, pp. 1621–1628, 2009.
- [87] M. Sattari-Najafabadi, M. Nasr Esfahany, Z. Wu et al., "Mass transfer between phases in microchannels: A review," *Chemical Engineering and Processing - Process Intensification*, vol. 127, pp. 213–237, 2018.
- [88] J. Tan, Y. C. Lu, J. H. Xu et al., "Mass transfer performance of gas-liquid segmented flow in microchannels," *Chemical Engineering Journal*, 181-182, pp. 229–235, 2012.
- [89] L. Hegely, J. Roesler, P. Alix et al., "Absorption methods for the determination of mass transfer parameters of packing internals: A literature review," *AIChE Journal*, vol. 63, no. 8, pp. 3246–3275, 2017.
- [90] Lynred, "Infrared technology and thermal cameras," 7/8/2021, <https://www.lynred.com/blog/infrared-technology-and-thermal-cameras-how-they-work>.
- [91] Zhendi Wang and J. R. Jocelyn Paré, "Gas Chromatography (GC): Principles and Applications," *Instrumental methods in food analysis*, 1997.

- [92] R. U. A Žukauskas, *Banks of plain and finned tubes*, Hemisphere publishing corporation, 1983.
- [93] B. Elliott Short, Peter E. Raad, and Donald C. Price, "Performance of pin fin cast aluminum coldwalls, Part 1: friction factor correlations," *Journal of thermophysics and heat transfer*, vol. 16, no. 3, 2002.
- [94] K. A. Moores, J. Kim, and Y. K. Joshi, "Heat transfer and fluid flow in shrouded pin fin arrays with and without tip clearance," *International Journal of Heat and Mass Transfer*, vol. 52, 25-26, pp. 5978–5989, 2009.
- [95] Kevin A. Moores and Yogendra K. Joshi, "Effect of tip clearance on the thermal and hydrodynamic performance of a shrouded pin fin array," *Journal of heat transfer*, vol. 125, pp. 999–1006, 2003.
- [96] S. W. Chang, T. L. Yang, C. C. Huang et al., "Endwall heat transfer and pressure drop in rectangular channels with attached and detached circular pin-fin array," *International Journal of Heat and Mass Transfer*, vol. 51, 21-22, pp. 5247–5259, 2008.
- [97] Peter J. Larkin, ed., *Infrared and raman spectroscopy: Principles and spectral interpretation*, Elsevier, Stanford, CT, United States, 2018.

Appendices

Appendix A

Table A- 1 Friction factor correlations for single-phase flow within micropillars region

References	Range of validity	Friction factor correlation																																																																																																																																																																																						
Zukauskas and Ulinskas [92]	<u>Circular in-line and staggered tube banks</u>	$f = 0.25 * \left(c_0 + \frac{c_1}{Re_\mu^{\alpha_1}} + \frac{c_2}{Re_\mu^{\alpha_2}} + \frac{c_3}{Re_\mu^{\alpha_3}} + \frac{c_4}{Re_\mu^{\alpha_4}} \right) * K_1$ <table border="1"> <thead> <tr> <th>Arrangement</th> <th>Condition</th> <th>Re</th> <th>c₀</th> <th>c₁</th> <th>c₂</th> <th>c₃</th> <th>c₄</th> <th>α₁</th> <th>α₂</th> <th>α₃</th> <th>α₄</th> </tr> </thead> <tbody> <tr> <td rowspan="5">In-line</td> <td rowspan="2">$\frac{S_L}{D} = 1.25$</td> <td>3<Re<2.10³</td> <td>0.272</td> <td>207</td> <td>102</td> <td>-286</td> <td>0</td> <td>1</td> <td>2</td> <td>3</td> <td>0</td> </tr> <tr> <td>3<Re<2.10³</td> <td>0.272</td> <td>207</td> <td>102</td> <td>-286</td> <td>0</td> <td>1</td> <td>2</td> <td>3</td> <td>0</td> </tr> <tr> <td rowspan="2">$\frac{S_L}{D} = 1.5$</td> <td>2*10³<Re<2*10⁶</td> <td>0.267</td> <td>2490</td> <td>-927*10⁴</td> <td>10¹⁰</td> <td>0</td> <td>1</td> <td>2</td> <td>3</td> <td>0</td> </tr> <tr> <td>3<Re<2*10³</td> <td>0.263</td> <td>86.7</td> <td>-2.02</td> <td>0</td> <td>0</td> <td>1</td> <td>2</td> <td>3</td> <td>0</td> </tr> <tr> <td rowspan="2">$\frac{S_L}{D} = 2.0$</td> <td>2*10³<Re<2*10⁶</td> <td>0.235</td> <td>1970</td> <td>-124*10⁵</td> <td>312*10⁸</td> <td>-274*10¹¹</td> <td>1</td> <td>2</td> <td>3</td> <td>4</td> </tr> <tr> <td>7<Re<800</td> <td>0.188</td> <td>56.6</td> <td>-646</td> <td>6010</td> <td>-183*10²</td> <td>1</td> <td>2</td> <td>3</td> <td>4</td> </tr> <tr> <td>$\frac{S_L}{D} = 2.5$</td> <td>800<Re<2*10⁶</td> <td>0.247</td> <td>-595*10⁻⁶</td> <td>15*10⁻¹³</td> <td>-137*10⁻²⁰</td> <td>396*10⁻²⁴</td> <td>-1</td> <td>-2</td> <td>-3</td> <td>-4</td> </tr> <tr> <td rowspan="8">Staggered</td> <td rowspan="2">$\frac{S_T}{D} = 1.25$</td> <td>600<Re<2*10⁵</td> <td>0.177</td> <td>-311*10⁻⁹</td> <td>117*10⁻¹⁴</td> <td>0</td> <td>0</td> <td>-1</td> <td>-2</td> <td>0</td> <td>0</td> </tr> <tr> <td>3<Re<10³</td> <td>0.795</td> <td>247</td> <td>335</td> <td>-1550</td> <td>2410</td> <td>1</td> <td>2</td> <td>3</td> <td>4</td> </tr> <tr> <td rowspan="2">$\frac{S_T}{D} = 1.5$</td> <td>10³<Re<2*10⁶</td> <td>0.245</td> <td>3390</td> <td>-984*10⁴</td> <td>132*10⁸</td> <td>-599*10¹⁰</td> <td>1</td> <td>2</td> <td>3</td> <td>4</td> </tr> <tr> <td>3<Re<10³</td> <td>0.683</td> <td>111</td> <td>-973*10⁻¹</td> <td>426</td> <td>-574</td> <td>1</td> <td>2</td> <td>3</td> <td>4</td> </tr> <tr> <td rowspan="3">$\frac{S_T}{D} = 2.0$</td> <td>10³<Re<2*10⁶</td> <td>0.203</td> <td>2480</td> <td>-758*10⁴</td> <td>104*10⁸</td> <td>-482*10¹⁰</td> <td>1</td> <td>2</td> <td>3</td> <td>4</td> </tr> <tr> <td>7<Re<10²</td> <td>0.713</td> <td>448*10⁻¹</td> <td>-126</td> <td>-582</td> <td>0</td> <td>1</td> <td>2</td> <td>3</td> <td>0</td> </tr> <tr> <td>10²<Re<10⁴</td> <td>0.343</td> <td>303</td> <td>-71700</td> <td>88*10⁵</td> <td>-38*10⁷</td> <td>1</td> <td>2</td> <td>3</td> <td>4</td> </tr> <tr> <td rowspan="2">$\frac{S_T}{D} = 2.5$</td> <td>10⁴<Re<2*10⁶</td> <td>0.162</td> <td>1810</td> <td>792*10⁵</td> <td>-165*10¹⁰</td> <td>872*10¹³</td> <td>1</td> <td>2</td> <td>3</td> <td>4</td> </tr> <tr> <td>10²<Re<5*10³</td> <td>0.33</td> <td>989*10⁻¹</td> <td>-148*10²</td> <td>192*10⁴</td> <td>-862*10⁵</td> <td>1</td> <td>2</td> <td>3</td> <td>4</td> </tr> </tbody> </table>	Arrangement	Condition	Re	c ₀	c ₁	c ₂	c ₃	c ₄	α ₁	α ₂	α ₃	α ₄	In-line	$\frac{S_L}{D} = 1.25$	3<Re<2.10 ³	0.272	207	102	-286	0	1	2	3	0	3<Re<2.10 ³	0.272	207	102	-286	0	1	2	3	0	$\frac{S_L}{D} = 1.5$	2*10 ³ <Re<2*10 ⁶	0.267	2490	-927*10 ⁴	10 ¹⁰	0	1	2	3	0	3<Re<2*10 ³	0.263	86.7	-2.02	0	0	1	2	3	0	$\frac{S_L}{D} = 2.0$	2*10 ³ <Re<2*10 ⁶	0.235	1970	-124*10 ⁵	312*10 ⁸	-274*10 ¹¹	1	2	3	4	7<Re<800	0.188	56.6	-646	6010	-183*10 ²	1	2	3	4	$\frac{S_L}{D} = 2.5$	800<Re<2*10 ⁶	0.247	-595*10 ⁻⁶	15*10 ⁻¹³	-137*10 ⁻²⁰	396*10 ⁻²⁴	-1	-2	-3	-4	Staggered	$\frac{S_T}{D} = 1.25$	600<Re<2*10 ⁵	0.177	-311*10 ⁻⁹	117*10 ⁻¹⁴	0	0	-1	-2	0	0	3<Re<10 ³	0.795	247	335	-1550	2410	1	2	3	4	$\frac{S_T}{D} = 1.5$	10 ³ <Re<2*10 ⁶	0.245	3390	-984*10 ⁴	132*10 ⁸	-599*10 ¹⁰	1	2	3	4	3<Re<10 ³	0.683	111	-973*10 ⁻¹	426	-574	1	2	3	4	$\frac{S_T}{D} = 2.0$	10 ³ <Re<2*10 ⁶	0.203	2480	-758*10 ⁴	104*10 ⁸	-482*10 ¹⁰	1	2	3	4	7<Re<10 ²	0.713	448*10 ⁻¹	-126	-582	0	1	2	3	0	10 ² <Re<10 ⁴	0.343	303	-71700	88*10 ⁵	-38*10 ⁷	1	2	3	4	$\frac{S_T}{D} = 2.5$	10 ⁴ <Re<2*10 ⁶	0.162	1810	792*10 ⁵	-165*10 ¹⁰	872*10 ¹³	1	2	3	4	10 ² <Re<5*10 ³	0.33	989*10 ⁻¹	-148*10 ²	192*10 ⁴	-862*10 ⁵	1	2	3	4
		Arrangement	Condition	Re	c ₀	c ₁	c ₂	c ₃	c ₄	α ₁	α ₂	α ₃	α ₄																																																																																																																																																																											
		In-line	$\frac{S_L}{D} = 1.25$	3<Re<2.10 ³	0.272	207	102	-286	0	1	2	3	0																																																																																																																																																																											
				3<Re<2.10 ³	0.272	207	102	-286	0	1	2	3	0																																																																																																																																																																											
			$\frac{S_L}{D} = 1.5$	2*10 ³ <Re<2*10 ⁶	0.267	2490	-927*10 ⁴	10 ¹⁰	0	1	2	3	0																																																																																																																																																																											
				3<Re<2*10 ³	0.263	86.7	-2.02	0	0	1	2	3	0																																																																																																																																																																											
			$\frac{S_L}{D} = 2.0$	2*10 ³ <Re<2*10 ⁶	0.235	1970	-124*10 ⁵	312*10 ⁸	-274*10 ¹¹	1	2	3	4																																																																																																																																																																											
		7<Re<800		0.188	56.6	-646	6010	-183*10 ²	1	2	3	4																																																																																																																																																																												
		$\frac{S_L}{D} = 2.5$	800<Re<2*10 ⁶	0.247	-595*10 ⁻⁶	15*10 ⁻¹³	-137*10 ⁻²⁰	396*10 ⁻²⁴	-1	-2	-3	-4																																																																																																																																																																												
		Staggered	$\frac{S_T}{D} = 1.25$	600<Re<2*10 ⁵	0.177	-311*10 ⁻⁹	117*10 ⁻¹⁴	0	0	-1	-2	0	0																																																																																																																																																																											
				3<Re<10 ³	0.795	247	335	-1550	2410	1	2	3	4																																																																																																																																																																											
			$\frac{S_T}{D} = 1.5$	10 ³ <Re<2*10 ⁶	0.245	3390	-984*10 ⁴	132*10 ⁸	-599*10 ¹⁰	1	2	3	4																																																																																																																																																																											
				3<Re<10 ³	0.683	111	-973*10 ⁻¹	426	-574	1	2	3	4																																																																																																																																																																											
			$\frac{S_T}{D} = 2.0$	10 ³ <Re<2*10 ⁶	0.203	2480	-758*10 ⁴	104*10 ⁸	-482*10 ¹⁰	1	2	3	4																																																																																																																																																																											
				7<Re<10 ²	0.713	448*10 ⁻¹	-126	-582	0	1	2	3	0																																																																																																																																																																											
10 ² <Re<10 ⁴	0.343			303	-71700	88*10 ⁵	-38*10 ⁷	1	2	3	4																																																																																																																																																																													
$\frac{S_T}{D} = 2.5$	10 ⁴ <Re<2*10 ⁶		0.162	1810	792*10 ⁵	-165*10 ¹⁰	872*10 ¹³	1	2	3	4																																																																																																																																																																													
	10 ² <Re<5*10 ³	0.33	989*10 ⁻¹	-148*10 ²	192*10 ⁴	-862*10 ⁵	1	2	3	4																																																																																																																																																																														
		<table border="1"> <thead> <tr> <th>Arrangement</th> <th>Condition</th> <th>Re</th> <th>K₁</th> </tr> </thead> <tbody> <tr> <td rowspan="4">In-line</td> <td rowspan="4">$0.06 < \left(\frac{S_T - D}{S_L - D} \right) < 6$</td> <td>$S_T = S_L$</td> <td>All values</td> <td>1</td> </tr> <tr> <td rowspan="3">$0.06 < \left(\frac{S_T - D}{S_L - D} \right) < 6$</td> <td>10³</td> <td>$1.009 \left(\frac{S_T - D}{S_L - D} \right)^{-0.744}$</td> </tr> <tr> <td>10⁴</td> <td>$1.007 \left(\frac{S_T - D}{S_L - D} \right)^{-0.655}$</td> </tr> <tr> <td>10⁵</td> <td>$1.004 \left(\frac{S_T - D}{S_L - D} \right)^{-0.539}$</td> </tr> </tbody> </table>	Arrangement	Condition	Re	K ₁	In-line	$0.06 < \left(\frac{S_T - D}{S_L - D} \right) < 6$	$S_T = S_L$	All values	1	$0.06 < \left(\frac{S_T - D}{S_L - D} \right) < 6$	10 ³	$1.009 \left(\frac{S_T - D}{S_L - D} \right)^{-0.744}$	10 ⁴	$1.007 \left(\frac{S_T - D}{S_L - D} \right)^{-0.655}$	10 ⁵	$1.004 \left(\frac{S_T - D}{S_L - D} \right)^{-0.539}$																																																																																																																																																																						
Arrangement	Condition	Re	K ₁																																																																																																																																																																																					
In-line	$0.06 < \left(\frac{S_T - D}{S_L - D} \right) < 6$	$S_T = S_L$	All values	1																																																																																																																																																																																				
		$0.06 < \left(\frac{S_T - D}{S_L - D} \right) < 6$	10 ³	$1.009 \left(\frac{S_T - D}{S_L - D} \right)^{-0.744}$																																																																																																																																																																																				
			10 ⁴	$1.007 \left(\frac{S_T - D}{S_L - D} \right)^{-0.655}$																																																																																																																																																																																				
			10 ⁵	$1.004 \left(\frac{S_T - D}{S_L - D} \right)^{-0.539}$																																																																																																																																																																																				

			10 ⁶	$1.218 - 0.297 \left(\frac{S_T-D}{S_L-D}\right) + 0.0265 \left(\frac{S_T-D}{S_L-D}\right)^2$	
			10 ⁷	1	
		Staggered	$\frac{2S_T}{S_L} = 1.155$	All values 1	
			$0.5 < \left(\frac{2S_T}{S_L}\right) < 1.2$	10 ³	$\left(\frac{2S_T}{S_L}\right)^{-0.048}$
			$0.45 < \left(\frac{2S_T}{S_L}\right) < 3.5$	10 ⁴	$1.28 - \frac{0.708}{\left(\frac{2S_T}{S_L}\right)} + \frac{0.55}{\left(\frac{2S_T}{S_L}\right)^2} - \frac{0.113}{\left(\frac{2S_T}{S_L}\right)^3}$
			$0.45 < \left(\frac{2S_T}{S_L}\right) < 3.5$	10 ⁵	$2.016 - 1.675 \left(\frac{2S_T}{S_L}\right) + 0.948 \left(\frac{2S_T}{S_L}\right)^2 - 0.234 \left(\frac{2S_T}{S_L}\right)^3 + 0.021 \left(\frac{2S_T}{S_L}\right)^4$
			$0.45 < \left(\frac{2S_T}{S_L}\right) < 1.6$	10 ⁶	$2.016 - 1.675 \left(\frac{2S_T}{S_L}\right) + 0.948 \left(\frac{2S_T}{S_L}\right)^2 - 0.234 \left(\frac{2S_T}{S_L}\right)^3 + 0.021 \left(\frac{2S_T}{S_L}\right)^4$
			$1.25 < \left(\frac{2S_T}{S_L}\right) < 3.5$	10 ²	$0.93 \left(\frac{2S_T}{S_L}\right)^{0.48}$
			$1.25 < \left(\frac{2S_T}{S_L}\right) < 3.5$	10 ³	$0.951 \left(\frac{2S_T}{S_L}\right)^{0.284}$
Short et al. [93]	<u>Circular staggered micropillars</u> $1.88 < \frac{H}{D} < 7.25$ $2.00 < \frac{S_T}{D} < 6.41$ $1.83 < \frac{S_L}{D} < 3.21$ $175 < Re_\mu < 45000$	<p>For all Re_μ</p> $f = 12.88 \left(\frac{S_L}{D}\right)^{-1.8} \left(\frac{S_T}{D}\right)^{-0.43} \left(\frac{H}{D}\right)^{-0.53} Re_\mu^{-0.28}$ <p>For all Re_μ and $H/D < 7.5$</p> $f = 7.48 \left(\frac{S_L}{D}\right)^{-1.4} \left(\frac{S_T}{D}\right)^{-0.61} \left(\frac{H}{D}\right)^{-0.11} Re_\mu^{-0.31}$ <p>For $Re_\mu < 1000$ and $H/D < 7.5$</p> $f = 140.4 \left(\frac{S_L}{D}\right)^{-1.3} \left(\frac{S_T}{D}\right)^{-0.78} \left(\frac{H}{D}\right)^{-0.55} Re_\mu^{-0.65}$ <p>For $Re_\mu > 1000$ and $H/D < 7.5$</p> $f = 0.884 \left(\frac{S_L}{D}\right)^{-1.4} \left(\frac{S_T}{D}\right)^{-0.54} \left(\frac{H}{D}\right)^{0.056} Re_\mu^{-0.08}$			
Moore et al. [94]	<u>Circular staggered micropillars</u> $0.52 < \frac{H}{D} < 1.09$	$f = 10.52 k_1 \left(\frac{H}{D}\right)^{0.28+(1-k_1)} Re_\mu^{-0.39+(1-k_2)}$ $k_1 = e^{4.3\left(\frac{d-H}{H}\right)}$			

	$1.3 < \frac{S_T}{D} < 1.36$ $1.13 < \frac{S_L}{D} < 1.18$ $\frac{d-H}{H} \leq 0.26$ $200 < Re_\mu < 20000$	$k_2 = e^{0.8\left(\frac{d-H}{H}\right)}$
<p>Moore and Joshi[95]</p>	<p><u>Circular staggered micropillars</u></p> $0.5 < \frac{H}{D} < 1.1$ $1.3 < \frac{S_T}{D} < 1.36$ $1.13 < \frac{S_L}{D} < 1.18$ $200 < Re_\mu < 10000$	<p>For $100 < Re_\mu < 1000$</p> $f = 19.04 \left(\frac{H}{D}\right)^{-0.742} \left(\frac{\frac{d-H}{H}+H}{H}\right)^{0.505} Re_\mu^{-0.502}$ <p>For $1000 < Re_\mu < 10000$</p> $f = 12.8 \left(\frac{H}{D}\right)^{-0.138} \left(\frac{\frac{d-H}{H}+H}{H}\right)^{-0.183} Re_\mu^{-0.420}$
<p>Mita and Qu [72]</p>	<p><u>Circular staggered micropillars</u></p> $\frac{H}{D} = 3.8$ $\frac{S_T}{D} = 2.2$ $\frac{S_L}{D} = 2.2$ $26 < Re_\mu < 776$	$f = 0.40947 + \frac{39.808}{Re_\mu} + \frac{727.13}{Re_\mu^2} - \frac{25465}{Re_\mu^3} - \frac{125650}{Re_\mu^4}$
<p>Chang et al. [96]</p>	$\frac{H}{D} = 32.5$ $\frac{S_T}{D} = 2$ $\frac{S_L}{D} = 2$ $0 \leq \frac{d-H}{d} \leq 0.75$ $10000 \leq Re_\mu \leq 30000$	$f = m * Re_\mu^n$ $m = 0.078 + 0.007e^{-2.16*\frac{d-H}{D}}$ $n = -0.397 + 0.608e^{-0.298*\frac{d-H}{d}}$

<p>Koşar et al. [63]</p>	<p><u>Diamond, staggered arrangement</u> $\frac{H}{D} = 2$ $\frac{S_T}{D} = \frac{S_L}{D} = 5$ $5 < Re_\mu < 128$</p>	$f = \frac{1126}{Re_\mu^{1.1}} \left(\frac{H}{D} + 1\right)^{1.5} \left(\frac{S_T S_L}{A_{\mu pillar}}\right)^{-0.4} + \frac{6.6}{Re_\mu^{0.7}} \left(\frac{1}{\frac{H}{D} + 1}\right)^{1.7} \left(\frac{S_T S_L}{A_{\mu pillar}}\right)^{-1}$
<p>[63]</p>	<p><u>Circular, in line arrangement</u> $\frac{H}{D} = 1$ $\frac{S_T}{D} = \frac{S_L}{D} = 1.5$ $5 < Re_\mu < 128$</p>	$f = \frac{7259}{Re_\mu^{1.7}} \left(\frac{H}{D} + 1\right)^{1.9} \left(\frac{S_T S_L}{A_{\mu pillar}}\right)^{-0.4} + \frac{54}{Re_\mu^{0.7}} \left(\frac{1}{\frac{H}{D} + 1}\right)^2 \left(\frac{S_T S_L}{A_{\mu pillar}}\right)^{-0.7}$
<p>Prasher et al. [64]</p>	<p><u>Square</u> $\frac{H}{D} = \{1.3; 2.48\}$ $\frac{S_T}{D} = \{2; 2.4\}$ $\frac{S_L}{D} = \{4; 2.4\}$ $40 < Re_\mu < 1000$</p>	<p>For $Re_\mu < 100$ $f_{square} = \frac{4}{\pi} f_{circular}$ where f_{square} and $f_{circular}$ are the friction factor coefficient for square and circular micropillars shape, respectively.</p> <p>For $Re_\mu > 100$ $f_{square} = \sqrt{\frac{4}{\pi}} f_{circular}$</p>
<p>Tullius et al.[66]</p>	<p><u>Ellipse, staggered arrangement</u> $\frac{H}{D} = 0.21$ $\frac{S_T}{D} = 2$ $\frac{S_L}{D} = 2$ $60 < Re_\mu < 1000$</p>	$f = 3.44 \left(\frac{S_L}{D}\right)^{0.2} \left(\frac{S_T}{D}\right)^{0.2} \left(\frac{H}{D}\right)^{0.18} \left(1 + \frac{d-H}{D}\right)^{0.2} Re_\mu^{-0.435}$

<p><u>Diamond, staggered arrangement</u></p> $\frac{H}{D} = 1$ $\frac{S_T}{D} = 2$ $\frac{S_L}{D} = 2$ $60 < Re_\mu < 600$	$f = 1.81 \left(\frac{S_L}{D}\right)^{0.2} \left(\frac{S_T}{D}\right)^{0.2} \left(\frac{H}{D}\right)^{0.18} \left(1 + \frac{d-H}{D}\right)^{0.2} Re_\mu^{-0.435}$
<p><u>Square, staggered arrangement</u></p> $0.25 < \frac{H}{D} < 0.75$ $1 < \frac{S_T}{D} < 5$ $1.5 < \frac{S_L}{D} < 5$ $60 < Re_\mu < 1000$	$f = 5.28 \left(\frac{S_L}{D}\right)^{0.2} \left(\frac{S_T}{D}\right)^{0.2} \left(\frac{H}{D}\right)^{0.18} \left(1 + \frac{d-H}{D}\right)^{0.2} Re_\mu^{-0.435}$
<p><u>Triangle, staggered arrangement</u></p> $\frac{H}{D} = 0.87$ $\frac{S_T}{D} = 2$ $\frac{S_L}{D} = 2$ $60 < Re_\mu < 650$	$f = 2.45 \left(\frac{S_L}{D}\right)^{0.2} \left(\frac{S_T}{D}\right)^{0.2} \left(\frac{H}{D}\right)^{0.18} \left(1 + \frac{d-H}{D}\right)^{0.2} Re_\mu^{-0.435}$
<p><u>Hexagon, staggered arrangement</u></p> $\frac{H}{D} = 0.58$ $\frac{S_T}{D} = 2$ $\frac{S_L}{D} = 2$	$f = 4.53 \left(\frac{S_L}{D}\right)^{0.2} \left(\frac{S_T}{D}\right)^{0.2} \left(\frac{H}{D}\right)^{0.18} \left(1 + \frac{d-H}{D}\right)^{0.2} Re_\mu^{-0.435}$

	$60 < Re_{\mu} < 1000$	
--	------------------------	--

Appendix B

Principle of operation of Raman spectroscopy

Raman microscopy is a non-destructive spectroscopic technique used to determine the molecular composition of a given sample based on inelastic scattering of photons. It specifically provides information about the chemical structure and level of contamination of a given sample. It is not only a qualitative analysis technique but may also be used as a quantitative one. When a monochromatic light is beamed onto a specific substrate from an emitting source (laser), its frequency is slightly modified because of its collision with the molecules of this medium. The light interacts with the vibrations occurred within the substrate, specifically the oscillating dipoles, inducing an energy shift of the photons of the light.

Under the effect of this external electromagnetic field, the electron cloud is deformed. This phenomenon is known as 'polarizability'. Thus, the generated dipole moment is the outcome of molecular polarizability. The electromagnetic radiation emerging from the substrate is collected and sent through a monochromator. The Rayleigh Scatter is the light having the same wavelength as the light source, whereas the Raman scatter is diffused at different wavelength depending on the substrate. Accordingly, the Raman Scatter provides valuable information about the substrate's chemical structure. Hence, the analysis of the diffused light gives information about the substrate.[97]

Appendix C

Table C-1 Experimental conditions and results obtained for the several distillation tests.

Test label	Feed		Residue withdrawal rate (μL/h)	Theoretical volumetric residue to feed flow rate ratio	Temperature gradient		mol% acetone		Mass Balance		Global mass balance	Experimental residue flow rate (μL/h)	Experimental volumetric residue to feed flow rate ratio	NTS	NTS/m
	Flow rate (μL/h)	Acetone mol%			Reboiler (°C)	Condenser (°C)	Distillate	Residue	Distillate	Residue					
Run_1A	200	20%	60	0.3	90.0	57.7	34.2%	1.8%	106%	83%	98%	49.9	0.2	0.9	14.9
Run_1B	200	20%	60	0.3	90	57	13.8%	54.4%	101%	77%	95%	45.9	0.2	-	-
Run_2	250	20%	75	0.3	89.9	57.7	34.5%	1.8%	101%	84%	95%	62.7	0.3	0.9	15.5
Run_3	300	20%	90	0.3	90.0	57.1	28.0%	2.1%	121%	60%	101%	54.2	0.2	0.7	11.0
Run_4A	200	20%	80	0.4	89.9	60.0	46.3%	1.8%	103%	88%	96%	70.4	0.4	1.2	20.0
Run_4B	200	20%	80	0.4	90	57	11.4%	49.6%	113%	81%	101%	64.9	0.3	-	-
Run_5A	250	20%	100	0.4	90.0	57.1	45.2%	1.9%	105%	88%	97%	87.5	0.4	1.2	19.3
Run_5B	250	20%	100	0.4	90	55.9	47.6%	1.4%	104%	91%	98%	91.0	0.4	1.3	22.1
Run_6A	300	20%	125	0.4	90	55.7	38.7%	4.8%	109%	90%	100%	112.6	0.4	0.6	10.1
Run_6B	300	20%	120	0.4	89.7	57.1	30.7%	2.5%	132%	52%	97%	62.9	0.2	0.7	11.0
Run_7A	200	20%	100	0.5	90.0	57.0	66.3%	2.4%	113%	86%	98%	85.5	0.4	1.6	26.2
Run_7B	200	20%	100	0.5	90.0	57.6	32.3%	11.0%	107%	83%	95%	83.4	0.4	0.3	5.7
Run_7C	200	20%	100	0.5	90.0	57.6	32.1%	11.5%	114%	81%	97%	81.4	0.4	0.3	5.5
Run_7D	200	20%	100	0.5	90.0	55.8	53.4%	1.7%	114%	83%	97%	83.2	0.4	1.4	22.9
Run_7E	200	20%	100	0.5	90.0	56.0	28.9%	1.9%	167%	39%	97%	39.3	0.2	0.7	12.1
Run_8A	250	20%	125	0.5	89.8	57.8	54.7%	2.6%	101%	89%	94%	110.7	0.4	1.2	20.4
Run_8B	250	20%	125	0.5	90	57	9.0%	47.1%	100%	80%	91%	100.1	0.4	-	-
Run_8C	250	20%	125	0.5	89.8	57.1	71.8%	2.0%	98%	90%	94%	112.6	0.5	1.8	29.3
Run_8D	250	20%	125	0.5	90	56.4	39.6%	7.9%	102%	96%	99%	113.1	0.5	0.5	8.6
Run_9A	300	20%	150	0.5	89.7	56.5	35.7%	2.3%	147%	56%	97%	84.1	0.3	0.8	13.6
Run_9B	300	20%	150	0.5	90	56.4	30.2%	13.3%	103%	94%	98%	140.4	0.5	0.3	4.6
Run_10A	200	20%	120	0.6	90.1	57.2	71.2%	3.9%	115%	87%	97%	104.9	0.5	1.5	25.5
Run_10B	200	20%	125	0.6	90	56	37.8%	10.2%	117%	93%	101%	116.7	0.6	0.4	7.4
Run_11A	250	20%	150	0.6	90.0	57.8	71.0%	5.5%	124%	91%	103%	137.2	0.5	1.3	22.2

Appendices

Run_11B	250	20%	150	0.6	90	57	11.8%	33.4%	126%	72%	95%	90.3	0.4	-	-
Run_11C	250	20%	150	0.6	90.0	57.0	46.0%	12.7%	96%	86%	90%	129.5	0.5	0.5	8.9
Run_11D	250	20%	150	0.6	90.0	56.8	66.4%	6.7%	112%	88%	96%	131.5	0.5	1.0	16.5
Run_12A	300	20%	180	0.6	90.0	57.7	36.0%	13.2%	110%	87%	96%	156.9	0.5	0.4	6.1
Run_12B	300	20%	175	0.6	90	56.4	12.9%	25.8%	112%	85%	97%	149.6	0.5	-	-
Run_13	250	20%	128	0.5	95.3	57.6	26.7%	1.5%	182%	33%	98%	42.2	0.2	0.8	13.1
Run_14	300	20%	154	0.5	95.0	57.3	45.8%	6.7%	114%	89%	100%	137.4	0.5	0.6	10.8
Run_15	250	20%	145	0.6	80.2	57.4	35.4%	12.1%	104%	90%	96%	130.2	0.5	0.4	6.2
Run_16	250	12%	176	0.7	90.3	56.8	23.8%	7.7%	125%	87%	97%	152.6	0.6	0.3	4.8
Run_17	250	42%	65	0.3	90.5	57.3	62.7%	13.1%	107%	74%	98%	47.9	0.2	0.8	13.3

Table C-2 Global and partial mass balances for the several distillation tests.

Test label	Acetone volume balance			Water volume balance			Acetone mass balance			Water mass balance		
	Acetone out	Acetone in	Global	Water out	Water in	Global	Acetone out	Acetone in	Global	Water out	Water in	Global
Run_1A	0.42	0.40	104%	0.37	0.40	94%	0.33	0.31	104%	0.37	0.40	94%
Run_1B	0.38	0.40	95%	0.38	0.40	94%	0.30	0.31	95%	0.38	0.40	94%
Run_2	0.50	0.50	100%	0.46	0.50	91%	0.39	0.39	100%	0.46	0.50	91%
Run_3	0.63	0.60	106%	0.59	0.60	98%	0.50	0.47	106%	0.59	0.60	98%
Run_4A	0.40	0.40	101%	0.37	0.40	93%	0.32	0.31	101%	0.37	0.40	93%
Run_4B	0.40	0.40	99%	0.41	0.40	103%	0.31	0.31	99%	0.41	0.40	103%
Run_5A	0.51	0.50	102%	0.47	0.50	94%	0.40	0.39	102%	0.47	0.50	94%
Run_5B	0.51	0.50	102%	0.48	0.50	95%	0.40	0.39	102%	0.48	0.50	95%
Run_6A	0.62	0.60	104%	0.59	0.60	98%	0.49	0.47	104%	0.59	0.60	98%
Run_6B	0.62	0.60	103%	0.55	0.60	92%	0.49	0.47	103%	0.55	0.60	92%
Run_7A	0.43	0.40	108%	0.36	0.40	90%	0.34	0.31	108%	0.36	0.40	90%
Run_7B	0.40	0.40	99%	0.37	0.40	92%	0.31	0.31	99%	0.37	0.40	92%
Run_7C	0.42	0.40	104%	0.37	0.40	92%	0.33	0.31	104%	0.37	0.40	92%
Run_7D	0.39	0.41	97%	0.39	0.41	97%	0.31	0.32	97%	0.39	0.41	97%
Run_7E	0.40	0.40	99%	0.38	0.40	95%	0.31	0.31	99%	0.38	0.40	95%
Run_8A	0.46	0.50	91%	0.48	0.50	97%	0.36	0.39	91%	0.48	0.50	97%
Run_8B	0.46	0.50	92%	0.45	0.50	90%	0.36	0.39	92%	0.45	0.50	90%
Run_8C	0.48	0.50	96%	0.46	0.50	92%	0.38	0.39	96%	0.46	0.50	92%
Run_8D	0.49	0.48	102%	0.46	0.48	96%	0.39	0.38	102%	0.46	0.48	96%
Run_9A	0.61	0.60	101%	0.56	0.60	94%	0.48	0.47	101%	0.56	0.60	94%

Appendices

Run_9B	0.62	0.60	103%	0.57	0.60	95%	0.48	0.47	103%	0.57	0.60	95%
Run_10A	0.38	0.40	96%	0.39	0.40	98%	0.30	0.31	96%	0.39	0.40	98%
Run_10B	0.39	0.40	98%	0.42	0.40	104%	0.31	0.31	98%	0.42	0.40	104%
Run_11A	0.55	0.50	110%	0.49	0.50	97%	0.43	0.39	110%	0.49	0.50	97%
Run_11B	0.36	0.38	95%	0.36	0.38	95%	0.28	0.29	95%	0.36	0.38	95%
Run_11C	0.50	0.50	100%	0.50	0.50	100%	0.39	0.39	100%	0.50	0.50	100%
Run_11D	0.50	0.50	100%	0.50	0.50	100%	0.41	0.39	103%	0.46	0.50	91%
Run_12A	0.61	0.60	102%	0.55	0.60	91%	0.48	0.47	102%	0.55	0.60	91%
Run_12B	0.56	0.60	94%	0.59	0.60	99%	0.44	0.47	94%	0.59	0.60	99%
Run_13	0.50	0.50	99%	0.48	0.50	97%	0.39	0.39	99%	0.48	0.50	97%
Run_14	0.64	0.60	106%	0.57	0.60	95%	0.50	0.47	106%	0.57	0.60	95%
Run_15	0.49	0.50	98%	0.47	0.50	94%	0.39	0.39	98%	0.47	0.50	94%
Run_16	0.36	0.35	103%	0.62	0.65	95%	0.28	0.28	103%	0.62	0.65	95%
Run_17	0.76	0.75	102%	0.22	0.25	88%	0.60	0.59	102%	0.22	0.25	88%

La microfluidique au service de l'intensification de la distillation : conception, caractérisation et optimisation d'un outil de laboratoire continu.

De nombreuses études sont désormais orientées sur la mise en œuvre d'une succession d'opérations en continu aux petites échelles. Bien que la miniaturisation des réacteurs soit actuellement bien maîtrisée, il existe encore des domaines peu explorés comme, par exemple, les microséparateurs continus qui sont essentiels pour contrôler, analyser et optimiser les procédés microfluidiques. La miniaturisation de la distillation se heurte à de nombreuses limitations principalement le fait qu'aux petites échelles, la gravité s'efface au profit des forces de surface. Plusieurs études ont essayé de miniaturiser la distillation et se répartissent principalement en trois catégories : microdistillation discontinue, continue de taille intermédiaire et continue sur puce. Cependant, la caractérisation de l'écoulement et les phénomènes qui régissent l'opération de la microdistillation n'ont pas encore été complètement étudiés. Cette étape est un prérequis essentiel pour l'optimisation du dispositif. Par conséquent, l'objet de ce travail est le développement d'une microdistillation performante utilisant des débits allant de 150 à 500 $\mu\text{L}/\text{h}$. Un nouveau « design », offrant deux avantages principaux par rapport à ceux reportés dans la littérature, a été proposé. Tout d'abord, il est apte à traiter des débits plus élevés, tout en maintenant une différence de pression gaz-liquide inférieure à la pression capillaire. Deuxièmement, ce « design » permet une augmentation significative de l'aire interfaciale gaz-liquide, améliorant ainsi le transfert de matière entre le gaz et le liquide. La caractérisation hydrodynamique de la colonne de microdistillation a été envisagée en mesurant la distribution des temps de séjour. Cet outil microfluidique offre de meilleures performances que celles de la littérature (30 étages/m contre 15 étages/m). L'impact de plusieurs paramètres opératoires sur les performances de séparation de l'outil développé a été également étudié.

Mots clés : microdistillation, forces capillaires, séparation multiétage, micropilliers

Microfluidics at the service of intensification of distillation: design, characterization and optimization of a continuous laboratory tool.

Most of the research is now focused towards the implementation of microscale unit operations in series. Reactor miniaturization is currently well-controlled, while a wide gap exists concerning continuous microseparators being critical for controlling, analyzing and optimizing microfluidic processes. Distillation downscaling faces many limitations, principally that interfacial forces outweigh gravity forces at the microscale. Several studies have effectively demonstrated microdistillation and are mainly split into three categories: batch, continuous of intermediate size and continuous on-chip microdistillations. However, the characterization of flow patterns and the phenomena that govern the microdistillation operation have not been fully investigated yet, even though it is an essential prerequisite for the device optimization. Therefore, the objective of this work is the development of an efficient microdistillation dealing with low flow rates (150 - 500 $\mu\text{L}/\text{h}$). A new design offering mainly two advantages compared to those reported in the literature was proposed. Firstly, it displays a significant gain in the gas-liquid interfacial area, thus improving the mass transfer between the gas and the liquid. Secondly, it can proceed with higher flow rates, while keeping the gas liquid pressure difference lower than the capillary one. The hydrodynamic characterization of the microdistillation device was considered by measuring the residence time distribution. It was demonstrated that better performances than those of the literature are obtained (30 stages/m vs 15 stages/m). The effect of the operating parameters on the separation performances of the developed tool was also investigated.

Key words : microdistillation, capillary forces, multistage separation, micropillars

Research unit

The Institute of Condensed Matter Chemistry of Bordeaux, UMR5026, 87 Avenue du Dr Albert Schweitzer, 33600 Pessac